

# Gravitational-wave astronomy of merging compact binaries: Effect of subdominant modes of gravitational radiation

A Thesis

Submitted to the  
Tata Institute of Fundamental Research, Mumbai  
Subject Board of Physics  
for the degree of Doctor of Philosophy

by

**Mukesh Kumar Singh**

International Centre for Theoretical Sciences,  
Tata Insitute of Fundamental Research,  
Bengaluru  
Dec, 2024



# Declaration

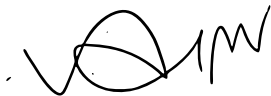
This thesis is a presentation of my original research work. Wherever contributions of others are involved, every effort is made to indicate this clearly, with due reference to the literature, and acknowledgement of collaborative research and discussions.

The work was done under the guidance of Professor Parameswaran Ajith, at the International Centre for Theoretical Sciences, Tata Institute of Fundamental Research, Bangalore.



Mukesh Kumar Singh

In my capacity as the formal supervisor of the record of the candidate's thesis, I certify that the above statements are true to the best of my knowledge.



Parameswaran Ajith

Date: 24 December, 2024

*Dedicated to my parents*

# Acknowledgement

*A journey is best measured in friends, rather than miles.*

– Tim Cahill

---

Navigating through PhD life is often compared to a solitary endeavor. I have felt that, while it does require immense individual dedication and effort, it equally relies on a network of support and collaboration. As this academic journey of PhD, filled with moments of joy and challenges, at times, comes to a close, it is my privilege and responsibility to acknowledge a number of people who stood by me through thick and thin. Without their support, I would not have been able to make it this far.

First and foremost, I would like to express my sincere and deepest gratitude to my supervisor, Prof. Parameswaran Ajith, for his invaluable guidance, and unwavering support throughout my PhD. Ajith has not only given me his expert advice concerning my research but also encouraged me to be an independent researcher. I owe Ajith a lot for enhancing my presentation skills, research ethics, and many more things, impossible to list here.

I am extremely grateful to my collaborators, in no particular order, Shasvath, Arif, Deep, Divyajyoti, Aditya V, Shriharsh, Sourabh. I have particularly admired Shasvath's ability to see through the ideas and turn them into concrete projects. Shasvath has been a co-author in all my papers going into this thesis which is a testament of how crucial his mentorship has been for the completion of my PhD. I would also like to thank Ajit, Abhirup, Apratim, Rahul, Sumit, Gayathri, and Haris for helping me during my visits to ICTS before joining PhD.

I am also grateful to my thesis monitoring committee, Prayush Kumar, Pallavi Bhat, and Sourav Chatterjee, for their insightful feed-

back, constructive criticism, and the time they invested in keeping track of my progress over the years.

To the members of the Astrophysical Relativity group, thank you for all the insightful discussions, be it our regular group meetings or unofficial gatherings. Thank you Bala for explaining to me the connection between radiative multipoles and source moments. A part of the second chapter is a culmination of the conversation with Bala and thanks to GW theory discussion group – Srashti, Uddepta, Souvik, Soumyadip, Aditya Sharma.

I would like to thank Sathya and his group at Penn State, particularly, Ish, Koustav, Shanika, Aviral, Estuti, and Divya, for making me feel like a part of their group. We had several interesting discussions during my visit as a Fulbright Nehru Doctoral Fellow.

I am very fortunate to be part of the LIGO Scientific Collaboration. It has not only provided me with a wealth of resources but also a platform to interact with researchers across the globe. In particular, I have been benefited from the interactions with the low-latency group, especially, Leo, and Shaon; and the rates and population group. A special thanks to Colm and Maya for their helpful suggestions in understanding the selection effects and population inference in GWs.

I am indebted to my teachers, Mukul, Sushma, Pramod, Deepak, Hari Shanker, and Ankit for igniting my interest in Science and Mathematics during grades 9-12 in my school years. Special thanks to Khempal Yadav for encouraging me to pursue my higher education in physics, which has led me to where I am today.

I also extend my heartfelt thanks to Pratima, Anant, and K Chandramani for inculcating my passion for physics beyond the coursework during my undergraduate studies. Thanks to Pranjal Trivedi for introducing me to Astrophysics and Cosmology. Thank you, Chandra, for offering me a project in gravitational-wave astronomy and introducing me to the ICTS Astrophysical Relativity group that I ended up joining as a graduate student. Thank you, Chandra, Suresh, Sunethra, Dawood, Ashwin, Vaibhav, and Satyanarayana, for being wonderful mentors during my postgraduate studies.

Thanks to my friends, Aakash, Tarun, Kamal Kant, Sunil, Satendra, Bubunu, Motilal, and Kamlesh, for the interesting discussions about physics and everything else. To my friends at ICTS, Uddepta,

Anup, and Souvik, it has been a privilege to share the graduate years both academically and otherwise. Thanks, Souvik for sharing the passion for eating Rava Dosa (especially during our morning classes at IISc). Uddeпта, Anup, and Ankur, it has been an absolute pleasure to play badminton with you guys. I have loved every moment of it.

To my officemates, Souummyadip, Godwin, Irshad, Arnab, Koustav, Monika, and Prashant, thank you for your patience and for bearing with the inconveniences I might have caused. I have enjoyed our middle-of-the-work conversations about things that were hardly relevant to research, well, most of the times.

To my parents, no words can express how grateful I am for all the sacrifices you have made to ensure that I got the best possible. You never showed disappointment in my failures but celebrated my tiniest achievements with immense pride. This thesis is dedicated to both of you.

I would also like to thank my brother, sister-in-law, grandparents, uncle, auntie, and cousins for their love and support. I am also very fortunate to share a significant portion of my schooling with my brother.

Last but not least, I am incredibly fortunate to have a partner in life, my wife, Divyajyoti, whose support has been instrumental in both my personal and academic life. Apart from being a collaborator in one of my papers, she has helped me with programming innumerable times.





# Abstract

Gravitational radiation from a compact binary merger, such as binary black hole (BBH), binary neutron star (BNS), and neutron star-black hole (NSBH) binary, is, at the leading order, quadrupolar. But there exist higher order terms (“subdominant” or “higher” modes, HMs) that are often neglected for GW data analysis. However, they make appreciable contribution to the radiation from asymmetric binaries (e.g., binaries with unequal masses or misaligned spins). While the first searches and parameter estimation (PE) efforts effectively neglected these effects, there has been an increasing appreciation of the effect of HMs in recent times. As the sensitivity of GW detectors continues to improve, they will detect a plethora of GW signals in the next decade. This will enable precision probes of fundamental physics, astrophysics, and cosmology. This necessitates accurate modelling of the detailed properties of the GW signals.

A substantial portion of this thesis focuses on improving the GW early warning of compact binary mergers by using the effect of HMs (Chapters 3 and 4). The idea is that HMs, that oscillate at higher multiples of the orbital frequency, enter the sensitivity band of the detector earlier than the dominant mode. This can potentially improve the early warning of compact binary mergers, enabling astronomers to point their telescopes to the source location to capture the prompt emission and precursors. Another aspect of this thesis pivots around understanding the impact of HMs on the inference of population properties (such as mass and redshift distributions of BHs) of the compact binary mergers detected through GWs (Chapter 5). Here we investigate the systematic biases in inferring the population properties when HMs are neglected in the PE of individual GW events. This will be crucial in understanding the stellar evolution, supernova physics, and formation channels of merging compact binaries.



# List of Figures

- 1.1 The effect of  $+$  and  $\times$  polarizations of the GWs passing through a ring of particles. (Credit: Belahcene [42]) 6
- 1.2 Crab Nebula, a remnant of a star's supernova explosion in Taurus constellation, one of the largest images ever taken by Hubble Space Telescope [credit: NASA, ESA, J. Hester, and A. Loll] 7
- 1.3 An example of a burst GW signal emitted by a core-collapse supernova (credit: A. Stuver/LIGO using data from C. Ott, D. Burrows, et al) 8
- 1.4 A schematic of a non-axisymmetric spinning NS and generation of monochromatic GWs (credit: <https://physics.anu.edu.au>) 8
- 1.5 A continuous GW signal [credit: A. Stuver/LIGO] 8
- 1.6 The cartoons in the top show the three stages of the BBH merger – inspiral, merger, and ringdown and the bottom section plot the strain amplitude emitted in GW<sub>150914</sub>, the first BBH merger detected. The grey shaded band correspond to the 90% probability regions of the reconstructed signal using theoretical models and the solid red line is a numerical relativity (NR) waveform with parameters consistent with those recovered from GW<sub>150914</sub>. (credit: Taken from Abbott et al. [2]) 10
- 1.7 A stochastic GW signal [credit: A. Stuver/LIGO] 11
- 1.8 GW spectrum showing frequencies and wavelengths corresponding to various sources and the relevant GW detectors. (Credit: P. Ajith/ICTS) 12
- 1.9 A schematic of a resonant bar detector with Joseph Weber working on a real one. 13
- 1.10 An interferometer. (Credit: Caltech/MIT/LIGO Lab; modified by myself) 14
- 1.11 Interference pattern. (Credit: [www.explainthatstuff.com](http://www.explainthatstuff.com)) 14
- 1.12 The relative orientation of sky frame and detector frame. (Image Credit: Sathyaprakash and Schutz 2009) 16

- 1.13 The antenna power pattern for a single interferometer averaged over the polarizations of the incoming wave. This also corresponds to the detection volume of the instrument or its maximum reach in different directions. (Credit: Schutz 2011) 16
- 1.14 The power spectral density for LIGO Livingston detector (in grey) corresponding to their second observing run (O2) along with various noise sources (Credit: Taken from Vajante et al (2019)) 19
- 1.15 Network of detectors (Credit: Caltech/MIT/LIGO Lab) 20
- 1.16 Depiction of the compact objects detected through LIGO-Virgo-KAGRA detectors as well as EM observations. (Credit: LVK/Aaron Geller/Northwestern) 22
- 1.17 Horizon distance for various current and future generations of detectors assuming BNS (yellow dots) and BBH (white dots) mergers as the sources of GWs. (Credit: Luck et al 2022) 26
- 2.1 The ratio of frequency domain amplitudes for the two subleading modes 33 (solid) and 44 (dashed) to dominant 22 mode. The larger mass ratio results in the larger amplitude ratios (in maroon). 35
- 2.2 The Fourier domain amplitudes of the dominant 22 (solid) and the next subleading 33 mode (dashed) are shown corresponding to two different total masses  $M_{\text{tot}} = 600, 1200M_{\odot}$ . The 22 mode spends less time (smaller frequency range) for heavier binary as compared to the 33 mode. The black dashed-dotted line is the noise amplitude spectral density, i.e.  $\sqrt{S_n(f)}$ , of the advanced LIGO detector. 36
- 2.3 The amplitudes of several multipoles, 22, 33, and 44 are plotted for a binary system with  $q = 1$ . The presence of precessing spins (in green) leads to modulations in the multipoles, especially prominent in 33 and 44 modes. In the absence of the precession (in brown), the 33 mode vanishes completely. 37
- 2.4 Inclination-dependent amplitude, Eq. 2.43 of the + polarization is plotted as a function of inclination. Most of the HMs (except the ones with  $m = 2$ ) vanish at near face-on configuration and contribute to near edge-on configuration. The  $m = 2$  modes are normalized at  $\iota = 0^\circ$  and the rest of the modes at  $\iota = 90^\circ$ , similar to Mills and Fairhurst [149]. 37

- 2.5 The orthogonal optimal SNR in the strongest HM,  $33$  (orange) is measured for GW190412 event at  $3\sigma$  confidence (dashed line) based on the expected distribution of optimal SNR due to Gaussian noise (black dotted line). There is marginal evidence of precession in this event but the median value of the expected SNR due to precession is consistent with the noise (blue) (Credit: R Abbott et al 2020) 39
- 2.6 The measurement of the luminosity distance and orbital inclination for GW190412 event is compared when using a dominant mode-only waveform model (in blue) to a multipolar waveform model (dashed). The inclusion of HMs has significantly improved the estimate of  $\iota$  and  $d_L$ . (Credit: R Abbott et al 2020) 41
- 3.1 Schematic illustration of how different modes appear in the detector band. We show the real part of the *whitened* modes  $h_{\ell m}$  (with  $\ell = m = \{2, 3, 4\}$ ) of a compact binary coalescence waveform ( $d_L = 500$  Mpc,  $q = 5$ ,  $m_1 + m_2 = 80M_\odot$ ), as a function of time. The modes are whitened by the noise PSD of Advanced LIGO to show their expected contribution to the SNR. The higher the  $m$ , the earlier it enters the frequency band of the detector. This can be seen by the appearance of the non-zero amplitudes of the HMs at a time  $\Delta\tau$  before the merger (dashed black vertical line), where  $\Delta\tau$  increases with increasing  $m$ . 46
- 3.2 Projected noise amplitude spectral densities for the three LIGO detectors (including LIGO India) and the Virgo detector for the O5 and Voyager scenarios, as well as for the two Cosmic Explorers and the Einstein Telescope. The lower limit on the detector bandwidths for O5 and Voyager is set to 10 Hz. For 3G, this limit is set to 5 Hz. (See [9, 120, 161, 159, 130, 5, 115]) 50
- 3.3 The sky area and SNR evolution as a function of time to coalescence for binary with parameters  $m_1 = 15M_\odot$ ,  $m_2 = 1.5M_\odot$ ,  $\iota = 60\text{deg}$ ,  $d_L = 40\text{Mpc}$  and optimal sky-location (that minimizes the sky area) in O5 observing scenario. The sky area is consistently smaller and SNR consistently larger with the inclusion of HMs in addition to the dominant mode (squares) as compared to only the dominant mode (circles) case. 51

- 3.4 Left plots: localisation sky-area (at 90% confidence) using HMs, for an early warning time of 45 s. Middle plots: the same as a fraction of the sky area achieved using only the dominant modes. Right plots: the gains in the early warning time for a fiducial sky area of 1000 sq. deg, due to the inclusion of HMs. These plots correspond to binaries with  $m_2 = 1 - 2.5M_\odot$  and  $q = 4 - 20$ , located at 40 Mpc (other extrinsic parameters set to their optimal values, with inclination  $i = 60$  deg.). Two sets of black contours, corresponding to 2H (solid) and SLy (dotted) EOSs for different values of BH spin  $\chi_1$  are plotted to demarcate the region of binaries that will potentially emit an EM counterpart. 52
- 3.5 Gains in early-warning time upon inclusion of HMs, for the 3G scenario, assuming a fiducial sky-area of 100 sq. deg., and sources located at 100 Mpc. The other extrinsic parameters are set to their optimal values, with inclination  $i = 60$  deg. These gains can be as much as 1.5 minutes for relatively low-mass systems that are highly asymmetric. For binaries that are likely to have EM counterparts even for moderate to low spins of the primary mass, the gains can be as much as a minute. 53
- 3.6 *Bottom*: Effect of varying distance on sky-area with (without) the inclusion of HMs, for three early-warning times, in the O5 scenario. The sky area reduces as the square of the distance. *Top*: Same as in *Bottom* plot but varying only inclination angle. The sky area is rather weakly dependent on the choice of inclination angle, while the improvement over the dominant mode is the largest for the near-edge-on configuration of the binary. 54
- 3.8 Same as Fig. 3.7, but for the  $\sim 55\%$  NSBH systems from the total population of 100,000 compact binaries. NSBH systems are selected from the total population such that  $m_1 \geq 5.0M_\odot$ . Employing HMs to determine localisation sky areas results in up to  $\sim 60\%$  and  $\sim 70\%$  of the NSBH systems having sky area reduction factors  $\gtrsim 2$  for O5 and Voyager scenario respectively as compared to only dominant mode. In the O5 scenario, at best  $\sim 90\%$  (70%),  $\sim 40\%$  (20%) and  $\sim 10\%$  ( $> 10\%$ ) events have localisation sky areas less than 1000 deg. sq. 20s, 40s, and 60s before the merger respectively when including (not including) HMs. These numbers increase to  $\sim 100\%$  (80%),  $\sim 65\%$  (35%) and  $\sim 30\%$  (10%) in Voyager. 56

3.9 Same as in Fig. 3.8, except that here we consider only EM-Bright systems. The EOS is assumed to be AP<sub>4</sub>, and the spin distribution for the primary component is assumed to be isotropic. Out of total NS-BHs ( $\sim 55\%$ ),  $\sim 2\%$  systems are found to be EM-Bright among which  $\sim 20\%$  and  $\sim 40\%$  events have localisation sky area improved by a factor  $\gtrsim 2$  for O<sub>5</sub> and Voyager respectively while using HMs. In the O<sub>5</sub> scenario, at best  $\sim 100\%$  ( $> 95\%$ ),  $\sim 80\%$  (70%) and  $\sim 45\%$  (30%) events have localisation sky areas less than 1000 deg. sq. 20s, 40s, and 60s before the merger respectively while using (not using) HMs. These numbers increase to  $\sim 100\%$  (100%),  $\sim 90\%$  (80%) and  $\sim 75\%$  (50%) in Voyager. 57

3.10 Same as Fig. 3.9 with the isotropic distribution of the primary's spin changed to an aligned one. In this case, out of the total NSBHs,  $\sim 15\%$  systems are found to be EM-Bright among which  $\sim 40\%$  and  $\sim 55\%$  events have localisation sky area improvement factor  $\gtrsim 2$  for O<sub>5</sub> and Voyager respectively while using HMs. In the O<sub>5</sub> scenario, at best  $\sim 97\%$  (95%),  $\sim 75\%$  (55%) and  $\sim 30\%$  (20%) events have localisation sky areas less than 1000 deg. sq. 20s, 40s, and 60s before the merger respectively while using (not using) HMs. These numbers increase to  $\sim 100\%$  ( $> 97\%$ ),  $\sim 90\%$  (75%) and  $\sim 65\%$  (40%) in Voyager. 58

3.11 Fraction of the NSBH population that are EM-Bright, for isotropic and aligned BH-spin distributions and a range of EOSs [10]. These fractions vary from  $\sim 0.5\% - 10\%$  for the isotropic spin distribution, and  $\sim 5\% - 35\%$  for the aligned spin distribution. 59

3.13 The early-warning time gains are shown while localizing compact binaries for three different sky areas of 100 (blue), 500 (orange), and 1000 (green) deg. sq. in 3G scenario. We get time gains up to several minutes while employing HMs in localisation as compared to when we would have used only quadrupole mode. Again, the analysis has been repeated for three upper limits on distance. 60

4.2 Same as in plot (4.1) but we show improvements in the measurement of orbital inclination ( $i$ ) of compact binary mergers with the inclusion of higher modes. The orbital inclination measurements improve by a factor  $\sim 1 - 1.5(1 - 2)[1 - 3]$ , with the inclusion of higher modes, for an early warning time of 45(45)[300] seconds, in O<sub>5</sub>(Voyager)[3G]. 73

- 4.3 *Top panel:* the total number of galaxies localized (at 90% confidence) that can be potential hosts of the compact binary merger with the inclusion of higher modes. This number can be as small as  $\sim 1000(200)[0.2]$  at 45(45)[300] seconds before the merger for binary systems that will have a potential EM counterpart in O5 (Voyager) [3G]. *Bottom panel:* the reduction in the number of potential host galaxies with the inclusion of higher modes relative to only dominant mode. This reduction factor can be as  $\sim 1 - 2.5(1.2 - 4)[1.2 - 10]$  for an early warning time of 45(45)[300] seconds before the merger in O5(Voyager)[3G]. 74
- 4.4 Distributions of the measurement errors in  $d_L$  and  $\iota$  for 1000 compact binary mergers with varying sky-locations and polarizations. The *left column* shows the cumulative distributions of  $d_L$  errors. Solid (dashed) lines correspond to errors computed including (neglecting) the higher mode contributions for three different early warning times of 20, 30,, and 45 seconds. In O5 (Voyager) scenario, the median  $d_L$ -errors are 44 - 81(25 - 51) Mpc at 20 - 45 seconds before the merger respectively. The *right column* shows the reductions of  $d_L$ -errors with the inclusion of higher modes relative to only dominant mode measurements. For over 50% of the binaries, inclusion of higher modes will cause the  $d_L$  errors to reduce by a factor of  $\sim 1.2 - 2(1.3 - 5)$  in O5 (Voyager). 75
- 5.1 The distribution of the injected total population (in purple) of non-spinning BBH mergers along with the detected one (in green) that is computed assuming the network matched-filter SNR is greater than the threshold value of 8. 86
- 5.3 The ratio of the effective bias ( $\epsilon^{22}/\epsilon^{\text{HM}+22}$ ) estimated for chirp mass, mass ratio, and luminosity distance recovery when using a multipolar waveform compared to a dominant mode waveform as a function of  $q$  and  $\iota$ . The size of the marker corresponds to the SNR contribution due to the HMs only. 88
- 5.4 Same as Fig. 5.3 but the color map represents the Bayes factors ( $\mathcal{B}$ ) between a multipolar (HM+22) and only dominant mode (22) waveform models. In the asymmetric region of parameter space (low  $q$  and non-face-on inclination), the multipolar waveform model is preferred over just the dominant mode. 89



5.7 Same as in Fig. 5.5 but the injections with  $45 \leq \iota \leq 135$  degrees. Increasing the fraction of events with observable contribution from HMs leads to larger bias in the estimates of hyper-parameters, especially, mass-ratio power-law spectral index  $\beta_q$ , maximum mass  $m_{\max}$  and merger rate evolution hyper-parameter  $\lambda_z$ . 95



# List of Tables

- 4.1 The priors on parameters for which the Fisher matrix is computed. Here  $U(a,b)$  denotes the uniform probability between  $a$  and  $b$ . The luminosity distance, mass, time, and all the angles are measured in Mpc,  $M_{\odot}$ , seconds, and radians respectively. 70
- 4.2 Median values of the distribution of uncertainties in the estimation of the luminosity distance  $d_L$  and inclination angle  $i$  using templates including the contribution of higher modes. These correspond to two observing scenarios (O5 and Voyager) and three different early warning times (20, 30, and 45 seconds). The median improvement factors (as compared to the estimates using only 22 mode) are shown in parentheses. 76
- 5.1 The population model hyper-parameters description and their corresponding priors chosen for hierarchical inference. Above,  $U(a,b)$  indicates uniform distribution between  $a$  and  $b$ . 85
- 7.1 Ellipsoid/ellipse axes scaling factor ( $\beta_q$ ) values at various credible intervals in  $q$ -dimensions [128, 81] 107



# Contents

<b>Acknowledgement</b>	<b>v</b>
<b>Abstract</b>	<b>ix</b>
<b>List of Figures</b>	<b>xi</b>
<b>List of Tables</b>	<b>xix</b>
<b>1 Introduction</b>	<b>3</b>
1.1 Gravitational Waves . . . . .	3
1.2 Sources . . . . .	7
1.2.1 Burst sources . . . . .	7
1.2.2 Continuous sources . . . . .	7
1.2.3 Binary systems . . . . .	8
1.2.4 Stochastic sources . . . . .	10
1.3 The gravitational-wave spectrum . . . . .	11
1.4 Detectors and Detection . . . . .	12
1.4.1 Resonant bar detectors . . . . .	12
1.4.2 Laser interferometers . . . . .	13
1.4.3 The response of a ground-based interferometer	14
1.4.4 Noise characteristics of the detector . . . . .	17
1.4.5 Current global network of detectors . . . . .	19
1.4.6 Detection . . . . .	20
1.5 Overview of LIGO-Virgo-KAGRA observations . . . . .	21
1.5.1 Science summary of observations . . . . .	24
1.6 Future Prospects: Future Detectors . . . . .	25
<b>2 Multipole Expansion of Gravitational Radiation</b>	<b>29</b>
2.1 Generation of GWs in linearized theory . . . . .	29
2.1.1 Weak field expansion . . . . .	30
2.1.2 Low-velocity expansion . . . . .	30

2.2	Multipolar gravitational waveforms . . . . .	34
2.2.1	Contribution of asymmetries to higher modes . . . . .	35
2.3	Impact of higher modes on the detection . . . . .	38
2.4	Observational evidence of higher modes . . . . .	39
2.5	Science gain due to higher modes . . . . .	39
2.5.1	Breaking degeneracies . . . . .	40
2.5.2	Improving the measurement of cosmology . . . . .	40
2.5.3	Unbiased and accurate inference . . . . .	41
2.5.4	New tests of GR . . . . .	41
2.6	Focus of this thesis . . . . .	42
<b>3</b>	<b>Improving Gravitational-Wave Early Warning of Compact Binary Mergers using Higher Modes</b>	<b>43</b>
3.1	Motivation . . . . .	43
3.2	Higher modes enter early in the detector's band . . . . .	45
3.3	localisation of GW sources with triangulation . . . . .	45
3.4	Observing scenarios . . . . .	49
3.5	Results . . . . .	50
3.5.1	Demonstration of early-warning with higher modes	51
3.5.2	Sky-localisation improvement as a function of masses . . . . .	51
3.5.3	Effect of varying distance and inclination . . . . .	54
3.5.4	Population Study . . . . .	54
3.5.5	Detection time-gains due to higher modes . . . . .	59
3.6	Summary . . . . .	61
<b>4</b>	<b>Early-Warning Estimates of Luminosity Distance and Orbital Inclination of Compact Binary Mergers using Higher Modes</b>	<b>67</b>
4.1	Motivation . . . . .	67
4.2	Parameter estimation . . . . .	68
4.3	Results . . . . .	71
4.3.1	Expected uncertainties as a function of component masses . . . . .	72
4.3.2	Variation of sky location and polarization angle	75
4.4	Summary . . . . .	76
<b>5</b>	<b>Impact of Higher Harmonics on Population Inference of Binary Black Holes</b>	<b>79</b>

5.1	Motivation . . . . .	79
5.2	Method . . . . .	81
5.2.1	Parameter inference . . . . .	81
5.2.2	Population inference . . . . .	82
5.2.3	Selection effects . . . . .	83
5.2.4	Population models . . . . .	84
5.3	Results . . . . .	85
5.3.1	Impact of higher modes on parameter inference	86
5.3.2	Inference of population properties . . . . .	89
5.4	Summary and Outlook . . . . .	94
<b>6</b>	<b>Summary and Outlook</b>	<b>99</b>
<b>7</b>	<b>Appendix</b>	<b>103</b>
7.1	Analytical Fisher matrix errors estimation . . . . .	103
7.2	Confidence interval calculation . . . . .	105
<b>8</b>	<b>Publications</b>	<b>109</b>
	<b>Bibliography</b>	<b>111</b>





# 1 | Introduction

Gravity is the fundamental force of nature that has intrigued mankind for centuries. In 1687, Sir Isaac Newton was the first to quantify this force as the universal law of attraction. He stated that the force of gravitational attraction between two objects is proportional to their masses and the inverse square of the distance between them <sup>1</sup>. This was a monumental feat in the thinking of humankind. Newton's theory of gravity was pivotal to understanding the motion of heavenly bodies, such as the moon, planets, stars, etc. In 1905, Albert Einstein published his theory of special relativity (SR) that prohibited the propagation of information faster than the speed of light in vacuum <sup>2</sup>. The universal law of attraction assumed its effect between two distant bodies instantly, i.e. an action at a distance, violating the constraint on the speed of the information exchange by the SR.

In November of 1915, Einstein proposed a solution to "an action at a distance" problem in his theory of general relativity (GR) <sup>3</sup>. In this framework, gravity is not conceptualized as a force but rather as the curvature in the geometry of spacetime <sup>4</sup> continuum induced by the massive objects. This curvature dictates the motion of other objects in the vicinity. In the words of John A. Wheeler, "matter tells spacetime how to curve, and spacetime tells matter how to move."

## 1.1 Gravitational Waves

In 1905, Henri Poincaré suggested that gravity was transmitted through a wave, which he called a gravitational wave (GW), that was generated by accelerated masses just as electromagnetic (EM) waves emitted from accelerating charges <sup>5</sup>. In 1916-18, Einstein published two papers on the existence of GWs as the ripples produced by the accelerated masses in the fabric of spacetime in the weak field limit of his theory of GR <sup>6</sup>. The existence of GWs was questioned for a long time by many scientists including Einstein himself. The reason was

<sup>1</sup> Isaac Newton. *Philosophiae Naturalis Principia Mathematica*. 1687. DOI: 10.3931/e-rara-440

<sup>2</sup> A. Einstein. Zur Elektrodynamik bewegter Körper. *Annalen der Physik*, 322(10):891-921, January 1905. DOI: 10.1002/andp.19053221004

<sup>3</sup> A. Einstein. Die Grundlage der allgemeinen Relativitätstheorie. *Annalen der Physik*, 354(7):769-822, January 1916. DOI: 10.1002/andp.19163540702

<sup>4</sup> The spacetime is a mathematical construct of three spatial dimensions and one dimension of time into a single four-dimensional continuum.

<sup>5</sup> M. H. Poincaré. Sur la dynamique de l'électron. *Rendiconti del Circolo Matematico di Palermo (1884-1940)*, 21(1):129-175, Dec 1906. ISSN 0009-725X. DOI: 10.1007/BF03013466

<sup>6</sup> Albert Einstein. Näherungsweise Integration der Feldgleichungen der Gravitation. *Sitzungsberichte der Königlich Preussischen Akademie der Wissenschaften*, pages 688-696, January 1916; and Albert Einstein. Über Gravitationswellen. *Sitzungsberichte der Königlich Preussischen Akademie der Wissenschaften*, pages 154-167, January 1918

an enormous amount of gauge freedom in the field equations and one mistake of not choosing a good coordinate system could have gauged away the gravitational radiation.

The geometry of the spacetime due to matter or energy is governed by Einstein's field equations (EFEs) as

$$R_{\mu\nu} - \frac{1}{2}g_{\mu\nu}R = \frac{8\pi G}{c^4}T_{\mu\nu} \quad (1.1)$$

where  $R_{\mu\nu}$  and  $R$  are Ricci tensor and Ricci scalar respectively that depend on the metric of spacetime,  $g_{\mu\nu}$  which is the solution to the above equations. The term on the right hand side is the source term with  $T_{\mu\nu}$  as the stress-energy tensor. The factor  $\frac{8\pi G}{c^4}$  is determined from the Newtonian limit of the above equations and suggests an extremely weak coupling between gravity and matter.

The EFEs are invariant under a huge symmetry group of coordinate transformations,  $x^\mu \rightarrow x'^\mu(x)$  under which the metric transforms as

$$g'_{\mu\nu}(x') = \frac{\partial x^\rho}{\partial x'^\mu} \frac{\partial x^\sigma}{\partial x'^\nu} g_{\rho\sigma}(x) \quad (1.2)$$

As a first step to understanding the generation of GWs far away from the source, one can consider the spacetime described by the flat Minkowskian metric  $\eta_{\mu\nu}$  and a small perturbation  $h_{\mu\nu}$  around it. That is,

$$g_{\mu\nu} = \eta_{\mu\nu} + h_{\mu\nu}; \quad |h_{\mu\nu}| \ll 1. \quad (1.3)$$

When we compute quantities such as the curvature tensor that are functions of the metric, we keep the terms that are only up to linear in  $h_{\mu\nu}$ ; hence the name *linearized theory*. This essentially means that one would have to find a reference frame where the numerical value of the components of  $h_{\mu\nu}$  satisfy the condition in Eq. 1.3 which breaks the invariance of EFEs under coordinate transformations. The EFEs in their linearized form can be obtained by substituting Eq. 1.1 in 1.3. This gives us <sup>7</sup>,

$$\square \bar{h}_{\mu\nu} + \eta_{\mu\nu} \partial^\rho \partial^\sigma \bar{h}_{\rho\sigma} - \partial^\rho \partial_\nu \bar{h}_{\mu\rho} - \partial^\rho \partial_\mu \bar{h}_{\nu\rho} = -\frac{16\pi G}{c^4} T_{\mu\nu} \quad (1.4)$$

where we have written the equation in terms of the trace-reversed perturbation:  $\bar{h}_{\mu\nu} = h_{\mu\nu} - \frac{1}{2}\eta_{\mu\nu}h$  with  $h = \eta^{\mu\nu}h_{\mu\nu}$  and  $\bar{h} = \eta^{\mu\nu}\bar{h}_{\mu\nu}$ . The operator  $\square$  is the d'Alembertian, which is  $\square = \eta_{\mu\nu}\partial^\mu\partial^\nu$  in flat space.

<sup>7</sup> See detailed steps in chapter 1 of Maggiore [140]

After choosing a frame in Eq. 1.3, there is still a residual gauge freedom which can be utilised to set some terms in Eq. 1.4 to zero. Choosing the Lorentz gauge<sup>8</sup>,

$$\partial^\nu \bar{h}_{\mu\nu} = 0 \quad (1.5)$$

In this gauge, the linearized form of EFEs in Eq. 1.4 reduces to

$$\square \bar{h}_{\mu\nu} = -\frac{16\pi G}{c^4} T_{\mu\nu} \quad (1.6)$$

Outside the source,  $T_{\mu\nu} = 0$ ,

$$\square \bar{h}_{\mu\nu} = 0 \quad (1.7)$$

Since  $\square = -(1/c^2)\partial_t^2 + \nabla^2$ , the equation 1.7 demonstrates that GWs travel with the speed of light. Notice that the form of  $h_{\mu\nu}$  can further be simplified by noticing a further coordinate transformation symmetry under  $x^\mu \rightarrow x^\mu + \xi^\mu$  with

$$\square \xi_\mu = 0 \quad (1.8)$$

The choice of  $\xi_\mu$  functions can impose four additional conditions apart from the Lorentz gauge. In particular, one can choose these functions such that  $h = 0$  and  $h^{0i} = 0$ . Then, we have a set of gauge conditions,

$$h_i^i = 0, h^{0\mu} = 0, \partial^j h_{ij} = 0. \quad (1.9)$$

This gauge is known as the *traceless-transverse gauge* or simply TT gauge. One should note that TT gauge can not be chosen inside the source, i.e. when  $T_{\mu\nu} \neq 0$ . Once we have set the Lorentz gauge, we can not set any further components of  $h_{\mu\nu}$  to zero.

The Eq. 1.7 has plane wave solutions in the form  $h_{ab}^{\text{TT}}(x) = e_{ij}(\mathbf{k})e^{ikx}$ , with  $k^\mu = (\omega/c, \mathbf{k})$  and polarization tensor  $e_{ij}(\mathbf{k})$ . Let us consider the plane wave is traveling along z-direction, i.e.  $\hat{z} = \mathbf{k}/|\mathbf{k}|$ , then imposing TT condition on  $h_{ij}$ , we have,

$$h_{ab}^{\text{TT}}(t, z) = \begin{pmatrix} h_+ & h_\times \\ h_\times & -h_+ \end{pmatrix}_{ab} \cos[\omega(t - z/c)] \quad (1.10)$$

where  $a, b = 1, 2$  are indices in the transverse  $x - y$  plane. The terms  $h_+$  and  $h_\times$  are known as ‘‘plus’’ and ‘‘cross’’ polarizations respec-

<sup>8</sup> Lorentz gauge condition in GR is similar to the one in electromagnetism,  $\partial_\mu A^\mu = 0$ . Historically, this gauge was used by L. V. Lorenz in 1867, when the more famous H. A. Lorentz was just 14 years old. However, this ‘misnomer’ has now entered the literature universally. (See J. D. Jackson and L. B. Okun, 2001)

tively. Eq. 1.10 can be written as

$$h_{ab}^{\text{TT}}(t, z) = (e_{ab}^+ h_+ + e_{ab}^\times h_\times) \cos[\omega(t - z/c)] \quad (1.11)$$

where

$$e_{ab}^+ = \begin{pmatrix} 1 & 0 \\ 0 & -1 \end{pmatrix}_{ab}, \quad e_{ab}^\times = \begin{pmatrix} 0 & 1 \\ 1 & 0 \end{pmatrix}_{ab} \quad (1.12)$$

are the polarizations tensors. One can also write the line element in terms of the perturbations as

$$ds^2 = -c^2 dt^2 + dz^2 + \{1 + h_+ \cos[\omega(t - z/c)]\} dx^2 + \{1 - h_+ \cos[\omega(t - z/c)]\} dy^2 + 2h_\times \cos[\omega(t - z/c)] dx dy \quad (1.13)$$

This implies that the proper distance between two particles changes

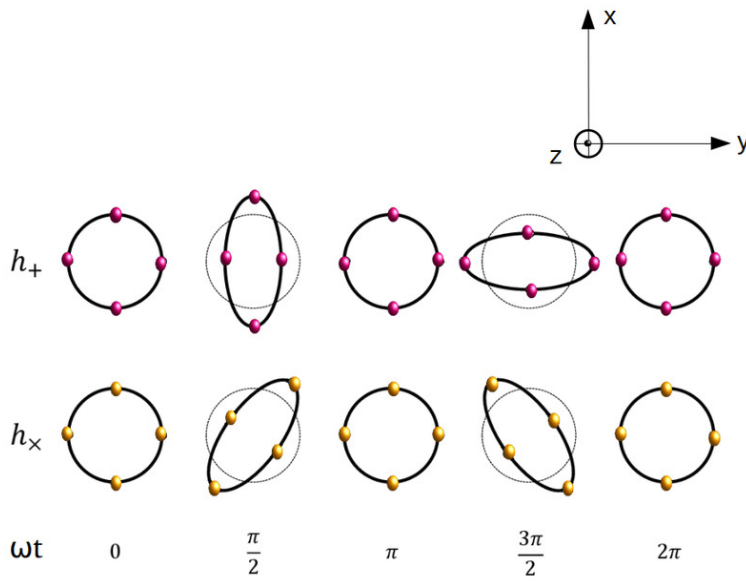


Figure 1.1: The effect of + and  $\times$  polarizations of the GWs passing through a ring of particles. (Credit: Belahcene [42])

upon the propagation of GWs. Let us assume a GW is passing through a ring of particles at  $z$  such that  $\omega z/c = \pi/2$ , then the deformations in the ring of particles at different times by + and  $\times$  polarizations are shown in Fig. 1.1. GWs stretch the ring of particles in one direction while squeezing them in the opposite direction.

## 1.2 Sources

GWs are emitted from a wide variety of sources ranging from merging compact binaries, such as binary black holes (BBHs), binary neutron stars (BNSs), and neutron star-black hole (NSBH) binaries; rotating NSs, supernovae explosions, and energetic processes in the early universe. Depending upon the mass and length scales involved, these sources will fall in different frequency bands. We highlight some of the key sources interesting for ground and space-based GW detectors.

### 1.2.1 Burst sources

The burst GW signals are primarily associated with the gravitational collapse of red giant stars or the core collapse of an accreting white dwarf into an NS or BH. The GWs are emitted if the collapse is nonspherical<sup>9</sup>. In such events, about  $10^{-7} - 10^{-5}$  of the total mass is radiated in GWs in a span of a fraction of a second to a couple of seconds (see Fig. 1.3). A rough estimate of the GW amplitude from a core-collapse supernova<sup>10</sup>

$$h \sim 6 \times 10^{-21} \left( \frac{E}{10^{-7}} \right)^{1/2} \left( \frac{1\text{ms}}{T} \right)^{1/2} \left( \frac{1\text{kHz}}{f} \right) \left( \frac{10\text{kpc}}{r} \right) \quad (1.14)$$

This estimate of the GW amplitude is loud enough to be detectable by current GW detectors if the supernova happens in our galaxy, but the rate of such events is not very high. In addition, the GW signals emitted from such explosions pose significant modeling challenges. Accurate predictions require simulating all the necessary physics: three-dimensional hydrodynamics, neutrino transport, magnetic field, rotation, etc. This further leads to difficulties in the detection of such signals in the absence of accurate/robust theoretical models.

### 1.2.2 Continuous sources

Rotating NSs or other compact objects with non-axisymmetric deformations (quantified, in the leading order in terms of the quadrupolar ellipticities; see Fig. 1.4) can lead to the emission of GWs. The rate of energy loss from these sources is extremely slow, resulting in nearly monochromatic signals (see Fig. 1.5). Even with ellipticity values  $\sim 10^{-9}$ , the GW signal strength is insufficient to make a de-

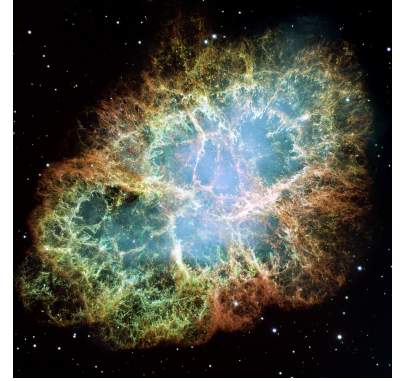


Figure 1.2: Crab Nebula, a remnant of a star's supernova explosion in Taurus constellation, one of the largest images ever taken by Hubble Space Telescope [credit: NASA, ESA, J. Hester, and A. Loll]

<sup>9</sup> Ernazar Abdikamalov, Giulia Pagliaroli, and David Radice. Gravitational Waves from Core-Collapse Supernovae. 10 2020. DOI: 10.1007/978-981-15-4702-7\_21-1

<sup>10</sup> B. S. Sathyaprakash and B. F. Schutz. Physics, Astrophysics and Cosmology with Gravitational Waves. *Living Rev. Rel.*, 12:2, 2009. DOI: 10.12942/lrr-2009-2

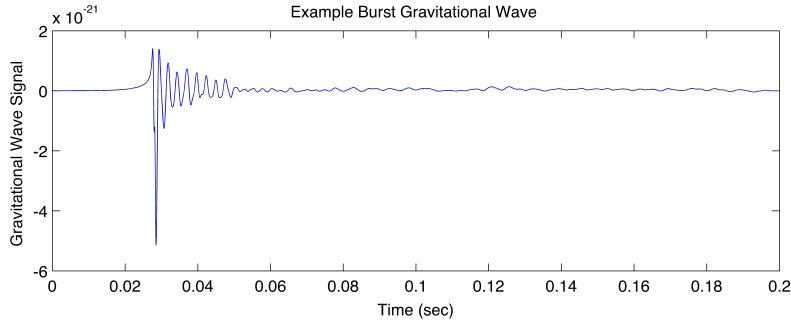


Figure 1.3: An example of a burst GW signal emitted by a core-collapse supernova (credit: A. Stuver/LIGO using data from C. Ott, D. Burrows, et al)

tection with the current generation of GW detectors. However, the integration of the signal for several years may lead to a detection. GWs from the long-lasting early phase of the inspiral of compact binary mergers can also be categorized as a continuous GW signal but the frequency range for that part of the signal could be much lower than what current ground-based GW detectors operate in. The space-based detectors such as LISA will detect these signals.

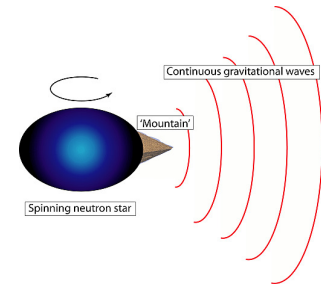


Figure 1.4: A schematic of a non-axisymmetric spinning NS and generation of monochromatic GWs (credit: <https://physics.anu.edu.au>)

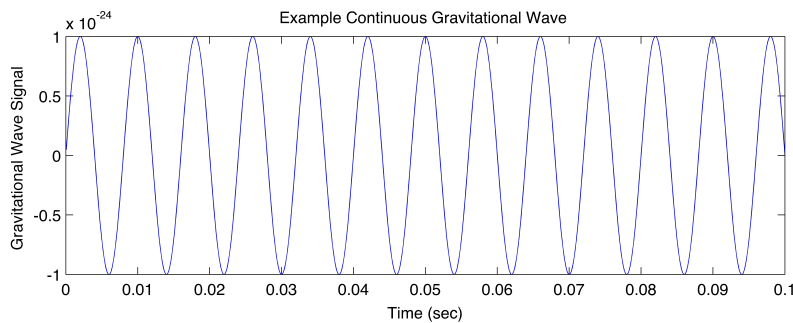


Figure 1.5: A continuous GW signal [credit: A. Stuver/LIGO]

### 1.2.3 Binary systems

Some of the strongest emitters of GWs are compact binary mergers, such as BBHs, BNSs, and NSBHs. The evolution of such binary systems can be divided into three stages (see the cartoons in the top panel in Fig. 1.6):

1. **Inspiral Phase:** During this stage, the component masses of the binary are well-separated and gradually spiral towards each other. As they do, the amplitude and frequency of the emitted GW signal increase. This steady rise in frequency with time is known as “chirp”. In the early part of this regime, the velocities of the objects are small compared to the speed of light, which is equiva-

lent to a weak gravity field for this gravitationally bound system. One can do a low-velocity expansion of the right-hand side of Eq. 1.6 to model the GW radiation. This technique is known as post-Newtonian (PN) expansion <sup>11</sup>.

2. **Merger Phase:** The frequency of the signal will not keep increasing forever; the slow inspiral phase will end and the orbit of the binary ceases to be circular when the distance between the stars is approximately equal to the innermost stable circular orbit (ISCO) <sup>12</sup>. At the ISCO radius, the frequency of the signal will be

$$f_{\text{ISCO}} \sim 2.2 \left( \frac{M_{\odot}}{M} \right) \text{ kHz} \quad (1.15)$$

where  $M$  is the total mass of the binary in units of solar mass  $M_{\odot}$ . The stars come in contact with each other and finally merge. The signal amplitude also peaks at this phase (see bottom panel of Fig. 1.6). Most of the energy is radiated in terms of GWs during this stage. The form of EFEs during the merger is highly non-linear and one would have to rely on numerical methods to compute the GW radiation <sup>13</sup>.

3. **Ringdown/Post-merger Phase:** After two BHs merge, there are perturbations in the remnant BH which radiates gravitationally through a spectrum of quasi-normal modes (QNMs) <sup>14</sup>. The amplitude of the signal falls exponentially with time. The information about the mass and spin, the only hairs of a Kerr BH <sup>15</sup>, is encoded in the damping times and frequencies of the QNMs. These can be used to test the “no-hair” theorem in GR. If both of the merging objects are compact objects other than BHs then post-merger is not governed by QNMs but rather it has a more complex form depending on the equation of state (EoS) of the matter in the remnant <sup>16</sup>.

In these cataclysmic events, up to 10% of the mass-energy of the binary systems is radiated in GWs. Mergers of NSs and stellar mass BHs are the very first sources detected by ground-based GW detectors. The white dwarfs (WDs) are less compact as compared to NSs and BHs, hence will have larger size and therefore will merge at larger separation emitting radiation at lower frequencies (in the mHz range). Supermassive BH (SMBH) binaries will also merge at lower

<sup>11</sup> Blanchet et al. 50, 49, Blanchet and Faye 47, Blanchet et al. 52, 51, Blanchet 45, Blanchet et al. 53, Blanchet and Iyer 48, Blanchet et al. 54, 55, 56, 57, 58, Blanchet 46, Blanchet et al. 59, 60, Boetzel et al. 61, 62, Bohe et al. 63, Bohé et al. 65, Bohé et al. 64, Arun et al. 38, 35, Buonanno et al. 68

<sup>12</sup> The smallest marginally stable circular orbit around a massive object in GR.

<sup>13</sup> Pretorius 158, Campanelli et al. 70, Baker et al. 40, Boyle et al. 67

<sup>14</sup> C.V. Vishveshwara. Scattering of gravitational radiation by a schwarzschild black-hole. *Nature*, 227: 936–938, 1970. DOI: 10.1038/227936a0

<sup>15</sup> For charged BHs, the charge is another hair.

<sup>16</sup> M. Shibata and K. Uryū. Gravitational waves from the merger of binary neutron stars in a fully general relativistic simulation. *Progress of Theoretical Physics*, 107:265–303, 2002. DOI: 10.1143/PTP.107.265

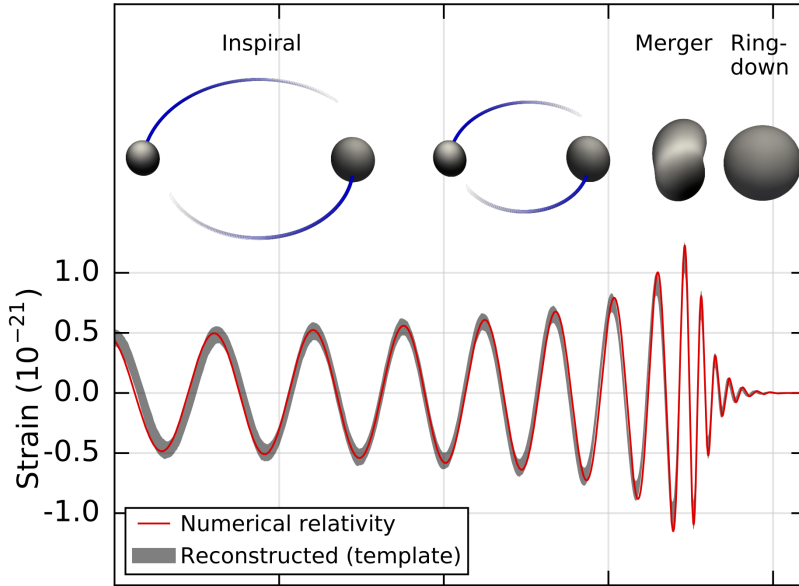


Figure 1.6: The cartoons in the top show the three stages of the BBH merger – inspiral, merger, and ringdown and the bottom section plot the strain amplitude emitted in GW<sub>150914</sub>, the first BBH merger detected. The grey shaded band correspond to the 90% probability regions of the reconstructed signal using theoretical models and the solid red line is a numerical relativity (NR) waveform with parameters consistent with those recovered from GW<sub>150914</sub>. (credit: Taken from Abbott et al. [2])

frequencies due to their large ISCO radius. The GW signals from both WDs and SMBHs in binaries will be detectable by space-based GW detectors.

#### 1.2.4 Stochastic sources

The stochastic GW signal will be a result of the incoherent superposition of GWs from numerous sources. The source could be astrophysical binaries from which the individual signals are not resolvable, leading to a combined signal known as the astrophysical stochastic background. Various energetic processes in the early universe (such as primordial fluctuations amplified during the inflation, phase transitions, etc.) could also result in this type of GW background, referred to as the primordial stochastic background. The stochastic background is a relic similar to cosmic microwave background (CMB)<sup>17</sup> and carries information about the early phases of the universe that we can not observe otherwise. As you can see in Fig. 1.7, the stochastic GW signal is indistinguishable from noise in the detectors posing a challenge to its detection. However, the cross-correlation among multiple detectors over a long period of time can lead to the detection of this signal.

<sup>17</sup> A. A. Penzias and R. W. Wilson. A measurement of excess antenna temperature at 4080 mc/s. *The Astrophysical Journal*, 142:419–421, 1965. DOI: 10.1086/148307



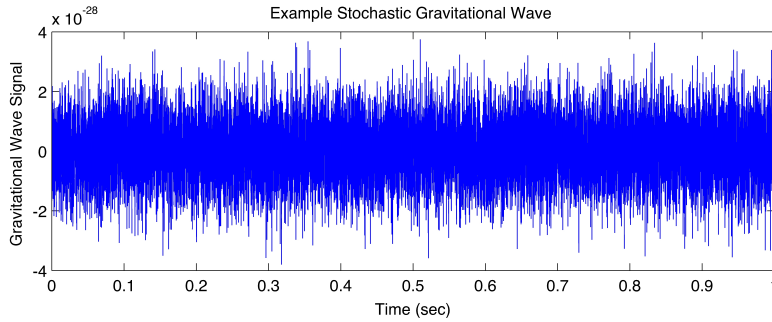


Figure 1.7: A stochastic GW signal [credit: A. Stuver/LIGO]

### 1.3 The gravitational-wave spectrum

The categorization of sources is done based on the signal morphology. The frequency at which the GWs are emitted largely depends on the mass and size of the compact object, especially in the case of merging binaries. Typically, stellar-mass compact objects, BHs or NSs whether in binary or rotating in isolation, emit GWs primarily in the frequency range of a few tens of Hz to a few kHz, which fall in the sensitivity band of the current ground-based GW detectors. The GW signals from supernovae (SNe) explosions, spinning NSs, and the stochastic background from astrophysical sources as well as random fluctuations during inflation are expected to fall in the frequency band of ground-based detectors.

In contrast, the inspiral and mergers of SMBHs will produce GWs in  $\mu\text{Hz}$  to  $\text{mHz}$  frequency range, suitable for space-based detectors, such as LISA. Additionally, the early inspiral phase of the SMBH binaries will generate a stochastic background of GWs in the  $\text{nHz}$  frequencies that can be detected by monitoring the timing of already known millisecond pulsars, using a pulsar timing array (PTA). Stochastic GW background from inflation can leave an imprint on the B-mode polarization of CMB at large angles in the sky. However, the efforts from recent missions BICEP2 and PLANCK<sup>18</sup> have been unsuccessful due to disentangling the dust emission contribution from our own galaxy from a possible GW signal. Several ongoing and upcoming ground-based CMB missions are still pursuing this challenging detection. Fig. 1.8 lists various GW detectors (present and future) and their corresponding sources of interest.

<sup>18</sup> P. A. R. Ade and et al. Detection of b-mode polarization at degree angular scales by bicep2. *Physical Review Letters*, 112(24), 2014. DOI: 10.1103/PhysRevLett.112.241101; and Cyrille Doux, Emmanuel Schaan, Eric Aubourg, Ken Ganga, Khee-Gan Lee, David N. Spergel, and Julien Tréguer. First detection of cosmic microwave background lensing and lyman- $\alpha$  forest bispectrum. *Phys. Rev. D*, 94:103506, Nov 2016. DOI: 10.1103/PhysRevD.94.103506. URL <https://link.aps.org/doi/10.1103/PhysRevD.94.103506>

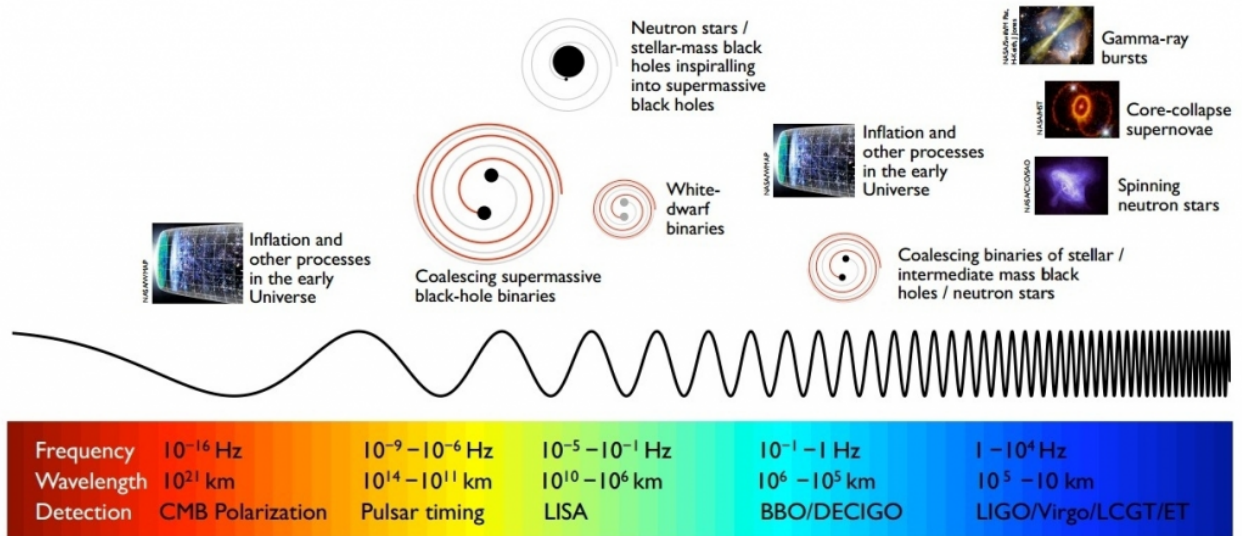


Figure 1.8: GW spectrum showing frequencies and wavelengths corresponding to various sources and the relevant GW detectors. (Credit: P. Ajith/ICTS)

## 1.4 Detectors and Detection

Measuring the effects of GWs passing through matter requires a standard ruler, but the ruler should be carefully chosen so that it is not affected by the GWs. There are mainly two types of GW detectors that have been seriously explored in the pursuit of detecting GWs: resonant bar detectors and laser interferometers. In resonant bar detectors, the GWs transfer energy to the metal bar resulting in resonant oscillations that can be observed. While in laser interferometers, GWs change the travel time of the light beam between two or more test masses that will be proportional to the magnitude of the disturbances.

### 1.4.1 Resonant bar detectors

In the 1960s, Joseph Weber built two aluminum bar detectors, each about 66 cm in diameter and 153 cm in length, weighing 3 tons. One was located at the University of Maryland and another, 950 km away, at Argonne National Laboratory near Chicago to eliminate spurious signals. The cylindrical bars were hung by a steel wire and surrounded by a vacuum chamber to isolate them from environmental vibrations (a schematic shown in Fig. 1.9). The cylinders were covered by a piezoelectric belt that generated an electrical signal upon the vibrations. Thermal agitations led to a change in the length of the cylinder by about  $10^{-16}$  meters<sup>19</sup>. On the other hand, a typical GW

<sup>19</sup>J. Weber. Observation of the thermal fluctuations of a gravitational-wave detector. *Phys. Rev. Lett.*, 17:1228–1230, Dec 1966. DOI: 10.1103/PhysRevLett.17.1228. URL <https://link.aps.org/doi/10.1103/PhysRevLett.17.1228>

burst of amplitude  $h \sim 10^{-21}$  will lead to vibration in the cylinder with an approximate amplitude

$$\delta l_{\text{gw}} \sim h \times \text{Length of the cylinder} \sim 10^{-21} \text{ meters.} \quad (1.16)$$

This meant the noise amplitude was far greater than the GW signal, making a confident detection impossible. Moreover, the narrow bandwidths of these detectors further limited the possibility of integrating a GW signal over a range of frequencies.

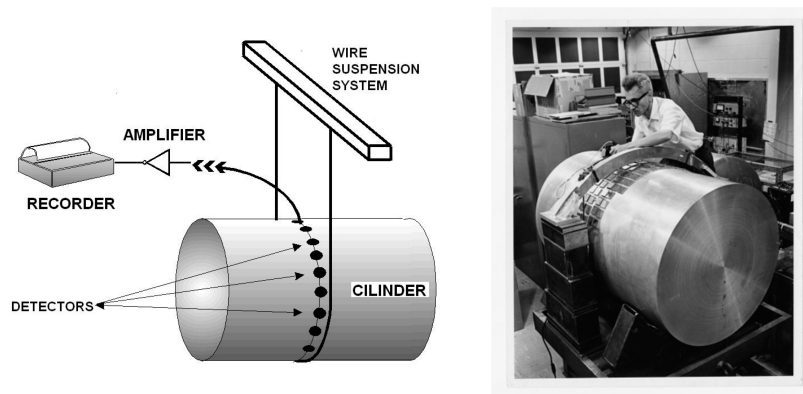


Figure 1.9: A schematic of a resonant bar detector with Joseph Weber working on a real one.

#### 1.4.2 Laser interferometers

Fig. 1.10 shows a schematic diagram of an interferometer. It consists of a light source (laser), a beam splitter (a half-silvered or semi-reflecting mirror), a pair of reflecting mirrors (that act as the test masses to detect the deformations of spacetime) placed at the end of the orthogonal arms, and a photodetector. The monochromatic light first hits the beam splitter which reflects half of it onto the mirror  $M_2$  and transmits the rest to the other mirror  $M_1$ . The light beams bounce off the mirrors and recombine at the splitter which then is reflected toward the photo detector at the bottom. The mirrors are placed at a distance from the beam splitter to create a destructive interference pattern (dark fringe)<sup>20</sup> in the detector. The passage of GWs leads to deviations from the dark fringe. The measurement of the change in the intensity of the light at the photodetector can track the change in the distance between the mirror and the beam splitter.

If the original arm length of the interferometer is  $L$ , a GW signal of amplitude  $h$  will create a total differential change of  $\Delta L = hL$  in its arm length. Thus,  $h = \Delta L/L$  can be thought of as the strain on the

<sup>20</sup> When the recombining light beams are out of phase with respect to each other, their amplitude will add up to zero. On the other hand, if they are in phase, the intensities will add up to provide maximum light. (See Fig. 1.11)

interferometer. For a given GW amplitude  $h$ , the displacement  $\Delta L$  will be larger for longer the arms of the interferometer. The effective arm length of the interferometer can be increased by folding the laser beams back and forth along the arms with the use of Fabry-Perot cavities (shown in Fig. 1.10). However, the effective arm length of the interferometer has to be lower than the GW wave length; otherwise, it will destroy the phase coherence of the measurement.

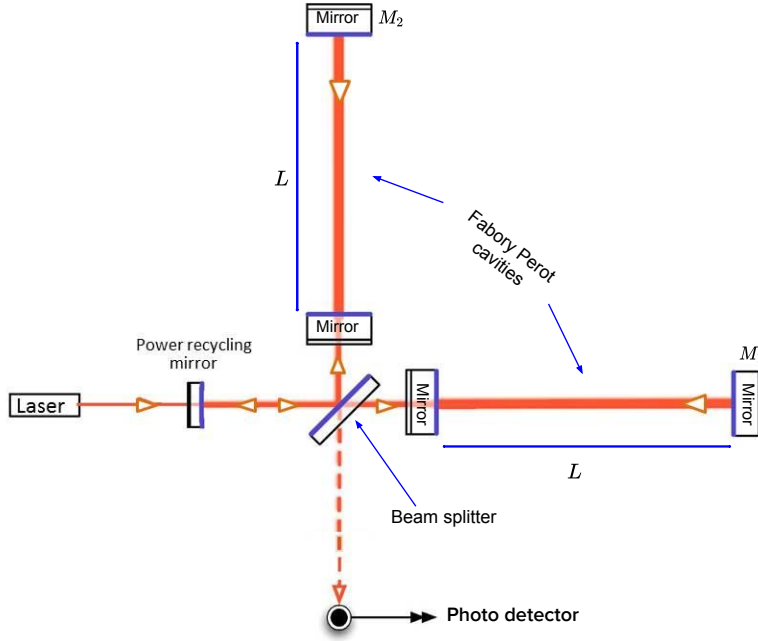


Figure 1.10: An interferometer. (Credit: Caltech/MIT/LIGO Lab; modified by myself)

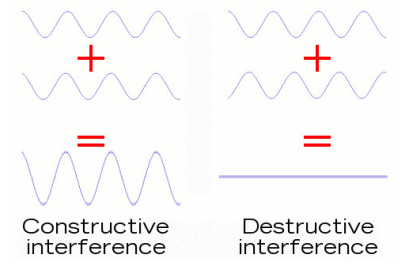


Figure 1.11: Interference pattern. (Credit: www.explainthatstuff.com)

### 1.4.3 The response of a ground-based interferometer

One can consider the arms of the detector along the unit vectors  $\hat{e}_x$  and  $\hat{e}_y$ . If the GW signal is coming from a direction  $\hat{N}$  defined by spherical coordinates  $\theta$  and  $\phi$  relative to detector axes. Let us define the radiation frame basis vectors to be  $\hat{e}_x^R$  and  $\hat{e}_y^R$ , where  $\hat{e}_x^R$  lie in plane associated with  $\hat{N}$  and  $\hat{e}_x$ , and  $\hat{e}_y^R$  is orthogonal to both  $\hat{N}$  and  $\hat{e}_x^R$  (see left panel in Fig. 1.12), then the strain in the radiation frame can be written according to Eq. 1.11 (wave tensor) as

$$\mathbf{h}(t) = \mathbf{e}^+ h_+(t) + \mathbf{e}^\times h_\times(t) \quad (1.17)$$

where the polarisation tensors are given by

$$\mathbf{e}^+ = \hat{e}_x^R \otimes \hat{e}_x^R - \hat{e}_y^R \otimes \hat{e}_y^R, \quad \mathbf{e}^\times = \hat{e}_x^R \otimes \hat{e}_y^R + \hat{e}_y^R \otimes \hat{e}_x^R \quad (1.18)$$

Here  $\otimes$  denotes the tensor product. Analogous to the wave tensor form, we define the detector tensor as

$$\mathbf{d} = L(\hat{e}_x \otimes \hat{e}_x - \hat{e}_y \otimes \hat{e}_y) \quad (1.19)$$

When dealing with a network of detectors, it is not convenient to associate the basis vectors of the sky plane with those of the detector frame as different detectors can have varying orientations with respect to one another. In that case, it is useful to define the polarization tensors in the sky plane by using a convenient astronomical reference frame, with basis vectors  $\hat{\alpha}$  and  $\hat{\beta}$  that are rotated by an angle  $\psi$  with respect to the basis used earlier. In this new basis, the polarisation tensors are

$$\epsilon_+ = (\hat{\alpha} \otimes \hat{\alpha} - \hat{\beta} \otimes \hat{\beta}) \quad (1.20)$$

$$\epsilon_\times = (\hat{\alpha} \otimes \hat{\beta} + \hat{\beta} \otimes \hat{\alpha}) \quad (1.21)$$

that can be derived from the previous basis vectors using the following transformations,

$$\epsilon_+ = \mathbf{e}_+ \sin 2\psi + \mathbf{e}_\times \cos 2\psi \quad (1.22)$$

$$\epsilon_\times = -\mathbf{e}_+ \cos 2\psi + \mathbf{e}_\times \sin 2\psi \quad (1.23)$$

Then the dimensionless amplitude,

$$\frac{\Delta L}{L} = F_+(\theta, \phi, \psi)h_+(t) + F_\times(\theta, \phi, \psi)h_\times(t) \quad (1.24)$$

where  $F_+$  and  $F_\times$  are antenna pattern functions of the detectors in the sky-plane basis:

$$F_{+, \times} \equiv d_{\ell m} e_{+, \times}^{\ell m} \quad (1.25)$$

Using geometry in the right figure of Fig. 1.12

$$F_+ = \frac{1}{2}(1 + \cos^2 \theta) \cos 2\phi \cos 2\psi - \cos \theta \sin 2\phi \sin 2\psi \quad (1.26)$$

$$F_\times = \frac{1}{2}(1 + \cos^2 \theta) \cos 2\phi \sin 2\psi + \cos \theta \sin 2\phi \cos 2\psi \quad (1.27)$$

The maximum values of both  $F_+$  and  $F_\times$  are 1. If the angle between the arms of the detector is not  $\pi/2$  but rather  $\eta$ , there is an additional factor of  $\sin \eta$  to be multiplied to  $F_+$  and  $F_\times$ . Since the direction of the incoming signal will be independent of its polarization, it will be use-

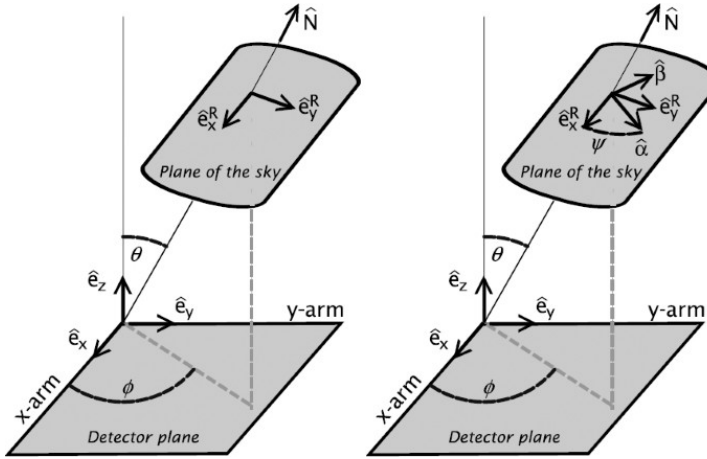


Figure 1.12: The relative orientation of sky frame and detector frame. (Image Credit: Sathyaprakash and Schutz 2009)

ful to estimate the directional sensitivity of a detector or a network of detectors by averaging over  $\psi$ . The average sensitivity of a detector in the sky can be defined in terms of the sum of the squares of the antenna functions corresponding to both the polarizations, known as *antenna power pattern*

$$P(\theta, \phi) = F_+^2 + F_\times^2 = \frac{1}{4}(1 + \cos^2 \theta)^2 \cos^2 2\phi + \cos^2 \theta \sin^2 2\phi \quad (1.28)$$

It is plotted in Fig. 1.13 and often referred to as the ‘peanut diagram’. It is clear from the plot that the detector has best sensitivity in the direction perpendicular to the plane of the detector and worse in the plane. The antenna power pattern for a network of detectors is a

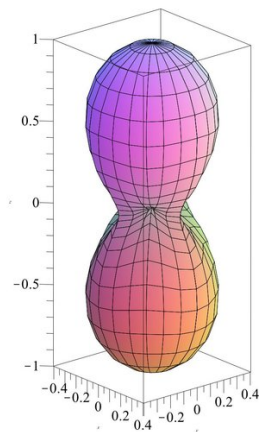


Figure 1.13: The antenna power pattern for a single interferometer averaged over the polarizations of the incoming wave. This also corresponds to the detection volume of the instrument or its maximum reach in different directions. (Credit: Schutz 2011)

simple extension of the single interferometer case

$$P_N(\theta, \phi) = \sum_k (F_{+,k}^2 + F_{\times,k}^2) \quad (1.29)$$

It should be noted that the average antenna power of a network of detectors does not depend on the relative orientation of the detectors with respect to each other.

#### 1.4.4 Noise characteristics of the detector

There are a plethora of noise sources that need to be understood and mitigated properly to use the interferometer for GW detection purposes. Some of the main sources are the following:

1. **Seismic (ground) vibrations:** The vibrations in the ground, due to mechanical or natural (seismic) activities in the vicinity, can cause the components of the interferometer (especially mirrors) to shift their positions. These vibrations are currently screened out by suspending the mirrors through pendulums which can filter out the frequencies above their natural frequency. Since this noise falls off at higher frequencies, suspension systems are ideal to mitigate this low-frequency noise. Multistage suspension can be significantly effective in isolating the mirrors from the ground motions.
2. **Thermal noise:** The thermal motion of the atoms in the mechanical suspension and mirrors, as they're at room temperature, can introduce noise in the measurement. Besides vibrations, thermal effects can change the bulk properties of the mirrors, which in turn changes their optical properties. The high reflectivity of the mirrors is achieved by means of multiple layers of coatings on the mirrors. Thermal vibrations of the coating materials are another source of noise.
3. **Quantum noise:** Intrinsic fluctuations in the number of photons in the laser make random fluctuations in the observed light intensity which is known as the *shot* noise. The reduction in the error due to fluctuations decreases with the number of photons  $N$  as

$$\delta I_{\text{shot}} \approx \lambda / (2\pi\sqrt{N}) \quad (1.30)$$

For the measurement of typical GW amplitudes, this requires a very high-power laser, beyond the capability of any existing laser. One can overcome this problem by power-recycling techniques. In the interferometer, the beams meet at the beam splitter after

bouncing off the mirrors. This light can again be used by placing a recycling mirror in front of the laser input and before the beam splitter (see Fig. 1.10). This can dramatically reduce the power requirements and one can work with laser powers of 5 – 10 W.

As laser power is increased to reduce the shot noise, the measurement accuracy of the position improves but the momentum transferred by photons to the mirrors can be inaccurate as dictated by the Heisenberg uncertainty principle. This can hinder the measurement of the GW signal. To mitigate this quantum radiation pressure noise, the researchers have used “squeezed” states of the light that basically refers to better measuring one trait (say phase) at the expense of increased uncertainty in its conjugate (amplitude). They have gone a step further in reducing this noise based on the frequency. For example, at low frequencies, the radiation pressure noise is large hence one can reduce the uncertainty in the amplitude (amplitude squeezing) at the expense of uncertainty in phase while at high frequencies, the amplitude accuracy can be sacrificed in comparison to phase (phase squeezing) to reduce the shot noise <sup>21</sup>.

<sup>21</sup> Ganapathy et al. [107]

4. **Gravity-gradient noise:** The changes in the local Newtonian gravitational field can also lead to variable tidal forces. This noise falls at high frequencies and may not be a problem for the current generation of detectors but it can pose a serious challenge for the next generation of detectors.

The performance of the interferometric GW detectors can be quantified by estimating the *power spectral density* (PSD) of the noise background. In the absence of a GW signal, the detector’s output is just the noise:  $s(t) = n(t)$ . Under the assumption of stationary (i.e.  $\langle n(t) \rangle = 0$ ) and Gaussian noise <sup>22</sup>, the statistical properties of the noise are completely determined by the PSD

$$\langle \tilde{n}(f) \tilde{n}^*(f') \rangle = \frac{1}{2} \delta(f - f') S_n(f) \quad (1.31)$$

where  $\langle \rangle$  denotes the ensemble average, and  $\sim$  and  $*$  denote the Fourier transform and complex conjugate respectively. Since  $n(t)$  is real,  $\tilde{n}(-f) = \tilde{n}^*(f)$  which implies  $S_n(-f) = S_n(f)$ , hence  $S_n(f)$  is known as the one-sided PSD. The sensitivity of LIGO-like detectors

<sup>22</sup> In reality, the noise in the detector is neither stationary nor exactly Gaussian. But for short-duration signals from compact binary mergers, it can be approximated close to stationary. There are transient noise glitches, non-Gaussian in nature, that need to be removed (vetoed) out before the data is used for analyses.



is limited by the seismic at the low frequencies, thermal noise in the middle, and shot noise at high frequencies. LIGO-Virgo detectors operate in  $\sim 10$ Hz to a few kHz frequency range (see Fig. 1.14).

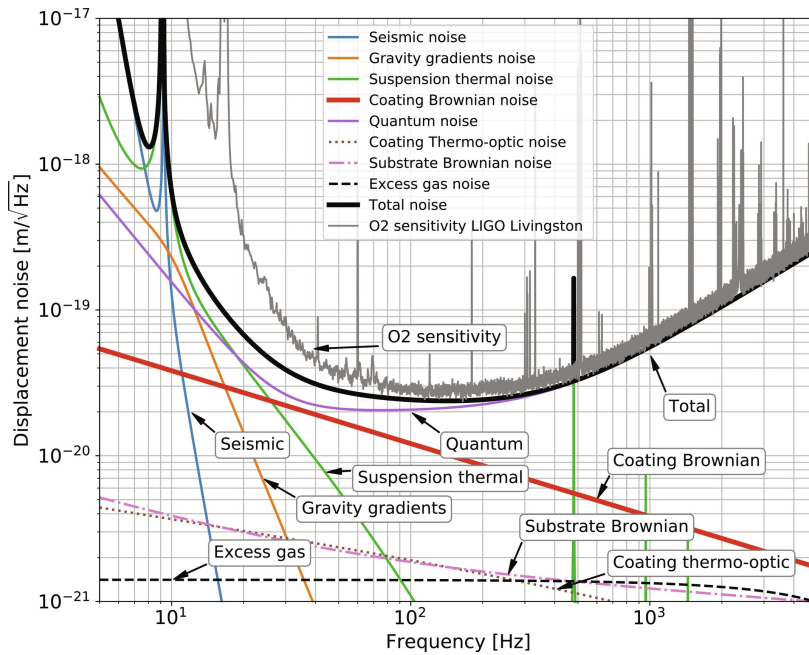


Figure 1.14: The power spectral density for LIGO Livingston detector (in grey) corresponding to their second observing run (O2) along with various noise sources (Credit: Taken from Vajante et al (2019))

#### 1.4.5 Current global network of detectors

Currently, an international network of five long-arm laser interferometers is under operation. This network includes two of the largest interferometers, LIGO, each with a 4 km arm length, at Louisiana, Livingston, and Hanford, Washington, in the USA. Another interferometer, Virgo with a 3 km arm-length, was built through European efforts in Cascina, Pisa, Italy. Additionally, a smaller detector with a 600 m arm length, known as GEO600, has been operational in Hanover, Germany since 2001. It has been crucial in developing new technologies and noise mitigating techniques which then later have been applied to LIGO and Virgo detectors. Recently, a new detector, KAGRA, was built in Hida, Japan. KAGRA has the same arm length as Virgo and has been operational since 2020. There is a planned LIGO-like detector in Maharashtra, India (see Fig. 1.15). The network of multiple detectors especially the ones with long-baseline will not only be crucial in reducing the noise transients through coincidences but also provide better sky-localizations hence improving the prospects for the multimessenger follow-up. There are planned

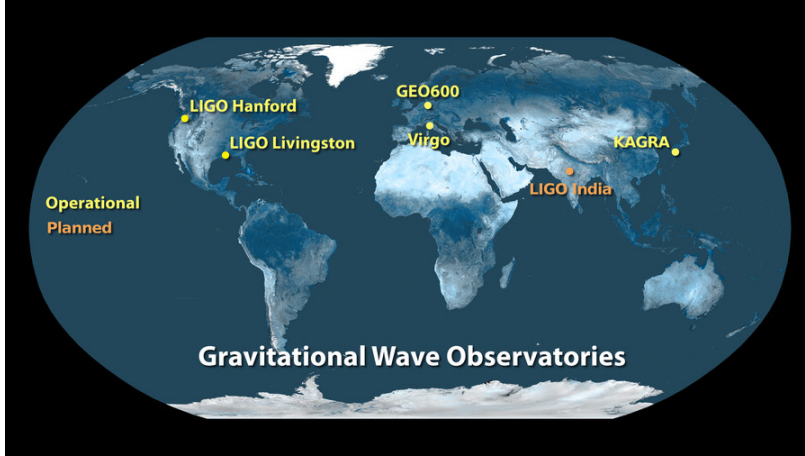


Figure 1.15: Network of detectors  
(Credit: Caltech/MIT/LIGO Lab)

space-based detectors, such as Laser Interferometer Space Antenna (LISA), DECIGO, and Lunar Gravitational Wave Antenna (LGWA), to be operating in the next decades. The frequency range covered by these detectors will be in the sub-mHz to sub-Hz region. In the nHz window, the International PTA is searching for stochastic background from the mergers of SMBHs by monitoring the timing of pulsars. The efforts to measure the B-mode polarization of CMB caused by the primordial GWs are underway with several ground-based CMB experiments.

#### 1.4.6 Detection

The detection of GW signals is based on comparing the data with the theoretically predicted waveform models, known as templates for these signals. The efficiency of the detection depends, apart from other things, on the accuracy of these theoretical models and what amount of physics they have incorporated during modeling.

Since the signal amplitude  $h(t)$  is way smaller than noise amplitude  $n(t)$ , i.e.  $|h(t)| \ll |n(t)|$ , one might ask how one can dig out the signal from the noise. The answer is yes if we know the form of  $h(t)$  up to some accuracy. One can compute the cross-correlation of the data containing the true signal and noise, i.e.  $s(t) = h(t) + n(t)$  with a linear filter  $K(t)$ , whose form needs to be determined, dependent on  $h(t)$ :

$$CC(t) = \int dt' s(t') K(t - t') \quad (1.32)$$

The cross-correlation  $CC(t)$  is maximized for  $\tilde{K}(f) \propto \tilde{h}(f)/S_n(f)$ ,

where  $\tilde{K}(f)$  is the frequency response of the filter. This technique is known as *matched filtering*. The matched filter can be defined in terms of the noise-weighted inner product as

$$(s|h) = 4 \operatorname{Re} \int_{f_{\text{low}}}^{f_{\text{high}}} df \frac{\tilde{s}^*(f) \tilde{h}(f)}{S_n(f)} \quad (1.33)$$

where  $\sim$  and  $*$  denote the Fourier transform and complex conjugate respectively. Note that Eq. 1.33 involves integration between  $f_{\text{low}}$  and  $f_{\text{high}}$  frequencies corresponding to the sensitivity band of the detector. The matched filter SNR  $\rho_{\text{mf}}$  can be defined as

$$\rho_{\text{mf}} = \frac{(s|h)}{\sqrt{(h|h)}} \quad (1.34)$$

where the denominator is known as the optimal SNR ( $\rho$ ) which is obtained when the data is noise-free, i.e.  $n(t) = 0$

$$\rho = \sqrt{(h|h)} = \left[ 4 \int_{f_{\text{low}}}^{f_{\text{high}}} df \frac{|\tilde{h}(f)|^2}{S_n(f)} \right]^{1/2} \quad (1.35)$$

In real-time GW searches, it is useful to compute the optimal number of templates over the expected region of the parameter space, known as the template bank, of the source. The data is filtered with each of these templates and if the template corresponding to the highest value of detection statistic (e.g.  $\rho_{\text{mf}}$ ) crosses the threshold for detection, a GW trigger is generated and further analyses follow. Currently, GstLAL, PyCBC, SPIIR, and MBTA<sup>23</sup> are some of the search pipelines based on the template banks used by the LVK collaboration.

## 1.5 Overview of LIGO-Virgo-KAGRA observations

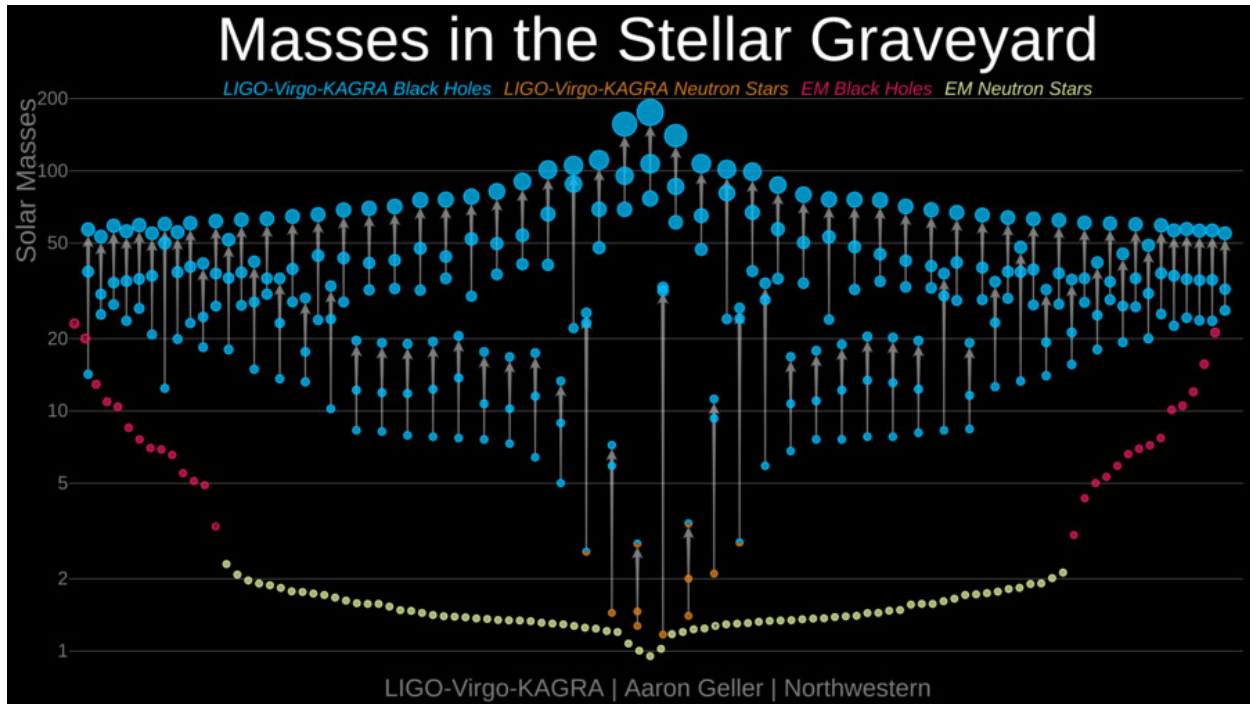
LVK collaboration has announced the detection of around  $\sim 90$  compact binary mergers from its three observing runs ( $O_1$ ,  $O_2$ ,  $O_3$ )<sup>24</sup>. Most of the GW signals are the product of BBH mergers. The catalog also includes GW signals from two BNS mergers and four NSBH binaries (two did not cross the commonly accepted SNR threshold)<sup>25</sup>. Some of the main events and their properties are as follows:

- **GW150914:** This was the first-ever direct detection of BBH merger. It was a two-detector event (LIGO-Livingston and LIGO-Hanford) with SNR  $\sim 24$  and false alarm rate (FAR) estimated to be less

<sup>23</sup> Cody Messick et al. Analysis framework for the prompt discovery of compact binary mergers in gravitational-wave data. *Phys. Rev. D*, 95(4):042001, February 2017. DOI: 10.1103/PhysRevD.95.042001; Samantha A. Usman et al. The PyCBC search for gravitational waves from compact binary coalescence. *Class. Quant. Grav.*, 33(21):215004, 2016. DOI: 10.1088/0264-9381/33/21/215004; Qi Chu. *Low-latency detection and localization of gravitational waves from compact binary coalescences*. PhD thesis, The University of Western Australia, 2017; and T Adams et al. Low-latency analysis pipeline for compact binary coalescences in the advanced gravitational wave detector era. *Classical and Quantum Gravity*, 33(17):175012, aug 2016. DOI: 10.1088/0264-9381/33/17/175012. URL <https://doi.org/10.1088/2F0264-9381%2F33%2F17%2F175012>

<sup>24</sup> Abbott et al. 13, Abbott et al. 20, 21, Abbott et al. 2

<sup>25</sup> Abbott et al. 15, Abbott et al. 14, Ligo Scientific Collaboration et al. 134



than 1 event per 200 thousands years, equivalent to a significance greater than  $5.1\sigma$ . The component BH masses were constrained to  $36^{+5}_{-4}M_{\odot}$  and  $29^{+4}_{-4}M_{\odot}$ , and final BH mass  $62^{+4}_{-4}M_{\odot}$  (90% credible interval). This meant that around  $3.0^{+0.5}_{-0.5}M_{\odot}$  mass-energy was radiated in terms of GWs. The luminosity distance of the source was constrained to  $410^{+160}_{-180}$  Mpc.

- **GW151226:** The second BBH merger with component masses:  $14.2^{+8.3}_{-3.7}M_{\odot}$  and  $7.5^{+2.3}_{-2.3}M_{\odot}$ . In this event, at least one of the BHs had a significant spin ( $> 0.2$ ). This was again a  $5\sigma$  detection.
- **GW170814:** The first BBH merger detected by Virgo detector in addition to two LIGO detectors with an SNR  $\sim 18$ . The BH masses inferred are  $30.5^{+5.7}_{-3.0}M_{\odot}$  and  $25.3^{+2.8}_{-4.2}M_{\odot}$ . The detection in three detectors significantly improved the sky localization area of the event from  $1160 \text{ deg}^2$  using only two LIGO detectors to  $60 \text{ deg}^2$  using all three detectors.
- **GW170817:** The first BNS inspiral detection as the merger was not detectable due to the poor sensitivity of the detectors at high frequencies. The inspiral of the BNS lasted for  $\sim 100$  s in the frequency band of the detectors accumulating an SNR of 32.4 and FAR  $\sim 1$  per  $8.0 \times 10^4$  years. The component masses were in-

Figure 1.16: Depiction of the compact objects detected through LIGO-Virgo-KAGRA detectors as well as EM observations. (Credit: LVK/Aaron Geller/Northwestern)

ferred to be between  $0.86$  and  $2.26M_{\odot}$  consistent with the known NS mass range. The source was localized to  $28 \text{ deg}^2$  region of the sky and located at a distance of  $40_{-14}^{+8}$  Mpc, the closest and most precisely localized event so far. The EM counterpart to this event was also detected from  $\gamma$ - rays to radio waves, marking the beginning of multimessenger astronomy with GWs.

- **GW190412:** This was the first observation of a BBH merger with unequal component masses  $30_{-5.3}^{+4.6}M_{\odot}$  and  $8_{-0.9}^{+1.6}M_{\odot}$  with an SNR  $\sim 19$ . The spin of the heavy BH spanned in  $0.22 - 0.60$ .
- **GW190425:** The second BNS merger detection for which the measurement of total mass  $3.1_{-0.1}^{+0.3}M_{\odot}$  and chirp mass  $1.44_{-0.02}^{+0.02}M_{\odot}$  indicated it was an outlier with respect to any known BNS. No EM counterpart was detected.
- **GW190814:** The most unequal component masses binary whose secondary object was either the heaviest NS or the lightest BH detected so far, the exact nature being unclear. The component masses were  $23.2_{-1.0}^{+1.1}M_{\odot}$  and  $2.59_{-0.09}^{+0.08}M_{\odot}$  with mass ratio  $q = m_2/m_1 \sim 0.1_{-0.009}^{+0.008}$ .
- **GW190521:** The heaviest BBH merger detected with primary and secondary masses  $85_{-14}^{+21}M_{\odot}$  and  $66_{-18}^{+17}M_{\odot}$  respectively. Both masses are much more heavier than any of the merging BHs detected by LIGO-Virgo so far. The remnant BH falls in a mass range that is attributed to intermediate-mass BHs (IMBHs).
- **GW200105 and GW200115:** The first detection of two NSBH mergers. The component masses were constrained to  $8.9_{-1.5}^{+1.2}M_{\odot}$  and  $1.9_{-0.2}^{+0.3}M_{\odot}$  for GW200105, whereas  $5.7_{-2.1}^{+1.8}M_{\odot}$  and  $1.5_{-0.3}^{+0.7}M_{\odot}$  for GW200115. GW200105 has a magnitude of the primary spin less than  $0.23$ , while there was an indication of a negative primary spin projection onto the orbital angular momentum at  $88\%$  probability. No EM counterparts were detected.
- **GW230529:** The first detection of a compact binary merger where primary mass ( $m_1 = 3.6_{-1.2}^{+0.8}M_{\odot}$ ) was not consistent with the range of masses previously observed for NSs or BHs but rather in the gap. The secondary ( $m_2 = 1.4_{-0.2}^{+0.6}M_{\odot}$ ) mass was consistent with an NS. This was notably a single detector event.

There have been marginal hints of precession and eccentricity<sup>26</sup> for a couple of events. But in the absence of precessing and eccentric waveform models, one can not confidently claim one effect over the other as these two effects are degenerate.

<sup>26</sup> Precession refers to the case when the spins of the component objects in the binary are not aligned with the orbital angular momentum. This leads to the wobbling of the plane of the binary. On the other hand, eccentricity quantifies the deviation of an orbit from a perfect circle.

### 1.5.1 Science summary of observations

The detection of GW<sub>150914</sub> not only confirmed the existence of GWs but also established that BHs can form binaries that inspiral and merge due to the emission of GWs. However, the BH masses  $36M_{\odot}$  and  $29M_{\odot}$  observed for this event were much heavier than the range of BH masses ( $\sim 10 - 20M_{\odot}$ ) inferred from x-ray observations. Since the first detection, LVK collaboration has confidently ( $FAR < 1/\text{year}$ ) observed  $\sim 69$  BBHs mergers that have masses  $\sim 7 - 85M_{\odot}$ . At the end of the third observing run (O<sub>3</sub>) of LVK, the intrinsic merger rate of BBHs is inferred to be  $16 - 61 \text{ Gpc}^{-3}\text{yr}^{-1}$ <sup>27</sup>. The planned upgrades to the current detectors will improve the sensitivity by a factor of a few allowing access to a larger volume. The high intrinsic merger rate has also led to the prediction of a stochastic background to be detectable in the next few years.

<sup>27</sup> The LIGO Scientific Collaboration, the Virgo Collaboration, and the KAGRA Collaboration. The population of merging compact binaries inferred using gravitational waves through GWTC-3. *arXiv e-prints*, art. arXiv:2111.03634, November 2021

The detection of many compact binary mergers allows us to infer their formation channels and astrophysical environments. Two of the main formation channels of these binaries are the dynamical exchanges in the dense star clusters and isolated evolution through the common envelope phase. The population inference of the BBHs from LVK observations reveals that the BH mass spectrum is found to peak at  $m \simeq 10M_{\odot}$ , inconsistent with the expected peak ( $> 10M_{\odot}$ ) from the dynamical formation channel for BBHs. Lighter BHs are expected to be ejected from the stellar clusters due to SN kicks. However, galactic nuclei can contribute due to a high limit on the escape velocity hence retaining even the low-mass objects in them. Isolated field evolution predicts a peak near  $m \simeq 10M_{\odot}$ , however, the normalization to the rate at the peak is poorly constrained due to various uncertain factors. This suggests multiple formation channels contributing to the population observed. There is an additional peak in the BH mass spectrum observed at  $m \simeq 35M_{\odot}$ , this is expected to arise due to pulsational pair-instability SN (PPISN). The merger rate does not sharply decrease beyond  $m \sim 40M_{\odot}$ , finding no clear

evidence of a pair-instability SN (PISN) gap approximately between  $\sim 40 - 120M_{\odot}$ <sup>28</sup>. BHs formed from the collapse of metal-poor stars (Pop III) might avoid the PISN and lead to the formation of heavy BHs. The lack of a sharp truncation might also indicate a hierarchical formation pathway for binaries. However, the absence of any fiducial mass and spin correlation, expected for a hierarchical formation, in the heavy mass regime casts doubt on the contribution of this formation channel. Current estimates indicate an evolution of merger rate with redshift although the error bars on the evolution are high. Spin measurements suggest a marginal preference for align-spin binaries.

The detection of GWs from BBHs has also allowed us to test GR in the strong and relativistic regime of gravity. The various tests of GR, performed on the GW events, have not found any deviation up until now.

The observations of BNSs are consistent with the masses of the galactic NSs. The detection has also enabled constraints on the tidal deformability of the NSs that contain information about the EoS of the nuclear matter. In addition, the BNS mergers are highly promising events for multimessenger observations. The joint detection of EM counterpart to GW signal from GW170817 has revealed the BNS mergers as the engines of the short gamma-ray bursts (sGRBs), and sites for heavy elements formation. It also provided new tools to study dense nuclear matter and cosmology<sup>29</sup>.

## 1.6 Future Prospects: Future Detectors

Current GW detectors, despite being the best precision measurement instruments, suffer from poor sensitivities at lower frequencies and high frequencies. Several proposed next-generation (XG or 3G) detectors will overcome these limitations. Proposed future detectors include two Cosmic Explorers (CEs) in the USA and one Einstein Telescope (ET) in Europe. They will have arm-lengths larger by a factor of 10 than the existing detectors, resulting in an improvement of three orders of magnitude in the sensitivity volume. This will lead to the detection of the farthest binaries possible in the universe (see horizon distance<sup>30</sup> plots for various detectors in Fig. 1.17). Specifically, the low-frequency sensitivity will be crucial, for detecting IMBH binaries, if they exist, at low frequencies, for the detection of the long

<sup>28</sup> These limits are uncertain due to huge uncertainty in the  $^{12}\text{C}(\alpha, \gamma)^{16}\text{O}$  reaction rates, which moderate the production of oxygen from the carbon.

<sup>29</sup> B. P. Abbott et al. Multi-messenger Observations of a Binary Neutron Star Merger. *Astrophys. J.*, 848(2):L12, 2017. DOI: 10.3847/2041-8213/aa91c9; Daniel Kasen et al. Origin of the heavy elements in binary neutron-star mergers from a gravitational-wave event. *Nature*, 551(7678):80–84, November 2017. DOI: 10.1038/nature24453; B. P. Abbott et al. GW170817: Measurements of Neutron Star Radii and Equation of State. *Phys. Rev. Lett.*, 121(16):161101, October 2018. DOI: 10.1103/PhysRevLett.121.161101; and B. P. Abbott et al. A gravitational-wave standard siren measurement of the Hubble constant. *Nature*, 551(7678):85–88, November 2017. DOI: 10.1038/nature24471

<sup>30</sup> Horizon distance of a detector/network is the distance up to which an optimally oriented binary could be detected.

inspiral of BNS and NSBH systems enabling the pre-merger detection and localization, and for enabling the detection of residual eccentricities. The sensitivity improvement at high frequencies will be crucial for post-merger detection of BNS, enabling an accurate probe of the EoS of the nuclear matter at ultra-nuclear densities. The rate of binaries will be very large, expecting overlap of multiple signals in the data.

The Laser Interferometer Space Antenna (LISA) is planned to be launched by the mid-2030s. LISA will be in a triangular shape with three spacecraft acting as the test masses. Due to its very long arms, LISA will be sensitive in a few  $\mu\text{Hz}$  to a few tens of mHz frequencies corresponding to the inspiral-merger of SMBH binaries. In addition, LISA will also see very early-inspiral of the stellar mass compact binaries and the merger of white dwarfs.

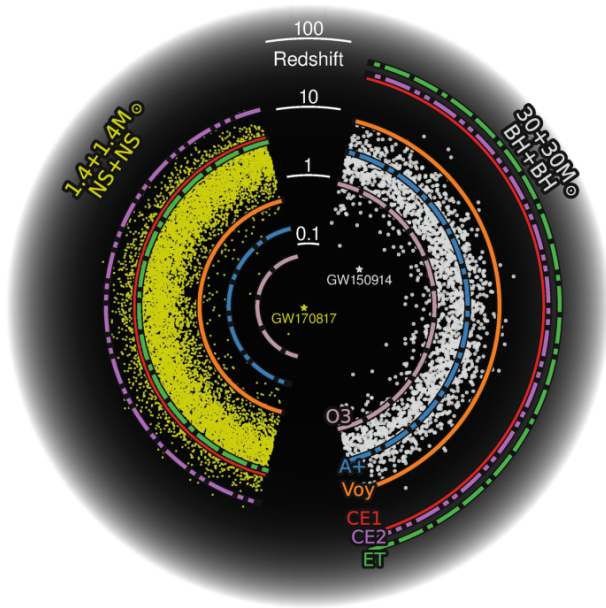


Figure 1.17: Horizon distance for various current and future generations of detectors assuming BNS (yellow dots) and BBH (white dots) mergers as the sources of GWs. (Credit: Luck et al 2022)

### Summary

The direct detection of GWs from the mergers of compact binaries has ushered a new era of GW astronomy. It has not only established the consistency of the signals with GR but has also pointed out that exotic compact objects like BHs, and NSs exist in nature. In this chapter, we highlighted the propagation of GWs with the speed of light in vacuum in linearized theory. We also discussed some of the possible sources of GWs ranging from the strongest compact binary mergers



to rotating NSs, supernovae explosions, and energetic processes in the early universe. Currently operating km scale laser interferometers along with their noise sources and detection capabilities were discussed in detail.

The detection of GWs from merging compact binaries is primarily based on comparing the data with theoretical waveform models. We defined the signal-to-noise ratio strength for the matched-filtering detection algorithm. Apart from the detection, parameter inference of a compact binary merger leads to probabilistic estimates of the source properties such as masses, spins, distances, orientations, etc. Inference of the source properties for many compact binary mergers has enabled an understanding of the population properties, shedding some light on their formation and evolutionary pathways. However, this is currently limited by the small number of events and large measurement uncertainties. The detection of GWs has also enabled the multimessenger astronomy and cosmology with GWs.



## 2 | Multipole Expansion of Gravitational Radiation

### 2.1 Generation of GWs in linearized theory

The previous chapter showed that the linearized form of EFEs established the existence of GWs far away from the source. In this section, we explore the generation of GWs from a source in linearized theory, closely following Maggiore [140]. The gravitational field generated by the source is sufficiently weak to assume the background as flat and the GW generation and propagation are governed by

$$\square \bar{h}_{\mu\nu} = -\frac{16\pi G}{c^4} T_{\mu\nu} \quad (2.1)$$

The general solution for the above Eq. is given by using the Green function method,

$$h_{ij}^{TT}(t, \mathbf{x}) = \frac{4G}{c^4} \Lambda_{ij,kl}(\hat{\mathbf{n}}) \int d^3x' \frac{1}{|\mathbf{x} - \mathbf{x}'|} T_{kl} \left( t - \frac{|\mathbf{x} - \mathbf{x}'|}{c}, \mathbf{x}' \right) \quad (2.2)$$

where  $\Lambda_{ij,kl}(\hat{\mathbf{n}})$  is the Lambda tensor that projects the GW traveling along the direction  $\hat{\mathbf{n}}$  onto the TT gauge and is defined as

$$\Lambda_{ij,kl}(\hat{\mathbf{n}}) = P_{ik}P_{jl} - \frac{1}{2}P_{ij}P_{kl} \quad \text{with} \quad P_{ij} = \delta_{ij} - n_i n_j \quad (2.3)$$

The notations  $\mathbf{x}$  and  $\mathbf{x}'$  correspond to the observer and source positions, respectively. The time coordinate of  $T_{kl}$  is  $t_{\text{ret}} = t - \frac{|\mathbf{x} - \mathbf{x}'|}{c}$ , known as the retarded time. Note that Eq 2.2 only depends on the spatial components of  $T_{kl}$ . This is because  $T_{0k}$  and  $T_{00}$  are related to  $T_{kl}$  by the conservation of stress-energy tensor and can be eliminated.

### 2.1.1 Weak field expansion

Far away from source, at  $|\mathbf{x}| = r \gg d$ , with  $d$  being the typical size of the source

$$|\mathbf{x} - \mathbf{x}'| = r - \mathbf{x}' \cdot \hat{\mathbf{n}} + \mathcal{O}(d^2/r) \quad (2.4)$$

The value of  $h_{\mu\nu}^{TT}$  at a large distance from the source, where the detectors are located, is computed up to  $\mathcal{O}(1/r)$ :

$$h_{ij}^{TT}(t, \mathbf{x}) = \frac{4G}{c^4} \Lambda_{ij,kl}(\hat{\mathbf{n}}) \int d^3x' \frac{1}{|\mathbf{x} - \mathbf{x}'|} T_{kl} \left( t - \frac{r}{c} + \frac{\mathbf{x}' \cdot \hat{\mathbf{n}}}{c}, \mathbf{x}' \right) \quad (2.5)$$

### 2.1.2 Low-velocity expansion

For a self-gravitating system, e.g. a gravitationally bound two-body system with reduced mass  $\mu$ , total mass  $m$ , and separation  $a$ , the virialization leads to:

$$\frac{1}{2} \mu v^2 = \frac{G\mu m}{2a} \quad (2.6)$$

and therefore

$$\frac{v^2}{c^2} = \frac{R_s}{2a} \quad (2.7)$$

where  $R_s = \frac{2Gm}{c^2}$  is the Schwarzschild radius associated with mass  $m$ . In this scenario, the weak field limit  $R_s \ll a$  is coupled with the low-velocity or slowly moving sources, i.e.  $v \ll c$ . For a source of size  $d$  and typical frequency  $\omega_s$  of the motion, the typical velocities inside the source  $v \sim \omega_s d$ . The frequency of the radiation  $\omega$  is also of the order of  $\omega_s$ , which means  $\omega \sim \omega_s \sim v/d$ . Thus, the reduced wavelength is given by

$$\lambda \equiv c/\omega \sim \frac{c}{v} d. \quad (2.8)$$

In the non-relativistic regime,  $v \ll c$ , therefore  $\lambda \gg d$ , known as the large wavelength approximation. Physically, this means when the radiation wavelength is much bigger than the size of the system, the coarse features of the source are sufficient to characterize the emission of radiation<sup>1</sup>. It will be easier to use the large wavelength approximation to get the multipole expansion of  $h_{\mu\nu}^{TT}$  at the spatial infinity if we write  $T_{kl}$  in Eqs. 2.5 in terms of its Fourier transform,

$$T_{kl} \left( t - \frac{r}{c} + \frac{\mathbf{x}' \cdot \hat{\mathbf{n}}}{c}, \mathbf{x}' \right) = \int \frac{d^4k}{(2\pi)^4} \tilde{T}_{kl}(\omega, \mathbf{k}) e^{-i\omega(t-r/c+\mathbf{x}' \cdot \hat{\mathbf{n}}/c) + i\mathbf{k} \cdot \mathbf{x}'} \quad (2.9)$$

<sup>1</sup> The flat space-time approximation used for this leading order calculation will become inaccurate when we consider  $\mathcal{O}(v/c)$  corrections. This is addressed through the PN expansion technique.

The integration in Eq. 2.5 is limited to  $|\mathbf{x}'| \leq d$ , the dominant contribution to  $h_{\mu\nu}^{TT}$  comes from the frequencies that satisfy

$$\frac{\omega}{c} \mathbf{x}' \cdot \hat{\mathbf{n}} \lesssim \frac{\omega_s d}{c} \ll 1 \quad (2.10)$$

and therefore

$$e^{-i\omega(t-r/c+\mathbf{x}' \cdot \hat{\mathbf{n}}/c)} = e^{-i\omega(t-r/c)} \sum_{\alpha=0}^{\infty} \frac{(-i\omega \mathbf{x}'^i \hat{n}^i)^\alpha}{\alpha!} \quad (2.11)$$

which is equivalent to

$$T_{kl} \left( t - \frac{r}{c} + \frac{\mathbf{x}' \cdot \hat{\mathbf{n}}}{c}, \mathbf{x}' \right) \simeq \sum_{\alpha=0}^{\infty} \frac{(x'^i \hat{n}^i)^\alpha}{\alpha!} \partial_t^\alpha T_{kl}(t - r/c, \mathbf{x}') \quad (2.12)$$

One can define various moments of the stress tensor

$$S^{ij}(t) = \int d^3x T^{ij}(t, \mathbf{x}), \quad (2.13)$$

$$S^{ij,k}(t) = \int d^3x T^{ij}(t, \mathbf{x}) x^k, \quad (2.14)$$

$$S^{ij,kl}(t) = \int d^3x T^{ij}(t, \mathbf{x}) x^k x^l \quad (2.15)$$

and similarly other higher-order moments. Plugging in Eqs. 2.13-2.15 and Eq. 2.9 in Eq. 2.5, the metric perturbations

$$h_{ij}^{TT}(t, \mathbf{x}) = \frac{4G}{rc^4} \Lambda_{ij,kl}(\hat{\mathbf{n}}) \left[ S^{kl} + \frac{1}{c} n_m \dot{S}^{kl,m} + \frac{1}{2c^2} n_m n_p \ddot{S}^{kl,mp} + \dots \right]_{\text{ret}} \quad (2.16)$$

The right-hand side is evaluated at the retarded time. This is known as the multipole expansion of GW radiation in terms of the source moments. It is noteworthy that  $S^{kl,m}$  has an additional factor of  $x^m \sim \mathcal{O}(d)$  as compared to  $S_{kl}$  and the time derivative brings a factor of  $\mathcal{O}(\omega_s)$ . Then the second term is a factor of  $\mathcal{O}(v/c)$  smaller than  $S^{kl}$  term, and the third term by a factor of  $\mathcal{O}(v^2/c^2)$ , so on. To understand the physical meaning of the terms in the multipole expansion, we can write Eq. 2.16 in terms of the moments of the energy density  $T^{00}$  and linear momentum  $T^{0i}$ . Defining

$$M = \frac{1}{c^2} \int d^3x T^{00}(t, \mathbf{x}), \quad (2.17)$$

$$M^i = \frac{1}{c^2} \int d^3x T^{00}(t, \mathbf{x}) x^i, \quad (2.18)$$

$$M^{ij} = \frac{1}{c^2} \int d^3x T^{00}(t, \mathbf{x}) x^i x^j, \quad (2.19)$$

$$M^{ijk} = \frac{1}{c^2} \int d^3x T^{00}(t, \mathbf{x}) x^i x^j x^k, \quad (2.20)$$

and

$$P^i = \frac{1}{c} \int d^3x T^{0i}(t, \mathbf{x}), \quad (2.21)$$

$$P^{i,j} = \frac{1}{c} \int d^3x T^{0i}(t, \mathbf{x}) x^j, \quad (2.22)$$

$$P^{i,jk} = \frac{1}{c} \int d^3x T^{0i}(t, \mathbf{x}) x^j x^k, \quad (2.23)$$

In linearized theory, the stress tensor  $T_{\mu\nu}$  satisfies the energy-momentum conservation, i.e.

$$\partial_\mu T^{\mu\nu} = 0 \quad (2.24)$$

Or

$$\partial_0 T^{\mu 0} = -\partial_i T^{\mu i} \quad (2.25)$$

Taking a box of volume  $V$  with  $T^{\mu\nu}$  vanishing at the boundary  $\partial V$ , and using the above Eq. with  $\mu = 0$ , we get

$$c\dot{M} = \int_V d^3x \partial_0 T^{00} = - \int_V d^3x \partial_i T^{0i} = \int_{\partial V} dS n_i T^{0i} = 0 \quad (2.26)$$

Similar identities can be derived for higher moments. The first few moments are given below

$$\dot{M} = 0, \quad (2.27)$$

$$\dot{M}^i = P^i, \quad (2.28)$$

$$\dot{M}^{ij} = P^{i,j} + P^{j,i}, \quad (2.29)$$

and

$$\dot{P}^i = 0, \quad (2.30)$$

$$\dot{P}^{i,j} = S^{ij}, \quad (2.31)$$

$$\dot{P}^{i,jk} = S^{ij,k} + S^{ik,j}, \quad (2.32)$$

The monopole  $M$  and dipole  $P^i$  terms vanish due to the conservation of mass and linear momentum in the linearized theory <sup>2</sup>. However, the absence of monopole and dipole radiation is true even in the full non-linear theory <sup>3</sup>.

**The Quadrupole formula:** From Eqs. 2.29 and 2.31

$$S^{ij} = \frac{1}{2} \dot{M}^{ij} \quad (2.33)$$

<sup>2</sup> From a field-theoretic point of view, the graviton is a massless particle with helicity  $\pm 2$  and can not be put in a state with total angular momentum  $j = 0$  (monopole term) or  $j = 1$  (dipole term).

<sup>3</sup> In full non-linear theory, the role of stress-energy tensor  $T_{kl}$  is played by the  $\tau_{kl}$  that also accounts for the contribution from the gravitational field.

Thus, in the leading order in  $v/c$ , Eq. 2.16,

$$h_{ij}^{TT}(t, \mathbf{x}) = \frac{2G}{c^4} \Lambda_{ij,kl}(\hat{\mathbf{n}}) \ddot{M}^{kl}(t - r/c) \quad (2.34)$$

Since  $\Lambda$  tensor converts any symmetric tensor into a traceless one, it is useful to split the trace-free and trace parts

$$M^{kl} = \left( M^{kl} - \frac{1}{3} \delta^{kl} M_{ii} \right) + \frac{1}{3} \delta^{kl} M_{ii} \quad (2.35)$$

Using the notation  $\rho = T^{00}/c^2$ , we define the quadrupole moment

$$Q^{ij} \equiv M^{kl} - \frac{1}{3} \delta^{kl} M_{ii} = \int d^3x \rho(t, \mathbf{x}) (x^i x^j - \frac{1}{3} r^2 \delta_{ij}) \quad (2.36)$$

This allows us to write Eq. 2.16 in terms of the second time derivative of the mass quadrupole moment.

$$[h_{ij}^{TT}(t, \mathbf{x})]_{\text{quad}} = \frac{2G}{c^4} \ddot{Q}_{ij}^{TT}(t - r/c) \quad (2.37)$$

The quadrupole formula gives the leading order calculation of the expected GW polarisations from an astrophysical source, e.g., inspiralling compact binaries (ICBs). Note that the binary will evolve due to the energy/momentum loss through GW emission ( $v$  will increase). So one has to solve the equation of motion (EOM) along with the quadrupole formula to compute the expected GW signal from an ICB.

Note that the quadrupole formula takes into account only the leading term in Eq. 2.16. As  $v$  increases, the higher-order corrections become important. These are computed using the PN approximation. This provides a systematic way of computing corrections to the (Newtonian) EOM and the contribution to the GWs due to higher order multipoles of the source.

Eventually,  $v/c$  reaches near 1, and the PN approximation breaks down and one needs to solve the full Einstein's equations (Eq. 1.1) numerically. In the past 2 decades, NR methods have been matured to solve the binary black hole problem. The waveform models used for GW data analysis, broadly, take the input from PN/NR calculations for the early/late part of the inspiral. The subsequent merger can only be modeled using NR. The final phase of the ringdown of the newly formed remnant can be computed using a combination of NR and BH perturbation theory.

## 2.2 Multipolar gravitational waveforms

A complex combination of the two polarizations  $+$  and  $\times$  of GWs,  $h(t) := h_+(t) - ih_\times(t)$ , from a compact binary merger can be expanded as <sup>4</sup>,

$$h(t) = \frac{1}{d_L} \sum_{\ell=2}^{\infty} \sum_{m=-\ell}^{\ell} h_{\ell m}(t, \vec{\lambda}) Y_{-2}^{\ell m}(\iota, \varphi_0), \quad (2.38)$$

where  $Y_{-2}^{\ell m}$  are the spin-2 spherical harmonics, while  $h_{\ell m}$  are the spherical harmonic modes of the gravitational radiation. In this way, all the intrinsic properties  $\vec{\lambda}$  of the radiation, such as component masses  $(m_1, m_2)$  and spins  $(\mathbf{S}_1, \mathbf{S}_2)$  in case of a binary, are captured by the modes  $h_{\ell m}$  while the angular dependence is captured by the spherical harmonics  $Y_{-2}^{\ell m}$  in terms of orbital inclination  $\iota$  (the angle between the line-of-sight of the observer and the orbital angular momentum vector) and initial phase  $\varphi_0$ .

In the PN approximation, the spherical harmonic modes of the radiation can be written in terms of radiative moments <sup>5</sup>:

$$h_{\ell m}(t) = \frac{G}{\sqrt{2}c^{\ell+2}} \left( U_{\ell m}(t) - \frac{i}{c} V_{\ell m}(t) \right) \quad (2.39)$$

where  $U_{\ell m}$  and  $V_{\ell m}$  are the mass and current moments that are related to source moments in Eq. 2.16 (see Kidder [125] for details). In NR simulations, the  $h_{\ell m}$ s can be computed by decomposing the radiation field  $h(\iota, \varphi_0)$  onto the spherical harmonic basis functions

$$h_{\ell m} = \int h(\iota, \varphi_0) Y_{-2}^{*\ell m}(\iota, \varphi_0) d\Omega \quad (2.40)$$

If the axis of decomposition is chosen along the direction of the total orbital angular momentum of the binary, the  $\ell = 2, m \pm 2$  mode will contain the dominant part of the radiation.

For non-precessing binaries, the GW polarizations can be written in the frequency domain

$$\tilde{h}_+(f) = \frac{1}{d_L} \sum_{\ell=2}^{\infty} \sum_{m=1}^{\ell} \tilde{h}_{\ell m}(f, \vec{\lambda}) A_+^{\ell m}(\iota) e^{im\varphi_0} \quad (2.41)$$

$$\tilde{h}_\times(f) = \frac{i}{d_L} \sum_{\ell=2}^{\infty} \sum_{m=1}^{\ell} \tilde{h}_{\ell m}(f, \vec{\lambda}) A_\times^{\ell m}(\iota) e^{im\varphi_0} \quad (2.42)$$

where  $A_{+,\times}^{\ell m}$  are the amplitudes dependent only on the inclination

<sup>4</sup> E. T. Newman and R. Penrose. Note on the bondi-metzner-sachs group. *Journal of Mathematical Physics*, 7(5):863–870, 1966. DOI: 10.1063/1.1931221. URL <https://doi.org/10.1063/1.1931221>

<sup>5</sup> Lawrence E. Kidder. Using full information when computing modes of post-Newtonian waveforms from inspiralling compact binaries in circular orbit. *Phys. Rev. D*, 77:044016, 2008. DOI: 10.1103/PhysRevD.77.044016



angle

$$A_+^{\ell m}(\iota) = Y_{-2}^{\ell m}(\iota, 0) + (-1)^\ell Y_{-2}^{\ell, -m}(\iota, 0) \quad (2.43)$$

$$A_\times^{\ell m}(\iota) = Y_{-2}^{\ell m}(\iota, 0) - (-1)^\ell Y_{-2}^{\ell, -m}(\iota, 0) \quad (2.44)$$

and  $\tilde{h}_{\ell m}$  are the frequency domain modes. The leading order contribution comes from the quadrupole mode ( $\ell = |m| = 2$  or simply 22). The subleading terms ( $\ell \geq 2, |m| \neq 2$ ) in the expansion, higher modes (HMs), are often neglected in GW data analysis. However, they can make an appreciable contribution to the radiation from asymmetric binaries (e.g., binaries with unequal component masses, high total mass, and misaligned high spins).

### 2.2.1 Contribution of asymmetries to higher modes

The main asymmetries that affect the contribution of subdominant modes to the GW radiation emitted by a binary depend on:

1. **Unequal masses:** this asymmetry is captured by the mass ratio  $q = m_1/m_2 \geq 1$ . The relative contribution of the HMs with respect to the dominant quadrupole mode increases for more unequal mass binary systems. Fig. 2.1 shows that the amplitude ratios of the next two subleading modes ( $\ell = 3, m = \pm 3$ , hereafter 33) and ( $\ell = 4, m = \pm 4$ , hereafter 44) to the dominant 22 mode are larger for high mass ratios.

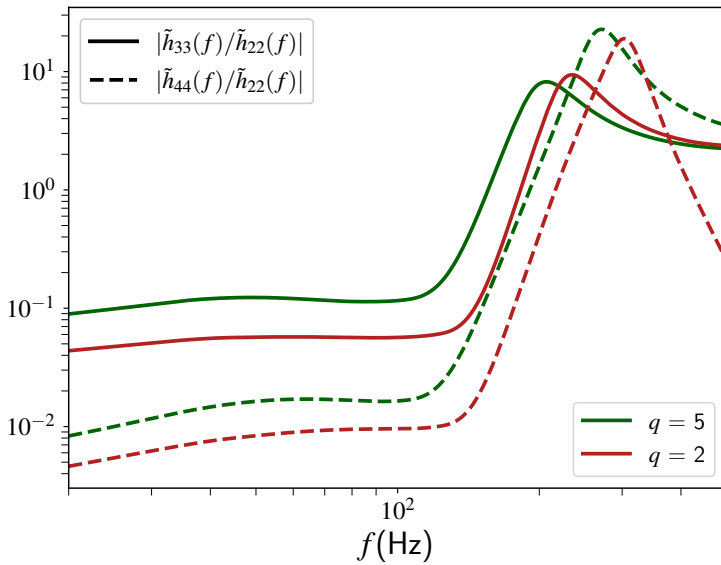


Figure 2.1: The ratio of frequency domain amplitudes for the two subleading modes 33 (solid) and 44 (dashed) to dominant 22 mode. The larger mass ratio results in the larger amplitude ratios (in maroon).

2. **High total mass:** The total mass, defined as the sum of the compo-

nent masses, i.e.  $M_{\text{tot}} = m_1 + m_2$ , governs the frequency at which the binary will merge. This is understood from the ISCO radius definition of the binary in Eq. 1.15. The larger the ISCO radius of a binary, the orbit will cease to be circular at larger separations, hence the binary will merge at smaller frequencies. Consequently, the dominant mode will spend less time (have a smaller frequency content) in the sensitivity band of the detector while HMs will still have a larger duration (frequency) span (see Fig 2.2). In particular, the contribution of HMs will be crucial for the binaries with high masses, for which the merger frequency of the dominant mode falls below or close to the lower frequency cut-off of the sensitivity band of the detectors.

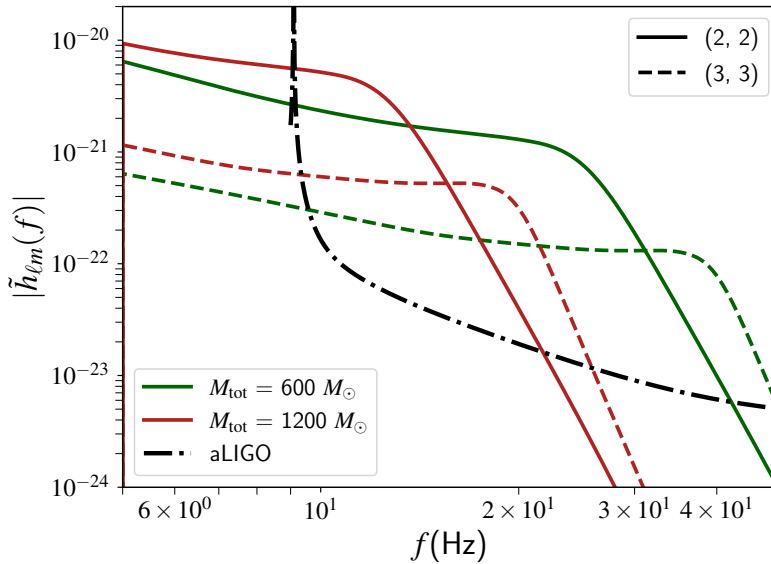


Figure 2.2: The Fourier domain amplitudes of the dominant 22 (solid) and the next subleading 33 mode (dashed) are shown corresponding to two different total masses  $M_{\text{tot}} = 600, 1200M_{\odot}$ . The 22 mode spends less time (smaller frequency range) for heavier binary as compared to the 33 mode. The black dashed-dotted line is the noise amplitude spectral density, i.e.  $\sqrt{S_n(f)}$ , of the advanced LIGO detector.

3. **Large misaligned spins:** The spins of the individual compact objects in the binary can change the shape of the GW signal waveform. When the component spin vectors of the compact objects are not misaligned with respect to the orbital angular momentum vector, the plane of the binary will precess. This will lead to modulations in the signal. The orbital precession can alter the multipolar structure of the waveform significantly, putting significant power in the HMs. The reason is that gravitational radiation is primarily beamed perpendicular to the orbital plane, which undergoes precession in this case (see green dashed line in Fig 2.3).
4. **Orientation:** The observability of HMs also depends on the extrinsic parameter, the inclination angle  $\iota$ , through the amplitudes

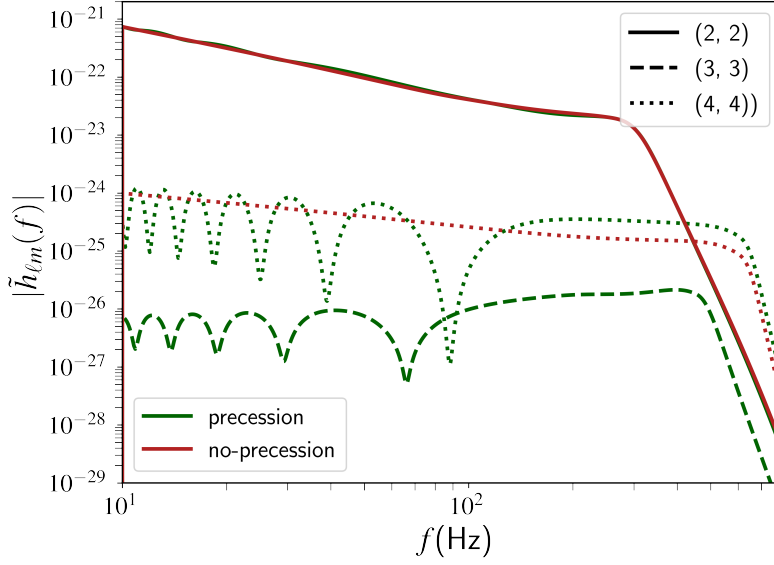


Figure 2.3: The amplitudes of several multipoles, 22, 33, and 44 are plotted for a binary system with  $q = 1$ . The presence of precessing spins (in green) leads to modulations in the multipoles, especially prominent in 33 and 44 modes. In the absence of the precession (in brown), the 33 mode vanishes completely.

$A_{+, \times}^{\ell m}(\iota)$ . In Fig. 2.4, the amplitude  $A_{+}^{\ell m}$  is plotted as a function of  $\iota$  for various radiation modes. All the modes with  $|m| \neq 2$  vanish for face-on ( $\iota = 0^\circ$ ) systems. However, as the systems transition from face-on to edge-on ( $\iota = 90^\circ$ ) configuration, the relative contribution of most of the HMs to the dominant mode increases. The amplitudes  $A_{\times}^{\ell m}$  peak for most of the modes around  $\iota \sim 40 - 45^\circ$  degrees but vanish in the edge-on configuration.

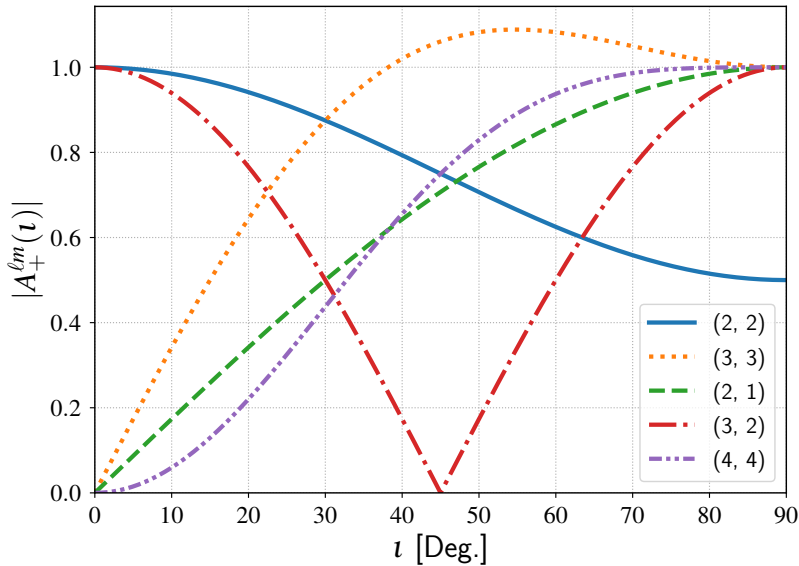


Figure 2.4: Inclination-dependent amplitude, Eq. 2.43 of the + polarization is plotted as a function of inclination. Most of the HMs (except the ones with  $m = 2$ ) vanish at near face-on configuration and contribute to near edge-on configuration. The  $m = 2$  modes are normalized at  $\iota = 0^\circ$  and the rest of the modes at  $\iota = 90^\circ$ , similar to Mills and Fairhurst [149].

### 2.3 Impact of higher modes on the detection

As discussed in section 1.4.6, the detecting GWs relies primarily on matched filtering data against a bank of theoretical templates. The efficiency of the templated GW searches, among other things, depends on the accuracy of the waveform model used for constructing the template bank. Currently, most GW searches employ quadrupolar, aligned-spin, and quasi-circular waveform models. Including effects such as subdominant modes, orbital precession, and eccentricity can improve the sensitivity of the search if such features are significant in the observed signals. However, the additional degrees of freedom in the search will lead to an increase in the size of the template banks. This will increase the computational cost of the matched filters as well as the prevalence of the noise triggers.

Assuming sensitivities of the advanced LIGO, neglecting HMs in the searches will have no major impact on the detection rate in the region of the parameter space where the asymmetries are not significantly high<sup>6</sup>. However, including HMs can increase the sensitivity of the searches up to a factor of 2 in volume for significantly unequal mass ( $q \gtrsim 4$ ) and high total mass ( $m_1 + m_2 \gtrsim 100M_\odot$ ) systems<sup>7</sup>. Please note this is a sensitivity-dependent statement. In future observing scenarios, the HMs searches could be important even for low mass-ratio and total mass systems.

Chandra et al. [75] were the first to develop a GW search using HMs for IMBH binary mergers with redshifted total mass range  $M_{\text{tot}}(1+z) \in (100, 500)M_\odot$  and mass ratios  $q \in (1, 10)$ . Unlike 22-mode searches,  $\iota$  and  $\varphi_0$  can not be analytically maximized due to differing amplitude and phase contributions to distinct modes, therefore, the templates were also laid out in  $\iota$  and  $\varphi_0$  apart from masses and aligned spins. It demonstrated the sensitivity increase in the volume by 450% although it was limited to near-edge-on inclinations  $\iota \in (75^\circ, 105^\circ)$ . However, the computational cost was significantly higher (a factor of  $\sim 200$ ) than existing quadrupolar searches. The increase in the number of templates also led to an increase in the false identification of noise triggers as GW signals. Recently, Wadekar et al. [190] have proposed a new HMs search that performs matched filtering mode-by-mode, currently for three leading harmonics 22, 33, and 44. The outputs of these mode-by-mode filters,

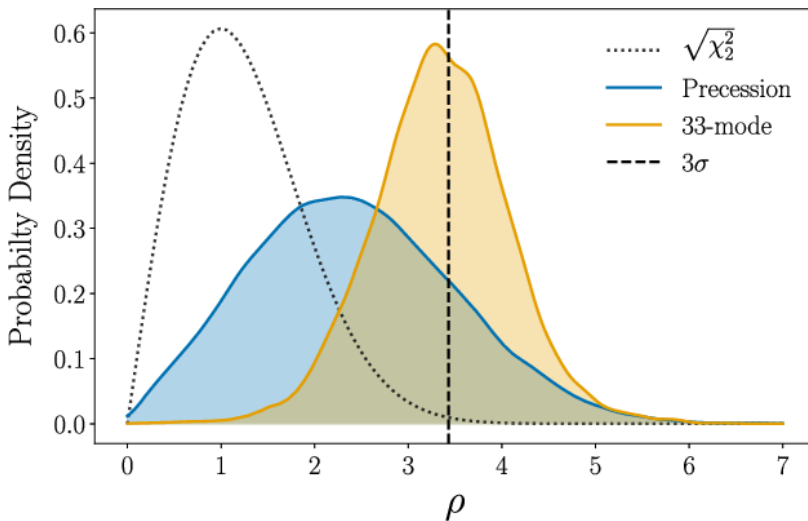
<sup>6</sup> In fact, including HMs in the searches in a conventional way will increase in its dimensionality leading to a slightly worse performance than the quadrupolar search for low total masses and mass ratios Capano et al. [72].

<sup>7</sup> Ian Harry, Juan Calderón Bustillo, and Alex Nitz. Searching for the full symphony of black hole binary mergers. *Phys. Rev. D*, 97:023004, Jan 2018. DOI: 10.1103/PhysRevD.97.023004. URL <https://link.aps.org/doi/10.1103/PhysRevD.97.023004>

the SNR time series for each harmonic, are then combined according to their expected amplitudes (corresponding to physical configurations of  $\iota$  and  $\varphi_0$ , as well as the intrinsic parameters for each mode). The unphysical combinations are weighted down to avoid the loss in the sensitivity of the search. The computational cost is just 3 times larger than 22-mode searches.

## 2.4 Observational evidence of higher modes

The existence of the HMs of gravitational radiation has been established in several unequal mass binaries detected by LIGO-Virgo detectors. For example, the first unequal mass BBH merger, GW190412<sup>8</sup> observed with  $q \sim 3.7$  and the network SNR  $\rho \sim 19$ , had significant orthogonal optimal SNR  $\sim 3.5$  in the next subdominant 33 mode (see Fig 2.5)<sup>9</sup>. Subsequently, the most unequal mass binary system detected to date, GW190814<sup>10</sup> with  $q \sim 10$  and the SNR  $\sim 25$ , had the largest contribution from HMs. The SNR in the 33 mode was inferred as  $\sim 6.4$ . Several other events were observed to have appreciable contributions from HMs during three observing runs of LVK (e.g. GW170729, etc).



<sup>8</sup> R. Abbott et al. GW190412: Observation of a binary-black-hole coalescence with asymmetric masses. *Phys. Rev. D*, 102:043015, Aug 2020. DOI: 10.1103/PhysRevD.102.043015. URL <https://link.aps.org/doi/10.1103/PhysRevD.102.043015>

<sup>9</sup> The orthogonal optimal SNR is computed from the part of the multipole perpendicular to the dominant multipole using the noise-weighted inner product (see Mills and Fairhurst [149]).

<sup>10</sup> R. Abbott et al. GW190814: Gravitational waves from the coalescence of a 23 solar mass black hole with a 2.6 solar mass compact object. *The Astrophysical Journal*, 896(2):L44, jun 2020. DOI: 10.3847/2041-8213/ab960f. URL <https://doi.org/10.3847/2041-8213%2Fab960f>

Figure 2.5: The orthogonal optimal SNR in the strongest HM, 33 (orange) is measured for GW190412 event at  $3\sigma$  confidence (dashed line) based on the expected distribution of optimal SNR due to Gaussian noise (black dotted line). There is marginal evidence of precession in this event but the median value of the expected SNR due to precession is consistent with the noise (blue) (Credit: R Abbott et al 2020)

## 2.5 Science gain due to higher modes

The observations of HMs have not only verified GR as an accurate prediction of gravity but also led to improving the science that can be done. These span from improving the search sensitivity, more

accurate and precise inference, tests of GR to cosmology, etc. We briefly touch upon some of the main feats achieved or expected to be with the use of HMs below.

### 2.5.1 *Breaking degeneracies*

A degeneracy exists between luminosity distance  $d_L$  and orbital inclination  $\iota$  of the source that enters the amplitude of the dominant mode GW radiation through  $Y_{-2}^{22}(\iota, \phi)/d_L$ . For a binary system whose orbital plane faces directly to the observer, i.e.  $\iota \sim 0$  or whose mass ratio is near unity, the GW radiation emitted will have contribution primarily from the dominant mode,  $h_{22}$  due to the vanishing of spherical harmonics for most of the HMs. This will lead to a degenerate estimate of  $\iota$  and  $d_L$ . However, when the system is asymmetric in masses as well as highly inclined, the linear dependence between the spherical harmonics and distance will be replaced by the sum for multiple harmonics. Consequently, the contribution from HMs will break or reduce this degeneracy leading to more accurate and robust estimates of source  $\iota$  and  $d_L$  (see Fig 2.6). There are other degeneracies, e.g. mass ratio and spin, polarization and phase, etc., that can be reduced with the inclusion of HMs in the GW waveform models.

### 2.5.2 *Improving the measurement of cosmology*

Since GWs travel almost unhindered, their detection allows us to measure the absolute luminosity of the source. If the source of GWs has an EM counterpart, it can be used to measure the redshift of the host galaxy. There is also a statistical method to measure the redshift of the source <sup>11</sup>. Using these independent measurements of the distances to the source, one can constrain the Hubble expansion rate of the universe and other cosmological parameters. However, the degeneracy in the measurement of distance with inclination from the GW side often leads to huge uncertainties in measuring cosmology. This is remedied to a significant extent when HMs are present in the GW signal detected. The increased SNR due to HMs further improves the error bars on distance leading to better estimates of the cosmological parameters <sup>12</sup>.

<sup>11</sup> B. F. Schutz. Determining the Hubble constant from gravitational wave observations. *Nature*, 323(6086):310–311, September 1986. DOI: 10.1038/323310a0

<sup>12</sup> Ish Gupta, Ssohrab Borhanian, Arnab Dhani, Debatri Chattopadhyay, Rahul Kashyap, V. Ashley Villar, and B. S. Sathyaprakash. Neutron star-black hole mergers in next generation gravitational-wave observatories. *Phys. Rev. D*, 107(12):124007, 2023. DOI: 10.1103/PhysRevD.107.124007

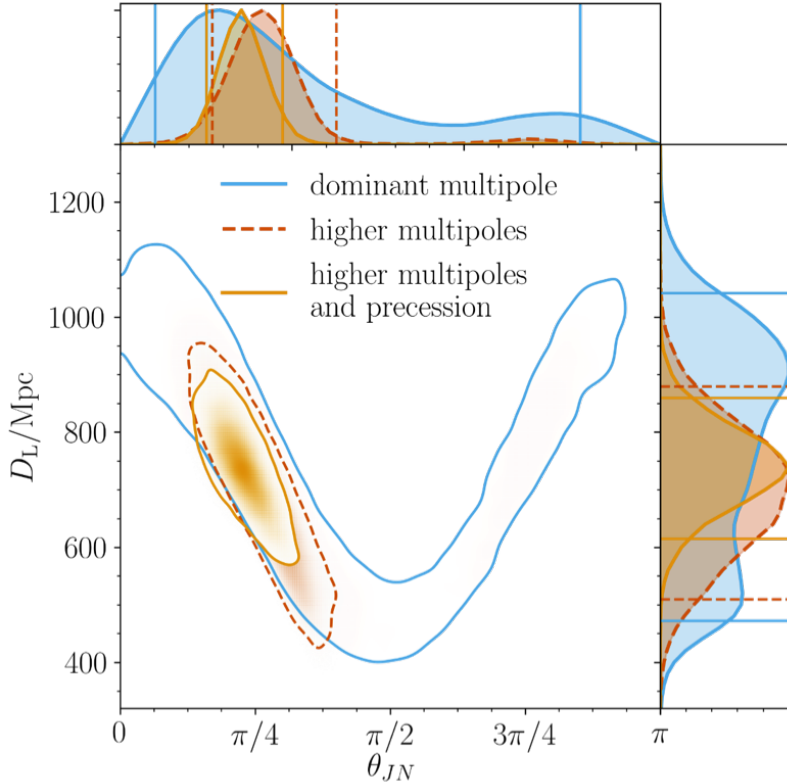


Figure 2.6: The measurement of the luminosity distance and orbital inclination for GW190412 event is compared when using a dominant mode-only waveform model (in blue) to a multipolar waveform model (dashed). The inclusion of HMs has significantly improved the estimate of  $\iota$  and  $d_L$ . (Credit: R Abbott et al 2020)

### 2.5.3 Unbiased and accurate inference

The absence of the HMs in the waveform models used for data analyses can lead to systematic biases in the inference of source properties of the source of the GW signal. Several investigations<sup>13</sup> have shown that neglecting HMs in the analyses of significantly unequal masses ( $q \gtrsim 4$ ) and high total mass ( $M_{\text{tot}} \gtrsim 150M_{\odot}$ ) compact binaries can lead to systematics greater than the statistical errors due to Gaussian noise. The inclusion of HMs will not only provide unbiased but also more precise inference of the source parameters. The properties most affected by such inference are masses, distance, orientation, phase, polarization, etc.

### 2.5.4 New tests of GR

Asymmetric mass systems provide an avenue previously unexplored to test the GR. Since there is a more complicated structure to the radiation beyond the quadrupolar nature, it could be prone to potential deviations from GR. The presence of HMs would allow us to perform some new tests otherwise inapplicable. For example, the

<sup>13</sup> Chris Van Den Broeck and Anand S. Sengupta. Binary black hole spectroscopy. *Classical and Quantum Gravity*, 24(5):1089–1113, March 2007. DOI: 10.1088/0264-9381/24/5/005; Vijay Varma, Parameswaran Ajith, Sascha Husa, Juan Calderon Bustillo, Mark Hannam, and Michael Pürrer. Gravitational-wave observations of binary black holes: Effect of non-quadrupole modes. *Phys. Rev. D*, 90(12):124004, 2014. DOI: 10.1103/PhysRevD.90.124004; and Vijay Varma and Parameswaran Ajith. Effects of nonquadrupole modes in the detection and parameter estimation of black hole binaries with nonprecessing spins. *Phys. Rev. D*, 96:124024, Dec 2017. DOI: 10.1103/PhysRevD.96.124024. URL <https://link.aps.org/doi/10.1103/PhysRevD.96.124024>

consistency between the parameters inferred from different spherical harmonic modes radiated by a BBH has been used to test the GR <sup>14</sup>. This has been applied to recently observed unequal mass systems, GW190412 and GW190814, finding no deviations from GR <sup>15</sup>. This is akin to checking the consistency between the cosmological parameters measured from the low and high multipoles of the CMB radiation <sup>16</sup>. Moreover, investigating the expected amplitude strengths in the multipoles of GW radiation enables another way to test GR <sup>17</sup>.

## 2.6 Focus of this thesis

There are selection effects that act against observing HMs. Binaries with highly unequal masses or high inclination angles, for which the observed signal will contain a larger relative contribution of HMs, are intrinsically dimmer. This means that only a small fraction of the observed GW signals contain imprints of HMs. Even such signals are rare, including HMs in GW data analysis can provide some significant scientific advantages, such as improving the early warning of compact binary mergers. This is explored in chapters 3 and 4. Additionally, even if the number of events with significant contributions from HMs is a small fraction of the total events, one might wonder, when we infer the population-level properties, such as astrophysical mass, spin distributions, and cosmology by combining a larger number of GW signals, these effects *might* become apparent. I have explored one such question in Chapter 5.

<sup>14</sup> Siddharth Dhanpal, Abhirup Ghosh, Ajit Kumar Mehta, Parameswaran Ajith, and B. S. Sathyaprakash. A no-hair test for binary black holes. *Phys. Rev. D*, 99:104056, May 2019. DOI: 10.1103/PhysRevD.99.104056. URL <https://link.aps.org/doi/10.1103/PhysRevD.99.104056>

<sup>15</sup> Collin D. Capano and Alexander H. Nitz. Binary black hole spectroscopy: A no-hair test of gw190814 and gw190412. *Phys. Rev. D*, 102:124070, Dec 2020. DOI: 10.1103/PhysRevD.102.124070. URL <https://link.aps.org/doi/10.1103/PhysRevD.102.124070>

<sup>16</sup> N. Aghanim et al. Planck 2018 results. VI. Cosmological parameters. *Astron. Astrophys.*, 641:A6, 2020. DOI: 10.1051/0004-6361/201833910. [Erratum: *Astron. Astrophys.* 652, C4 (2021)]

<sup>17</sup> Tousif Islam, Ajit Kumar Mehta, Abhirup Ghosh, Vijay Varma, Parameswaran Ajith, and B. S. Sathyaprakash. Testing the no-hair nature of binary black holes using the consistency of multipolar gravitational radiation. *Phys. Rev. D*, 101(2):024032, 2020. DOI: 10.1103/PhysRevD.101.024032



# 3 | Improving Gravitational-Wave Early Warning of Compact Binary Mergers using Higher Modes

## 3.1 Motivation

Multimessenger detections of compact binary mergers have the potential to answer longstanding astrophysical questions and shed light on complex phenomena that require observational data to constrain theoretical models. This potential was spectacularly demonstrated with GW170817<sup>1</sup> for which EM counterparts were detected in  $\gamma$ -rays to radio by EM telescopes worldwide<sup>2</sup>. This joint GW-EM observation revealed BNS mergers to be engines of short gamma-ray bursts<sup>3</sup> and kilonovae<sup>4</sup>, and sites where heavy elements get synthesized<sup>5</sup>. It further allowed a new probe of the EOS of ultra-dense nuclear matter<sup>6</sup>, a remarkably stringent test of the equality between the speed of GWs and the speed of light<sup>7</sup>, as well as a distance-ladder-independent measurement of the Hubble constant to complement existing measurements<sup>8</sup>. This marked the beginning of the era of multimessenger astronomy with GWs.

A GW early warning (pre-merger detection and localisation) of such electromagnetically bright (EM-Bright) BNS and NSBH events would further shed light on the complex physics surrounding the merger. It can help astronomers to slew their telescopes to the source location for detecting prompt EM emissions before they fade away. A sufficient GW early warning can also enable observations of any possible precursors<sup>9</sup>, a better understanding of the kilonova physics and the formation of heavy elements by identifying the peak of kilonova lightcurves<sup>10</sup>, and possible signatures of any intermediate merger products<sup>11</sup> that might have been found.

<sup>1</sup> Benjamin P. Abbott et al. GW170817: Observation of gravitational waves from a binary neutron star inspiral. *Phys. Rev. Lett.*, 119:161101, 2017. DOI: 10.1103/PhysRevLett.119.161101

<sup>2</sup> B. P. Abbott et al. Multi-messenger Observations of a Binary Neutron Star Merger. *Astrophys. J.*, 848(2):L12, 2017. DOI: 10.3847/2041-8213/aa91c9; and B. P. Abbott et al. Low-latency Gravitational-wave Alerts for Multimessenger Astronomy during the Second Advanced LIGO and Virgo Observing Run. *ApJ*, 875(2):161, April 2019. DOI: 10.3847/1538-4357/ab0e8f

<sup>3</sup> Ehud Nakar. Short-hard gamma-ray bursts. *Physrep*, 442(1-6):166–236, April 2007. DOI: 10.1016/j.physrep.2007.02.005

<sup>4</sup> Brian D. Metzger. Kilonovae. *Living Reviews in Relativity*, 20(1):3, May 2017. DOI: 10.1007/s41114-017-0006-z

<sup>5</sup> Daniel Kasen et al. Origin of the heavy elements in binary neutron-star mergers from a gravitational-wave event. *Nature*, 551(7678):80–84, November 2017. DOI: 10.1038/nature24453

<sup>6</sup> Abbott et al. [8], Abbott et al. [10]

<sup>7</sup> Abbott et al. [11], Liu et al. [135]

<sup>8</sup> B. P. Abbott et al. A gravitational-wave standard siren measurement of the Hubble constant. *Nature*, 551(7678):85–88, November 2017. DOI: 10.1038/nature24471

<sup>9</sup> David Tsang, Jocelyn S. Read, Tanja Hinderer, Anthony L. Piro, and Ruxandra Bondarescu. Resonant Shattering of Neutron Star Crusts. *Phys. Rev. Lett.*, 108(1):011102, January 2012. DOI: 10.1103/PhysRevLett.108.011102

<sup>10</sup> Cowperthwaite et al. [83], Drout et al. [89]

<sup>11</sup> Kenta Hotokezaka et al. Remnant massive neutron stars of binary neutron star mergers: Evolution process and gravitational waveform. *Phys. Rev. D*, 88(4):044026, August 2013. DOI: 10.1103/PhysRevD.88.044026

Current GW early-warning efforts are targeted toward BNS mergers that are traditionally expected to emit an EM counterpart<sup>12</sup>. The dominant mode of a GW signal from a BNS merger lasts for several minutes in the sensitivity band of the current ground-based detectors. This duration could be sufficient for accumulating enough signal-to-noise ratio (SNR), at an early-warning time (ideally tens of seconds to minutes before the merger), leading to tight enough sky maps for telescopes, enabling them to point to the source location before the merger<sup>13</sup>.

However, the early warning of heavier compact binary mergers such as NSBHs will be limited by the short duration of the GW signal if only the dominant mode is considered (signal duration:  $\tau \propto M^{-2/3}$ ). A possible way to achieve early warning is to detect these systems early in the inspiral, although that would require ground-based detectors to be sensitive at very low frequencies. We propose an alternate way that can circumvent this impediment to an extent if the subdominant modes of GW radiation, which are sufficiently excited for asymmetric mass systems, are used in the real-time GW searches<sup>14</sup>. Since HMs vibrate at higher harmonics of the orbital frequency than the dominant mode, they will enter the detectors' frequency band well before the dominant mode — a fact that can be used to enhance early warning targeted at heavier asymmetric binaries.

In this chapter, we quantify the improvements in GW early warning for compact binary mergers when using the subdominant modes of GWs. Section 3.2 discusses the oscillation frequencies of HMs and consequently large durations in comparison to the dominant mode. Further, section 3.3 elaborates on the triangulation method used for localizing the GW events, and section 3.5 highlights early-warning improvements due to HMs for a range of compact binary mergers. In the end, section 3.6 gives an overview of the study conducted as well as broad conclusions drawn from the study that advocates the use of HMs in real-time GW searches to enhance their early-warning abilities.

<sup>12</sup>Surabhi Sachdev et al. An Early-warning System for Electromagnetic Follow-up of Gravitational-wave Events. *Astrophys. J. Lett.*, 905(2):L25, 2020. DOI: 10.3847/2041-8213/abc753; Alexander H. Nitz, Marlin Schäfer, and Tito Dal Canton. Gravitational-wave Merger Forecasting: Scenarios for the Early Detection and Localization of Compact-binary Mergers with Ground-based Observatories. *apjl*, 902(2):L29, October 2020. DOI: 10.3847/2041-8213/abbc10; and Q. Chu et al. Capturing the electromagnetic counterparts of binary neutron star mergers through low-latency gravitational wave triggers. *MNRAS*, 459(1):121–139, June 2016. DOI: 10.1093/mnras/stw576  
<sup>13</sup>Kipp Cannon et al. Toward Early-warning Detection of Gravitational Waves from Compact Binary Coalescence. *ApJ*, 748(2):136, April 2012. DOI: 10.1088/0004-637X/748/2/136

<sup>14</sup>Cody Messick et al. Analysis framework for the prompt discovery of compact binary mergers in gravitational-wave data. *Phys. Rev. D*, 95(4):042001, February 2017. DOI: 10.1103/PhysRevD.95.042001; Samantha A. Usman et al. The PyCBC search for gravitational waves from compact binary coalescence. *Class. Quant. Grav.*, 33(21):215004, 2016. DOI: 10.1088/0264-9381/33/21/215004; Qi Chu. *Low-latency detection and localization of gravitational waves from compact binary coalescences*. PhD thesis, The University of Western Australia, 2017; and T Adams et al. Low-latency analysis pipeline for compact binary coalescences in the advanced gravitational wave detector era. *Classical and Quantum Gravity*, 33(17):175012, aug 2016. DOI: 10.1088/0264-9381/33/17/175012. URL <https://doi.org/10.1088/2F0264-9381%2F33%2F17%2F175012>

### 3.2 Higher modes enter early in the detector's band

The majority of HMs (those with  $\ell > 2$ ), apart from being subdominant, oscillate at higher multiples of orbital frequency  $f_{\text{orb}}(t)$  than the dominant mode. In the inspiral of a non-precessing compact binary merger, the instantaneous frequency of  $\ell m$  mode:

$$f_{\ell m}(t) \simeq m f_{\text{orb}}(t), \quad (3.1)$$

This means the HMs enter the frequency band of the detector at fixed frequency intervals earlier than the dominant mode (see Fig. 3.1). Furthermore, the time to coalescence for  $\ell m$  mode of the GW signal can be approximated when the binary is reached at the orbital frequency of  $f_{\text{orb}}(t)$ <sup>15</sup>

$$\tau \approx \frac{5}{256} \mathcal{M}^{-5/3} (2\pi f_{\text{orb}})^{-8/3} \propto (f_{\ell m}/m)^{-8/3}. \quad (3.2)$$

where  $\mathcal{M} := (m_1 m_2)^{3/5} / (m_1 + m_2)^{1/5}$  is the chirp mass of the binary. It is obvious from the above equation that  $\ell m$  mode will have in-band duration a factor of  $(m/2)^{8/3}$  larger than the dominant mode. The next two subleading modes, 33 and 44 will spend  $\sim 3$  and  $\sim 6$  times larger time than just the dominant (22) mode. This effective increase in the signal duration due to the inclusion of HMs can be used to improve the early detection and localisation as well as measuring the orientation of the asymmetric compact binary mergers, such as NSBH binaries.

### 3.3 localisation of GW sources with triangulation

Working with the assumption that the GW detector noise is stationary and Gaussian, determining a trigger to be significant enough for follow-up comes down to setting some pre-defined threshold on the matched filter SNR. This is because the statistical properties of zero-mean, stationary Gaussian noise are entirely determined by the PSD,  $S_n(f)$ , and the optimal filter to search for known signals buried in it is the matched filter. The localisation area pertaining to a confidence interval can be estimated from the separation of the detectors, their individual effective bandwidths, and the SNRs. We briefly discuss below the method<sup>16</sup> to evaluate the localisation sky area, which

<sup>15</sup> B.S. Sathyaprakash. Filtering post-Newtonian gravitational waves from coalescing binaries. *Phys. Rev. D*, 50(12): 7111–7115, 1994. DOI: 10.1103/PhysRevD.50.R7111

<sup>16</sup> Note that this is a Fisher matrix-based approach which provides a lower bound on statistical errors.

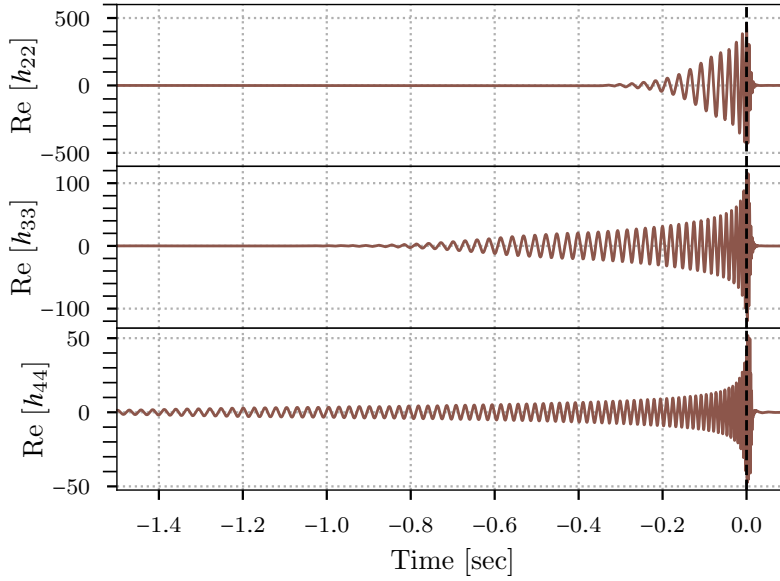


Figure 3.1: Schematic illustration of how different modes appear in the detector band. We show the real part of the *whitened* modes  $h_{\ell m}$  (with  $\ell = m = \{2, 3, 4\}$ ) of a compact binary coalescence waveform ( $d_L = 500$  Mpc,  $q = 5$ ,  $m_1 + m_2 = 80M_\odot$ ), as a function of time. The modes are whitened by the noise PSD of Advanced LIGO to show their expected contribution to the SNR. The higher the  $m$ , the earlier it enters the frequency band of the detector. This can be seen by the appearance of the non-zero amplitudes of the HMs at a time  $\Delta\tau$  before the merger (dashed black vertical line), where  $\Delta\tau$  increases with increasing  $m$ .

is based entirely on <sup>17</sup>; the reader may refer to these for additional details.

It is convenient to express the SNR and the bandwidth of a detector in terms of the frequency moments:

$$\overline{f^n} = 4 \int_0^\infty f^n \frac{|h(f)|^2}{S(f)} df \quad (3.3)$$

where  $h(f)$  is the Fourier transform of the GW waveform. The SNR ( $\rho$ ) is computed from the zeroth ( $n = 0$ ) moment (the network SNR is the quadrature sum of the individual detector SNRs), and the effective bandwidth ( $\sigma_f$ ) is computed from the first ( $n = 1$ ) and second ( $n = 2$ ) moments:

$$\rho^2 = \overline{f^0} \quad (3.4)$$

$$\sigma_f^2 = \frac{1}{\rho^2} \overline{f^2} - \left( \frac{1}{\rho^2} \overline{f} \right)^2 \quad (3.5)$$

The uncertainty ( $\sigma_t$ ) in the time of arrival of the GW at a detector can be computed from the SNR and the bandwidth under the quadratic approximation to the full likelihood <sup>18</sup>:

$$\sigma_t = \frac{1}{2\pi\rho\sigma_f} \quad (3.6)$$

Working in an earth-centered coordinate system, we define the source position by  $\mathbf{R}$  and the time at which the signal passes through the

<sup>17</sup> Stephen Fairhurst. Source localization with an advanced gravitational wave detector network. *Classical and Quantum Gravity*, 28(10):105021, May 2011. DOI: 10.1088/0264-9381/28/10/105021

<sup>18</sup> Stephen Fairhurst. Triangulation of gravitational wave sources with a network of detectors. *New Journal of Physics*, 11(12):123006, December 2009. DOI: 10.1088/1367-2630/11/12/123006

center of the earth as  $T_0$ .  $\mathbf{R}$  is a unit vector since we are interested in the sky-location of the source and not in distance. If we denote the location of the detector  $i$  with respect to the center of the earth by  $\mathbf{d}_i$  (in units of time by dividing by the speed of light), the time at which the signal passes through the detector  $i$  is given by:

$$T_i = T_0 - \mathbf{R} \cdot \mathbf{d}_i \quad (3.7)$$

Then, the probability of the measured value of arrival times  $t_i$  in different detectors, given the true arrival times  $T_i$ , is given by:

$$p(t_i|T_i) = \prod_i \frac{1}{\sqrt{2\pi}\sigma_i} \exp \left[ \frac{-(t_i - T_i)^2}{2\sigma_i^2} \right] \quad (3.8)$$

where  $\sigma_i$  is the timing uncertainty defined in Eq. (3.6). We have assumed that timing errors are Gaussian distributed. Eq. (3.8) is nothing but the likelihood for the measured value of arrival times  $t_i$  given their true values. Using Bayes' theorem, we obtain the posterior for the true arrival times  $T_i$  assuming a prior  $p(T_i)$ .

$$p(T_i|t_i) \propto p(T_i) \exp \left[ \sum_i \frac{-(t_i - T_i)^2}{2\sigma_i^2} \right] \quad (3.9)$$

Since our final goal is to obtain a posterior on the sky-location of the event, we need to express the posterior  $p(T_i | t_i)$  in terms of  $\mathbf{R}$ . To that end, we write down the relation between the measured sky position  $\mathbf{r}$  and measured arrival time  $t_i$  in analogy with Eq.(3.7) as:

$$t_i = t_0 - \mathbf{r} \cdot \mathbf{d}_i \quad (3.10)$$

We make use of Eq. (3.7) to eliminate  $T_i$  from (3.9) in terms of  $\mathbf{R}$  and  $T_0$ , and Eq. (3.10) to replace  $t_i$  in terms of  $\mathbf{r}$  and  $\mathbf{d}_i$ . We choose prior distributions to be uniform over the sphere (for  $\mathbf{R}$ ) and uniform in time (for  $T_0$ ). The posterior distribution for sky-position  $\mathbf{R}$ , after marginalization over  $T_0$ , is then given by:

$$p(\mathbf{R}|\mathbf{r}) \propto p(\mathbf{R}) \exp \left[ -\frac{1}{2}(\mathbf{r} - \mathbf{R})^T \mathbf{M}(\mathbf{r} - \mathbf{R}) \right] \quad (3.11)$$

where superscript T denotes the matrix transpose. The Fisher matrix

$\mathbf{M}$ , describing the localisation uncertainty, is given by:

$$\mathbf{M} = \frac{1}{\sum_k \sigma_k^{-2}} \sum_{i,j} \frac{\mathbf{D}_{ij} \mathbf{D}_{ij}^T}{2\sigma_i^2 \sigma_j^2} \quad (3.12)$$

and  $\mathbf{D}_{ij} = \mathbf{d}_i - \mathbf{d}_j$  represents the separation between  $i^{\text{th}}$  and  $j^{\text{th}}$  detectors. The pre-factor in matrix  $\mathbf{M}$ , is nothing but the square sum of timing uncertainties in all detectors in the network, which arises while marginalising over geocentric time  $T_0$ . One should note from Eq. 3.11 that the measurement of time at a pair of detectors can only restrict the location of the source in the form of a ring with finite width in the direction parallel to their separation.

Due to the symmetric nature of matrix  $\mathbf{M}$ , it can be diagonalised to obtain three orthogonal eigen-directions ( $\hat{e}_x, \hat{e}_y, \hat{e}_z$ ) with localisation accuracies  $\sigma_x, \sigma_y, \sigma_z$  respectively. Therefore, the posterior distribution for the sky location:

$$p(\mathbf{R}|\mathbf{r}) \propto p(\mathbf{R}) \exp \left[ -\frac{1}{2} \left( \frac{(x-X)^2}{\sigma_x^2} + \frac{(y-Y)^2}{\sigma_y^2} + \frac{(z-Z)^2}{\sigma_z^2} \right) \right] \quad (3.13)$$

where  $\mathbf{R} = (X, Y, Z)$  are the coordinates of the source in the network eigenbasis and  $\mathbf{r} = (x, y, z)$  denotes the measured position of the source.

When computing the source localisation regions, one must take into account the fact that the sky position  $\mathbf{R} = (X, Y, Z)$  is constrained to lie on a sphere. The Eq. (3.13), geometrically, represents an ellipsoid of a constant likelihood whose intersection with the unit sphere results in localisation ellipses on the sky. If the source will be localized to a small enough patch (in most cases) of this sphere that can be approximated to a plane ignoring the curvature. In that case,  $\mathbf{M}$  is projected onto directions orthogonal to  $\mathbf{r}$  using the projection operator

$$\mathbf{P}(\mathbf{r}) = \mathbf{I} - \mathbf{r}\mathbf{r}^T \quad (3.14)$$

where  $\mathbf{I}$  is the identity matrix. The projection gives

$$\mathbf{M}(\mathbf{r}) = \mathbf{P}(\mathbf{r})\mathbf{M}\mathbf{P}(\mathbf{r}) \quad (3.15)$$

The eigenvectors and corresponding eigenvalues of  $\mathbf{M}(\mathbf{r})$  denote the two-dimensional localisation ellipse for the source. The source is

localized with a probability within an area

$$\text{Area}(p) \approx 2\pi\sigma_1\sigma_2[-\ln(1-p)] \quad (3.16)$$

where  $\sigma_1$  and  $\sigma_2$  are the localisation accuracies of the eigen-directions of the projected matrix  $\mathbf{M}(\mathbf{r})$ . We make use of the above expression to compute the localisation in this chapter.

Using a Fisher matrix analysis, the localisation sky area of a source at a given right ascension (RA) and declination (Dec) can be computed from the pair-wise separation of the detectors, as well as each detectors' timing errors. Individual GW detectors do not provide any directional information about the source. Source localisation is achieved only through the triangulation of arrival times at a network of detectors. Note that if the detectors are approximately coplanar, then the mirror degeneracy with respect to the plane of the detector needs to be broken by additional waveform consistency tests between detectors. One would need a network of 4 or more non-coplanar detectors to compute a unique sky-location of the source. Other than that, the non-detection of a source in one of the detectors helps in localizing the source as it rules out the region of sensitivity of that detector as the location of the source.

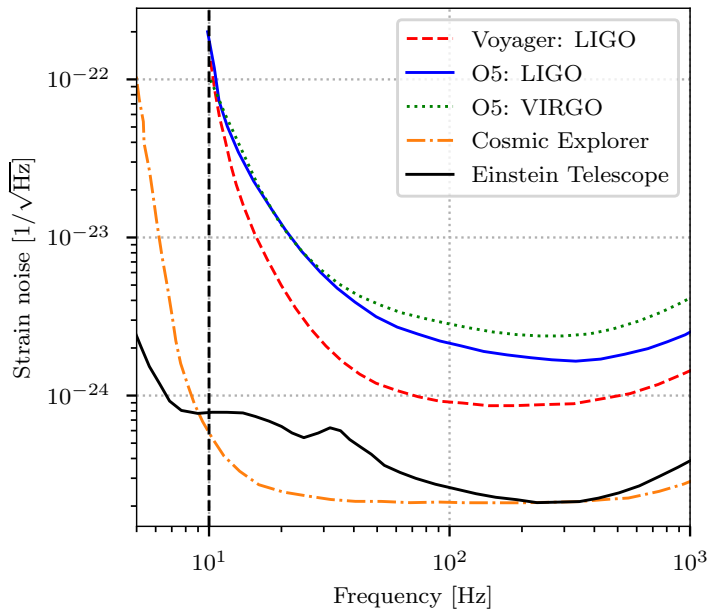
One should also take into account the errors and uncertainties that can impact the sky-localisation. The inaccurate/incomplete waveform models used in GW searches can affect the estimates of timing accuracies that in turn affect the sky-location. The calibration uncertainties of the detector can also lead to inaccurate estimates of sky-location. However, apart from some of the loudest sources, these uncertainties should be smaller than statistical errors in current observing scenarios.

### 3.4 Observing scenarios

We consider three observing scenarios involving networks of ground-based interferometric detectors. *O5*: The fifth observing run involves a network of five detectors, consisting of the three LIGO detectors (LIGO Hanford, LIGO Livingston and LIGO-India) with an A+ sensitivity, which corresponds to a BNS range of 330 Mpc; the Virgo detector with a BNS range of 260 Mpc; and a KAGRA detector assumed to have a sensitivity similar to the Virgo sensitivity<sup>19</sup>. *Voyager*: In the

<sup>19</sup>B. P. Abbott et al. Prospects for observing and localizing gravitational-wave transients with Advanced LIGO, Advanced Virgo and KAGRA. *Living Reviews in Relativity*, 21(1):3, April 2018. DOI: 10.1007/s41114-018-0012-9; and Collaboration KAGRA, LIGO Scientific Collaboration, and Virgo Collaboration. Advanced ligo, advanced virgo and kagra observing run plans, 2019. URL <https://dcc.ligo.org/public/0161/P1900218/002/SummaryForObservers.pdf>

Voyager scenario, we assume that all the LIGO detectors, including LIGO-India, are upgraded to Voyager sensitivity, which corresponds to a BNS comoving range of 1100 Mpc, and the Virgo and KAGRA detectors are upgraded to A+ sensitivity<sup>20</sup>. 3G: The third generation network consists of two Cosmic Explorers (BNS comoving range of 4200 Mpc) with geographical coordinates identical to those of LIGO Hanford and LIGO Livingston, and an Einstein telescope (in its L-shaped configuration, and BNS range similar to Cosmic Explorer) with coordinates equal to that of Virgo<sup>21</sup>. The projected noise amplitude spectral densities of these detectors, pertaining to the three observing scenarios, are plotted in Fig. (3.2). The lower limit on the detector bandwidths for O5 and Voyager is set to 10 Hz. For 3G, this limit is set to 5 Hz. Our study does not consider the variation in the antenna patterns due to the rotation of earth for the duration of GW signals in the sensitivity band of the detectors. While one can neglect this effect for O5 and Voyager, it will be important for 3G detectors. We also expect these additional modulations in the antenna patterns will further improve the sky-localization of GW signals.



<sup>20</sup> R X Adhikari et al. Astrophysical science metrics for next-generation gravitational-wave detectors. *Classical and Quantum Gravity*, 36(24): 245010, nov 2019. DOI: 10.1088/1361-6382/ab3c9f. URL <https://doi.org/10.1088/1361-6382/ab3c9f>; LIGO Scientific Collaboration. Instrument science white paper, 2015. URL <https://dcc.ligo.org/public/0120/T1500290/002/T1500290.pdf>; and LIGO Scientific Collaboration. Instrument science white paper 2018, 2018. URL <https://dcc.ligo.org/public/0151/T1800133/004/T1800133-instrument-science-white-v4.pdf>

<sup>21</sup> LIGO Scientific Collaboration [131], Abbott et al. [5], Hild [115]

Figure 3.2: Projected noise amplitude spectral densities for the three LIGO detectors (including LIGO India) and the Virgo detector for the O5 and Voyager scenarios, as well as for the two Cosmic Explorers and the Einstein Telescope. The lower limit on the detector bandwidths for O5 and Voyager is set to 10 Hz. For 3G, this limit is set to 5 Hz. (See [9, 120, 161, 159, 130, 5, 115])



### 3.5.1 Demonstration of early-warning with higher modes

The effect of HMs on the sky-localisation for a non-spinning compact binary merger with component masses  $m_1 = 15M_\odot$  and  $m_2 = 1.5M_\odot$  located at 40 Mpc, assuming O5 observing scenario, is illustrated in Fig. 3.3. Considering the near-edge-on configuration  $\iota = 60$  deg. and the optimal sky-location (that minimizes the sky area), we show that the inclusion of HMs will lead to a better sky-localisation and larger SNRs, at an early-warning time, than just using dominant mode. For a fiducial sky-localisation of  $\sim 1000$  sq. deg., the inclusion of HMs provides an early warning time gain of  $\sim 20$  seconds over the dominant mode.

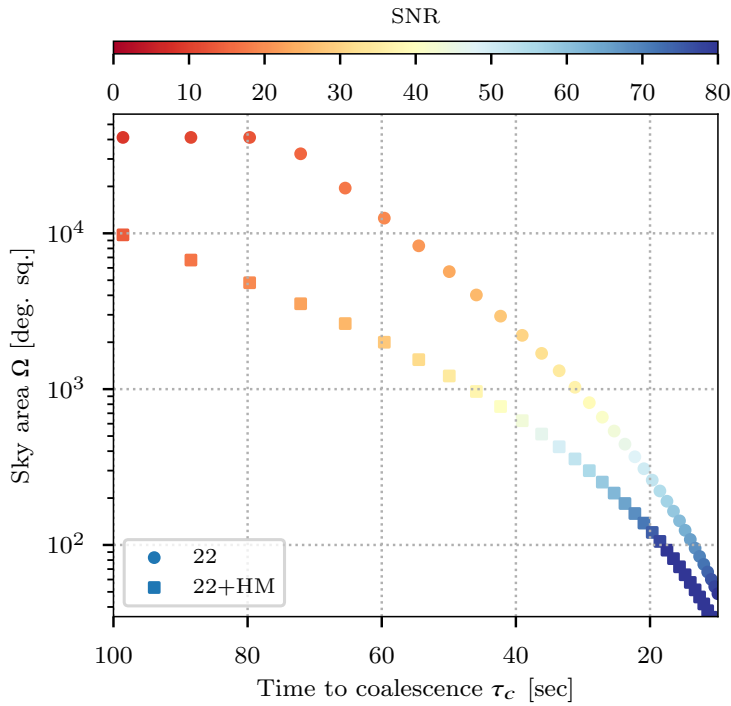
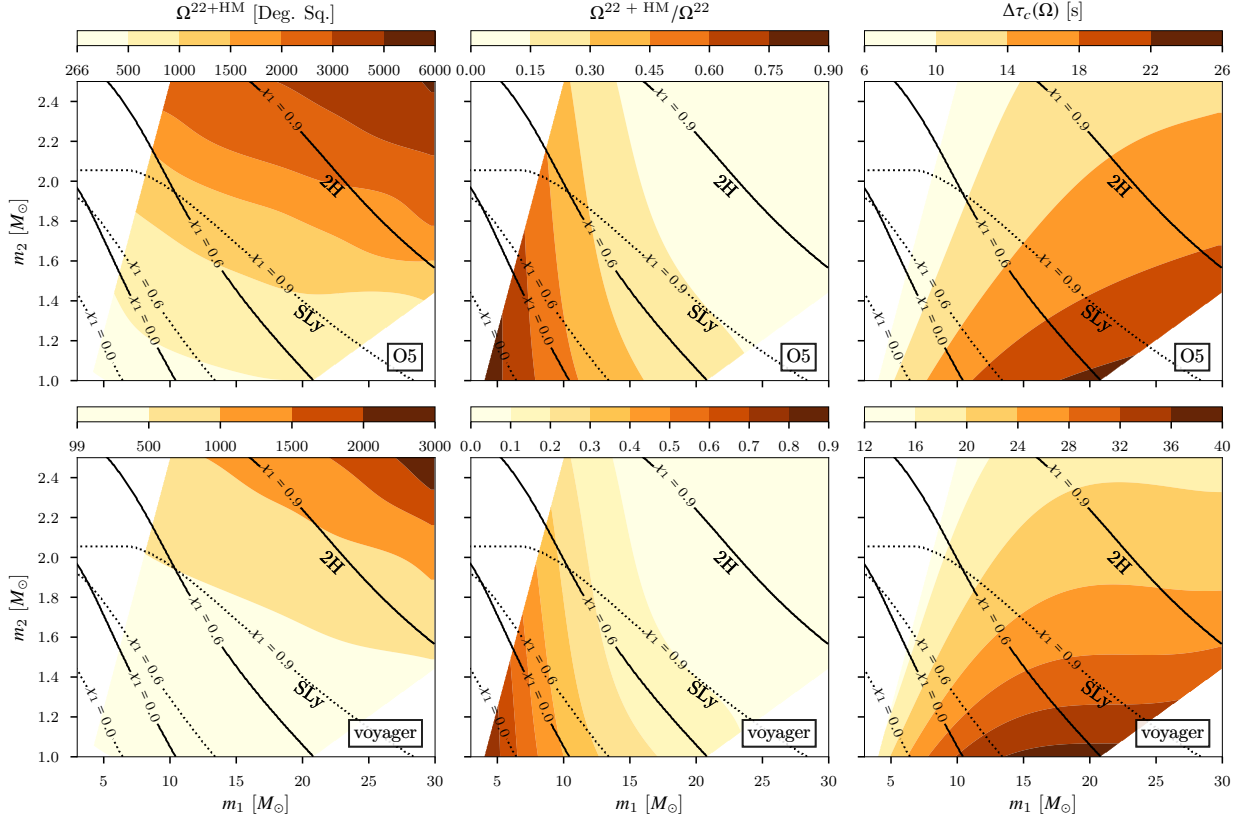


Figure 3.3: The sky area and SNR evolution as a function of time to coalescence for binary with parameters  $m_1 = 15M_\odot$ ,  $m_2 = 1.5M_\odot$ ,  $\iota = 60$  deg.,  $d_L = 40$  Mpc and optimal sky-location (that minimizes the sky area) in O5 observing scenario. The sky area is consistently smaller and SNR consistently larger with the inclusion of HMs in addition to the dominant mode (squares) as compared to only the dominant mode (circles) case.

### 3.5.2 Sky-localisation improvement as a function of masses

Fig. 3.4 shows the localisation sky-area computed, 45 seconds before the merger, and the early warning time gains for a fiducial sky-localisation area of 1000 sq. deg. when the effect of HMs is considered. 45 seconds is comparable to the typical slew times ( $\sim 30 - 60$  seconds) of a number of telescopes. We explore this for an optimised population of asymmetric compact binaries with secondary mass  $m_2 = 1 - 2.5M_\odot$  and mass-ratio  $q = 4 - 20$ . The rest of the ex-



trinsic parameters are fixed as follows:  $d_L = 40$  Mpc,  $\iota = 60$  deg., and sky-location to the optimal value (that provides minimum sky-area). The sky-localisation area computation does not take into account the effect of spin since the results do not change appreciably with spin. The mass range chosen here corresponds to NSBH binaries. We have done this for two reasons: (i) NSBH are expected to produce an EM emission if tidal disruption of NS matter happens outside the ISCO radius (see Eq. 1.15) of the BH. (ii) NSBHs have sufficiently unequal component masses ( $q \gg 1$ ) which enhances the contribution from HMs. We also plot the contours that demarcate the region in the  $m_1 - m_2$  plane corresponding to the binaries that are expected to produce an EM counterpart for different values of primary spin and two NS EoS: 2H and SLy. The former is a stiff EoS that predicts a larger number of EM bright systems<sup>22</sup>, while the latter is a more realistic EoS consistent with the properties measured from GW170817. For each EoS, a larger spin of the primary predicts a broader region of binary masses that will be EM bright. The ISCO radius of the BH reduces with increasing spin leading to larger chances of the tidal

Figure 3.4: Left plots: localisation sky-area (at 90% confidence) using HMs, for an early warning time of 45 s. Middle plots: the same as a fraction of the sky area achieved using only the dominant modes. Right plots: the gains in the early warning time for a fiducial sky area of 1000 sq. deg, due to the inclusion of HMs. These plots correspond to binaries with  $m_2 = 1 - 2.5M_\odot$  and  $q = 4 - 20$ , located at 40 Mpc (other extrinsic parameters set to their optimal values, with inclination  $\iota = 60$  deg.). Two sets of black contours, corresponding to 2H (solid) and SLy (dotted) EoS for different values of BH spin  $\chi_1$  are plotted to demarcate the region of binaries that will potentially emit an EM counterpart.

<sup>22</sup> A neutron star with a stiff EoS will resist the compression due to gravity more effectively, resulting in a larger radius for a given mass compared to a softer EoS. This in turn will lead to an easier tidal disruption of the NS outside the ISCO radius of the BH.

disruption of the NS even at smaller separations.

When HMs are considered, we find that a putative region of EM Bright binaries will have a sky area of a few hundred sq. deg. 45s before the merger. This corresponds to a factor of 3 – 4 (5 – 6) improvement in the sky-localisation area with the inclusion of HMs in addition to the quadrupole mode as compared to when using only the dominant mode in O5 (Voyager) observing scenario. The inclusion of HMs can lead to early-warning time gains as large as  $\sim 25(40)$ s for a fiducial localisation of 1000 sq. deg. The time gained in reaching a fiducial threshold SNR or sky area depends on two competing factors: On one hand, HMs contribute significantly to the signal when the binary is sufficiently asymmetric (hence also heavier). On the other hand, heavier binaries merge quicker in the detector band according to eq 3.2. Thus, the region that maximizes the gains due to HMs corresponds to the binaries that are significantly asymmetric to excite the HMs but not too heavy to make them rush through the frequency band of the detector. This region will depend on the sensitivity of the detectors. Additionally, in 3G detectors, the early-warning time gains for a fiducial sky area of 100 sq. deg. can be as much as a minute for binaries that will likely have an EM counterpart. (see Fig. 3.5).

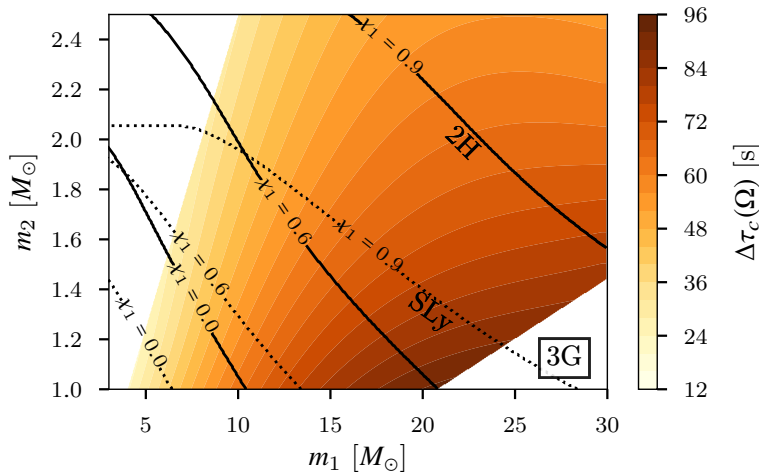


Figure 3.5: Gains in early-warning time upon inclusion of HMs, for the 3G scenario, assuming a fiducial sky-area of 100 sq. deg., and sources located at 100 Mpc. The other extrinsic parameters are set to their optimal values, with inclination  $\iota = 60$  deg. These gains can be as much as 1.5 minutes for relatively low-mass systems that are highly asymmetric. For binaries that are likely to have EM counterparts even for moderate to low spins of the primary mass, the gains can be as much as a minute.

We also estimate the time gained in reaching an SNR threshold of 4 for trigger selection with the inclusion of HMs. For O5 (Voyager), we get gains of up to  $\sim 1$  (2) min, which correspond to a gain of up to  $\sim 50\%$  (80%), as compared to the same using the dominant

mode. For 3G, the gains reach 50 minutes, corresponding to a 500% increase. This could potentially be useful for wide-field telescopes (e.g. all-sky gamma-ray burst monitors) to discover precursors and prompt emission and to trigger follow-up observations.

### 3.5.3 Effect of varying distance and inclination

In the previous cases, we have fixed the distance and inclination of the binaries. Fig. 3.6 shows the effect of varying distance and inclination on the sky-localisation capabilities. The sky area scales inversely with the square of the distance and is weakly dependent on the inclination angle (especially when HMs are included in addition to the dominant mode). The improvement in localisation is the largest for higher inclination or near edge on binary systems.

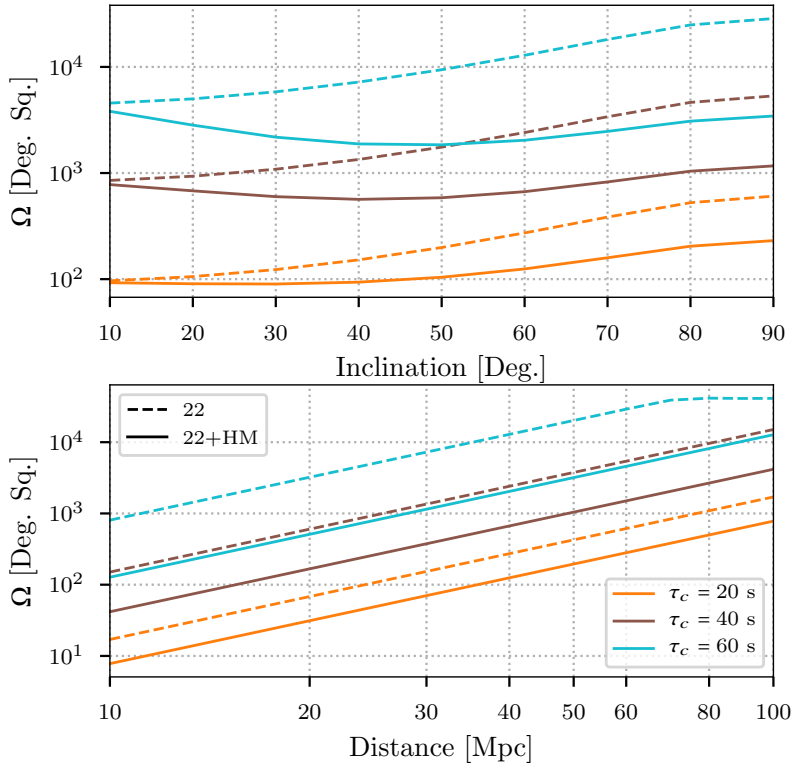


Figure 3.6: *Bottom:* Effect of varying distance on sky-area with (without) the inclusion of HMs, for three early-warning times, in the O5 scenario. The sky area reduces as the square of the distance. *Top:* Same as in *Bottom* plot but varying only inclination angle. The sky area is rather weakly dependent on the choice of inclination angle, while the improvement over the dominant mode is the largest for the near-edge-on configuration of the binary.

### 3.5.4 Population Study

We simulate 100,000 synthetic GWs<sup>23</sup> from a population of compact binaries and inject them in stationary Gaussian noise. The component masses, distributed log-uniformly, span  $m_1 \in [1, 60] M_\odot$ ,

<sup>23</sup> We use the IMRPHENOMHM [136] approximant as implemented in the LALSUITE software package [132]

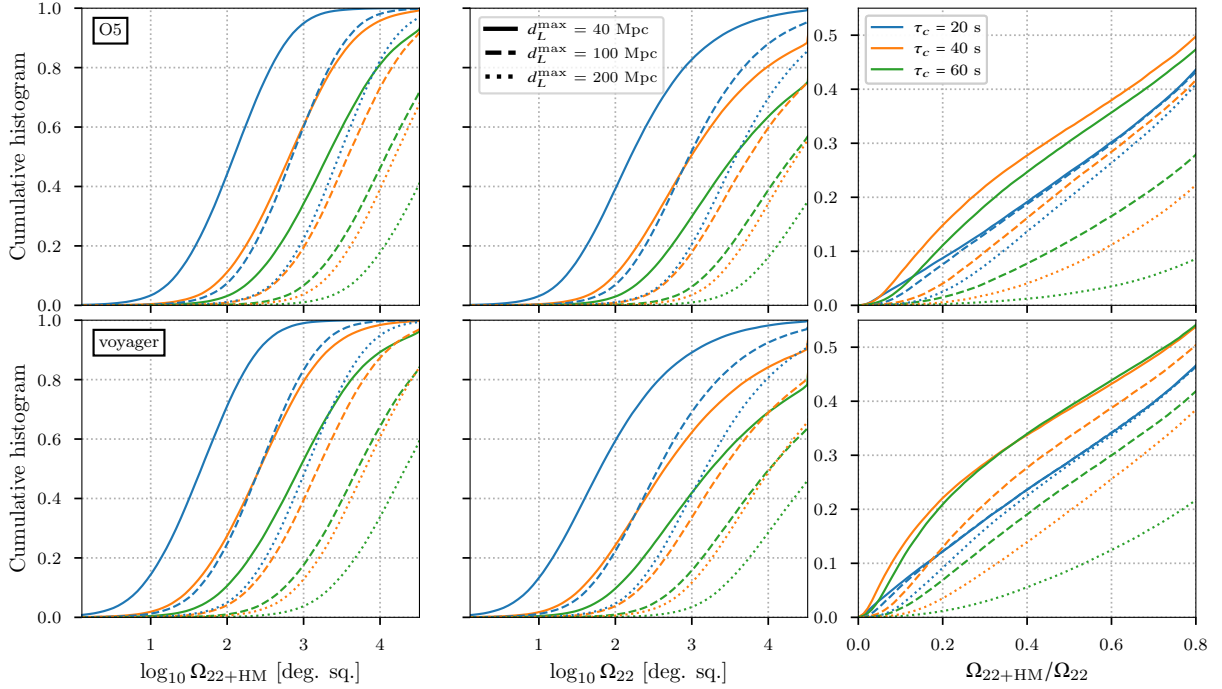
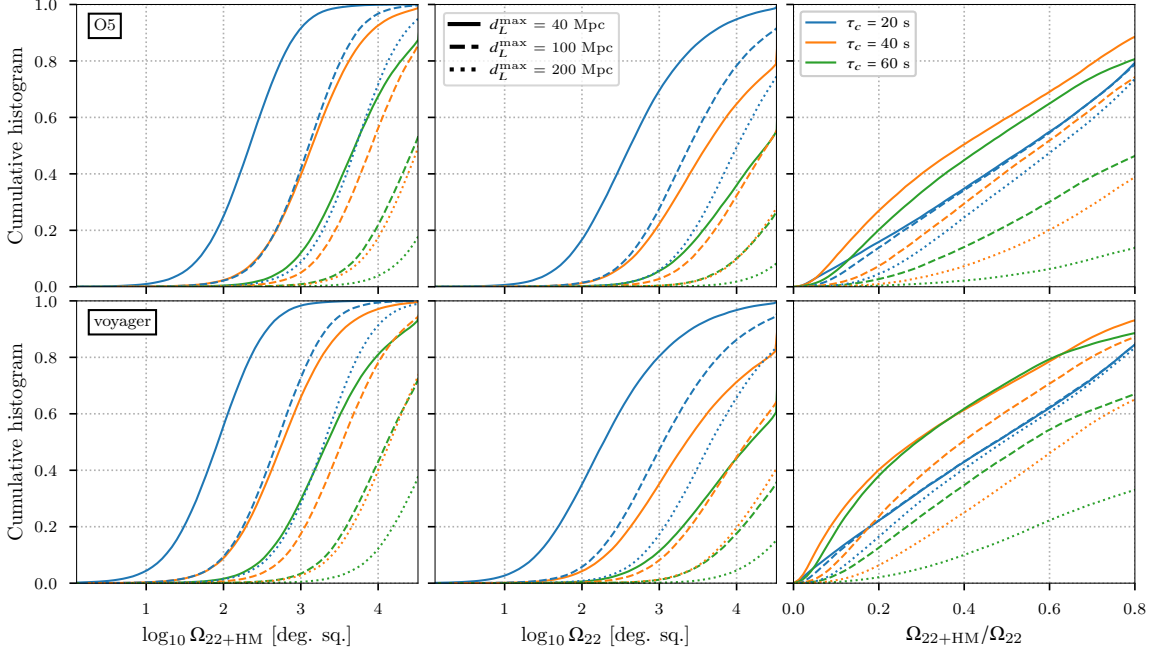


Figure 3.7: Cumulative histograms of localisation sky areas for the simulated population of compact binaries 20 sec. (blue), 40 sec. (orange), and 60 sec. (green) before the merger. *left*: localisation sky area using HMs in addition to the dominant mode. *middle*: the same while using only the dominant mode. *right*: ratio of sky areas with/without HMs. The solid, dashed, and dotted lines correspond to three limiting distances 40, 100, and 200 Mpc, respectively, while distributing the compact binaries uniformly in comoving volume. While employing HMs for localisation sky area, up to  $\sim 30\%$  and  $\sim 40\%$  events have a reduction factor  $\gtrsim 2$  (sky area ratio  $\leq 0.5$ ) in O5 and Voyager scenarios respectively for early-warning times of 40 – 60 sec. In the O5 scenario, at best  $\sim 95\%$  (80%),  $\sim 60\%$  (50%) and  $\sim 35\%$  (30%) events have localisation sky areas less than 1000 deg. sq. 20s, 40s, and 60s before the merger respectively when including (not including) HMs. These numbers increase to  $\sim 100\%$  (90%),  $\sim 80\%$  (60%) and  $\sim 55\%$  (40%) in Voyager.

$m_2 \in [1, 3] M_\odot$ , covering the region of mass-space thought to encompass BNSs and NSBHs; however, a mass-ratio cut  $q \equiv m_1/m_2 \leq 20$  is applied because reliable synthetic GW waveforms, which include HMs, are currently unavailable for  $q \gtrsim 20$ . The binaries are distributed uniformly in co-moving volume up to a limiting distance  $d_L^{\max}$ , as well as in right-ascension ( $\alpha \in [0, 2\pi]$ ), declination ( $\sin \delta \in [-1, 1]$ ), polarization ( $\psi \in [0, 2\pi]$ ), and inclination angle ( $\cos \iota \in [-1, 1]$ ).<sup>24</sup> For each binary coalescence event considered, we compute the localisation sky area for three fiducial times to coalescence comparable to typical slew-times of EM telescopes: 20, 40, 60 seconds. We do so using  $\ell = m = 2$  mode waveforms, as well as those that include the  $\ell = m = 3$  and  $\ell = m = 4$  modes in addition to the  $\ell = m = 2$  mode, and evaluate the sky area reduction factor due to the inclusion of the HMs. We repeat this exercise for three limiting distances:  $d_L^{\max} = 40, 100, 200$  Mpc<sup>25</sup>, as well as the two observing scenarios:

<sup>24</sup> Of the 100,000 events, only those were selected that crossed an SNR threshold of 8. It turns out, however, since the distances are relatively small, that all events for the considered observing scenarios, cross this threshold. The only exception is the O5 scenario assuming a limiting distance of 200 Mpc, where out of the 100,000 events, only  $\sim 30$  are undetected

<sup>25</sup> Note that we consider 100,000 binaries for each of the limiting distances. This is to ensure that we are not statistically limited at lower distances.

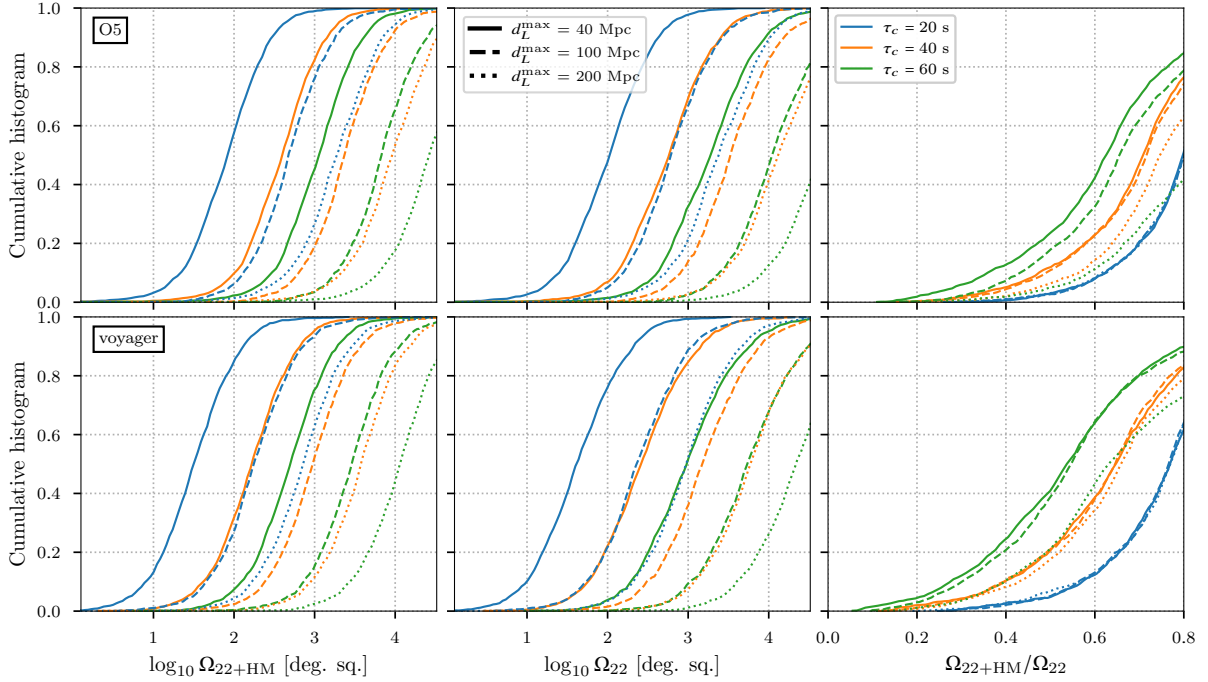


O5 and Voyager described in the method section.

The results are summarized via cumulative histograms plotted in Fig. 3.7. When HMs are included, the localisation area was reduced by more than a factor of two for  $\sim 30\%$  ( $40\%$ ) of the binaries in O5 (Voyager) for early-warning times of 40 – 60 sec, and a limiting distance of 40 Mpc. In the O5 scenario, up to  $\sim 95\%$  ( $80\%$ ),  $\sim 60\%$  ( $50\%$ ) and  $\sim 35\%$  ( $30\%$ ) events have localisation sky areas less than 1000 deg. sq. 20s, 40s, and 60s before the merger respectively when HMs are included (not included). These numbers increase to  $\sim 100\%$  ( $90\%$ ),  $\sim 80\%$  ( $60\%$ ) and  $\sim 55\%$  ( $40\%$ ) in the Voyager scenario.

Of the 100,000 binaries considered,  $\sim 55\%$  are NSBHs. However, this fraction may change depending on the choice of astrophysical distribution of masses of binary systems. Since a larger fraction of these events have heavier masses, this population on average spends a shorter time in the frequency band of the detectors. As a result, the fraction of events with smaller localisation areas is reduced, as shown in Fig. 3.8. On the other hand, a larger proportion of these events have asymmetric masses. Therefore the fraction of these events for which the reduction factor is  $\gtrsim 2$  increases significantly. For example, for the O5 (Voyager) scenario, assuming an early-warning time of 40 seconds and a limiting distance of 40 Mpc, this fraction is  $\sim 60\%$  ( $70\%$ ). In fact, we see that for  $30\%$  ( $40\%$ ) of the events,

Figure 3.8: Same as Fig. 3.7, but for the  $\sim 55\%$  NSBH systems from the total population of 100,000 compact binaries. NSBH systems are selected from the total population such that  $m_1 \geq 5.0M_\odot$ . Employing HMs to determine localisation sky areas results in up to  $\sim 60\%$  and  $\sim 70\%$  of the NSBH systems having sky area reduction factors  $\gtrsim 2$  for O5 and Voyager scenario respectively as compared to only dominant mode. In the O5 scenario, at best  $\sim 90\%$  ( $70\%$ ),  $\sim 40\%$  ( $20\%$ ) and  $\sim 10\%$  ( $> 10\%$ ) events have localisation sky areas less than 1000 deg. sq. 20s, 40s, and 60s before the merger respectively when including (not including) HMs. These numbers increase to  $\sim 100\%$  ( $80\%$ ),  $\sim 65\%$  ( $35\%$ ) and  $\sim 30\%$  ( $10\%$ ) in Voyager.



the sky area is improved by more than a factor of 4. The fraction of events with high reduction factors decreases for other early warning times, as well as larger limiting distances. Nevertheless, this fraction is significantly higher in general than for the total population, which also includes nearly symmetric-mass BNS systems. This highlights the power of using HMs for early-warning of asymmetric mass systems<sup>26</sup>.

We then focus on potentially EM-Bright binaries among the NSBH systems. Determining whether an NSBH system will produce an EM counterpart is in general complicated and arguably still an open question. However, the expectation is that a system that produces a counterpart will also produce a post-merger remnant baryonic mass<sup>27</sup>, which we take to be a proxy for the existence of the counterpart<sup>28</sup>.

While the early warning times and localisation sky areas early in the inspiral have negligible dependence on the component spins of the binary, the production of the remnant baryonic mass (and thus potential EM-Brightness) is crucially dependent on the spin of the black hole, as well as the EOS of the neutron star. We consider a range of EOSs that include both stiff and realistic (consistent with GW170817 [10]) ones. We also choose two spin distributions: an isotropic distribution (spin magnitudes uniformly distributed between 0 and 1 and spin angles isotropically distributed)

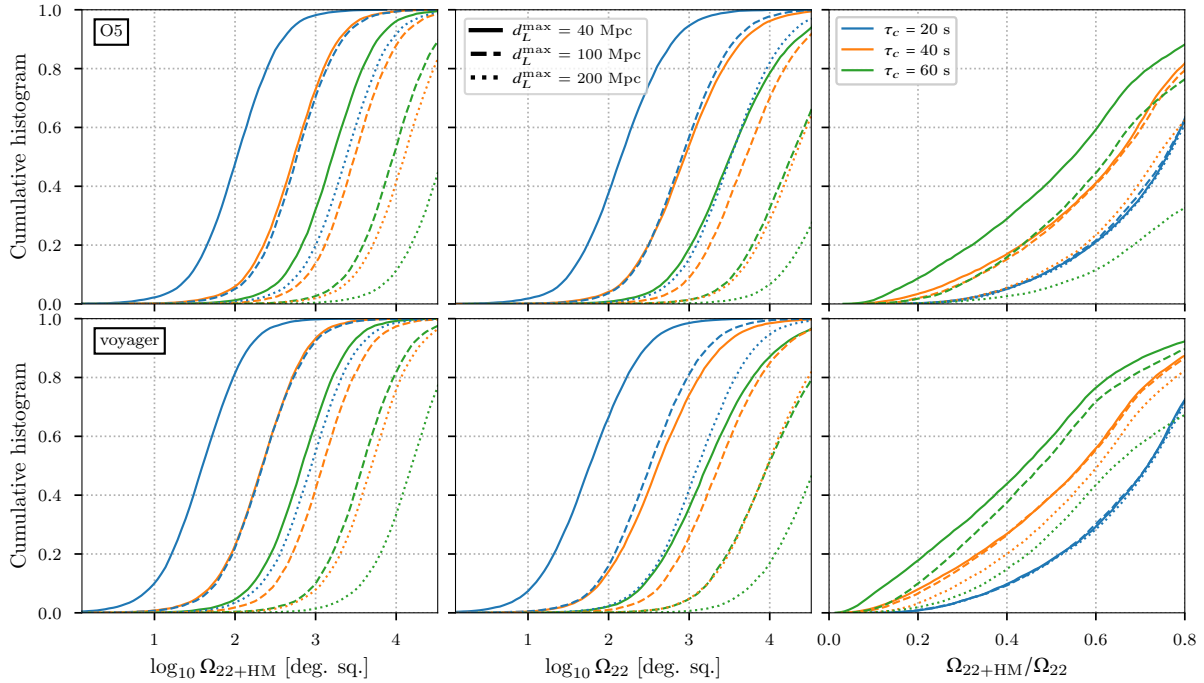
Figure 3.9: Same as in Fig. 3.8, except that here we consider only EM-Bright systems. The EOS is assumed to be AP4, and the spin distribution for the primary component is assumed to be isotropic. Out of total NSBHs ( $\sim 55\%$ ),  $\sim 2\%$  systems are found to be EM-Bright among which  $\sim 20\%$  and  $\sim 40\%$  events have localisation sky area improved by a factor  $\gtrsim 2$  for O5 and Voyager respectively while using HMs. In the O5 scenario, at best  $\sim 100\%$  ( $> 95\%$ ),  $\sim 80\%$  ( $70\%$ ) and  $\sim 45\%$  ( $30\%$ ) events have localisation sky areas less than 1000 deg. sq. 20s, 40s, and 60s before the merger respectively while using (not using) HMs. These numbers increase to  $\sim 100\%$  ( $100\%$ ),  $\sim 90\%$  ( $80\%$ ) and  $\sim 75\%$  ( $50\%$ ) in Voyager.

<sup>26</sup> We set a conservative upper limit on the mass of the neutron star to be  $3M_{\odot}$ , and a lower limit on the mass of the black hole to be  $5M_{\odot}$ . The lower limit on the neutron mass is set to  $1M_{\odot}$ .

<sup>27</sup> Note that there are models of NSs [179] that predict the emission of a counterpart before the NSBH (or BNS) merger, and therefore before a remnant baryonic mass gets produced. We use the P-ASTRO PyPI software package [76] to determine whether an NSBH is EM-Bright.

<sup>28</sup> Foucart [104], Foucart et al. [105]

and an aligned distribution (same distribution of spin magnitudes, but spin vector always aligned with the orbital angular momentum of the binary).



Of the total NSBH binaries (55% of the total population), 2% (15%) are EM-Bright for the AP4 EOS [31] assuming an isotropic (aligned) spin distributions<sup>29</sup> The isotropic-spin (aligned-spin) population producing a small (large) fraction of EM-Bright binaries is consistent with our expectation — smaller (larger) aligned spin black holes have bigger (shorter) radii for their innermost stable circular orbits (ISCO), and hence will result in a smaller (larger) fraction of systems with unbound tidal/merger ejecta. The improvements in the sky localisation for these EM-Bright populations are plotted in Figs. 3.9 and 3.10. The fraction of these EM-Bright systems that produce sky area reduction factors  $\gtrsim 2$  is reduced with respect to the same fraction for the total NSBH population, for the isotropic spin distribution. This is not entirely unexpected – unbound tidal/merger ejecta is produced predominantly for nearly equal-mass binaries<sup>30</sup>, where the improvements due to HMs are relatively modest. Nevertheless, for the Voyager scenario, one finds that the fraction of events with reduction factor  $\gtrsim 2$  can be as large as  $\sim 40\%$ . For the aligned spin distribution, this fraction can be as large as  $\sim 40\%$ (60%) in O5 (Voyager). These estimates pertain to the case when all binary systems

Figure 3.10: Same as Fig. 3.9 with the isotropic distribution of the primary’s spin changed to an aligned one. In this case, out of the total NSBHs,  $\sim 15\%$  systems are found to be EM-Bright among which  $\sim 40\%$  and  $\sim 55\%$  events have localisation sky area improvement factor  $\gtrsim 2$  for O5 and Voyager respectively while using HMs. In the O5 scenario, at best  $\sim 97\%$  (95%),  $\sim 75\%$  (55%) and  $\sim 30\%$  (20%) events have localisation sky areas less than 1000 deg. sq. 20s, 40s, and 60s before the merger respectively while using (not using) HMs. These numbers increase to  $\sim 100\%$  ( $> 97\%$ ),  $\sim 90\%$  (75%) and  $\sim 65\%$  (40%) in Voyager.

<sup>29</sup>These fractions might change depending on the choice of astrophysical mass distribution.



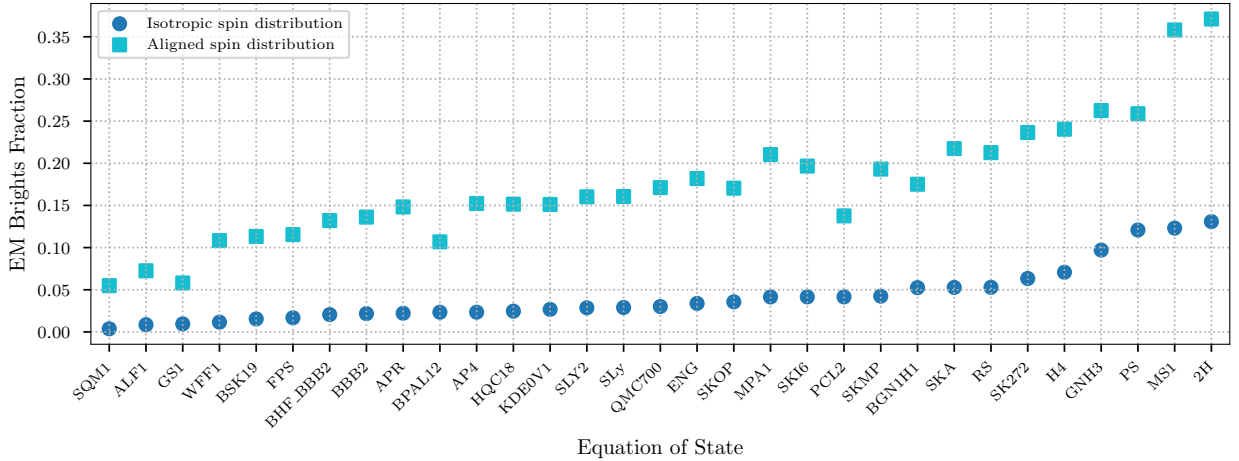


Figure 3.11: Fraction of the NSBH population that are EM-Bright, for isotropic and aligned BH-spin distributions and a range of EOSs [10]. These fractions vary from  $\sim 0.5\% - 10\%$  for the isotropic spin distribution, and  $\sim 5\% - 35\%$  for the aligned spin distribution.

are located within a limiting distance of 40 Mpc. Comparable results are also found for a limiting distance of 100 Mpc.

In Fig. 3.11 and 3.12, we study the effect of varying the EOS on the fraction of the NSBH population distributed up to a limiting distance of 100 Mpc that are EM-Bright, and on the fraction of EM-Bright systems that provides significant early-warning gains upon inclusion of the HMs. We consider 31 EOSs (as implemented in the LALSUITE [132] software package), and find that the EM-Bright fraction varies from  $\sim 0.5 - 14\%$  for isotropic spins, and  $\sim 5 - 35\%$  for aligned spins. On the other hand, varying the EOS changes the fraction of EM-Bright systems that produce reduction factors  $\gtrsim 2$  by  $\sim 10\%$ .

We also evaluate the use of HMs for early warning for the 3G network of detectors described in Sec. 3.4. We compute the early-warning time gained with the inclusion of HMs, for three values of the localisation sky area: 100, 500, and 1000 sq. deg, and the full population of 100,000 binaries that include both BNS and NSBH systems. The results are summarized in Fig. 3.13. For a limiting distance of 40 Mpc,  $\sim 60\%$  of the events have early-warning time gains of over a minute for a 1000 sq. deg localisation area and above 40 sec. for a localisation area of 500 sq. deg. Even at 100 Mpc, the median improvement is about 30 seconds for a 500 sq. deg. localisation area.

### 3.5.5 Detection time-gains due to higher modes

Even if an early-warning sky area is not sufficiently small to allow for small-field-of-view telescopes to rapidly cover, detectors that only

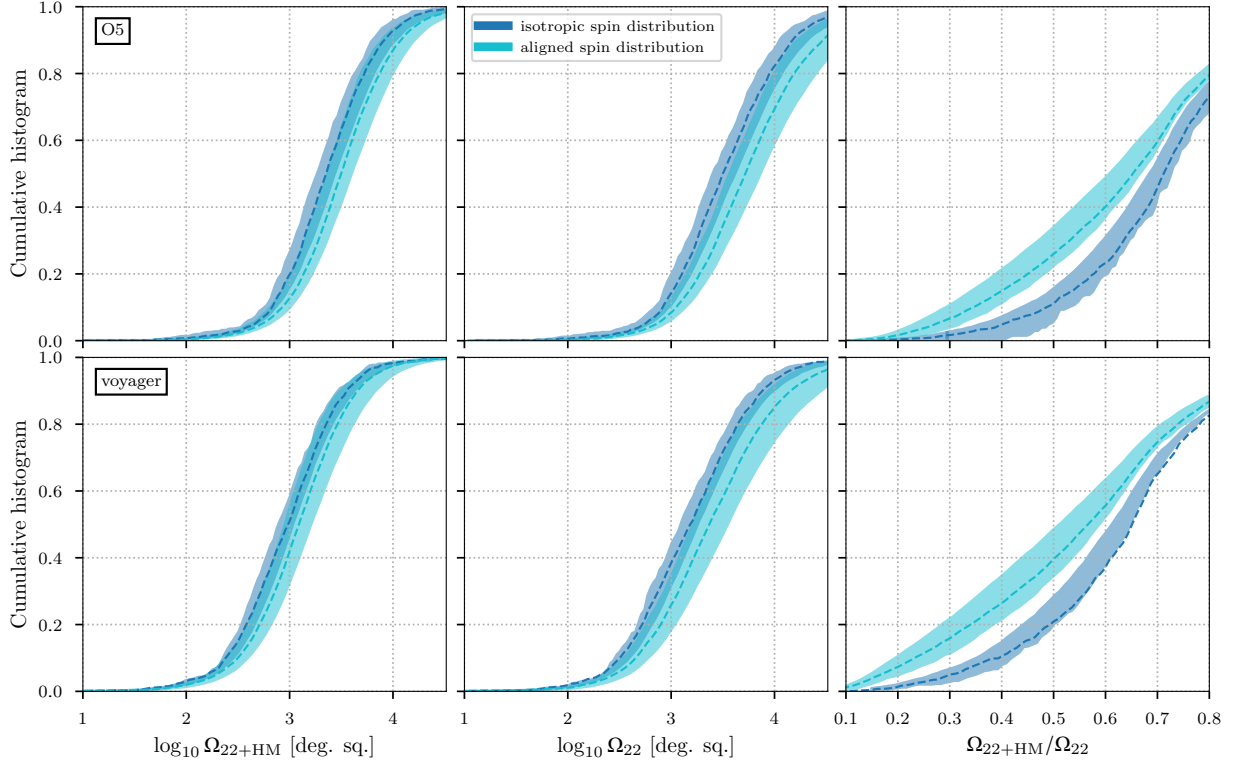


Figure 3.12: Same as in Fig. 3.9, except that we focus on the EM-Bright NSBHs. We consider a range of EsoS, isotropic and aligned BH spin distributions, and only one limiting distance (100 Mpc) and early-warning time (40 seconds). The shaded band covers all the EOSs considered, and the dashed lines correspond to the AP4 EOS. The fraction of the EM-Bright systems for which the localisation sky area reduction factor  $\gtrsim 2$  is greater by  $\sim 20\%$  for the aligned spin distribution than for the isotropic spin distribution. On the other hand, the variation of this fraction due to different EOSs is only  $\sim 10\%$ .

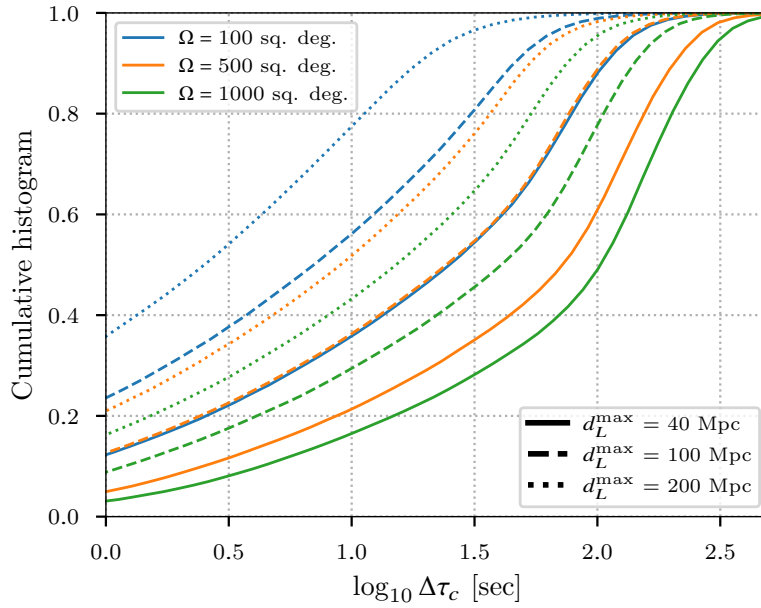


Figure 3.13: The early-warning time gains are shown while localizing compact binaries for three different sky areas of 100 (blue), 500 (orange), and 1000 (green) deg. sq. in 3G scenario. We get time gains up to several minutes while employing HMs in localisation as compared to when we would have used only quadrupole mode. Again, the analysis has been repeated for three upper limits on distance.

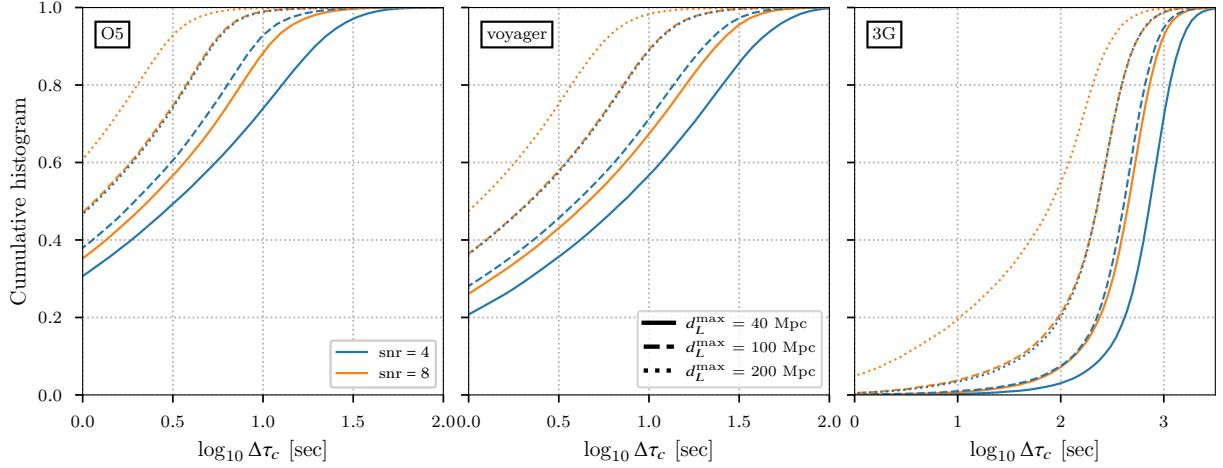


Figure 3.14: Gains in early warning times, given fiducial SNRs, for the full population, as well as three scenarios and limiting luminosity distances. Up to  $\sim 30\%$  of the binaries have gains of greater than 10 sec. in O5. This increases to  $\sim 40\%$  in Voyager. In the 3G scenario, up to 80% of the events have time gains  $> 500$  sec.

need a broad localisation area would benefit from an early-warning detection of the event well before the merger. To that end, we compute the gain in early-warning times with the inclusion of HMs, for fiducial values of the network SNR (SNR = 4, 8)<sup>31</sup>. In Fig. 3.14, we consider the full population of 100,000 binaries. Up to  $\sim 30\%$  of the binaries have gains of greater than 10 sec. in O5. This increases to  $\sim 40\%$  in Voyager. In the 3G scenario, up to 80% of the events have time gains  $> 500$  sec. In Fig. 3.15, we consider the population of  $\sim 55\%$  NSBH systems. Up to  $\sim 60\%$  of the NSBHs have gains of greater than 10 sec. in O5. This increases to  $\sim 80\%$  in Voyager. In the 3G scenario, up to 80% of the events have time gains  $> 500$  sec. In the 3G scenario, the gains are similar to that of the full population, except for  $d_L^{\max} = 200$  Mpc. where there are  $\sim 10\%$  more events with time gains  $> 100$  sec.

<sup>31</sup> At present, some of the dominant mode searches (e.g. GstLAL; Sachdev et al 2020) are capable of sending EW detection triggers, provided that the signal spends a sufficient amount of time in the sensitivity band of the detector. While including HMs in the searches will further aid the pre-merger detection, it will also lead to a marginal increase in the computation time. Additionally, one should keep in mind that adding HMs to a search will lead to additional degrees of freedom in the search, increasing its false alarm rate. This is an active area of research, with only limited success so far (see, e.g., Wadekar et al. [190]).

## 3.6 Summary

BNS and NSBH mergers, which have the potential to produce EM counterparts, have at best been confidently detected only a handful of times. The complex physics of the merger process, especially related to the EM emission, therefore remains unconstrained by observational data. The relative rarity of such events, compared to BBH mergers (which were an almost regular occurrence in O3), as well as the complex physics involved, motivates the need for GW early

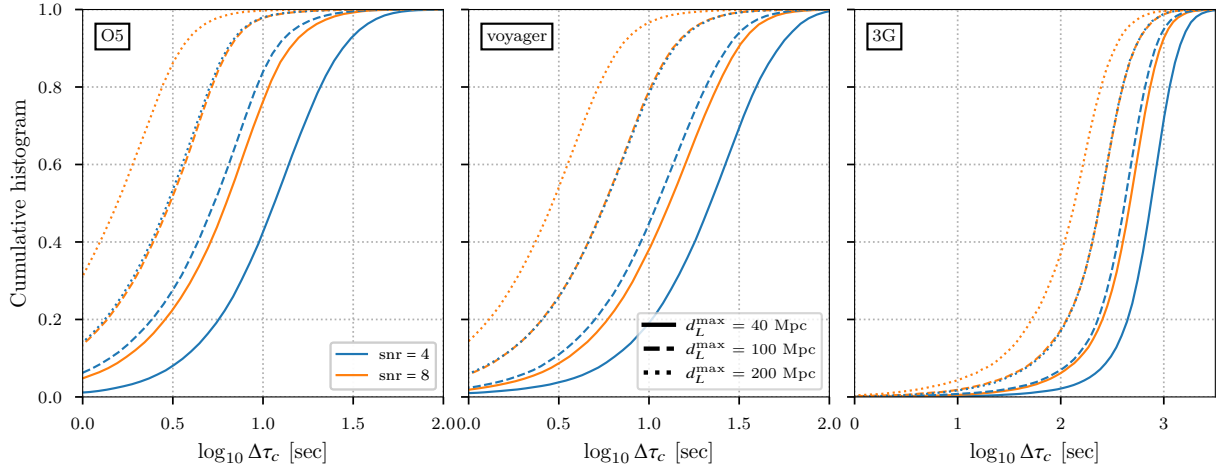


Figure 3.15: Gains in early warning times, given fiducial SNRs, for the NSBH population, as well as three scenarios and luminosity distances. Up to  $\sim 60\%$  of the binaries have gains of greater than 10 sec. in O5. This increases to  $\sim 80\%$  in Voyager. In the 3G scenario, up to 80% of the events have time gains  $> 500$  sec. In the 3G scenario, the gains are similar to that of the full population, except for  $d_L^{\max} = 200$  Mpc. where there are  $\sim 10\%$  more events with time gains  $> 100$  sec.

warning of such events.

The LIGO-Virgo collaboration has already commissioned a trial system that is able to relay the discovery of BNSs up to tens of seconds pre-merger on making use of the  $\sim 100$  sec. time evolution of such low-mass binaries<sup>32</sup>. Current large-field-of-view instruments like the Zwicky Transient Facility (ZTF) ( $47$  sq. degs.) have the potential to follow-up  $\mathcal{O}(100)$  sq. degs.) sky localisations in a few pointings. Given the few-degrees-per-second slew times<sup>33</sup>, early warning triggers present a unique opportunity for such instruments to begin scheduling operations from GW events before the merger. Next-generation instruments like the Vera Rubin Observatory (VRO)<sup>34</sup> will reach unprecedented depths in the follow-up of EM-GW counterparts. Early warning will open an entirely new area to early photometric and spectroscopic observations of the prompt high energy physics in the EM spectrum<sup>35</sup>.

While research towards GW early warning for BNS systems is currently being pursued, early warning for NSBH systems remains relatively unexplored. Our work<sup>36</sup> has demonstrated the reduction in localisation sky areas upon the inclusion of higher order modes currently used in templated real-time GW searches. This reduction is significant for a range of asymmetric mass systems and inclination angles, a fraction of which could produce EM-counterparts under

<sup>32</sup> Collaboration KAGRA, LIGO Scientific Collaboration, and Virgo Collaboration. Public user guide, 2019. URL [https://emfollow.docs.ligo.org/userguide/early\\_warning.html](https://emfollow.docs.ligo.org/userguide/early_warning.html)

<sup>33</sup> Eric C. Bellm et al. The Zwicky Transient Facility: System Overview, Performance, and First Results. *PASP*, 131(995):018002, January 2019. DOI: 10.1088/1538-3873/aaecbe

<sup>34</sup> Željko Ivezić et al. LSST: From Science Drivers to Reference Design and Anticipated Data Products. *ApJ*, 873(2): 111, March 2019. DOI: 10.3847/1538-4357/ab042c

<sup>35</sup> Brian Metzger et al. Kilonovae: nUV/Optical/IR Counterparts of Neutron Star Binary Mergers with TSO. *Astro2020: Decadal Survey on Astronomy and Astrophysics*, 2020:306, May 2019

<sup>36</sup> Shasvath J. Kapadia, Mukesh Kumar Singh, Md Arif Shaikh, Deep Chatterjee, and Parameswaran Ajith. Of Harbingers and Higher Modes: Improved Gravitational-wave Early Warning of Compact Binary Mergers. *ApJ*, 898(2):L39, August 2020. DOI: 10.3847/2041-8213/aba42d; and Mukesh Kumar Singh, Shasvath J. Kapadia, Md Arif Shaikh, Deep Chatterjee, and Parameswaran Ajith. Improved early warning of compact binary mergers using higher modes of gravitational radiation: a population study. *MNRAS*, 502(2):1612–1622, April 2021. DOI: 10.1093/mnras/stab125

different assumptions of the EOS, and moderately spinning BH component. We also determine, in a statistical sense, the early-warning gains upon inclusion of HMs, for a fiducial population of 100,000 binaries that include BNS and NSBH systems. We consider component masses, log-uniformly distributed, spanning  $m_1 \in [1, 60] M_\odot$  and  $m_2 \in [1, 3] M_\odot$  with an applied mass ratio cut of  $q \leq 20$ . The source location is isotropically distributed, as well as uniformly in co-moving volume. A significant fraction of events have improved localisation by a factor  $\gtrsim 2$ . This fraction can be as high as  $\sim 30\%$  and  $\sim 40\%$  for a limiting distance of 40 Mpc in O5 and Voyager respectively (Fig. 3.7).

These fractions improve by over  $\sim 10\% - 40\%$  when only NSBHs are considered, but remain relatively unchanged when only EM-Bright sub-populations of the NSBH population are considered, assuming an isotropic spin distribution. However, for aligned spin distributions, the fractions are only marginally worse than those for the total NSBH population. By varying the EOS to encompass a range of stiffnesses, we find that the fraction of NSBH systems that are EM-Bright can vary by up to 30% for the aligned spin distribution, and the fraction of EM-Bright events with reduction factor  $\gtrsim 2$  varies by  $\sim 10\%$  for both the aligned and isotropic spin distributions.

Translating the fraction of events where early-warning gains due to HMs are significant, to an actual frequency during an observing run, is straightforward provided the true rate of these events is known. Unfortunately, given the paucity of BNS and NSBH detections, the rates of these events to date remain highly uncertain. Nevertheless, as an example, let us consider the optimistic NSBH rate of  $\sim 600 \text{ Gpc}^{-1}\text{yr}^{-1}$ <sup>37</sup>, which corresponds to about 5 detections per year within 200 Mpc, assuming all NSBH mergers within the corresponding volume are detected, as would be expected in the Voyager scenario. From Fig. 3.8,  $\sim 30\%$  of the NSBH population have a reduction factor  $\gtrsim 2$  for an early-warning time of 40 sec, which corresponds to  $\sim 3$  NSBH detections in 2 years.

Note that triangulation method with Fisher matrix approximation will provide sky-localization estimates comparable to Bayesian analysis for sufficiently loud GW signals. However, the triangulation method may overestimate the sky-localization area as it suffers from the lack of amplitude and phase consistency of the GW signal in in-

<sup>37</sup>B. P. Abbott et al. GWTC-1: A Gravitational-Wave Transient Catalog of Compact Binary Mergers Observed by LIGO and Virgo during the First and Second Observing Runs. *Phys. Rev. X*, 9(3):031040, 2019. DOI: 10.1103/PhysRevX.9.031040

dividual detectors. We are working on implementing the effect of HMs in BAYESTAR <sup>38</sup>, a rapid Bayesian analysis code for rapid sky-localisation, to deliver more robust early-warning estimates.

While HMs may provide significant reduction factors, these may not always result in tight sky area localisations. Nevertheless, even though sky areas of several hundreds of square degrees may not be covered by a single telescope sufficiently rapidly to capture the transient event, a joint effort involving multiple telescopes could do so, especially if assisted by a galaxy catalog. Employing a hierarchical tiling strategy that prioritizes regions of the skymap with higher probability values as well as galaxy locations within the skymap, multiple telescopes could cover a large sky area efficiently enough to capture the EM-counterpart at its onset <sup>39</sup>. One might also envision an optimal set-up involving a coordinated effort between the GW network of detectors, and a global network of EM-telescopes (see, for example, Antier et al. [33]), where the evolving and shrinking GW skymaps are continuously streamed to robotic/automated telescopes that continuously track them.

Sky maps that are  $\mathcal{O}(1000)$  sq. deg. wide could also be exploited by large field-of-view telescopes. The Swift gamma-ray burst (GRB) satellite has a large field of view component, BAT (Burst Alert Telescope), which covers  $\sim 4600$  sq. deg. A GRB detected by BAT triggers the XRT (X-Ray Telescope) and UVOT (Ultra-Violet and Optical Telescope) components with significantly smaller fields of view, and slew-times of 20-75 sec, for follow-up. <sup>40</sup>. A skymap with an area a factor of a few smaller than the BAT field of view could allow XRT and UVOT to start slewing toward the location of the counterpart before its onset, potentially gaining tens of seconds to a minute of early warning time. In fact, if BAT is itself pointing in a direction that mostly excludes the early-warning GW skymap, it could start slewing towards the localisation region so as to encompass the maximum probability region within its field of view before the onset of the counterpart. Similar strategies can also be applied for the Astrosat telescope <sup>41</sup>.

The Konus-Wind (KW) gamma-ray burst spectrometer <sup>42</sup> could take advantage of an early-warning detection, even though its omnidirectional instruments are unlikely to benefit from an early-warning skymap. KW records triggers above some predefined threshold.

<sup>38</sup> Leo P. Singer and Larry R. Price. Rapid Bayesian position reconstruction for gravitational-wave transients. *Phys. Rev. D*, 93(2):024013, 2016. DOI: 10.1103/PhysRevD.93.024013

<sup>39</sup> Michael W Coughlin et al. Optimizing searches for electromagnetic counterparts of gravitational wave triggers. *Monthly Notices of the Royal Astronomical Society*, 478(1):692–702, 04 2018. ISSN 0035-8711. DOI: 10.1093/mnras/sty1066. URL <https://doi.org/10.1093/mnras/sty1066>

<sup>40</sup> N. Gehrels. The Swift Gamma-Ray Burst Mission. In E. Fenimore and M. Galassi, editors, *Gamma-Ray Bursts: 30 Years of Discovery*, volume 727 of *American Institute of Physics Conference Series*, pages 637–641, September 2004. DOI: 10.1063/1.1810924

<sup>41</sup> Kulinder Pal Singh et al. ASTROSAT mission. In *Space Telescopes and Instrumentation 2014: Ultraviolet to Gamma Ray*, volume 9144 of *Society of Photo-Optical Instrumentation Engineers (SPIE) Conference Series*, page 91441S, July 2014. DOI: 10.1117/12.2062667

<sup>42</sup> A. Tsvetkova, D. Frederiks, S. Golenetskii, A. Lysenko, P. Oleynik, V. Pal'shin, D. Svinkin, M. Ulanov, T. Cline, K. Hurley, and R. Aptekar. The Konus-Wind Catalog of Gamma-Ray Bursts with Known Redshifts. I. Bursts Detected in the Triggered Mode. *ApJ*, 850(2):161, December 2017. DOI: 10.3847/1538-4357/aa96af

Thus, an algorithm that triggers on GW early-warning detection could ensure that subthreshold GRB triggers over the duration of the CBC transient could be recorded for subsequent offline analyses.

Radio telescopes are also likely to benefit from early warning of GW events. The MWA radio telescope has a 600 sq. deg. field of view and can start following up events  $\sim 20$  sec. after its detection<sup>43</sup>. Therefore even a  $\mathcal{O}(1000)$  sq. deg. skymap at an early-warning time of 60 sec. would save tens of seconds, since MWA should be able to cover this area in a few pointings. The ASKAP radio telescope has a significantly smaller field of view ( $\sim 30$  sq. deg.), and a slewing rate of a few degrees per second, and could therefore take advantage of a  $\mathcal{O}(100)$  sq. deg. skymap with tens of seconds of early-warning time<sup>44</sup>. Telescopes with much larger fields of view  $\mathcal{O}(10,000)$  sq. deg. buffer data periodically. A triggering algorithm, based on the GW early warning, could ensure that the relevant data is recorded for offline analyses.

While localisation skymap is arguably the most important information for telescopes to follow-up a GW early-warning event, other information such as estimates of the luminosity distance, inclination angle, mass ratio, and spin could also allow astronomers to determine whether the event is worthy of follow-up. For example, the optical telescopes have a limiting distance to which they can view an event with short exposure times; furthermore, better estimates of the mass ratio and spin could better help determine if the event is EM-Bright. In the next chapter, we investigate the improvement in measuring luminosity distance and orbital inclination due to HMs.

<sup>43</sup> D. L. Kaplan, A. Rowlinson, K. W. Bannister, M. E. Bell, S. D. Croft, T. Murphy, S. J. Tingay, R. B. Wayth, and A. Williams. A Deep Search for Prompt Radio Emission from the Short GRB 150424A with the Murchison Widefield Array. *ApJ*, 814(2):L25, December 2015. DOI: 10.1088/2041-8205/814/2/L25

<sup>44</sup> D. Dobie et al. An optimised gravitational wave follow-up strategy with the Australian Square Kilometre Array Pathfinder. *PASA*, 36:e019, May 2019. DOI: 10.1017/pasa.2019.9





# 4 | Early-Warning Estimates of Luminosity Distance and Orbital Inclination of Compact Binary Mergers using Higher Modes

## 4.1 Motivation

In the last chapter, we showed that the inclusion of subdominant modes in low-latency searches, that currently consist of only the dominant harmonic <sup>1</sup>, would improve early-warning detection and sky-localization. This is by virtue of the fact that these modes enter the frequency band of the detectors well before the dominant mode<sup>2</sup>. Not only the sky-localization but also the measurement of luminosity distance and orbital inclination, in the early-warning time, can be improved with the inclusion of higher modes in online GW searches. This is thanks to the fact that the increased information content in the higher modes can also help in breaking degeneracies between the luminosity distance and inclination.

The improved measurements of luminosity distance will help in better understanding if the EM emission from the source can be observed by the existing ground/space-based telescopes. Similarly, better estimates of inclination angle will help in informing about the observability of any beamed EM emission <sup>3</sup>. Thus, the improved measurements of both of these quantities will help astronomers to decide their follow-up strategies accordingly.

In this chapter, we demonstrate the benefits of including subdominant modes in real-time searches, in the context of EW. Specifically, using a Fisher Matrix-based analysis <sup>4</sup>, we show that estimates of luminosity distance and orbital inclination, improve considerably in EW time, with the inclusion of higher modes. We again consider the same three observing scenarios as described in section 3.4: O<sub>5</sub>,

<sup>1</sup>Cody Messick et al. Analysis framework for the prompt discovery of compact binary mergers in gravitational-wave data. *Phys. Rev. D*, 95(4):042001, February 2017. DOI: 10.1103/PhysRevD.95.042001; T Adams et al. Low-latency analysis pipeline for compact binary coalescences in the advanced gravitational wave detector era. *Classical and Quantum Gravity*, 33(17):175012, aug 2016. DOI: 10.1088/0264-9381/33/17/175012.

URL <https://doi.org/10.1088/0264-9381/33/17/175012>; Samantha A. Usman et al. The PyCBC search for gravitational waves from compact binary coalescence. *Class. Quant. Grav.*, 33(21):215004, 2016. DOI: 10.1088/0264-9381/33/21/215004; and Qi Chu. *Low-latency detection and localization of gravitational waves from compact binary coalescences*. PhD thesis, The University of Western Australia, 2017

<sup>2</sup>In Tsutsui et al. [181, 180], the effect of precession has also been explored as a potential way to improve the early warning of NSBH binary mergers.

<sup>3</sup>K. G. Arun, Hideyuki Tagoshi, Archana Pai, and Chandra Kant Mishra. Synergy of short gamma ray burst and gravitational wave observations: Constraining the inclination angle of the binary and possible implications for off-axis gamma ray bursts. *Phys. Rev. D*, 90:024060, Jul 2014. DOI: 10.1103/PhysRevD.90.024060. URL <https://link.aps.org/doi/10.1103/PhysRevD.90.024060>

<sup>4</sup>Curt Cutler and Eanna E. Flanagan. Gravitational waves from merging compact binaries: How accurately can one extract the binary's parameters from the inspiral waveform? *Phys. Rev. D*, 49:2658–2697, Mar 1994. DOI: 10.1103/PhysRevD.49.2658. URL <https://link.aps.org/doi/10.1103/PhysRevD.49.2658>

Voyager, and 3G.

We find that the inclusion of higher modes reduces the uncertainties on the luminosity distance estimates of potentially EM-Bright<sup>5</sup> NSBH binaries located at 100 Mpc by a factor of  $\sim 1 - 1.5(1.1 - 2)[1.1 - 5]$  in the O5 (Voyager) [3G] scenario, 45(45)[300] seconds before merger<sup>6</sup>. Combining these uncertainties with sky area estimates, and assuming a galaxy number density of  $0.01\text{Mpc}^{-3}$  (Gehrels et al. [109]), we find that the number of galaxies within the uncertainty volume is reduced by a factor of  $\sim 1 - 2.5(1.2 - 4)[1.2 - 10]$ <sup>7</sup>.

The rest of the chapter is organized as follows. Section 4.2 summarizes the Fisher Matrix/quadratic approximation to the GW PE likelihood. It also describes the key error-uncertainty formulae. Section 4.3 outlines the results that demonstrate the benefits of the inclusion of higher modes in early warning efforts targeted at NSBH systems. The chapter concludes with Section 4.4 where the EW gains afforded by higher modes are discussed in the context of EM follow-up.

## 4.2 Parameter estimation

A fully Bayesian GW PE<sup>8</sup> exercise to infer the parameters  $\vec{\theta}$  of the binary that produced a CBC signal in the data  $s$  requires the sampling of the likelihood  $p(s|\vec{\theta})$  in a large-dimensional parameter space. However, this turns out to be computationally expensive and time-consuming in general. A common workaround is to expand the log-likelihood in source parameters and truncate at quadratic order. The covariance of the resulting multidimensional Gaussian is given by the inverse of the Fisher information matrix<sup>9</sup>. This approximation works well for high-SNR signals and breaks down at very low SNRs<sup>10</sup>.

We denote by  $s(t)$  the detector strain time series, which consists of noise  $n(t)$ , and a GW CBC signal  $h(t)$  as well:

$$s(t) = n(t) + h(t). \quad (4.1)$$

Assuming that the noise is stationary and Gaussian, the likelihood on the binary's parameters  $\vec{\theta}$  is given by:

$$p(s|\vec{\theta}) \propto e^{-(s-h(\vec{\theta})|s-h(\vec{\theta}))/2}, \quad (4.2)$$

<sup>5</sup>Deep Chatterjee et al. A Machine Learning-based Source Property Inference for Compact Binary Mergers. *ApJ*, 896(1):54, June 2020. DOI: 10.3847/1538-4357/ab8dbe

<sup>6</sup>We choose 100 Mpc as a fiducial distance for observation because EM-counterparts produced by BNS and EM-Bright NSBH mergers will be detectable within this distance. EM-counterparts at distances greater than a few 100s of Mpc are unlikely to be observable by a number of existing facilities or even their future upgrades.

<sup>7</sup>The factors of improvements in the measurement of various parameters with the inclusion of higher modes quoted in this work are more realistic in comparison to the factors of improvements in skyarea-localization in Kapadia et al. [122] and Singh et al. [170]. These works overestimate the improvement-factors since they do not account for the effect of priors.

<sup>8</sup>See section 5.2.1 for a detailed discussion on Bayesian inference PE.

<sup>9</sup>Curt Cutler and Éanna E. Flanagan. Gravitational waves from merging compact binaries: How accurately can one extract the binary's parameters from the inspiral waveform? *Phys. Rev. D*, 49:2658–2697, Mar 1994. DOI: 10.1103/PhysRevD.49.2658. URL <https://link.aps.org/doi/10.1103/PhysRevD.49.2658>

<sup>10</sup>The general expectation is that the Fisher Matrix (FM) approximation will work well for SNRs  $\gtrsim 10$  [e.g. 28], although this statement must be qualified carefully. This is because the information contained in the detected GW signal also depends on the effective bandwidth (which is a measure of the number of cycles in the band). The FM-based inference of the parameters also depends on the dimensionality of the problem, and in general, the greater the dimensionality, the larger the SNR needs to be in order for the FM to produce meaningful constraints on the parameters [184]. Recent work that uses FM for early-warning [see, e.g. 181] use an SNR of 8 as the threshold for their FM analysis). In our work, at  $d_L = 100$  Mpc, and 45 sec before the merger, the majority of the SNRs of NSBHs considered lie between 10-20.

where  $(\cdot|\cdot)$  denotes the noise-weighted inner product defined in 1.33.

Expanding the log-likelihood to quadratic order about the peak of the distribution yields:

$$p(s | \vec{\theta}) \propto e^{-\frac{1}{2}\Gamma_{ij}\Delta\theta_i\Delta\theta_j}, \quad (4.3)$$

where  $\Delta\theta_i \equiv \theta_i - \bar{\theta}_i$ , and  $\bar{\theta}_i$  corresponds to the peak of the likelihood. The quantity  $\Gamma$  is the so-called Fisher information matrix and is defined for the  $k^{\text{th}}$  detector as,

$$\Gamma_{ij}^k = \left( \frac{\partial h^k}{\partial \theta_i} \middle| \frac{\partial h^k}{\partial \theta_j} \right), \quad (4.4)$$

The net Fisher matrix in case of a network of detectors is

$$\Gamma = \sum_k \Gamma^k. \quad (4.5)$$

The size of the approximate likelihood function [as well as the posterior distribution  $p(\theta|s)$  assuming flat priors] is given by the covariance matrix ( $\Sigma$ ), which is related to Fisher information matrix as follows,

$$\Sigma_{ij} = \langle \Delta\theta_i \Delta\theta_j \rangle = (\Gamma_{ij})^{-1} \quad (4.6)$$

We can relate the width of the 1-sigma confidence region of the posterior of parameter  $\theta_i$  (marginalized over all other parameters) to the diagonal elements of the covariance matrix as,

$$\sigma_i = \sqrt{\Sigma_{ii}} \quad (4.7)$$

The off-diagonal elements of the covariance matrix contain information about the correlation between different parameters. We compute the Fisher matrix in the following 9-dimensional parameter space

$$\boldsymbol{\theta} \equiv \{\ln \mathcal{M}, \eta, \ln d_L, \cos \iota, t_c, \phi_c, \alpha, \sin \delta, \psi\} \quad (4.8)$$

Equation (4.7) assumes that the likelihood is not cut by the prior boundaries, which can happen in real situations. In order to mimic this, we draw a large number of random samples from the 9-dimensional Gaussian likelihood (computed using the Fisher matrix; see Eq. (4.3)), and discard those samples that lie outside the prior boundaries. From the remaining samples, we compute the marginalized 1-dimensional posteriors in  $d_L$  as well as  $\iota$ , and estimate the width of the 90% con-

fidence regions centered around their median values. These are considered as our error estimates in  $d_L$  and  $\iota$ . We use the priors for the parameters as shown in Table 4.1.

Parameter ( $\theta$ )	Prior
$\ln(d_L/\text{Mpc})$	$U(0, 11.5)$
$\cos \iota$	$U(-1, 1)$
$t_c$ (sec)	$U(-1, 1)$
$\phi_c$	$U(0, 2\pi)$
$\ln(\mathcal{M}/M_\odot)$	$U(0, 4.6)$
$\eta$	$U(0, 0.25)$
$\sin \delta$	$U(-1, 1)$
$\alpha$	$U(0, 2\pi)$
$\psi$	$U(0, 2\pi)$

Computing the 90% confidence regions in multi-dimensional parameter space (e.g., the three-dimensional volume in the sky) is a bit more computationally complex. Hence we resort to the following approximation: From the posterior samples that generate as described above, we compute the covariance matrix  $\bar{\Sigma}^{3D}$  in three dimensions ( $\alpha$ ,  $\sin \delta$ , and  $d_L$ ) numerically<sup>11</sup>. Then, the errors in the 3-dimensional sky-volume  $\Delta V$  are given in terms of this marginalized covariance matrix  $\bar{\Sigma}^{3D}$  as

$$\Delta V = \frac{4}{3}\pi \sqrt{\begin{vmatrix} \bar{\Sigma}_{d_L d_L}^{3D} & d_L \bar{\Sigma}_{d_L \alpha}^{3D} & d_L \bar{\Sigma}_{d_L \sin \delta}^{3D} \\ d_L \bar{\Sigma}_{d_L \alpha}^{3D} & d_L^2 \bar{\Sigma}_{\alpha \alpha}^{3D} & d_L^2 \bar{\Sigma}_{\alpha \sin \delta}^{3D} \\ d_L \bar{\Sigma}_{d_L \sin \delta}^{3D} & d_L^2 \bar{\Sigma}_{\alpha \sin \delta}^{3D} & d_L^2 \bar{\Sigma}_{\sin \delta \sin \delta}^{3D} \end{vmatrix}} \quad (4.9)$$

Note that equation (4.9) provides the uncertainties in the localization volume at 68% confidence. To convert these  $1\text{-}\sigma$  errors into errors at confidence level  $C$ , we will have to multiply them by a scaling factor ( $\beta$ )<sup>12</sup>. We have estimated this scaling factor in different dimensions in appendix 7.2. All the error estimates correspond to the 90% credible interval unless otherwise stated. The above errors at 90% confidence level will be,

$$\Delta V_{90\%} = (\beta_3)^3 \Delta V \quad (4.10)$$

where  $\beta_n$  corresponds to the scaling factor at 90% confidence level

Table 4.1: The priors on parameters for which the Fisher matrix is computed. Here  $U(a, b)$  denotes the uniform probability between  $a$  and  $b$ . The luminosity distance, mass, time, and all the angles are measured in Mpc,  $M_\odot$ , seconds, and radians respectively.

<sup>11</sup> If the original 9-dimensional likelihood is not cut by the prior boundaries, the marginalized posterior in 2 dimensions will also be a Gaussian, which is fully described by this covariance matrix. However, the prior boundaries can cut the 9-dimensional Gaussian. We, still approximate the 3D distributions to be Gaussians, described by the covariance matrix  $\bar{\Sigma}^{3D}$ .

<sup>12</sup> M. Lampton, B. Margon, and S. Bowyer. Parameter estimation in X-ray astronomy. *ApJ*, 208:177–190, August 1976. DOI: 10.1086/154592

in  $n$ -dimensions. We are more interested in finding the number of galaxies localized ( $\Delta N$ ) that can be the potential host of the merger. Therefore

$$\Delta N_{90\%} = n_{\text{galaxy}} \Delta V_{90\%} \quad (4.11)$$

where  $n_{\text{galaxy}}$  is the number density of the galaxies in the universe.

The inversion of the Fisher matrix (for computing the covariance matrix) is performed numerically using the LU decomposition method in `mpmath` library with arbitrary precision<sup>13</sup> in Python. Since the numerical techniques used in inverting  $\Gamma$  may affect the inversion accuracy, we have to define a fiducial threshold of inaccuracies above which the results can not be trusted. This can be checked by inferring the deviation of the identity matrix from the multiplication of the inversion of the covariance matrix to the original Fisher matrix. The measure of accuracy can be defined as  $\epsilon_{\text{inv}} = \max_{i,j} |\Gamma_{ik} \Sigma_{kj} - \delta_{ij}|$ . We find the values of  $\epsilon_{\text{inv}} \lesssim 10^{-8}$  in our calculations which is well within the acceptable limits<sup>14</sup>.

<sup>13</sup> Fredrik Johansson et al. *mpmath: a Python library for arbitrary-precision floating-point arithmetic (version 0.18)*, December 2013. <http://mpmath.org/>

<sup>14</sup> Emanuele Berti, Alessandra Buonanno, and Clifford M. Will. Estimating spinning binary parameters and testing alternative theories of gravity with lisa. *Phys. Rev. D*, 71:084025, Apr 2005. DOI: 10.1103/PhysRevD.71.084025. URL <https://link.aps.org/doi/10.1103/PhysRevD.71.084025>

### 4.3 Results

We have used a non-spinning multipolar waveform model by Mehta et al. [145] which is calibrated against the numerical relativity simulations. We use two subdominant multipoles  $\ell = 3, m = \pm 3$  and  $\ell = 4, m = \pm 4$  in addition to the dominant mode  $\ell = 2, m = \pm 2$  throughout the analysis. The derivatives of the waveform with respect to the binary source parameters  $\vec{\theta}$ , which are being used to compute the Fisher information matrix, have been calculated in Mathematica<sup>15</sup> analytically to avoid any numerical errors due to finite differencing. We compute the expected uncertainties in the luminosity distance and orbital inclination as a function of the component masses (after fixing the sky location and polarization angle). We also simulate a population of binaries (with fixed masses, but different sky locations and polarization angles) and compute the distribution of expected uncertainties.

<sup>15</sup> Wolfram Research. Mathematica, Version 13.0.0. 2021. URL <https://www.wolfram.com/mathematica>. Champaign, IL

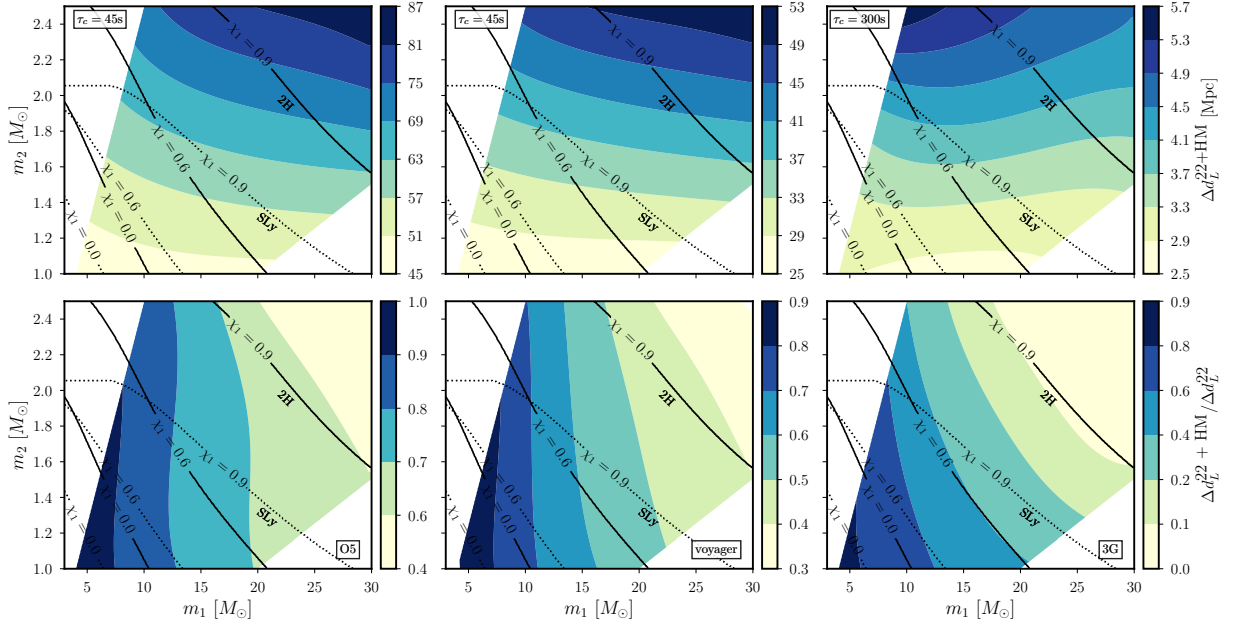


Figure 4.1: *Top panel:* Expected uncertainties in estimating the luminosity distance  $d_L$  (at 90% confidence) with the inclusion of higher modes for non-spinning compact binary mergers, located at 100Mpc, in three observing scenarios. We consider the component masses:  $m_1 = 4 - 30M_\odot, m_2 = 1 - 2.5M_\odot$ . Other parameters of the binary systems are assumed to be fixed at their “optimal” values (values producing the best estimates of the distance) including  $\iota = 60\text{deg}$ . The black contours demarcate the regions of binaries, that will have potential EM emission i.e. non-zero ejecta mass in the merger, for various values of the spin ( $\chi_1$ ) of the primary [104]. The black solid and dotted line contours correspond to the equations of state, 2H and SLy for the neutron star. *Bottom panel:* fractional improvements in the luminosity distance measurements with the inclusion of higher modes, relative to the measurements carried out using only dominant mode. In O5 (voyager)[3G] scenario, the luminosity distance measurements improve by a factor of  $\sim 1 - 1.5(1.1 - 2)[1.1 - 5], 45(45)[300]$  seconds prior to the merger.

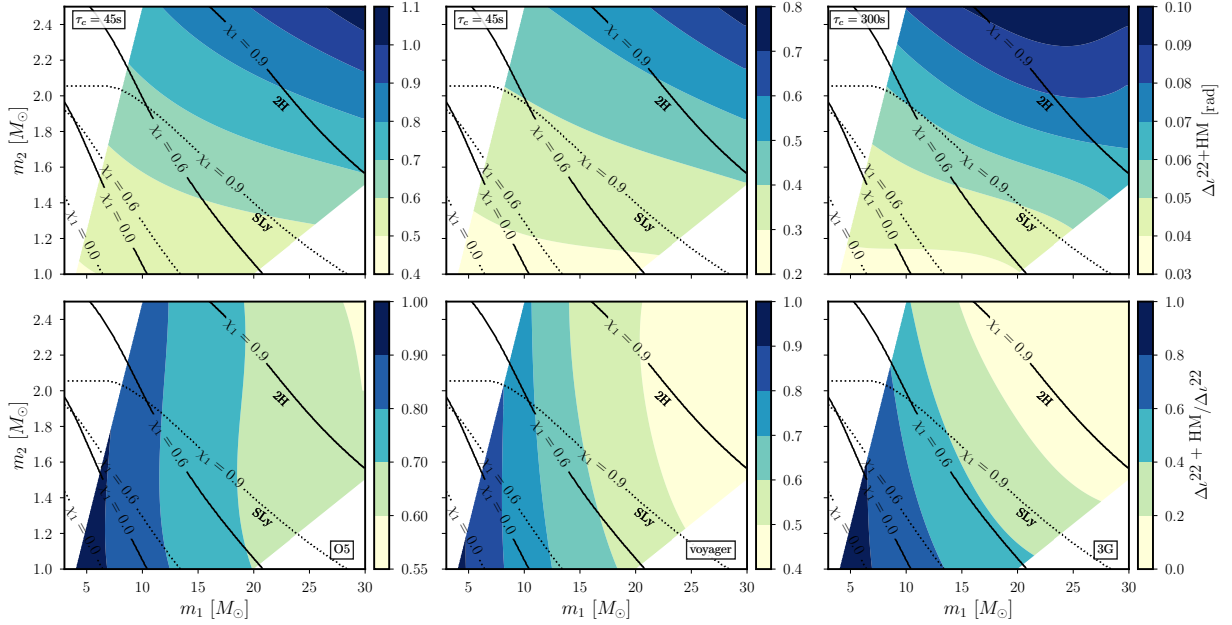
#### 4.3.1 Expected uncertainties as a function of component masses

The first set of results are generated by simulating signals in a grid of masses spanning  $m_1 = 4 - 30M_\odot, m_2 = 1 - 3M_\odot$  which corresponds to the mass range of NSBH binaries. We have chosen other extrinsic parameters as follows: inclination angle  $\iota = 60\text{ deg}$ ., luminosity distance  $d_L = 100\text{Mpc}$ , and sky-location ( $\alpha, \delta$ ) and polarization angle ( $\psi$ ) corresponding to the values which provide most precise estimates of localization sky area of the source. The NSBH systems considered here are detected given the SNR threshold of 8 since they are located relatively nearby.

In Figure 4.1, we show the improvements in the measurement of luminosity distance ( $d_L$ ) with the inclusion of higher modes at different fiducial early warning times in various observing scenarios. We quantify the improvement in terms of the ratio of the width of the 90% credible interval in the marginalized posteriors of  $d_L$ . We

find that in O5(Voyager), the measurement of luminosity distance is improved by a factor as large as  $\sim 1 - 1.5(1 - 2)$  with the inclusion of higher order modes, 45 seconds before the merger. A significant number of these mergers are also expected to produce an EM counterpart<sup>16</sup>. The possibility of an EM emission in a merger increases with the spin of the primary component (black hole in case of an NSBH) in a binary. This is a consequence of decreasing ISCO radius with increasing spins, hence leading to higher chances of tidal disruption of matter happening outside the ISCO. The EM bright nature of the compact binary merger also depends on the EoS of the neutron star component. The stiffer the EoS of a neutron star, the greater the chances of the binary being EM-bright. In 3G, the luminosity

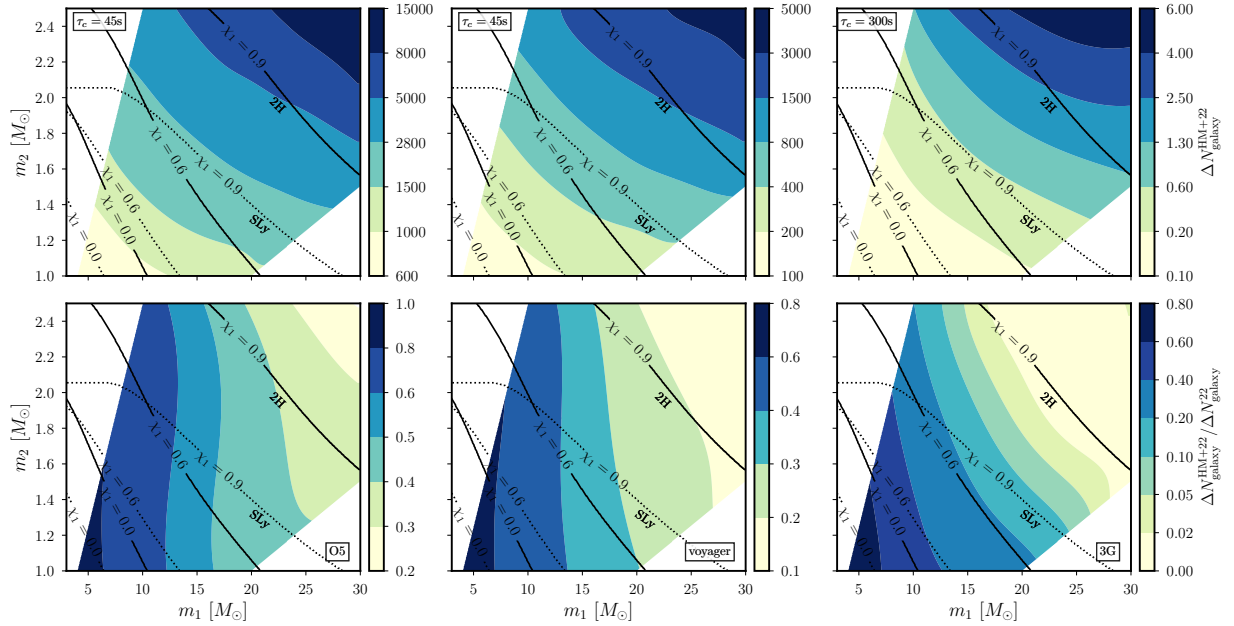
<sup>16</sup> Throughout this chapter, we have assumed that a merger producing a non-zero remnant mass outside the innermost stable circular orbit (ISCO) of the final black hole will be EM bright [104]



distance measurements can improve by a factor up to  $\sim 1.1 - 5$  at 300 seconds before the merger for a significant number of binaries. The early warning time for 3G observing scenario has been chosen as 300 seconds to keep in mind the fact that 3G detectors will be sensitive to frequencies as low as 5Hz (see Figure 3.2). This will give us a longer early warning time. Figure 4.2 shows the orbital inclination angle ( $i$ ) measurements at the same early warning times for all three observing scenarios. The improvement factors in the measurement of  $i$  are  $\sim 1 - 1.5(1 - 2)[1 - 3]$  in O5(Voyager)[3G] for many compact binary mergers with a significant fraction of them being EM bright

Figure 4.2: Same as in plot (4.1) but we show improvements in the measurement of orbital inclination ( $i$ ) of compact binary mergers with the inclusion of higher modes. The orbital inclination measurements improve by a factor  $\sim 1 - 1.5(1 - 2)[1 - 3]$ , with the inclusion of higher modes, for an early warning time of 45(45)[300] seconds, in O5(Voyager)[3G].

similar to that of luminosity distance measurements. Although the improvements in orbital inclination measurements are not that significant, it can help in better constraining the orientation of a beamed EM emission, if there exists any, from the NSBH mergers more accurately than what could have been done using only the dominant mode.

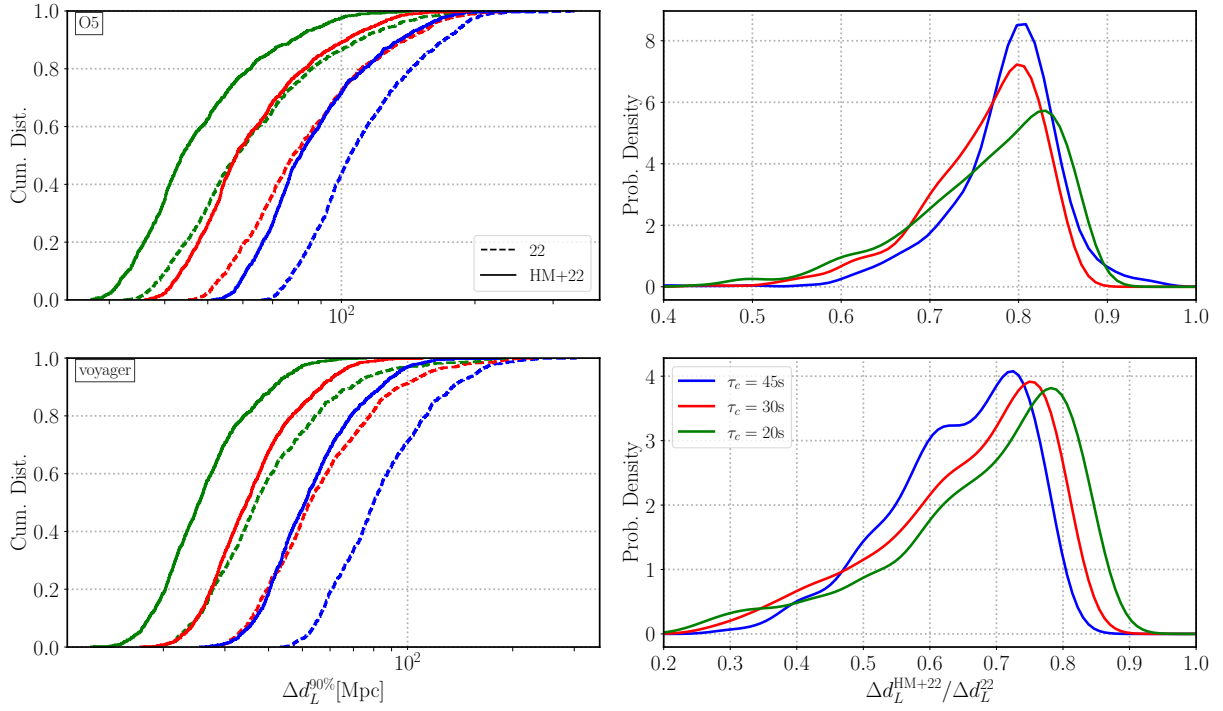


Given the measurements of luminosity distance and localization sky area, we can also estimate the error volume in which a source can be localized. This error volume further can be translated into the number of galaxies given the number density of galaxies in the universe. An estimate of the number of galaxies in this error volume is one of the most important parameters in which astronomers will be interested while searching for EM counterparts of a binary merger.

In Figure 4.3, we show the expected number of galaxies ( $\Delta N$ ) localized, at 90% confidence, with the inclusion of higher modes and also the improvements relative to only dominant mode estimates, at different EW times in various observing scenarios. We have assumed the number density of galaxies in the universe as  $n_{\text{galaxy}} = 0.01 \text{Mpc}^{-3}$  <sup>17</sup>. In the best-case scenario, the number of galaxies localized ( $\Delta N$ ), with the inclusion of higher modes, can be as small as  $\sim 1000(200)[0.2]$  at 45(45)[300] seconds before the merger in O5(Voyager)[3G]. Including higher modes apart from the domi-

Figure 4.3: *Top panel:* the total number of galaxies localized (at 90% confidence) that can be potential hosts of the compact binary merger with the inclusion of higher modes. This number can be as small as  $\sim 1000(200)[0.2]$  at 45(45)[300] seconds before the merger for binary systems that will have a potential EM counterpart in O5 (Voyager) [3G]. *Bottom panel:* the reduction in the number of potential host galaxies with the inclusion of higher modes relative to only dominant mode. This reduction factor can be as  $\sim 1 - 2.5(1.2 - 4)[1.2 - 10]$  for an early warning time of 45(45)[300] seconds before the merger in O5(Voyager)[3G].





nant mode can help in reducing the number of galaxies localized by a factor as large as  $\sim 1 - 2.5(1.2 - 4)[1.2 - 10]$  for an early warning time of 45(45)[300] seconds before the merger in O5(Voyager)[3G]. 3G detectors will almost always be able to pinpoint the source to a single galaxy for a significant number of binary mergers that will also potentially be EM bright.

#### 4.3.2 Variation of sky location and polarization angle

In the final set of results, we look at the variation of the sky-location and polarization on the error measurements of luminosity distance and orbital inclination while keeping the rest of the parameters fixed. The fixed parameters are again  $m_1 = 15M_\odot, m_2 = 1.5M_\odot, \iota = 60$  deg., and  $d_L = 100\text{Mpc}$ . We simulate 1000 uniformly distributed sky-locations and polarizations of compact binary mergers. The left column in Figure 4.4 shows the cumulative histograms of luminosity distance measurement errors with and without the inclusion of higher modes at three different early-warning times: 45, 30, and 20 seconds in both O5 and Voyager observing scenarios. The right column corresponds to the fractional improvements in the measurement errors of luminosity distance with the inclusion of higher modes.

Figure 4.4: Distributions of the measurement errors in  $d_L$  and  $\iota$  for 1000 compact binary mergers with varying sky-locations and polarizations. The *left column* shows the cumulative distributions of  $d_L$  errors. Solid (dashed) lines correspond to errors computed including (neglecting) the higher mode contributions for three different early warning times of 20, 30, and 45 seconds. In O5 (Voyager) scenario, the median  $d_L$ -errors are 44 – 81(25 – 51) Mpc at 20 – 45 seconds before the merger respectively. The *right column* shows the reductions of  $d_L$ -errors with the inclusion of higher modes relative to only dominant mode measurements. For over 50% of the binaries, inclusion of higher modes will cause the  $d_L$  errors to reduce by a factor of  $\sim 1.2 - 2(1.3 - 5)$  in O5 (Voyager).

Median values of these distributions are tabulated in Table 4.2. The improvements are better at early times than near the merger since the relative contribution of higher modes is larger at earlier times<sup>18</sup>. Similarly, Figure 4.5 shows the improvements in the measurement of inclination angle while varying the sky-locations and polarizations.

<sup>18</sup> This is because the higher modes oscillate in the most sensitive frequency band of the detector, while the dominant mode is largely buried in the low-frequency noise.

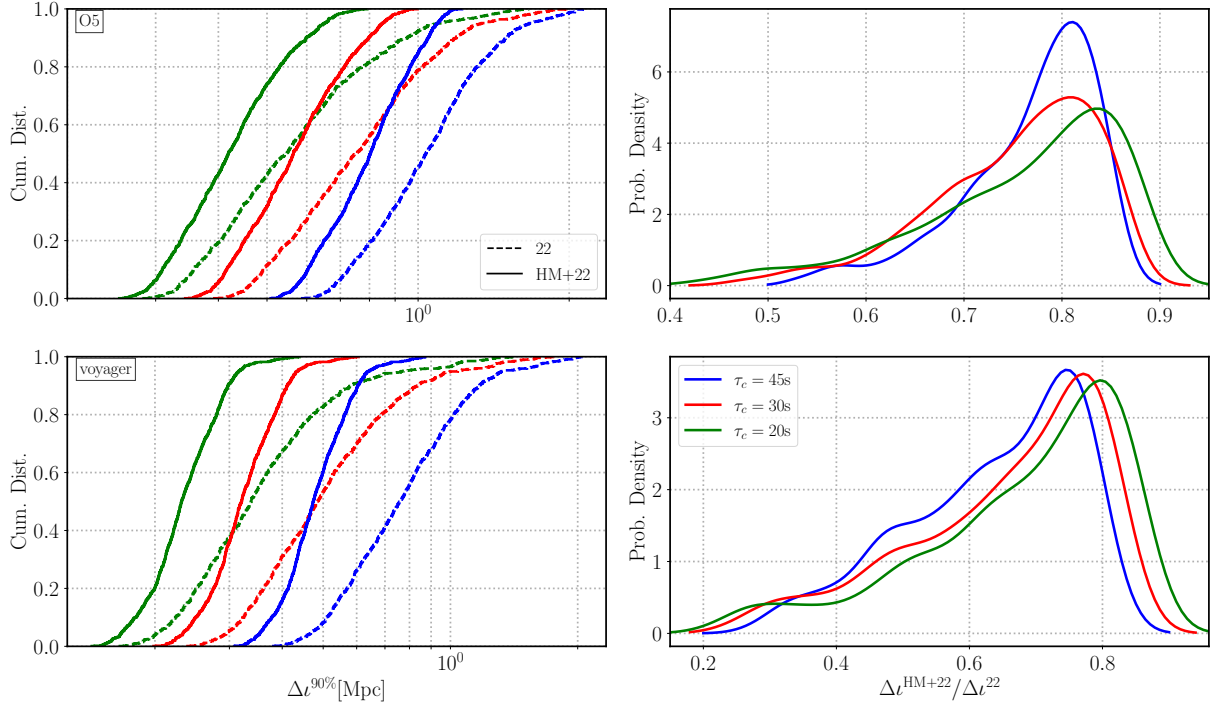


Figure 4.5: Same as figure 4.4 but histograms show the inclination errors here. For over 50% of the binaries, the errors are reduced by a factor of  $\sim 1.2 - 2(1.3 - 5)$  in O5 (Voyager).

	O5			Voyager		
$\tau_c$ [seconds]	20	30	45	20	30	45
$\Delta d_L^{HM+22}$ in Mpc	44	58	81	25	35	51
(Reduction factor)	(1.2)	(1.3)	(1.2)	(1.4)	(1.5)	(1.5)
$\Delta \iota^{HM+22}$ in radians	0.41	0.55	0.77	0.23	0.31	0.46
(Reduction factor)	(1.3)	(1.3)	(1.3)	(1.4)	(1.4)	(1.5)

#### 4.4 Summary

Joint GW-EM observations of EM-bright CBCs promise to shed light on the complex physics of the merger and associated phenomena. Among them, BNS mergers within  $\mathcal{O}(100)$  Mpc are the most likely to produce observable EM counterparts. It is not surprising that a number of GW early-warning efforts targeted at BNS mergers are currently under way<sup>19</sup>.

Table 4.2: Median values of the distribution of uncertainties in the estimation of the luminosity distance  $d_L$  and inclination angle  $\iota$  using templates including the contribution of higher modes. These correspond to two observing scenarios (O5 and Voyager) and three different early warning times (20, 30, and 45 seconds). The median improvement factors (as compared to the estimates using only 22 mode) are shown in parentheses.

<sup>19</sup> Sachdev et al. [162], Magee et al. [139], Magee and Borhanian [138], Nitz et al. [153], Kovalam et al. [126], Akcay [30], Chan et al. [74], Li et al. [129]

On the other hand, EW studies focussed on potentially EM-Bright NSBH binaries have only recently gained attention <sup>20</sup>, due primarily to the fact that their inspiral duration within the frequency band of ground-based detectors is significantly shorter than BNSs. Nevertheless, our work <sup>21</sup> demonstrated that including higher harmonics of GW radiation in templated low-latency searches could considerably increase the duration of the signal in-band. As a result, we showed that EW detection and sky-localisation could be improved considerably in future observing runs (O5, Voyager, 3G).

We follow up our previous work by demonstrating the EW benefits of including higher modes in reducing the localisation sky-volume, while also improving estimates of orbital inclination. Adopting the Fisher Matrix analysis, we find that for a range of potentially EM-Bright NSBH systems located at 100 Mpc, the error bars on the distance reduce by a factor of  $\sim 1 - 1.5(1.1 - 2)[1.1 - 5]$  at early warning times of 45 (45) [300] seconds, pertaining to observing runs O5 (Voyager) [3G]. We then pick a fiducial NSBH binary with masses  $15 - 1.5M_{\odot}$  which could potentially be EM-Bright for a moderately spinning BH, and vary its sky-location and polarization angle. Of the 1000 randomly selected locations and polarizations, we find that the median  $d_L$ -errors range from  $44 - 81(25 - 51)$  Mpc at  $20 - 45$  seconds before the merger. These correspond to  $d_L$ -error reduction factors of  $\sim 1.2(1.5)$  upon the inclusion of higher modes, in O5 (Voyager) scenario.

Improved early-warning estimates of the luminosity distance and sky-volume could aid astronomers in determining their follow-up strategy. Different EM telescopes have limiting distances to which they can probe. Of course, increasing the exposure time would enable them to probe larger distances. However, for transient GW events that are to be followed up in early-warning time, large exposure times are not feasible.

Furthermore, even if a telescope had a sufficient depth of view, it would need to slew to the appropriate sky-location, scan the localization volume, and point at the NSBH before it merges. Assisted by a galaxy catalog, as well as a coordinated search involving multiple telescopes, capturing the EM-counterpart at its onset could in principle be achieved <sup>22</sup>. With this in mind, we also highlight that using higher modes, the number of galaxies to be searched over can

<sup>20</sup> Takuya Tsutsui, Atsushi Nishizawa, and Soichiro Morisaki. Early warning of precessing neutron-star black-hole binary mergers with the near-future gravitational-wave detectors, 2021; and Takuya Tsutsui, Atsushi Nishizawa, and Soichiro Morisaki. Early warning of precessing compact binary merger with third-generation gravitational-wave detectors. *Phys. Rev. D*, 104:064013, Sep 2021. DOI: 10.1103/PhysRevD.104.064013. URL <https://link.aps.org/doi/10.1103/PhysRevD.104.064013>

<sup>21</sup> Shasvath J. Kapadia, Mukesh Kumar Singh, Md Arif Shaikh, Deep Chatterjee, and Parameswaran Ajith. Of Harbingers and Higher Modes: Improved Gravitational-wave Early Warning of Compact Binary Mergers. *ApJ*, 898(2):L39, August 2020. DOI: 10.3847/2041-8213/aba42d; and Mukesh Kumar Singh, Shasvath J. Kapadia, Md Arif Shaikh, Deep Chatterjee, and Parameswaran Ajith. Improved early warning of compact binary mergers using higher modes of gravitational radiation: a population study. *MNRAS*, 502(2):1612–1622, April 2021. DOI: 10.1093/mnras/stab125

<sup>22</sup> Michael W Coughlin et al. Optimizing searches for electromagnetic counterparts of gravitational wave triggers. *Monthly Notices of the Royal Astronomical Society*, 478(1):692–702, 04 2018. ISSN 0035-8711. DOI: 10.1093/mnras/sty1066. URL <https://doi.org/10.1093/mnras/sty1066>; and S. Antier et al. GRANDMA observations of advanced LIGO's and advanced Virgo's third observational campaign. *MNRAS*, 497(4):5518–5539, June 2020. DOI: 10.1093/mnras/staa1846

be reduced by as much  $\sim 1 - 2.5(1.2 - 4)$ , 45 seconds before merger for NSBH systems located at 100 Mpc in the O<sub>5</sub>(Voyager) scenario.

It would be worth mentioning here that the Fisher Matrix likelihood, being an expansion truncated at quadratic order of the full GW PE likelihood, can deviate from the full likelihood non-trivially. While this is true in general for lower SNR events, we also show in Appendix 7.1, that this could occur at small inclinations as well. For the fiducial inclination angle of 60 degrees chosen in this work (see Figures 7.1), we find that the full and Fisher Matrix likelihoods agree well.

# 5 | Impact of Higher Harmonics on Population Inference of Binary Black Holes

## 5.1 Motivation

From the observations of compact binary mergers, we have inferred their intrinsic (masses and spins of the compact objects) and extrinsic (distance, orientation, sky-location, etc., of the binary) parameters<sup>1</sup>. These observations suggest the existence of a new population of heavier and mildly spinning BHs<sup>2</sup>. This is in contrast to lighter masses and relatively high spin of BHs observed in X-ray binaries [154, 144]<sup>3</sup>. Determining the formation channel(s) of these merging BBHs is thus an area of active study<sup>4</sup>. A key step to constraining the formation channels is the inference of population properties of BBHs, which can be achieved by estimating the parameters that govern the shape of the distributions of the source parameters<sup>5</sup>.

Recently, the LVK collaboration has carried out population analyses using 76 compact binary mergers<sup>6</sup> in the third GW transients catalog (GWTC-3). They inferred the underlying mass, spin, and redshift distributions of these binaries along with constraining the merger rates<sup>7</sup>. Among various features, they found a peak in the BH mass spectrum near  $\sim 34M_{\odot}$  and a dearth of BHs beyond  $\sim 60M_{\odot}$  potentially suggesting the presence of an upper mass gap associated with pulsational pair-instability supernovae (PPISNe)<sup>8</sup> and pair-instability supernovae (PISNe)<sup>9</sup> respectively. The lack of BHs with masses below  $\sim 6M_{\odot}$  also points to the lower mass gap<sup>10</sup>. The presence of these mass gaps in the mass spectrum is subject to the uncertainties caused by the limited number of detections. This analysis also observed a mild preference for positive aligned spins and a merger rate increasing with redshift.

The inference of the true astrophysical population features de-

<sup>1</sup> B. P. Abbott et al. Properties of the binary black hole merger gw150914. *Phys. Rev. Lett.*, 116:241102, Jun 2016. DOI: 10.1103/PhysRevLett.116.241102. URL <https://link.aps.org/doi/10.1103/PhysRevLett.116.241102>

<sup>2</sup> Abbott et al. [18], and LIGO Scientific Collaboration et al. [32]

<sup>3</sup> Fishbach and Kalogera [101] show that there is no evidence of the BH mass distributions inferred using GWs and X-rays being different if one accounts for selection effects correctly in both scenarios. However, the spin distributions of BHs from GW and X-ray observations are in tension at  $> 99.9\%$  level.

<sup>4</sup> Zevin et al. [194], Bouffanais et al. [66], Zevin et al. [195], Stevenson and Clarke [173]

<sup>5</sup> Ilya Mandel, Will M. Farr, and Jonathan R. Gair. Extracting distribution parameters from multiple uncertain observations with selection biases. *MNRAS*, 486(1):1086–1093, June 2019. DOI: 10.1093/mnras/stz896; and Eric Thrane and Colm Talbot. An introduction to Bayesian inference in gravitational-wave astronomy: Parameter estimation, model selection, and hierarchical models. *PASA*, 36:e010, March 2019. DOI: 10.1017/pasa.2019.2

<sup>6</sup> The LIGO Scientific Collaboration, the Virgo Collaboration, and the KAGRA Collaboration. The population of merging compact binaries inferred using gravitational waves through GWTC-3. *arXiv e-prints*, art. arXiv:2111.03634, November 2021

<sup>7</sup> Abbott et al. [3], Abbott et al. [16], The LIGO Scientific Collaboration et al. [176]

<sup>8</sup> Barkat et al. [41], Woosley and Weaver [193]

<sup>9</sup> Fowler and Hoyle [106], Rakavy and Shaviv [160], Barkat et al. [41]

<sup>10</sup> Farah et al. [98]

pends not only on the flexibility of the population model chosen in the analysis and the number of detected GW events but also on the accuracy of the estimates of the source properties. Any missing physics in the waveform models, such as the effect of subdominant modes, spin precession, orbital eccentricity, etc, can bias the inference of individual source properties that in turn will affect the inferred shape of the population distributions.

Neglecting subdominant modes of gravitational radiation can bias the parameter inference of compact binary mergers with significant asymmetries <sup>11</sup>. This can also lead to a loss of detections of BBH mergers when the HMs are not included in GW searches <sup>12</sup>. Including HMs in GW analyses provides unbiased and more precise measurements of the source parameter <sup>13</sup>, and can improve GW early-warning (Chapters 3 and 4). An important reason for the improved precision in some of the parameters is that the HMs also reduce correlations among them, such as luminosity distance and orbital inclination, initial phase and polarization angle, spin and mass ratio, etc. (also discussed in section 2.5). In particular, the better measurement of luminosity distance and inclination angle through HMs would be useful in constraining cosmology <sup>14</sup> and any beamed EM emission (e.g. short GRBs) <sup>15</sup>.

In this chapter, we study the effect of neglecting HMs on the inference of population properties of non-spinning BBH mergers. Since the binary systems with approximate symmetry (near-equal component masses, aligned spins, etc.) are louder than the ones with significant asymmetry, the detected population is dominated by the former as a consequence of the Malmquist selection bias <sup>16</sup>. Due to the beaming of gravitational radiation along the direction of the orbital angular momentum, there is also a selection bias towards face-on binaries, for which the effect of HMs is minimal. This means including/neglecting HMs in the analysis will not play a major role in the parameter estimation for most of the detected binaries that are nearly symmetric. However, even if neglecting HMs does not cause a significant bias (the shift in the peak of the posterior from the true value is smaller than statistical uncertainties) in individual binaries, it might show up in the population-level parameters when accumulated over many sources. This is the question that we address in this chapter. We quantify the effect of subdominant modes in the

<sup>11</sup> Vijay Varma, Parameswaran Ajith, Sascha Husa, Juan Calderon Bustillo, Mark Hannam, and Michael Pürrer. Gravitational-wave observations of binary black holes: Effect of non-quadrupole modes. *Phys. Rev. D*, 90(12):124004, 2014. DOI: 10.1103/PhysRevD.90.124004; and Vijay Varma and Parameswaran Ajith. Effects of nonquadrupole modes in the detection and parameter estimation of black hole binaries with nonprecessing spins. *Phys. Rev. D*, 96:124024, Dec 2017. DOI: 10.1103/PhysRevD.96.124024. URL <https://link.aps.org/doi/10.1103/PhysRevD.96.124024>

<sup>12</sup> Calderón Bustillo et al. [69], Capano et al. [72], Harry et al. [113], Divyajyoti et al. [86]

<sup>13</sup> Van Den Broeck and Sengupta [185], Arun et al. [34], Graff et al. [111]

<sup>14</sup> Ish Gupta, Ssohrab Borhanian, Arnab Dhani, Debatri Chattopadhyay, Rahul Kashyap, V. Ashley Villar, and B. S. Sathyaprakash. Neutron star-black hole mergers in next generation gravitational-wave observatories. *Phys. Rev. D*, 107(12):124007, 2023. DOI: 10.1103/PhysRevD.107.124007; and Yi Gong, Zhoujian Cao, Junjie Zhao, and Lijing Shao. Including higher harmonics in gravitational-wave parameter estimation and cosmological implications for LISA. *arXiv e-prints*, art. arXiv:2308.13690, August 2023. DOI: 10.48550/arXiv.2308.13690

<sup>15</sup> K. G. Arun, Hideyuki Tagoshi, Archana Pai, and Chandra Kant Mishra. Synergy of short gamma ray burst and gravitational wave observations: Constraining the inclination angle of the binary and possible implications for off-axis gamma ray bursts. *Phys. Rev. D*, 90:024060, Jul 2014. DOI: 10.1103/PhysRevD.90.024060. URL <https://link.aps.org/doi/10.1103/PhysRevD.90.024060>

<sup>16</sup> K. G. Malmquist. On some relations in stellar statistics. *Meddelanden fran Lunds Astronomiska Observatorium Serie I*, 100:1–52, March 1922; and K. G. Malmquist. A contribution to the problem of determining the distribution in space of the stars. *Meddelanden fran Lunds Astronomiska Observatorium Serie I*, 106:1–12, February 1925

population inference of BBHs.

We have organized the rest of the chapter as follows: In section 5.2 we discuss the Bayesian parameter inference, followed by a brief introduction to population inference and selection effects. The results are presented in section 5.3 including parameter estimation of individual BBHs as well as population inference. Section 5.4 summarizes the results and discusses the future directions.

## 5.2 Method

### 5.2.1 Parameter inference

Under the assumption that the noise  $n$  is a stationary Gaussian random process, we can write the likelihood of the data  $d$  given the source parameters  $(\theta)$  of the GW signal  $h$  as (same as in Eq. 4.2)

$$\mathcal{L}(d|\theta) \propto \exp \left[ -\frac{1}{2} (d - h(\theta) | d - h(\theta)) \right], \quad (5.1)$$

Assuming the prior information on the distribution of the parameters, i.e.  $\pi(\theta)$ , one can use Bayes' theorem to write the posterior on the parameters  $\theta$  given the data  $d$

$$p(\theta|d) = \frac{\mathcal{L}(d|\theta)\pi(\theta)}{\mathcal{Z}(d)}, \quad (5.2)$$

where  $\mathcal{Z}(d)$  is the normalization to the posterior probability distribution, also known as the evidence or marginalized likelihood

$$\mathcal{Z} = \int d\theta \mathcal{L}(d|\theta)\pi(\theta). \quad (5.3)$$

Evidence is not essential for inferring the parameters but it is crucial when comparing two hypotheses (e.g. two theoretical models for the GW signal), say A and B, the ratio of evidences also known as Bayes' factor ( $\mathcal{B}$ ) of model A with respect to B is:

$$\mathcal{B}_B^A = \frac{\mathcal{Z}_A}{\mathcal{Z}_B}. \quad (5.4)$$

When the two hypotheses have different prior probabilities for being true, a more sensible way of comparing models is the odds ratio

$$\mathcal{O}_B^A = \frac{\mathcal{Z}_A \pi_A}{\mathcal{Z}_B \pi_B}, \quad (5.5)$$

where the factor  $\pi_A/\pi_B$  known as priors odds accounts for our prior belief in models chosen in the analysis. In this work, we do not give any preference for a multipolar over dominant mode waveform model before we carry out the inference, so we choose this ratio to be unity. The odds ratio will be the same as Bayes' factor in that case. Computing posteriors  $p(\theta|d)$  is not an easy feat, especially when the dimensionality of the problem is large. For example, in the case of a BBH merger, the parameter space is 15-dimensional and it will be an impossible task to compute the probabilities on a grid. So one has to rely on stochastic sampling methods, such as Markov Chain Monte Carlo <sup>17</sup>, nested sampling <sup>18</sup>, etc., to compute the posteriors in a reasonable amount of time.

### 5.2.2 Population inference

Once we have a large number of GW events coming from an underlying source population, we can start estimating the properties of that population. This *population inference* can be done in a hierarchical way: We first estimate the properties of individual sources as described in Sec 5.2.1. Using these posteriors and evidences from individual events, we infer the distribution of the population properties.

Suppose we have observed  $N$  GW signals denoted by the data set  $\mathcal{D} \equiv \{d_1, d_2, \dots, d_N\}$ , then the posterior probability distribution for the population hyper-parameters  $\Lambda$ , marginalized over the merger rate  $\mathcal{R}$  <sup>19</sup>, is given by

$$p(\Lambda|\mathcal{D}) \propto \frac{1}{p_{\text{det}}^N(\Lambda)} \frac{\mathcal{L}(\mathcal{D}|\Lambda)\pi(\Lambda)}{\mathcal{Z}(\mathcal{D})}, \quad (5.6)$$

where  $\mathcal{L}(\mathcal{D}|\Lambda)$  and  $\pi(\Lambda)$  are the population likelihood (also known as hyper-likelihood) and prior (also known as hyper-prior) on hyper-parameters. The term  $\mathcal{Z}(\mathcal{D})$  is the hyper-evidence that plays an important role when comparing two population models and is just a proportionality constant. In the above equation,  $p_{\text{det}}(\Lambda)$  encodes detector selection effects (see Sec. 5.2.3 for details). Under the assumption that different observations are independent of each other, we can write the population likelihood as:

$$\mathcal{L}(\mathcal{D}|\Lambda) = \prod_{i=1}^N \mathcal{L}(d_i|\Lambda) = \prod_{i=1}^N \int d\theta_i \mathcal{L}(d_i|\theta_i) \pi(\theta_i|\Lambda), \quad (5.7)$$

<sup>17</sup>Nelson Christensen and Renate Meyer. Using Markov chain Monte Carlo methods for estimating parameters with gravitational radiation data. *Phys. Rev. D*, 64:022001, 2001. DOI: 10.1103/PhysRevD.64.022001

<sup>18</sup>John Skilling. Nested sampling for general Bayesian computation. *Bayesian Analysis*, 1(4):833 – 859, 2006. DOI: 10.1214/06-BA127. URL <https://doi.org/10.1214/06-BA127>

<sup>19</sup>Thomas J. Loredo. Accounting for Source Uncertainties in Analyses of Astronomical Survey Data. In Rainer Fischer, Roland Preuss, and Udo Von Toussaint, editors, *Bayesian Inference and Maximum Entropy Methods in Science and Engineering: 24th International Workshop on Bayesian Inference and Maximum Entropy Methods in Science and Engineering*, volume 735 of *American Institute of Physics Conference Series*, pages 195–206, November 2004. DOI: 10.1063/1.1835214; Ilya Mandel, Will M. Farr, and Jonathan R. Gair. Extracting distribution parameters from multiple uncertain observations with selection biases. *MNRAS*, 486(1):1086–1093, June 2019. DOI: 10.1093/mnras/stz896; and Salvatore Vitale, Davide Gerosa, Will M. Farr, and Stephen R. Taylor. Inferring the Properties of a Population of Compact Binaries in Presence of Selection Effects. In *Handbook of Gravitational Wave Astronomy*, page 45. 2022. DOI: 10.1007/978-981-15-4702-7\_45-1



where  $d_i$  denotes the data measurement for  $i^{\text{th}}$  event which has its own set of parameters  $\theta_i$ . Here  $\pi(\theta_i|\Lambda)$  denotes the population model prior for the distribution of  $\theta$  conditioned upon the hyper-parameters  $\Lambda$ . This assumes that all detected events have been drawn from the same population model. Now, the hyper-posterior upon substitution from Eq. 5.7 is given by

$$p(\Lambda|\mathcal{D}) \propto \frac{\pi(\Lambda)}{p_{\text{det}}^N(\Lambda)} \prod_{i=1}^N \int d\theta_i p(\theta_i|d_i) \frac{\pi(\theta_i|\Lambda)}{\pi(\theta_i)}, \quad (5.8)$$

where we have used Bayes' theorem, Eq. (5.2), to write the likelihood for individual BBH events in terms of the posterior, prior, and evidence. The multiplication of evidences  $\prod_{i=1}^N \mathcal{Z}(d_i)$  is absorbed in the proportionality as it is constant. It is clear from the above equation that computing posteriors on hyper-parameters requires many evaluations of an integral which amounts to calculating the expectation value of the ratio of population prior to PE prior for each event in the catalog. The integral can be evaluated numerically via Monte-Carlo integration as:

$$\int d\theta_i p(\theta_i|d_i) \frac{\pi(\theta_i|\Lambda)}{\pi(\theta_i)} \approx \frac{1}{N_s^i} \sum_{j=1}^{N_s^i} \frac{\pi(\theta_i^j|\Lambda)}{\pi(\theta_i^j)} \Bigg|_{\theta_i^j \sim p(\theta_i|d_i)} \quad (5.9)$$

where  $\theta_i^j$  denotes the  $j^{\text{th}}$  sample drawn from the posterior of the  $i^{\text{th}}$  event. The above approximation holds when there are a sufficient number of posterior samples. This number is dependent on the SNR of individual events and typically ranges  $\mathcal{O}(10^3 - 10^5)$ .

### 5.2.3 Selection effects

The detection of GW signals is limited by their loudness that depends on various parameters such as masses, spins, luminosity distance, orientation, the sky location (weakly), etc. This is known as the Malmquist bias <sup>20</sup>. It is important to account for this bias as a correction factor in the population likelihood (notice the denominator of Eq. 5.8) if one wants to understand the true astrophysical population properties of merging compact binaries. The detection probability for an astrophysical model with hyper-parameters  $\Lambda$  can be computed by marginalizing the detection probability of binaries

<sup>20</sup> Malmquist [141, 142]

with various source parameters predicted by that model.

$$p_{\text{det}}(\Lambda) = \int d\theta p_{\text{det}}(\theta) \pi(\theta|\Lambda), \quad (5.10)$$

with

$$p_{\text{det}}(\theta) = \int_{d:f(d) \geq f_{\text{th}}} dd p(d|\theta), \quad (5.11)$$

where in the last equation, the integration is carried out only on those likelihoods for which data is such that it leads to the detection statistic  $f(d)$  (e.g. matched-filter SNR or false alarm rate) greater than its threshold value  $f_{\text{th}}$ . Computing  $p_{\text{det}}(\theta)$  numerically requires an extensive injection campaign of simulated GW signals in the detector noise followed by the calculation of the detection statistic. The finite number of simulations carried out introduces an uncertainty in the selection function estimated which must be mitigated by injecting enough synthetic GW signals <sup>21</sup>.

<sup>21</sup> Will M. Farr. Accuracy Requirements for Empirically Measured Selection Functions. *Research Notes of the American Astronomical Society*, 3(5):66, May 2019. DOI: 10.3847/2515-5172/ab1d5f; Reed Essick and Will Farr. Precision Requirements for Monte Carlo Sums within Hierarchical Bayesian Inference. *arXiv e-prints*, art. arXiv:2204.00461, April 2022. DOI: 10.48550/arXiv.2204.00461; Colm Talbot and Jacob Golomb. Growing Pains: Understanding the Impact of Likelihood Uncertainty on Hierarchical Bayesian Inference for Gravitational-Wave Astronomy. *MNRAS*, September 2023. DOI: 10.1093/mnras/stad2968; and Reed Essick. Semianalytic sensitivity estimates for catalogs of gravitational-wave transients. *Phys. Rev. D*, 108:043011, Aug 2023. DOI: 10.1103/PhysRevD.108.043011. URL <https://link.aps.org/doi/10.1103/PhysRevD.108.043011>

#### 5.2.4 Population models

As a simple model, we choose a mass distribution model inspired by well-known initial mass functions of stars that are typically power laws <sup>22</sup>. In our simulations, we use a *truncated* power-law model <sup>23</sup>, known as “Model-B” in [133] <sup>24</sup>. The primary mass  $m_1$  (the heavier BH in the BBH system) distribution with spectral index  $\alpha$  is given by,

$$p(m_1|\alpha, m_{\text{min}}, m_{\text{max}}) \propto \begin{cases} m_1^{-\alpha}, & m_{\text{min}} < m_1 < m_{\text{max}} \\ 0, & \text{Otherwise,} \end{cases} \quad (5.12)$$

where  $m_{\text{min}}/m_{\text{max}}$  is the lower/upper limit of the mass function. The distribution of the mass ratio  $q \equiv m_2/m_1$  with power-law spectral index  $\beta_q$  is,

$$p(q|\beta_q, m_{\text{min}}, m_1) \propto \begin{cases} q^{\beta_q}, & m_{\text{min}} < m_2 < m_1 \\ 0, & \text{Otherwise.} \end{cases} \quad (5.13)$$

We assume the redshift distribution with power-law spectral index  $\lambda_z$  that captures the evolution of the BBH merger rate with redshift [102]

$$p(z) \propto \frac{1}{1+z} \frac{dV_c}{dz} (1+z)^{\lambda_z}. \quad (5.14)$$

<sup>22</sup> Edwin E. Salpeter. The Luminosity Function and Stellar Evolution. *ApJ*, 121:161, January 1955. DOI: 10.1086/145971

<sup>23</sup> Ely D. Kovetz, Ilias Cholis, Patrick C. Breyse, and Marc Kamionkowski. Black hole mass function from gravitational wave measurements. *Phys. Rev. D*, 95(10):103010, May 2017. DOI: 10.1103/PhysRevD.95.103010; and Maya Fishbach and Daniel E. Holz. Where Are LIGO’s Big Black Holes? *ApJ*, 851(2):L25, December 2017. DOI: 10.3847/2041-8213/a9bfb6

<sup>24</sup> Note that the truncated power-law model is already in tension with the BH mass spectrum inferred from GW observations [16, 176]. For example, it can not explain the features in the mass spectrum at  $\sim 35M_{\odot}$ .

Parameter	Description	Prior
$\alpha$	primary mass power-law spectral index	$U(-2, 4)$
$\beta_q$	mass ratio power-law spectral index	$U(-3, 5)$
$m_{\min}$	lower limit on the mass of the BH	$U(1, 15)$
$m_{\max}$	upper limit on the mass of the BH	$U(60, 150)$
$\lambda_z$	power-law spectral index of redshift distribution	$U(-6, 6)$

With  $\lambda_z = 0$ , the above model corresponds to the distribution of BBHs uniform in 3-comoving volume and source frame time. The model hyper-parameters  $\Lambda \equiv \{\alpha, \beta_q, m_{\min}, m_{\max}, \lambda_z\}$  are summarised in Table 5.1 along with their priors chosen for hierarchical inference.

Table 5.1: The population model hyper-parameters description and their corresponding priors chosen for hierarchical inference. Above,  $U(a, b)$  indicates uniform distribution between  $a$  and  $b$ .

### 5.3 Results

We simulate an astrophysical population of 3900 non-spinning BBH mergers assuming that the primary mass  $m_1$  is drawn from a log-uniform ( $\alpha = 1$ ) and the mass-ratio  $q$  from a linear ( $\beta_q = 1$ ) distribution with minimum and maximum mass of a BH as  $m_{\min} = 5M_{\odot}, m_{\max} = 100M_{\odot}$  respectively. The BBH mergers are distributed uniformly in the source frame (uniform in comoving volume and source frame time) with redshift evolution hyper-parameter  $\lambda_z = 0$ . We model these GW signals using a multipolar waveform approximant, IMRPhenomXPHM<sup>25</sup>, a phenomenological frequency domain model implemented in LALSimulation<sup>26</sup> and inject them into Gaussian noise, assuming the design sensitivity of the LIGO and Virgo detector network<sup>27</sup>.

We find  $\sim 750$  injections were detected with a network matched-filter SNR threshold of 8. Fig. 5.1 shows the distribution of injected and detected distribution of BBH mergers. We detect more massive and closer BBHs than lighter and farther away systems as expected by the selection effects. It is also noticeable that binaries with unequal masses and high inclination angles (for which the HMs are expected to make a significant contribution) are rarer in the detected population. This is because asymmetric (small  $q$ ) compact binary mergers are less efficient at emitting GWs than near-symmetric ones<sup>28</sup>. Also, the radiation is primarily beamed along the direction of the orbital angular momentum. These effects will result in smaller SNRs, on average, for asymmetric and inclined binaries.

<sup>25</sup> Geraint Pratten, Cecilio García-Quirós, Marta Colleoni, Antoni Ramos-Buades, Héctor Estellés, Maite Mateu-Lucena, Rafel Jaume, Maria Haney, David Keitel, Jonathan E. Thompson, and Sascha Husa. Computationally efficient models for the dominant and subdominant harmonic modes of precessing binary black holes. *Phys. Rev. D*, 103(10):104056, May 2021. DOI: 10.1103/PhysRevD.103.104056

<sup>26</sup> LIGO Scientific Collaboration. LIGO Algorithm Library - LALSuite. free software (GPL), 2020

<sup>27</sup> J Aasi et al. Advanced LIGO. *Classical and Quantum Gravity*, 32(7):074001, mar 2015. DOI: 10.1088/0264-9381/32/7/074001. URL <https://doi.org/10.1088/2F0264-9381%2F32%2F7%2F074001>; and F Acernese et al. Advanced virgo: a second-generation interferometric gravitational wave detector. *Classical and Quantum Gravity*, 32(2):024001, dec 2015. DOI: 10.1088/0264-9381/32/2/024001. URL <https://doi.org/10.1088/2F0264-9381%2F32%2F2%2F024001>

<sup>28</sup> The optimal SNR of a binary is proportional to the square root of the symmetric mass ratio  $\eta := q/(1+q)^2$  [see, e.g., Eq. (B11) of Ajith et al. [29]]. Since the detection volume for a binary is proportional to the cube of the SNR, the fraction of detected events should roughly scale as  $\eta^{3/2}$ , which is consistent with what we see in Fig. 5.1.

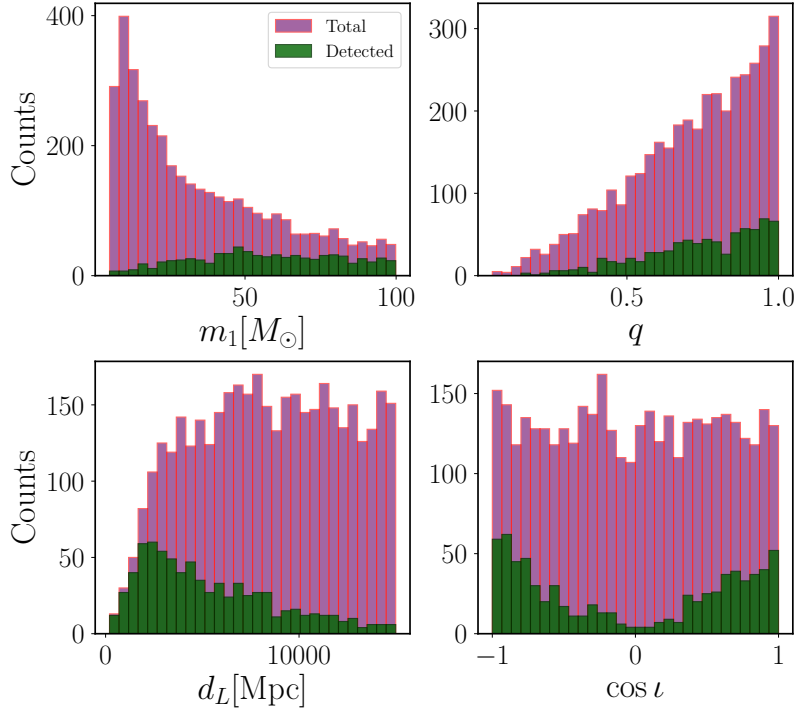


Figure 5.1: The distribution of the injected total population (in purple) of non-spinning BBH mergers along with the detected one (in green) that is computed assuming the network matched-filter SNR is greater than the threshold value of 8.

### 5.3.1 Impact of higher modes on parameter inference

We performed PE on the detected injections using both a dominant mode only (IMRPhenomXP) and multipolar (IMRPhenomXPHM) waveform model<sup>29</sup>. We used Bayesian Inference Library, Bilby<sup>30</sup> that employs the dynesty<sup>31</sup> sampler to stochastically sample the posteriors on various parameters (masses, sky-location, luminosity distance, orbital inclination, polarization, and arrival time and phase) of the binaries. Fig. 5.2 shows the two- and one-dimensional probability distributions of some of the important parameters (chirp mass  $\mathcal{M} := (m_1 m_2)^{3/5} / (m_1 + m_2)^{1/5}$ , mass ratio  $q$ , inclination angle  $i$ , and luminosity distance  $d_L$ ) after marginalizing over the rest. These marginalized distributions, plotted using the corner package [103]<sup>32</sup>, correspond to a moderately asymmetric ( $q \sim 0.3, i = 103$  degrees) BBH system recovered using IMRPhenomXP and IMRPhenomXPHM. The parameter estimation is more accurate and precise when HMs are included in the analysis. This shows the importance of HMs in parameter estimation, consistent with the findings of many previous studies<sup>33</sup>.

To further quantify the effect of neglecting HMs on the parameter inference of the BBH population, we compute a combined effective

<sup>29</sup> Pratten et al. [157]

<sup>30</sup> Ashton et al. [39]

<sup>31</sup> Edward Higson, Will Handley, Mike Hobson, and Anthony Lasenby. Dynamic nested sampling: an improved algorithm for parameter estimation and evidence calculation. *Statistics and Computing*, 29(5):891–913, September 2019. DOI: 10.1007/s11222-018-9844-0; and Joshua S. Speagle. DYNESTY: a dynamic nested sampling package for estimating Bayesian posteriors and evidences. *MNRAS*, 493(3):3132–3158, April 2020. DOI: 10.1093/mnras/staa278

<sup>32</sup> The 2D probability contours that we compute will have some dependence on the bin size of the histogram: If the bin width is too large, it will not be able to resolve small differences between the posteriors from the “22” mode and “HM+22” parameter estimation. If the bin width is too narrow, this will create statistical fluctuations due to the limited number of samples per bin. We have chosen some intermediate bin width, with which the statistical fluctuations due to the limited number of posterior samples are insignificant. At the same time, the bin width is small enough so that we can see the difference between the two posteriors.

<sup>33</sup> Van Den Broeck and Sengupta [185], Arun et al. [34], Graff et al. [111], Varma et al. [187], Varma and Ajith [186]

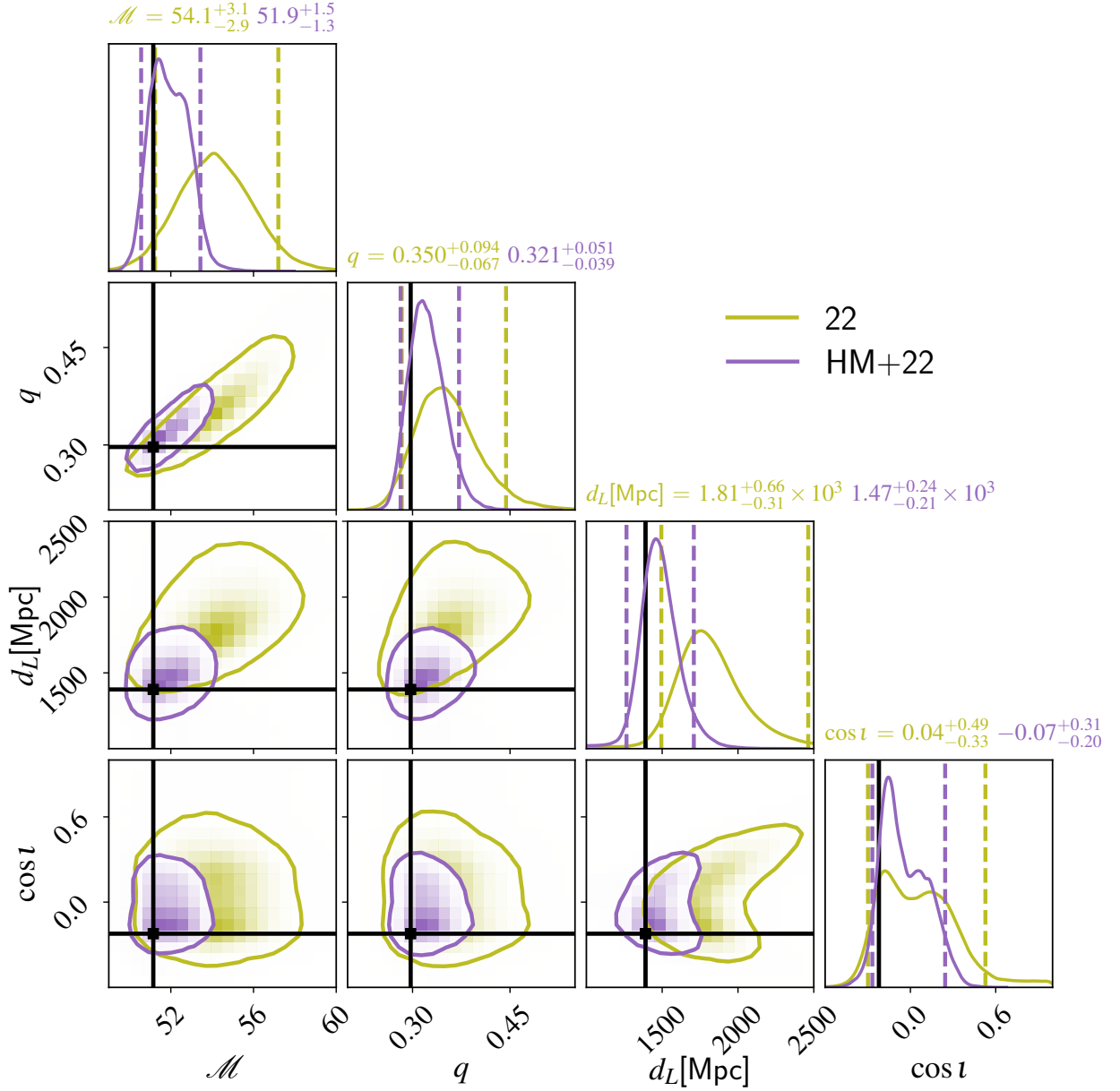


Figure 5.2: The two-dimensional along with one-dimensional posterior distributions on a few source parameters ( $\mathcal{M}, q, d_L, i$ ) of a moderately asymmetric ( $q \sim 0.3, i \sim 103$  degrees) BBH merger. Posteriors employing the HMs are more accurate (peaking closer to the injected value, shown by the vertical black line) and precise (smaller spread in the posteriors; 90% credible regions in the one-dimensional posteriors are shown by vertical dashed lines). On the other hand, when the HMs are neglected in parameter inference, it leads to not only the broadening of the posteriors but also the biased inference of the luminosity distance. The inclusion of HMs has also reduced the degeneracy in inferring the source parameters, especially in  $i - d_L$  and  $\mathcal{M} - q$ .

bias for the recovery of the chirp mass, mass ratio, and luminosity distance as

$$\epsilon = \sqrt{\left(\frac{\hat{\mathcal{M}}}{\mathcal{M}^{\text{tr}}} - 1\right)^2 + \left(\frac{\hat{q}}{q^{\text{tr}}} - 1\right)^2 + \left(\frac{\hat{d}_L}{d_L^{\text{tr}}} - 1\right)^2}, \quad (5.15)$$

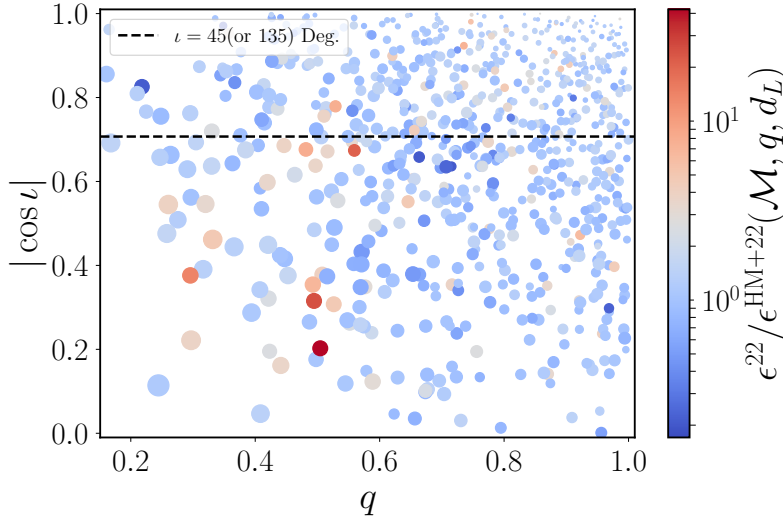


Figure 5.3: The ratio of the effective bias ( $\epsilon^{22}/\epsilon^{\text{HM}+22}$ ) estimated for chirp mass, mass ratio, and luminosity distance recovery when using a multipolar waveform compared to a dominant mode waveform as a function of  $q$  and  $\iota$ . The size of the marker corresponds to the SNR contribution due to the HMs only.

where  $\hat{\cdot}$  denotes the point estimates of the source parameters (median of the marginalized 1D posteriors in our case) and  $\theta^{\text{tr}}$  corresponds to the true values of the source parameters. We plot this effective bias  $\epsilon$  as a function of  $q$  and  $|\cos \iota|$ , the parameters that primarily determine the relative contribution of HMs to the observed GW signal (see Fig. 5.3). The size of the marker represents the SNR contribution due to non-quadrupolar modes<sup>34</sup> which increases when moving from near equal masses and face-on systems to unequal masses and edge-on systems as expected. Note that the increase in the SNR is not monotonic as a function of the degree of asymmetry in the system. This is because the SNR contribution from HMs for a given observing scenario is also determined by the source parameters such as total mass (spins also but we are assuming non-spinning binaries here) other than mass-ratio and inclination angle. The color-map density corresponds to the ratio of the effective biases ( $\epsilon^{22}/\epsilon^{\text{HM}+22}$ ) estimated using a dominant mode only (22) waveform model to a multipolar (HM+22) one. The events with ratio  $\epsilon^{22}/\epsilon^{\text{HM}+22} > 1$  denote that including HMs improves the parameter estimation. We see an indication of a trend in the effective bias ratio which is mildly correlated with the SNR contained in the subdominant modes. The effective bias ratio is larger for more asymmetric events in general which means the HMs play a significant role in inferring source parameters. We also plot the log-Bayes factor (ratio of the evidences) while comparing the parameter inference with a

<sup>34</sup> The SNR contribution due to HMs (21,33,44) is estimated by computing an orthogonal set of subdominant modes with respect to the dominant mode (2). If these orthogonal modes have the SNRs denoted by  $\rho'_{\ell m'}$ , then the SNR contained in HMs is  $\rho_{\text{HM}} = (\rho'^2_{21} + \rho'^2_{33} + \rho'^2_{44})^{1/2}$ . The size of the marker in Fig. 5.3 and 5.4 corresponds to the ratio  $\rho_{\text{HM}}/\rho_{22}$  [149].

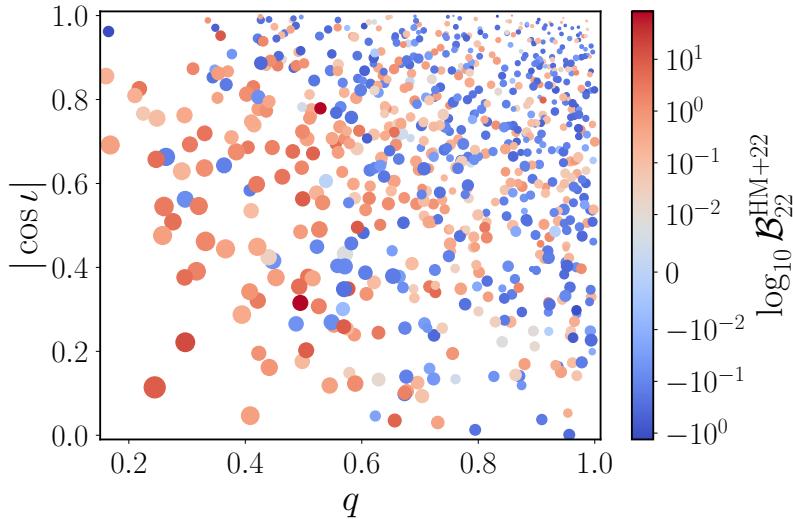


Figure 5.4: Same as Fig. 5.3 but the color map represents the Bayes factors ( $\mathcal{B}$ ) between a multipolar (HM+22) and only dominant mode (22) waveform models. In the asymmetric region of parameter space (low  $q$  and non-face-on inclination), the multipolar waveform model is preferred over just the dominant mode.

multipolar and dominant mode-only waveform model (see Fig. 5.4). Again, the waveform model with subdominant modes is preferred over the dominant mode-only model when there is significant asymmetry in the binary system.

### 5.3.2 Inference of population properties

We consider posterior samples, from all the detected injections, obtained through nested sampling<sup>35</sup> using both multipolar and dominant mode waveform models. Specifically, this study focuses on the mass and redshift population properties of BBH mergers hence we only use posterior samples for masses ( $m_1, q$ ) and redshift ( $z$ ) in our analysis. We also compute a joint sampling prior (prior used during parameter estimation on individual events)  $\pi(m_1, q, z)$  that is used to reweight the population prior  $\pi(m_1, q, z|\Lambda)$  (the term inside the summation in Eq. 5.9) in hierarchical inference. Further, the selection effects were estimated by injecting 50 million GW signals into Gaussian noise and then computing the detection statistic, the network matched-filter SNR in our case, both when employing the multipolar and dominant mode waveform model. The found injections (GW signals with network matched-filter SNR  $\geq 8$ ) were used to compute the selection effects<sup>36</sup>. In the case of real observations, this process becomes computationally expensive as it requires injecting signals in the detector noise and recording the detection statistics by running the search pipelines. In an ideal simulation, one should

<sup>35</sup> John Skilling. Nested sampling for general Bayesian computation. *Bayesian Analysis*, 1(4):833 – 859, 2006. DOI: 10.1214/06-BA127. URL <https://doi.org/10.1214/06-BA127>

<sup>36</sup> Vaibhav Tiwari. Estimation of the Sensitive Volume for Gravitational-wave Source Populations Using Weighted Monte Carlo Integration. *Class. Quant. Grav.*, 35(14):145009, 2018. DOI: 10.1088/1361-6382/aac89d; Will M. Farr. Accuracy Requirements for Empirically Measured Selection Functions. *Research Notes of the American Astronomical Society*, 3(5): 66, May 2019. DOI: 10.3847/2515-5172/ab1d5f; and Reed Essick and Will Farr. Precision Requirements for Monte Carlo Sums within Hierarchical Bayesian Inference. *arXiv e-prints*, art. arXiv:2204.00461, April 2022. DOI: 10.48550/arXiv.2204.00461

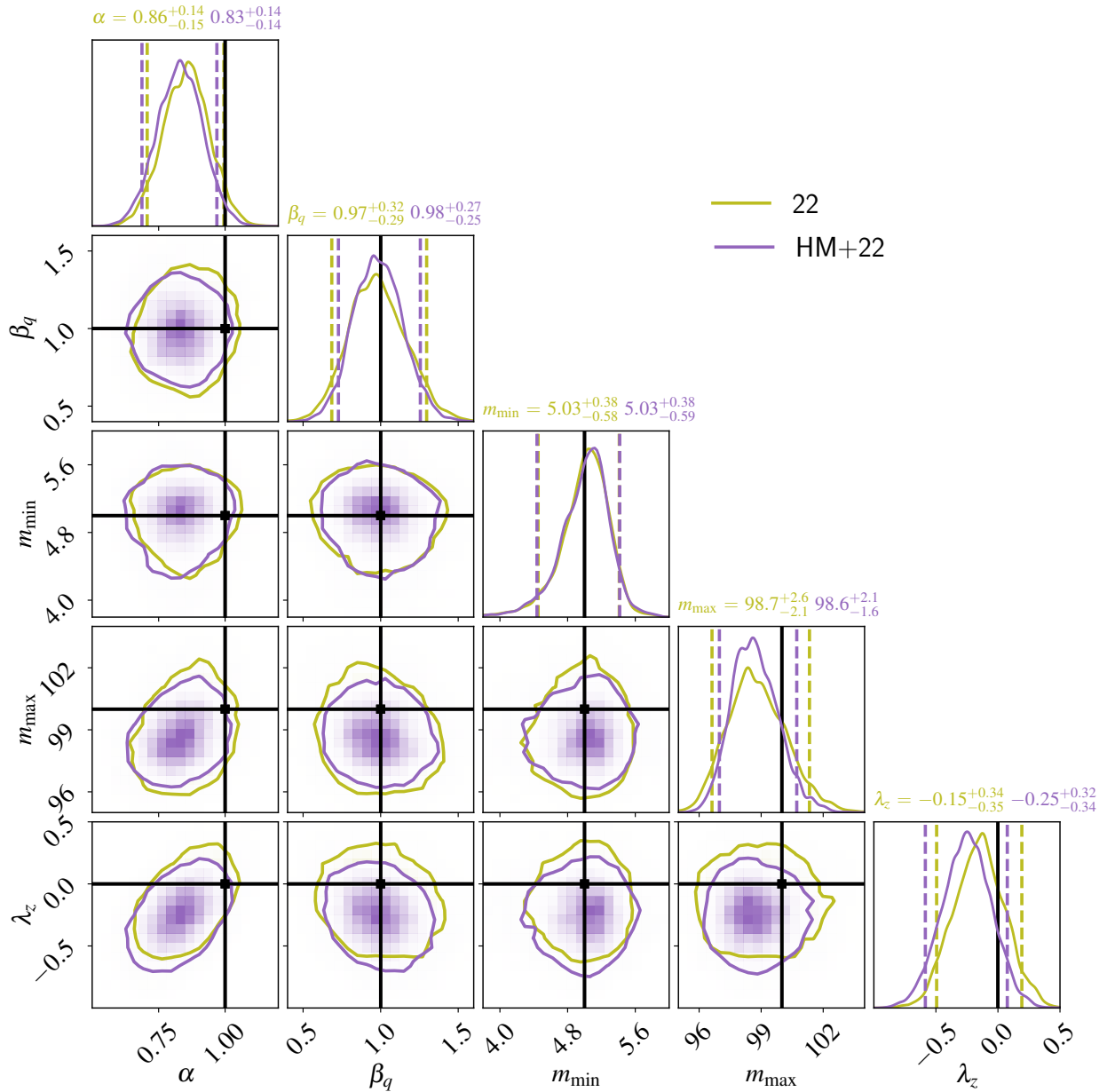


Figure 5.5: Two-dimensional posterior distributions along with the marginals of population hyper-parameters with (purple)/without (olive) using HMs in the hierarchical inference of 750 simulated GW events. Neglecting HMs does not induce any significant bias in inferring the population properties but including them leads to more precise estimates of hyper-parameters, especially  $m_{\max}$  and  $\beta_q$ . We also notice small biases in estimating  $\alpha$  and  $\lambda_z$  when HMs are considered.

replicate the exact data analysis procedure used to detect GW signals in real data, which will have non-Gaussian tails. We leave this study for the future.

We infer the population properties of the mass and redshift of BBH mergers using a GPU-accelerated population inference code `GWPopulation`<sup>37</sup>. Fig. 5.5 shows the posteriors as well as 2D probability distributions on various hyper-parameters. We find that the

<sup>37</sup> Colm Talbot, Rory Smith, Eric Thrane, and Gregory B. Poole. Parallelized inference for gravitational-wave astronomy. *Phys. Rev. D*, 100(4):043030, August 2019. DOI: 10.1103/PhysRevD.100.043030



population level parameters (especially  $m_{\max}$ ,  $\beta_q$ , and  $\lambda_z$ ) are more precisely measured when HMs are included in the analysis. However, we do not observe any significant bias in inferring the hyper-parameters when HMs are neglected. This can be understood from Fig. 5.3—the number of highly asymmetric (low  $q$  and near-edge-on inclination) BBH systems detected is rather scarce and the population is dominated by near-symmetric BBH mergers. This happens primarily due to two reasons. Firstly, the intrinsic population of BBHs is dominated by equal mass binaries. Secondly, we have an intrinsic selection effect against observing unequal mass binaries, since they emit weaker GW signals as compared to equal-mass binaries. Additionally, there is an extrinsic selection effect against detecting highly inclined systems as their overall observable GW amplitude is diminished.

In Fig. 5.5, note that while 1D posterior on hyper-parameter  $\alpha$  presents a small bias for both models (dominant mode only and multipolar), it is recovered within the 90% probability contours for 2D posterior distributions. Note that there is a  $\sim 10\%$  chance for the true value to be outside the 90% credible region of the posterior. So, the fact that we are not recovering the true value of one parameter among six is not totally unexpected. However, we see a slightly larger bias in the multipolar posterior (as compared to the dominant mode). This could be an artifact of the Poisson fluctuations due to using only one catalog of events (one realization of the observing scenario). Due to the computational costs involved, we are unable to create a new catalog of simulated events. Hence we tested this hypothesis by doing the hyper-parameter estimation on different sub-catalogs (subsets) of events drawn from our existing catalog of 750 simulated events. We do see random fluctuations in the posteriors estimated from different sub-catalogs, consistent with our broad expectations. However, this issue needs to be investigated in detail in the future.

As the number of detections increases, we will get more precise estimates of population properties. We speculated that even though the effect of neglecting subdominant modes in the parameter inference may not cause any significant biases in the source properties of individual binary systems, it could bias the inference of population properties when accumulated over many events. We test this by esti-

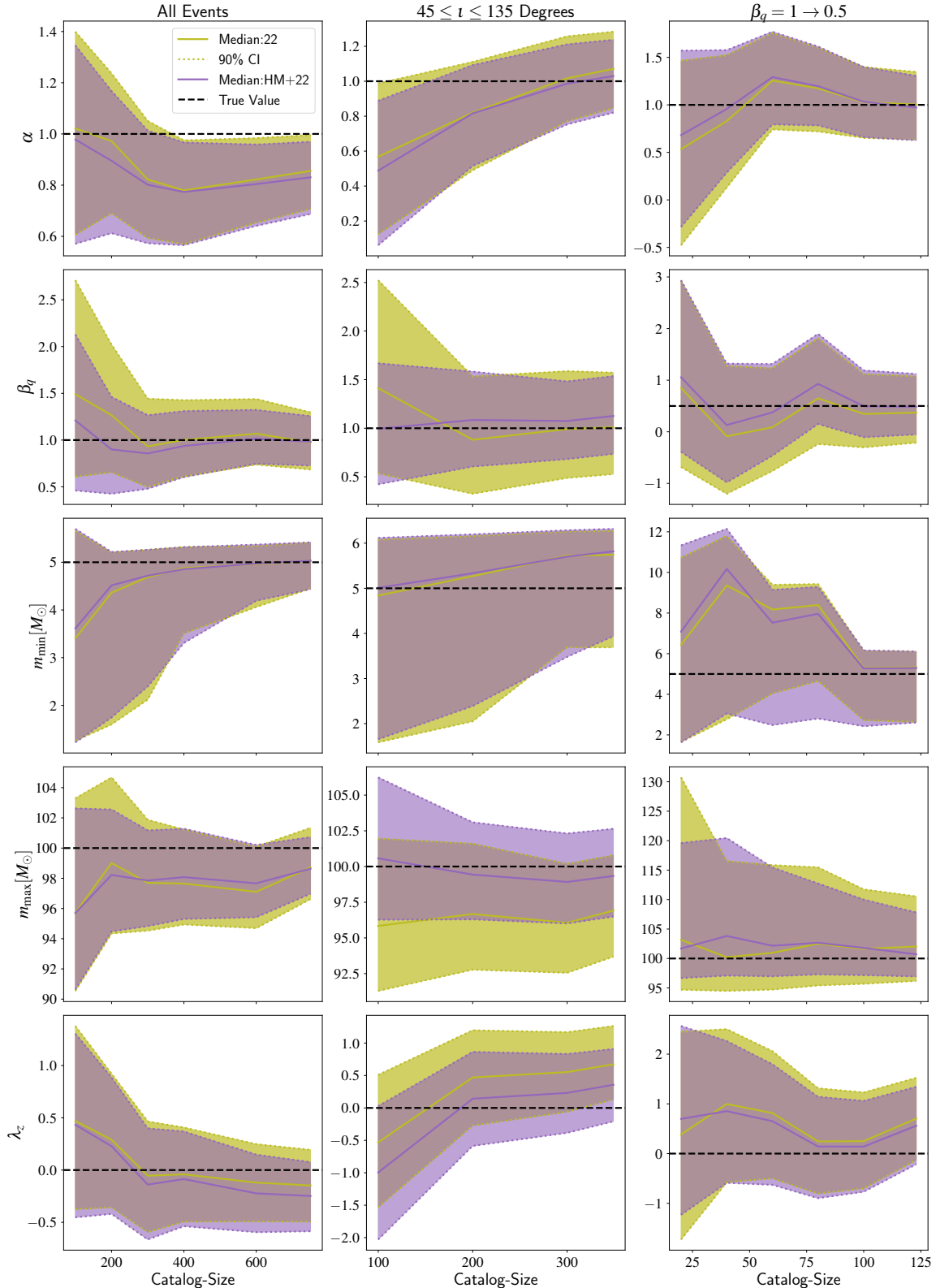


Figure 5.6: *The left panel:* the 90% width (between dotted lines) of the posteriors centered on the median values (solid lines) for various hyper-parameters as a function of catalog size (number of events in the catalog) when using all modes in the analysis (HM+22) along with only dominant mode (22) estimates. It is clear that there is some improvement in the statistical uncertainty in the hyper-posterior but we do not see any relative bias due to neglecting HMs. *The middle panel:* same thing as on the left but for injections with  $45 \leq \iota \leq 135$  degrees. The increased fraction of events that have an observable contribution from HMs leads to larger biases (still true value is within the 90% confidence interval) for  $m_{\max}$  and  $\beta_q$  when HMs are neglected. The hyper-parameter  $\lambda_z$  is biased (at 90% confidence interval) due to neglecting HMs. On the other hand, the inclusion of HMs leads to unbiased estimates of  $\lambda_z$ . *The right panel:* Same as the left panel, except that the true value for  $\beta_q$  is 0.5 (as opposed to  $\beta_q = 1$  in the left panel). This results in a larger fraction of asymmetric events (compared to the left panel), and still does not show any prominent biases. However, this might be limited by the smaller number of events ( $\sim 120$ ) in the catalog.

imating the errors in measuring the hyper-parameters as a function of the catalog size (the number of events detected). In the left panel of Fig. 5.6, we have plotted the 90% width of the hyper-parameter posteriors centered on median values as a function of the catalog size. The inference of hyper-parameters (statistical uncertainty) becomes more precise when the number of detections grows. However, even with the accumulation of small biases over  $\sim \mathcal{O}(700)$  events, we have not yet observed any significant bias in population-level parameters due to the neglect of subdominant modes in the analysis.

Note that the above conclusions are based on a single set of hyper-parameters used to generate the mock catalog of events. Ideally, one will have to repeat the population inference using different simulated values of hyper-parameters. Due to computational limitations, we leave this more exhaustive study for future work. However, we do partially investigate this by generating a population of simulated events corresponding to a new population model by selecting a subset of events from the original catalog using reweighting. We choose the mass-ratio hyper-parameter  $\beta_q = 0.5$  with the rest of the hyper-parameter values unchanged for the new model. This model will produce a larger fraction of asymmetric events but also does not differ drastically from the old model. We find  $\sim 120$  events detected for the new model out of 750 events from the old model. In the right panel of Fig. 5.6, we again plot the 90% CI of the hyper-posteriors along with median values as a function of catalog size. We do not find any strong indication of bias in the population inference when HMs are neglected in the analysis.

It will also be interesting to see how the bias in the population properties depends on the fraction of detected events that have a significant contribution from HMs. Since more inclined systems will have a higher contribution from HMs, we check if increasing the fraction of highly inclined binaries in the catalog changes the amount of bias. Specifically, we choose a subset of  $\sim 350$  out of 750 simulated GW events which have inclinations  $45 \leq \iota \leq 135$  degrees. Although a large fraction of the binaries are in this range, since highly inclined binaries are harder to detect than near-face-on configurations, the above inclination range includes only  $\sim 47\%$  of total detected events.

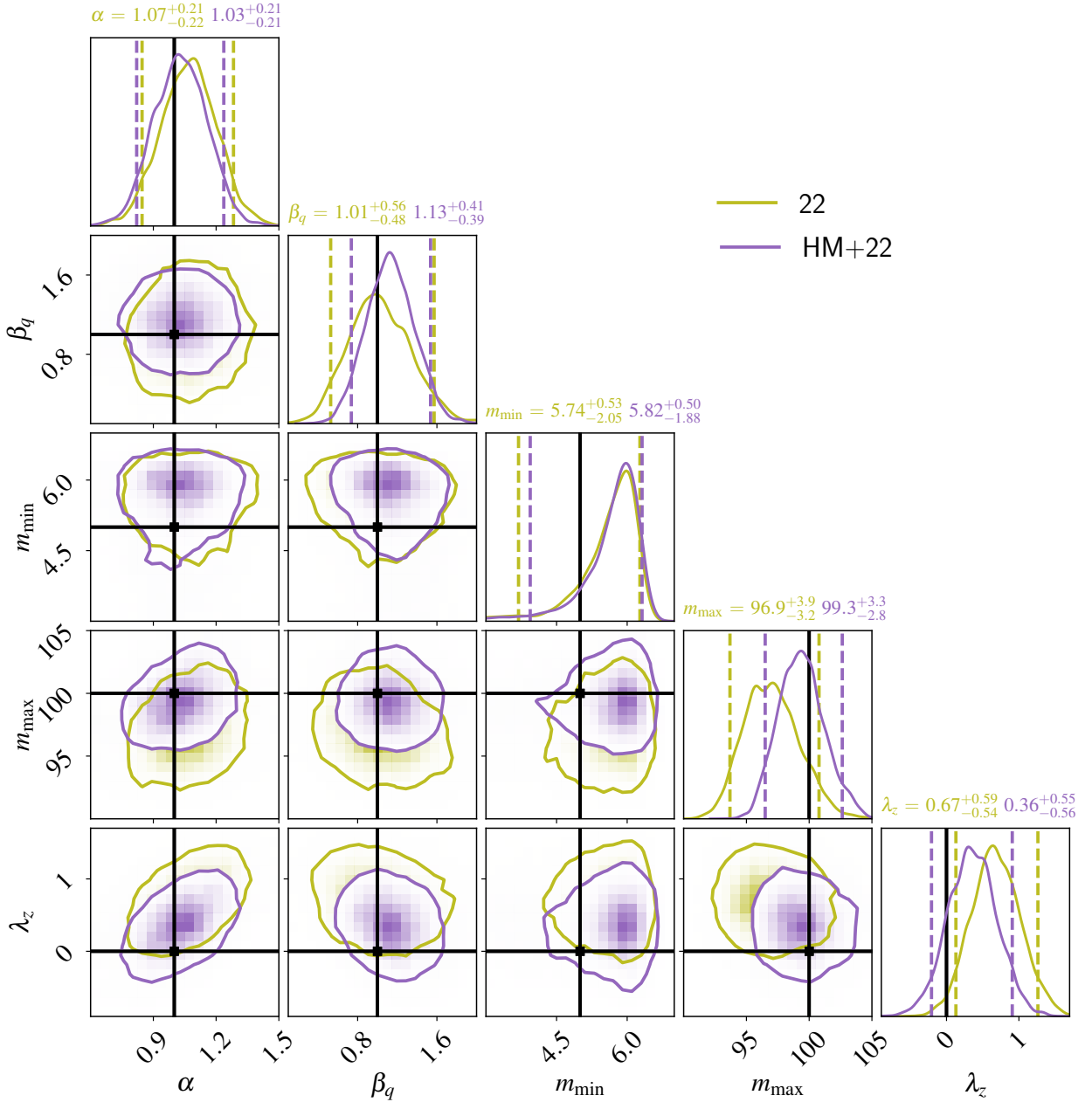
Confining the sub-population within a specified inclination range changes the underlying astrophysical distribution of inclinations, and

this should be accounted for while inferring population-level properties. For this purpose, we restrict the PE samples per event as well as injections for selection effects within the new inclination range to avoid any false biases. The hierarchical inference reveals notable biases in  $\beta_q$  and  $m_{\max}$  although the true value is within the 90% CI when subdominant modes are neglected in the analysis (see Fig. 5.7). The hyper-parameter  $\lambda_z$  is biased (at 90% CI) when HMs are neglected. However, including HMs recovers the true value of  $\lambda_z$ . We check the stability of this bias by creating multiple realizations by drawing events randomly from the subpopulation with replacement and find that population inference recovers  $\lambda_z$  (at 90% CI) when including the effect of HMs. The dominant mode analysis still leads to biased estimates. The hyper-parameters  $m_{\max}$  and  $\beta_q$  exhibit biases towards lower values when neglecting subdominant modes.

The dominant mode templates corresponding to lower masses and more asymmetric systems will have a longer duration in an attempt to mimic a more extended signal with HMs. Similarly, the bias in  $\lambda_z$  towards larger values shows the loss of SNR due to neglecting subdominant modes in the analysis. It is noteworthy that the absence of HMs in the parameter inference does not induce any bias in inferring the lower edge of BH mass spectrum  $m_{\min}$ , which can be explained by the fact that lighter systems are not expected to be asymmetric for HMs to play any significant role. If the true population (in nature) has a significant fraction of detectable asymmetric events, the population properties will incur significant biases upon neglecting HMs. Although we have not explored this, NSBH and massive binaries will be prone to this kind of systematics.

## 5.4 Summary and Outlook

While the dominant mode of gravitational radiation is quadrupolar, HMs can contribute to the signal when the binary is highly asymmetric or is in highly inclined orbits. Neglecting the effect of HMs in the parameter estimation of such binaries can cause considerable systematic biases in the inferred source parameters. Fortunately, such binaries are expected to be rare in the detected population, due to (expected) population properties and detector selection effects. However, one might wonder whether neglecting HMs will affect the in-



ference of *population* properties because this effectively involves the stacking of posteriors from individual events (and hence potentially adding up small biases).

In this work, we study the impact of neglecting higher-order modes in inferring population properties of BBH mergers. We find that, *if* the detected population of BBH mergers does not harbour a significant fraction of asymmetric systems (as predicted by standard population models), the inference of population hyper-parameters will not be biased due to neglecting subdominant modes, assuming an

Figure 5.7: Same as in Fig. 5.5 but the injections with  $45 \leq \iota \leq 135$  degrees. Increasing the fraction of events with observable contribution from HMs leads to larger bias in the estimates of hyper-parameters, especially, mass-ratio power-law spectral index  $\beta_q$ , maximum mass  $m_{\max}$  and merger rate evolution hyper-parameter  $\lambda_z$ .

observing scenario with Advanced LIGO-Virgo detectors (O4) containing not more than  $\sim 750$  observable events. It turns out that the accumulation of small biases over many mildly asymmetric systems is not significant enough to bias the inference of hyper-parameters. However, including the effect of HMs in the parameter estimation will lead to smaller statistical uncertainties on hyper-parameters. Additionally, if the detected population has a significant number of events that have detectable contributions from HMs, it can bias the maximum mass  $m_{\text{max}}$  of the BH, mass-ratio power-law spectral index  $\beta_q$ , and the merger rate evolution spectral index  $\lambda_z$ . This can limit our understanding of various astrophysical implications such as the existence of an upper mass gap in the BH mass spectrum, formation mechanisms of asymmetric compact binary mergers, and evolution of BBH merger rate as a function of redshift.

We list some caveats of this work: First, we neglected the effect of BH spins in this study. There are known correlations between the BH spin and mass ratio of the binary, which can reduce the precision in the estimation of hyper-parameters describing the mass ratio distribution of binaries. Second, we assume that the detector data is Gaussian, neglecting the effect of non-Gaussian tails in the data. Third, our conclusions are primarily based on simulation studies using one set of hyper-parameters. Fourth, we consider only one realization of the simulated catalog of BBH mergers and neglect the Poisson fluctuations expected in different realizations. Despite these limitations, we believe that this study provides a useful first understanding of the effect of neglecting HMs in the population inference.

The contribution of HMs is even more pronounced when the binary system has a high and misaligned spin, and when the orbit is non-circular (eccentric). We plan to do a follow-up analysis on the population inference of spinning BBH mergers and see if the inference of population properties improves with the inclusion of subdominant modes in the analysis. An unbiased inference of spin distribution is crucial for understanding the formation channels of compact binary mergers. Another parameter of interest could be eccentricity which could induce a bias in the inference of population properties if not accounted for in waveform models. We leave the study of the effect of neglecting eccentricity in waveform models on the estimation of hyper-parameters for future work.







## 6 | Summary and Outlook

In 2015, the direct detection of a GW signal from the merger of a BBH by LIGO detectors laid the foundation of a unique branch of astronomy. This detection not only verified the existence of GWs but also confirmed that compact objects, such as BHs, can exist in binaries and merge within the age of the universe. Since then, LIGO-Virgo detectors have observed  $\sim 90$  compact binary mergers. The detection of EM counterparts from one of the two BNS mergers has marked the beginning of the era of multimessenger astronomy with GWs. In the upcoming years, the LVK detectors with improved sensitivities will detect several hundred (and possibly thousands) GW signals, allowing for the precision probes of fundamental physics, astrophysics, and cosmology. This will require accurate modelling of detailed properties, such as precession, eccentricity, and subdominant modes of the GW radiation.

Chapter 2 discussed how gravitational radiation from a compact binary merger can be written as a multipole expansion. The leading order contribution to the gravitational radiation comes from the quadrupole mode. The subdominant modes are often neglected when modeling the radiation for data analysis purposes. However, they can contribute significantly to the signal if the binary system is highly asymmetric, e.g. has unequal masses, misaligned spins, etc. Therefore, neglecting HMs in modeling GW waveforms can lead to a loss in the detection of merging compact binaries as well as a biased inference of their source parameters. Both of these problems have been investigated extensively in the literature. These studies have demonstrated that including HMs in the waveform models will improve the detection sensitivity of the searches and provide an unbiased and accurate inference of the source properties of the merging binaries. However, this thesis explores the impact of HMs on improving the GW early warning as well as inferring population properties

of merging compact binaries.

GW early warning of compact binary mergers is very useful for the multimessenger follow-up. The joint GW-EM detection holds the potential to uncover the complex physics and astrophysics of the mergers, constrain the EoS of the matter at ultra-nuclear densities, and measure the cosmic expansion history. Moreover, an early warning will be useful in capturing any EM precursors and investigating the possible signatures of any intermediate merger products. Current GW early-warning efforts using the dominant mode of GW radiation are limited for heavy binary systems. In Chapter 3, we discuss how these limitations can be evaded to some extent with the use of HMs. We show that the inclusion of HMs can effectively increase the signal duration, attributed to the early entry of HMs in contrast to the dominant mode in the frequency band of the detectors, to significantly improve early detection and localization. We find that for significantly asymmetric compact binary mergers, such as NSBHs, the inclusion of the HMs in addition to dominant mode can improve the localization by a factor of  $\sim 3 - 4(5 - 6)$  as compared to when using only dominant mode in O5 (Voyager) observing scenario. The maximum early warning time gains due to the inclusion of HMs over dominant mode can be as large as 25(40) seconds for a fiducial localization of 1000 sq. deg. In 3G detectors, these time gains can be as large as a few minutes even for a localization sky area of 100 sq. deg. We also compute the improvement in the localization sky area due to HMs for a population of compact binary mergers consisting of BNSs and NSBHs. We find that  $\sim 30\%(40\%)$  binary systems distributed up to a limiting distance of 40Mpc will have a sky area reduction factor  $\gtrsim 2$  when considering HMs in addition to the dominant mode. This implies  $\sim 3$  NSBH detections in 2 years for the current optimistic NSBH rates.

The improvements in the localization sky area due to HMs may not always mean tight enough skymap. However, the large skymaps  $\mathcal{O}(1000)$  sq. deg. can be exploited by large field-of-view telescopes such as swift BAT, GBM, etc. A joint effort involving multiple telescopes can also cover these skymaps in a few pointings, especially when assisted by a galaxy catalog. The radio telescopes with wide FOV can also benefit from GW early warning.

The triangulation method does not take into account the consis-

tency of amplitudes and phases in different GW detectors and may overestimate the sky areas. Moreover, the Fisher matrix approximation will provide a lower bound to the sky area if the SNR of the GW signal is not sufficiently large ( $\rho \lesssim 10$ ). We are currently working on incorporating the effects of HMs in BAYESTAR, a rapid Bayesian inference tool to localize GW sources, to provide more robust estimates of sky areas in early warning.

In Chapter 4, we highlight that inclusion of HMs not only improves the early detection and sky-localization of compact binaries but also provides a better measurement of the luminosity distance and orbital inclination of the binaries. This will help astronomers to decide their follow-up strategies of whether the source would be worth following up on. For example, the observability of any beamed emission will crucially rely on breaking the degeneracy between the distance and inclination of the source. This can be done very efficiently with the inclusion of HMs. When the improvement in the luminosity distance is combined with the sky-localization, it can be translated to a reduction in the number of galaxies that could potentially host the merger in a localization volume. Inclusion of HMs might also improve the early-warning estimates of the mass ratio and spin. The existence of unbound ejecta, which determines the presence of the EM counterpart, in a merger depends, among others, on these parameters. Thus inclusion of HMs will improve our ability to predict the possible existence of an EM counterpart, thus aiding the follow-up strategies. This is left for a future study.

As the number of GW sources grows, it is interesting to infer their population properties, such as mass, spin, and merger rate distributions. This will be crucial in shedding some light on the formation channels of compact binary mergers, supernova physics, as well as stellar evolution in general. It is known that neglecting HMs can impact the inference of the source properties of individual binary mergers. In Chapter 5, we investigated the effect of neglecting HMs on the population inference of non-spinning BBH mergers. We find that neglecting HMs does not lead to biased estimates of the population properties of BBH mergers predicted by current models but can play a significant role if the fraction of events that will have a substantial observable contribution from HMs is sufficiently large. In that case, if one neglects the contribution from HMs, it would lead

to biased estimates of population properties that will further have an impact on the astrophysical and cosmological models of the formation and evolution of compact binaries. The current study assumed the non-spinning BH, Gaussian noise, one set of hyper-parameters, and only one realization of the simulated catalog. In the future, these assumptions should be relaxed to provide more robust conclusions. We also plan to explore the impact of neglecting eccentricity in the waveform models on the population inference.

# 7 | Appendix

## 7.1 Analytical Fisher matrix errors estimation

As discussed in section 4.2, the Fisher matrix provides a quadratic (Gaussian) approximation of the true Bayesian likelihood. While this might work for most cases, this might not provide a good approximation when the posteriors are multimodal, or when they have non-trivial shapes. We found that the Gaussian likelihood in  $\cos \iota - d_L$  provided by the Fisher matrix is not a good approximation of the true Bayesian likelihood for certain choices for  $\iota$  (Fig 7.1). This is especially the case for the analysis using only dominant mode when the true likelihood is significantly wide, due to correlations between parameters. When the HMs are included, this reduces the correlation between  $\iota - d_L$  and reduces the size of the likelihood, rendering the Gaussian approximation more accurate. We restrict our study to the values of  $\iota$  where the approximation is a reasonable one ( $\iota = 60$ ). To get an understanding of the deviation of Fisher matrix likelihood from the true likelihood at low inclination angles, we perform some analytical calculations for the Fisher matrix analysis with dominant mode.

For the dominant mode of GW radiation, the  $+$  and  $\times$  polarizations of a GW signal in frequency domain <sup>1</sup> can be written as

$$\tilde{h}_+(f) = \frac{1 + \cos^2 \iota}{2d_L} \tilde{h}_{22}(f; \vec{\lambda}), \quad (7.1)$$

$$\tilde{h}_\times(f) = \frac{-i}{d_L} (\cos \iota) \tilde{h}_{22}(f; \vec{\lambda}) \quad (7.2)$$

where  $\tilde{h}_{22}(f; \vec{\lambda})$  depends only on the intrinsic parameters of the source. The total signal is

$$\tilde{h}(f) = F_+ \tilde{h}_+(f) + F_\times \tilde{h}_\times(f), \quad (7.3)$$

<sup>1</sup> Ajit Kumar Mehta, Chandra Kant Mishra, Vijay Varma, and Parameswaran Ajith. Accurate inspiral-merger-ringdown gravitational waveforms for nonspinning black-hole binaries including the effect of subdominant modes. *Phys. Rev. D*, 96:124010, Dec 2017. doi: 10.1103/PhysRevD.96.124010. URL <https://link.aps.org/doi/10.1103/PhysRevD.96.124010>

where  $F_+(\alpha, \delta, \psi)$  and  $F_\times(\alpha, \delta, \psi)$  are antenna pattern functions of the detector. Considering only a single detector and substituting Eqs. (7.1) and (7.2) into Eq. (7.3), we get

$$\tilde{h}(f) = \frac{e^{-\ln d_L}}{2} \left[ (1 + \cos^2 \iota) F_+ - i(2 \cos \iota) F_\times \right] \tilde{h}_{22}(f; \vec{\lambda}). \quad (7.4)$$

Evaluating Fisher matrix (FM) requires the computation of derivatives of the waveform with respect to the parameters. Assuming the parameterization  $(\ln d_L, \cos \iota)$ , we calculate the derivatives of  $\tilde{h}(f)$  as

$$\tilde{h}_{(\ln d_L)}(f) = \partial_{(\ln d_L)} \tilde{h}(f) = -\frac{e^{-\ln d_L}}{2} \left[ (1 + \cos^2 \iota) F_+ - i(2 \cos \iota) F_\times \right] \tilde{h}_{22}(f; \vec{\lambda}) \quad (7.5)$$

$$\tilde{h}_{(\cos \iota)}(f) = \partial_{(\cos \iota)} \tilde{h}(f) = \frac{e^{-\ln d_L}}{2} [(2 \cos \iota) F_+ - 2i F_\times] \tilde{h}_{22}(f; \vec{\lambda}) \quad (7.6)$$

The FM elements for  $\ln d_L$  and  $\cos \iota$  are

$$F_{(\ln d_L)(\ln d_L)} = \left( h_{(\ln d_L)}(f) \middle| h_{(\ln d_L)}(f) \right) = A \frac{e^{-2 \ln d_L}}{4} \times \left[ (1 + \cos^2 \iota)^2 F_+^2 + (2 \cos \iota)^2 F_\times^2 \right] \quad (7.7)$$

where  $A = \left( \tilde{h}_{22}(f; \vec{\lambda}) \middle| \tilde{h}_{22}(f; \vec{\lambda}) \right)$  is constant throughout our estimates of FM elements since it depends only on intrinsic parameters which are fixed. Similarly,

$$F_{(\ln d_L)(\cos \iota)} = \left( h_{(\ln d_L)}(f) \middle| h_{(\cos \iota)}(f) \right) = -A \frac{e^{-2 \ln d_L}}{4} (2 \cos \iota) \times \left[ (1 + \cos^2 \iota) F_+^2 + 2 F_\times^2 \right] = F_{(\cos \iota)(\ln d_L)}, \quad (7.8)$$

and

$$F_{(\cos \iota)(\cos \iota)} = A \frac{e^{-2 \ln d_L}}{4} \left[ (2 \cos \iota)^2 F_+^2 + (2 F_\times)^2 \right] \quad (7.9)$$

The FM is given as

$$F = \begin{pmatrix} F_{(\ln d_L)(\ln d_L)} & F_{(\ln d_L)(\cos \iota)} \\ F_{(\ln d_L)(\cos \iota)} & F_{(\cos \iota)(\cos \iota)} \end{pmatrix}. \quad (7.10)$$

We have to invert the above matrix to get the covariance matrix ( $\Sigma$ ) which will render the errors and correlations between different parameters. Let us calculate the determinant of  $F$ , i.e.  $|F|$  or  $\det(F)$ , to

find out if  $F$  is invertible.

$$|F| = \det(F) = 4F_+^2 F_\times^2 (1 - \cos^2 \iota)^2 \quad (7.11)$$

Therefore, it is clear that  $|F| \neq 0$  in general (except for  $\iota = 0$ ). The covariance matrix ( $\Sigma$ ) is given as

$$\Sigma = \frac{Ad_L^2}{F_+^2 F_\times^2 (1 - \cos^2 \iota)^2} \begin{pmatrix} F_\times^2 + (\cos^2 \iota) F_+^2 & 2F_\times^2 + (1 + \cos^2 \iota) F_+^2 \\ 2F_\times^2 + (1 + \cos^2 \iota) F_+^2 & 4(\cos^2 \iota) F_\times^2 + (1 + \cos^2 \iota)^2 F_+^2 \end{pmatrix} \quad (7.12)$$

The term in the denominator  $(1 - \cos^2 \iota)^2$  is a increasing function of  $\iota \in [0, \pi/2]$ . This is the dominating term which governs the overall increasing behaviour of all the covariance matrix elements (the errors and correlations) at low inclinations  $\iota \lesssim 50$  deg. (see left plot in Fig. ??). Focusing on errors in  $\ln d_L$  and  $\cos \iota$  the expressions are given by

$$\sigma_{\ln d_L} = \frac{\sqrt{Ad_L}}{F_+ F_\times (1 - \cos^2 \iota)} \sqrt{F_\times^2 + (\cos^2 \iota) F_+^2} \quad (7.13)$$

and

$$\sigma_{\cos \iota} = \frac{\sqrt{Ad_L}}{F_+ F_\times (1 - \cos^2 \iota)} \sqrt{4(\cos^2 \iota) F_\times^2 + (1 + \cos^2 \iota)^2 F_+^2} \quad (7.14)$$

which diverge at  $\iota \sim 0$ . Inclusion of HMs will not lead to divergence factor  $(1 - \cos^2 \iota)$  in the denominator of errors and correlations hence the Fisher matrix is a good approximation to the true likelihood even at low values of inclination angle (see right plot in Fig. 7.1).

## 7.2 Confidence interval calculation

A multivariate Gaussian distribution in  $N$  dimensions is given by

$$p(\vec{x}) = \mathcal{N} \exp \left[ -\frac{1}{2} (\vec{x} - \vec{\mu})^T \Sigma^{-1} (\vec{x} - \vec{\mu}) \right] \quad (7.15)$$

when positions  $\vec{x} = \{x_1, x_2, \dots, x_N\}$  and mean  $\vec{\mu} = \{\mu_1, \mu_2, \dots, \mu_N\}$  are given. When the covariance matrix  $\Sigma$  is non-singular, it can be diagonalized to render the distribution as

$$p(\vec{x}) = \mathcal{N} \exp \left[ -\sum_{i=1}^N \frac{(x_i - \mu_i)^2}{2\sigma_i^2} \right] \quad (7.16)$$

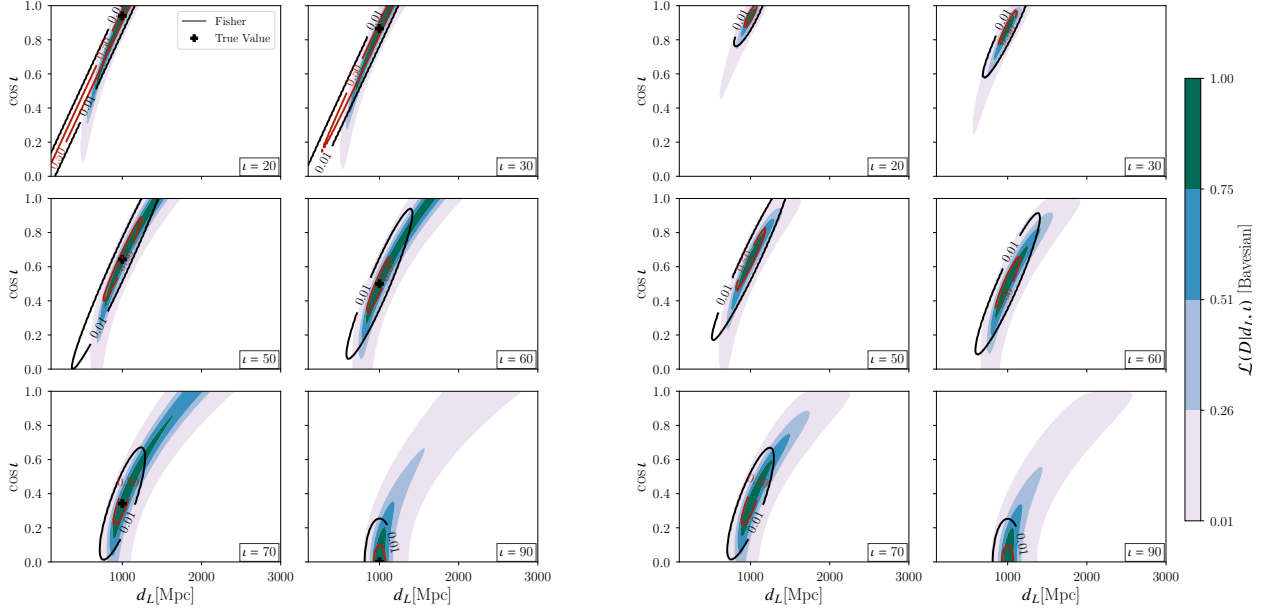


Figure 7.1: Fisher and Bayesian likelihood comparison in distance and inclination angle plane while varying inclination angle with only dominant mode (left) and multipolar (right) waveform.

where  $\sigma_i^2$ 's are the eigenvalues of the covariance matrix  $\Sigma$ . The aim is to find the  $C\%$  confidence region of this multivariate distribution. Let us look at this problem in 3-dimensions. The probability density is

$$p(x, y, z) = \frac{1}{(2\pi)^{3/2} \sigma_x \sigma_y \sigma_z} \exp \left[ -\frac{(x - \mu_x)^2}{2\sigma_x^2} - \frac{(y - \mu_y)^2}{2\sigma_y^2} - \frac{(z - \mu_z)^2}{2\sigma_z^2} \right] \quad (7.17)$$

To estimate the volume of the ellipsoid at a particular confidence interval, we have to perform the integration on ellipsoidal symmetry. Just to estimate the scaling factor  $\beta_3$  of different principle axes, let us choose the parametrization as follows:

$$x = \mu_x + \sigma_x r \sin \theta \cos \phi \quad (7.18)$$

$$y = \mu_y + \sigma_y r \sin \theta \sin \phi \quad (7.19)$$

$$z = \mu_z + \sigma_z r \cos \theta \quad (7.20)$$

where  $r > 0$  parametrizes the concentric ellipsoids,  $\theta$  and  $\phi$  are spherical polar angles. The volume element in these coordinates can be written as  $dV = \sigma_x \sigma_y \sigma_z r^2 \sin \theta dr d\theta d\phi$ . In these coordinates, Eq. (7.17) reduces to

$$p(r, \theta, \phi) = \frac{1}{(2\pi)^{3/2}} e^{-r^2/2} \quad (7.21)$$



Let us assume that sphere of radius  $\beta_3$  encloses a probability  $C$ , then

$$C = \frac{1}{(2\pi)^{3/2}} \int_0^{\beta_3} r^2 dr \int_0^\pi \sin \theta d\theta \int_0^{2\pi} d\phi e^{-r^2/2} \quad (7.22)$$

Or

$$C = \sqrt{\frac{2}{\pi}} \int_0^{\beta_3} r^2 dr e^{-r^2/2} \quad (7.23)$$

Or

$$C = \sqrt{\frac{2}{\pi}} \left[ \int_0^{\beta_3} dr e^{-r^2/2} - \int_0^{\beta_3} d(re^{-r^2/2}) \right] \quad (7.24)$$

Or

$$C = \operatorname{erf} \left( \frac{\beta_3}{\sqrt{2}} \right) - \sqrt{\frac{2}{\pi}} \left( \beta_3 e^{-\beta_3^2/2} \right) \quad (7.25)$$

This transcendental equation can be solved for  $\beta_3$  numerically, given the probability value  $C$ . Table (7.1) shows the values of  $\beta_3$  at various credible intervals  $C$ . Thus, the volume of the ellipsoid at confidence  $C$  will be

$$\Delta V_{C\%} = \frac{4}{3} \pi \beta_3^3 (\sigma_x \sigma_y \sigma_z) = \frac{4}{3} \pi \beta_3^3 \sqrt{\det(\Sigma)} \quad (7.26)$$

where  $\det(\Sigma)$  is the determinant of the covariance matrix  $\Sigma$ .

Confidence (C)	$\sigma$ -values	$\beta_1$ (1-D)	$\beta_2$ (2-D)	$\beta_3$ (3-D)
0.20	$0.25\sigma$	0.25	0.668	1.005
0.683	$1.0\sigma$	1.0	1.516	1.879
0.90	$1.6\sigma$	1.6	2.146	2.500
0.99	$2.6\sigma$	2.6	3.035	3.368

Table 7.1: Ellipsoid/ellipse axes scaling factor ( $\beta_q$ ) values at various credible intervals in  $q$ -dimensions [128, 81]



## 8 | Publications

### *Publications relevant to the thesis*

- **M. K. Singh**, S. J. Kapadia, A. Vijaykumar, P. Ajith, *Impact of higher harmonics of gravitational radiation on the population inference of binary black holes*, arXiv:2312.07376 (2023), Accepted in ApJ
- **M. K. Singh**, Divyajyoti, S. J. Kapadia, M.A. Shaikh, P. Ajith, *Improved early-warning estimates of luminosity distance and orbital inclination of compact binary mergers using higher modes of gravitational radiation*, MNRAS, Vol. 513, Iss. 3, pages 3798-3809 (2022), arXiv: 2202.05802
- **M. K. Singh**, S. J. Kapadia, M.A. Shaikh, D. Chatterjee, P. Ajith, *Improved early warning of compact binary mergers using higher modes of gravitational radiation: a population study*, MNRAS, Vol. 502, Iss. 2, pages 1612-1622 (2021), arXiv: 2010.12407
- S. J. Kapadia, **M. K. Singh**, M. A. Shaikh, D. Chatterjee, P. Ajith, *Of Harbingers and Higher Modes: Improved gravitational-wave early-warning of compact binary mergers*, The Astrophysical Journal Letters, Vol. 898, L39, No. 2 (2020), arXiv: 2005.08830

### *Other publications*

- **M. K. Singh**, S. J. Kapadia, S. Basak, P. Ajith, S. P. Tendulkar, *Associating fast radio bursts with compact binary mergers via gravitational lensing*, MNRAS, 527, 2, 4234-4243 (2023), arXiv:2304.02879
- S. Magare, S. J. Kapadia, A. More, **M. K. Singh**, P. Ajith, A. N. Ramprakash, *Gear-up for the Action Replay: Leveraging Lensing for Enhanced Gravitational-Wave Early-Warning*, ApJL 955 L31 (2023), arXiv: 2302.02916



# Bibliography

- [1] J Aasi et al. Advanced LIGO. *Classical and Quantum Gravity*, 32(7):074001, mar 2015. DOI: 10.1088/0264-9381/32/7/074001. URL <https://doi.org/10.1088/0264-9381/32/7/074001>.
- [2] B. P. Abbott, R. Abbott, T. D. Abbott, M. R. Abernathy, F. Acernese, K. Ackley, C. Adams, and et al. Observation of gravitational waves from a binary black hole merger. *Physical Review Letters*, 116(6): 061102, 2016. DOI: 10.1103/PhysRevLett.116.061102.
- [3] B. P. Abbott, R. Abbott, T. D. Abbott, LIGO Scientific Collaboration, and Virgo Collaboration. Binary Black Hole Population Properties Inferred from the First and Second Observing Runs of Advanced LIGO and Advanced Virgo. *ApJ*, 882(2):L24, September 2019. DOI: 10.3847/2041-8213/ab3800.
- [4] B. P. Abbott et al. Properties of the binary black hole merger gw150914. *Phys. Rev. Lett.*, 116: 241102, Jun 2016. DOI: 10.1103/PhysRevLett.116.241102. URL <https://link.aps.org/doi/10.1103/PhysRevLett.116.241102>.
- [5] B P Abbott et al. Exploring the sensitivity of next generation gravitational wave detectors. *Classical and Quantum Gravity*, 34(4):044001, jan 2017. DOI: 10.1088/1361-6382/aa51f4. URL <https://doi.org/10.1088/1361-6382/aa51f4>.
- [6] B. P. Abbott et al. A gravitational-wave standard siren measurement of the Hubble constant. *Nature*, 551(7678):85–88, November 2017. DOI: 10.1038/nature24471.
- [7] B. P. Abbott et al. Multi-messenger Observations of a Binary Neutron Star Merger. *Astrophys. J.*, 848 (2):L12, 2017. DOI: 10.3847/2041-8213/aa91c9.
- [8] B. P. Abbott et al. GW170817: Measurements of Neutron Star Radii and Equation of State. *Phys. Rev. Lett.*, 121(16):161101, October 2018. DOI: 10.1103/PhysRevLett.121.161101.
- [9] B. P. Abbott et al. Prospects for observing and localizing gravitational-wave transients with Advanced LIGO, Advanced Virgo and KAGRA. *Living Reviews in Relativity*, 21(1):3, April 2018. DOI: 10.1007/s41114-018-0012-9.
- [10] B. P. Abbott et al. Properties of the Binary Neutron Star Merger GW170817. *Physical Review X*, 9: 011001, Jan 2019. DOI: 10.1103/PhysRevX.9.011001.

- [11] B. P. Abbott et al. Tests of general relativity with gw170817. *Phys. Rev. Lett.*, 123:011102, Jul 2019. DOI: 10.1103/PhysRevLett.123.011102. URL <https://link.aps.org/doi/10.1103/PhysRevLett.123.011102>.
- [12] B. P. Abbott et al. Low-latency Gravitational-wave Alerts for Multimessenger Astronomy during the Second Advanced LIGO and Virgo Observing Run. *ApJ*, 875(2):161, April 2019. DOI: 10.3847/1538-4357/ab0e8f.
- [13] B. P. Abbott et al. GWTC-1: A Gravitational-Wave Transient Catalog of Compact Binary Mergers Observed by LIGO and Virgo during the First and Second Observing Runs. *Phys. Rev. X*, 9(3):031040, 2019. DOI: 10.1103/PhysRevX.9.031040.
- [14] B. P. Abbott et al. *arXiv e-prints*, art. arXiv:2001.01761, January 2020.
- [15] Benjamin P. Abbott et al. GW170817: Observation of gravitational waves from a binary neutron star inspiral. *Phys. Rev. Lett.*, 119:161101, 2017. DOI: 10.1103/PhysRevLett.119.161101.
- [16] R. Abbott, T. D. Abbott, et al. Population properties of compact objects from the second LIGO–virgo gravitational-wave transient catalog. *The Astrophysical Journal Letters*, 913(1):L7, may 2021. DOI: 10.3847/2041-8213/abe949. URL <https://doi.org/10.3847/2041-8213/abe949>.
- [17] R. Abbott et al. Gw190412: Observation of a binary-black-hole coalescence with asymmetric masses. *Phys. Rev. D*, 102:043015, Aug 2020. DOI: 10.1103/PhysRevD.102.043015. URL <https://link.aps.org/doi/10.1103/PhysRevD.102.043015>.
- [18] R. Abbott et al. Gw190521: A binary black hole merger with a total mass of  $150 M_{\odot}$ . *Phys. Rev. Lett.*, 125:101102, Sep 2020. DOI: 10.1103/PhysRevLett.125.101102. URL <https://link.aps.org/doi/10.1103/PhysRevLett.125.101102>.
- [19] R. Abbott et al. GW190814: Gravitational waves from the coalescence of a 23 solar mass black hole with a 2.6 solar mass compact object. *The Astrophysical Journal*, 896(2):L44, jun 2020. DOI: 10.3847/2041-8213/ab960f. URL <https://doi.org/10.3847/2041-8213/ab960f>.
- [20] R. Abbott et al. GWTC-2: Compact Binary Coalescences Observed by LIGO and Virgo During the First Half of the Third Observing Run. *arXiv e-prints*, art. arXiv:2010.14527, October 2020.
- [21] R. Abbott et al. GWTC-3: Compact Binary Coalescences Observed by LIGO and Virgo During the Second Part of the Third Observing Run. *arXiv e-prints*, art. arXiv:2111.03606, November 2021.
- [22] Ernazar Abdikamalov, Giulia Pagliaroli, and David Radice. Gravitational Waves from Core-Collapse Supernovae. 10 2020. DOI: 10.1007/978-981-15-4702-7\_21-1.
- [23] F Acernese et al. Advanced virgo: a second-generation interferometric gravitational wave detector. *Classical and Quantum Gravity*, 32(2):024001, dec 2015. DOI: 10.1088/0264-9381/32/2/024001. URL <https://doi.org/10.1088/0264-9381/32/2/024001>.

- [24] T Adams et al. Low-latency analysis pipeline for compact binary coalescences in the advanced gravitational wave detector era. *Classical and Quantum Gravity*, 33(17):175012, aug 2016. DOI: 10.1088/0264-9381/33/17/175012. URL <https://doi.org/10.1088/0264-9381/33/17/175012>.
- [25] P. A. R. Ade and et al. Detection of b-mode polarization at degree angular scales by bicep2. *Physical Review Letters*, 112(24), 2014. DOI: 10.1103/PhysRevLett.112.241101.
- [26] R X Adhikari et al. Astrophysical science metrics for next-generation gravitational-wave detectors. *Classical and Quantum Gravity*, 36(24):245010, nov 2019. DOI: 10.1088/1361-6382/ab3cff. URL <https://doi.org/10.1088/1361-6382/ab3cff>.
- [27] N. Aghanim et al. Planck 2018 results. VI. Cosmological parameters. *Astron. Astrophys.*, 641:A6, 2020. DOI: 10.1051/0004-6361/201833910. [Erratum: *Astron. Astrophys.* 652, C4 (2021)].
- [28] P. Ajith and Sukanta Bose. Estimating the parameters of nonspinning binary black holes using ground-based gravitational-wave detectors: Statistical errors. *Phys. Rev. D*, 79:084032, Apr 2009. DOI: 10.1103/PhysRevD.79.084032. URL <https://link.aps.org/doi/10.1103/PhysRevD.79.084032>.
- [29] P. Ajith et al. A Template bank for gravitational waveforms from coalescing binary black holes. I. Non-spinning binaries. *Phys. Rev. D*, 77:104017, 2008. DOI: 10.1103/PhysRevD.77.104017. [Erratum: *Phys. Rev. D* 79, 129901 (2009)].
- [30] Sarp Akcay. Forecasting gamma-ray bursts using gravitational waves. *Annalen der Physik*, 531(1):1800365, 2019. DOI: <https://doi.org/10.1002/andp.201800365>. URL <https://onlinelibrary.wiley.com/doi/abs/10.1002/andp.201800365>.
- [31] A. Akmal, V. R. Pandharipande, and D. G. Ravenhall. Equation of state of nucleon matter and neutron star structure. *Phys. Rev. C*, 58:1804–1828, Sep 1998. DOI: 10.1103/PhysRevC.58.1804. URL <https://link.aps.org/doi/10.1103/PhysRevC.58.1804>.
- [32] and LIGO Scientific Collaboration, Virgo Collaboration, et al. Properties and Astrophysical Implications of the 150  $M_{\odot}$  Binary Black Hole Merger GW190521. *ApJ*, 900(1):L13, September 2020. DOI: 10.3847/2041-8213/aba493.
- [33] S. Antier et al. GRANDMA observations of advanced LIGO’s and advanced Virgo’s third observational campaign. *MNRAS*, 497(4):5518–5539, June 2020. DOI: 10.1093/mnras/staa1846.
- [34] K. G. Arun, Bala R. Iyer, B. S. Sathyaprakash, Siddhartha Sinha, and Chris Van Den Broeck. Higher signal harmonics, lisa’s angular resolution, and dark energy. *Phys. Rev. D*, 76:104016, Nov 2007. DOI: 10.1103/PhysRevD.76.104016. URL <https://link.aps.org/doi/10.1103/PhysRevD.76.104016>.
- [35] K. G. Arun, Alessandra Buonanno, Guillaume Faye, and Evan Ochsner. Higher-order spin effects in the amplitude and phase of gravitational waveforms emitted by inspiraling compact bi-

- naries: Ready-to-use gravitational waveforms. *Phys. Rev. D*, 79:104023, 2009. DOI: 10.1103/PhysRevD.79.104023. [Erratum: Phys.Rev.D 84, 049901 (2011)].
- [36] K. G. Arun, Hideyuki Tagoshi, Archana Pai, and Chandra Kant Mishra. Synergy of short gamma ray burst and gravitational wave observations: Constraining the inclination angle of the binary and possible implications for off-axis gamma ray bursts. *Phys. Rev. D*, 90:024060, Jul 2014. DOI: 10.1103/PhysRevD.90.024060. URL <https://link.aps.org/doi/10.1103/PhysRevD.90.024060>.
- [37] K. G. Arun, Hideyuki Tagoshi, Archana Pai, and Chandra Kant Mishra. Synergy of short gamma ray burst and gravitational wave observations: Constraining the inclination angle of the binary and possible implications for off-axis gamma ray bursts. *Phys. Rev. D*, 90:024060, Jul 2014. DOI: 10.1103/PhysRevD.90.024060. URL <https://link.aps.org/doi/10.1103/PhysRevD.90.024060>.
- [38] K.G. Arun, Luc Blanchet, Bala R. Iyer, and Moh'd S.S. Qusailah. The 2.5PN gravitational wave polarisations from inspiralling compact binaries in circular orbits. *Class. Quant. Grav.*, 21:3771–3802, August 2004. DOI: 10.1088/0264-9381/21/15/010. [Erratum: Class. Quant. Grav. 22, 3115 (2005)].
- [39] Gregory Ashton, Moritz Hübner, Paul D. Lasky, Colm Talbot, Kendall Ackley, Sylvia Biscoveanu, Qi Chu, Atul Divakarla, Paul J. Easter, Boris Goncharov, Francisco Hernandez Vivanco, Jan Harms, Marcus E. Lower, Grant D. Meadors, Denyz Melchor, Ethan Payne, Matthew D. Pitkin, Jade Powell, Nikhil Sarin, Rory J. E. Smith, and Eric Thrane. BILBY: A User-friendly Bayesian Inference Library for Gravitational-wave Astronomy. *ApJS*, 241(2):27, April 2019. DOI: 10.3847/1538-4365/ab06fc.
- [40] John G. Baker, Joan Centrella, Dae-Il Choi, Michael Koppitz, and James van Meter. Gravitational-wave extraction from an inspiraling configuration of merging black holes. *Phys. Rev. Lett.*, 96:111102, Mar 2006. DOI: 10.1103/PhysRevLett.96.111102. URL <https://link.aps.org/doi/10.1103/PhysRevLett.96.111102>.
- [41] Z. Barkat, G. Rakavy, and N. Sack. Dynamics of supernova explosion resulting from pair formation. *Phys. Rev. Lett.*, 18:379–381, Mar 1967. DOI: 10.1103/PhysRevLett.18.379. URL <https://link.aps.org/doi/10.1103/PhysRevLett.18.379>.
- [42] Imène Belahcene. *Searching for gravitational waves produced by cosmic strings in LIGO-Virgo data*. Theses, Université Paris Saclay (COMUE), October 2019. URL <https://theses.hal.science/tel-02878783>.
- [43] Eric C. Bellm et al. The Zwicky Transient Facility: System Overview, Performance, and First Results. *PASP*, 131(995):018002, January 2019. DOI: 10.1088/1538-3873/aaecbe.
- [44] Emanuele Berti, Alessandra Buonanno, and Clifford M. Will. Estimating spinning binary parameters and testing alternative theories of gravity with lisa. *Phys. Rev. D*, 71:084025, Apr 2005. DOI: 10.1103/PhysRevD.71.084025. URL <https://link.aps.org/doi/10.1103/PhysRevD.71.084025>.



- [45] Luc Blanchet. Gravitational radiation from postNewtonian sources and inspiraling compact binaries. *Living Rev. Rel.*, 5:3, 2002. DOI: 10.12942/lrr-2002-3.
- [46] Luc Blanchet. Gravitational Radiation from Post-Newtonian Sources and Inspiralling Compact Binaries. *Living Rev. Rel.*, 17:2, 2014. DOI: 10.12942/lrr-2014-2.
- [47] Luc Blanchet and Guillaume Faye. General relativistic dynamics of compact binaries at the third postNewtonian order. *Phys. Rev. D*, 63:062005, 2001. DOI: 10.1103/PhysRevD.63.062005.
- [48] Luc Blanchet and Bala R. Iyer. Hadamard regularization of the third post-Newtonian gravitational wave generation of two point masses. *Phys. Rev. D*, 71:024004, 2005. DOI: 10.1103/PhysRevD.71.024004.
- [49] Luc Blanchet, Thibault Damour, and Bala R. Iyer. Gravitational waves from inspiralling compact binaries: Energy loss and wave form to second postNewtonian order. *Phys. Rev. D*, 51:5360, 1995. DOI: 10.1103/PhysRevD.51.5360. [Erratum: *Phys.Rev.D* 54, 1860 (1996)].
- [50] Luc Blanchet, Thibault Damour, Bala R. Iyer, Clifford M. Will, and Alan G. Wiseman. Gravitational radiation damping of compact binary systems to second postNewtonian order. *Phys. Rev. Lett.*, 74: 3515–3518, 1995. DOI: 10.1103/PhysRevLett.74.3515.
- [51] Luc Blanchet, Guillaume Faye, Bala R. Iyer, and Benoit Joguet. Gravitational-wave inspiral of compact binary systems to  $7/2$  post-newtonian order. *Phys. Rev. D*, 65:061501(R), 2002. DOI: 10.1103/PhysRevD.71.129902. Erratum-ibid 71, 129902(E) (2005).
- [52] Luc Blanchet, Bala R. Iyer, and Benoit Joguet. Gravitational waves from inspiralling compact binaries: Energy flux to third post-newtonian order. *Phys. Rev. D*, 65:064005, 2002. DOI: 10.1103/PhysRevD.65.064005. Erratum-ibid 71, 129903(E) (2005).
- [53] Luc Blanchet, Thibault Damour, and Gilles Esposito-Farese. Dimensional regularization of the third postNewtonian dynamics of point particles in harmonic coordinates. *Phys. Rev. D*, 69:124007, 2004. DOI: 10.1103/PhysRevD.69.124007.
- [54] Luc Blanchet, Thibault Damour, Gilles Esposito-Farèse, and Bala R. Iyer. Gravitational radiation from inspiralling compact binaries completed at the third post-newtonian order. *Phys. Rev. Lett.*, 93: 091101, 2004. DOI: 10.1103/PhysRevLett.93.091101.
- [55] Luc Blanchet, Thibault Damour, Gilles Esposito-Farese, and Bala R. Iyer. Dimensional regularization of the third post-Newtonian gravitational wave generation from two point masses. *Phys. Rev. D*, 71: 124004, 2005. DOI: 10.1103/PhysRevD.71.124004.
- [56] Luc Blanchet, Alessandra Buonanno, and Guillaume Faye. Higher-order spin effects in the dynamics of compact binaries. II. Radiation field. *Phys. Rev. D*, 74:104034, 2006. DOI: 10.1103/PhysRevD.81.089901. [Erratum: *Phys.Rev.D* 75, 049903 (2007), Erratum: *Phys.Rev.D* 81, 089901 (2010)].

- [57] Luc Blanchet, Guillaume Faye, Bala R. Iyer, and Siddhartha Sinha. The Third post-Newtonian gravitational wave polarisations and associated spherical harmonic modes for inspiralling compact binaries in quasi-circular orbits. *Class. Quant. Grav.*, 25:165003, August 2008. DOI: 10.1088/0264-9381/25/16/165003. [Erratum: *Class. Quant. Grav.* 29, 239501 (2012)].
- [58] Luc Blanchet, Alessandra Buonanno, and Guillaume Faye. Tail-induced spin-orbit effect in the gravitational radiation of compact binaries. *Phys. Rev. D*, 84:064041, 2011. DOI: 10.1103/PhysRevD.84.064041.
- [59] Luc Blanchet, Guillaume Faye, Quentin Henry, François Larrouturou, and David Trestini. Gravitational-Wave Phasing of Compact Binary Systems to the Fourth-and-a-Half post-Newtonian Order. 4 2023.
- [60] Luc Blanchet, Guillaume Faye, Quentin Henry, François Larrouturou, and David Trestini. Gravitational Wave Flux and Quadrupole Modes from Quasi-Circular Non-Spinning Compact Binaries to the Fourth Post-Newtonian Order. 4 2023.
- [61] Yannick Boetzel, Abhimanyu Susobhanan, Achamveedu Gopakumar, Antoine Klein, and Philippe Jetzer. Solving post-Newtonian accurate Kepler Equation. *Phys. Rev. D*, 96(4):044011, August 2017. DOI: 10.1103/PhysRevD.96.044011.
- [62] Yannick Boetzel, Chandra Kant Mishra, Guillaume Faye, Achamveedu Gopakumar, and Bala R. Iyer. Gravitational-wave amplitudes for compact binaries in eccentric orbits at the third post-Newtonian order: Tail contributions and postadiabatic corrections. *Phys. Rev. D*, 100(4):044018, 2019. DOI: 10.1103/PhysRevD.100.044018.
- [63] Alejandro Bohe, Sylvain Marsat, Guillaume Faye, and Luc Blanchet. Next-to-next-to-leading order spin-orbit effects in the near-zone metric and precession equations of compact binaries. *Class. Quant. Grav.*, 30:075017, 2013. DOI: 10.1088/0264-9381/30/7/075017.
- [64] Alejandro Bohé, Guillaume Faye, Sylvain Marsat, and Edward K. Porter. Quadratic-in-spin effects in the orbital dynamics and gravitational-wave energy flux of compact binaries at the 3PN order. *Class. Quant. Grav.*, 32(19):195010, 2015. DOI: 10.1088/0264-9381/32/19/195010.
- [65] Alejandro Bohé, Sylvain Marsat, and Luc Blanchet. Next-to-next-to-leading order spin-orbit effects in the gravitational wave flux and orbital phasing of compact binaries. *Class. Quant. Grav.*, 30:135009, 2013. DOI: 10.1088/0264-9381/30/13/135009.
- [66] Yann Bouffanais, Michela Mapelli, Davide Gerosa, Ugo N. Di Carlo, Nicola Giacobbo, Emanuele Berti, and Vishal Baibhav. Constraining the Fraction of Binary Black Holes Formed in Isolation and Young Star Clusters with Gravitational-wave Data. *ApJ*, 886(1):25, November 2019. DOI: 10.3847/1538-4357/ab4a79.

- [67] Michael Boyle, Duncan A. Brown, Lawrence E. Kidder, Abdul H. Mroué, Harald P. Pfeiffer, Mark A. Scheel, Gregory B. Cook, and Saul A. Teukolsky. High-accuracy comparison of numerical relativity simulations with post-newtonian expansions. *Phys. Rev. D*, 76:124038, Dec 2007. DOI: 10.1103/PhysRevD.76.124038. URL <https://link.aps.org/doi/10.1103/PhysRevD.76.124038>.
- [68] Alessandra Buonanno, Guillaume Faye, and Tanja Hinderer. Spin effects on gravitational waves from inspiraling compact binaries at second post-Newtonian order. *Phys. Rev. D*, 87(4):044009, 2013. DOI: 10.1103/PhysRevD.87.044009.
- [69] Juan Calderón Bustillo, Sascha Husa, Alicia M. Sintes, and Michael Pürrer. Impact of gravitational radiation higher order modes on single aligned-spin gravitational wave searches for binary black holes. *Phys. Rev. D*, 93:084019, Apr 2016. DOI: 10.1103/PhysRevD.93.084019. URL <https://link.aps.org/doi/10.1103/PhysRevD.93.084019>.
- [70] M. Campanelli, C. O. Lousto, P. Marronetti, and Y. Zlochower. Accurate evolutions of orbiting black-hole binaries without excision. *Phys. Rev. Lett.*, 96:111101, Mar 2006. DOI: 10.1103/PhysRevLett.96.111101. URL <https://link.aps.org/doi/10.1103/PhysRevLett.96.111101>.
- [71] Kipp Cannon et al. Toward Early-warning Detection of Gravitational Waves from Compact Binary Coalescence. *ApJ*, 748(2):136, April 2012. DOI: 10.1088/0004-637X/748/2/136.
- [72] Collin Capano, Yi Pan, and Alessandra Buonanno. Impact of higher harmonics in searching for gravitational waves from nonspinning binary black holes. *Phys. Rev. D*, 89:102003, May 2014. DOI: 10.1103/PhysRevD.89.102003. URL <https://link.aps.org/doi/10.1103/PhysRevD.89.102003>.
- [73] Collin D. Capano and Alexander H. Nitz. Binary black hole spectroscopy: A no-hair test of gw190814 and gw190412. *Phys. Rev. D*, 102:124070, Dec 2020. DOI: 10.1103/PhysRevD.102.124070. URL <https://link.aps.org/doi/10.1103/PhysRevD.102.124070>.
- [74] Man Leong Chan, Chris Messenger, Ik Siong Heng, and Martin Hendry. Binary neutron star mergers and third generation detectors: Localization and early warning. *Phys. Rev. D*, 97:123014, Jun 2018. DOI: 10.1103/PhysRevD.97.123014. URL <https://link.aps.org/doi/10.1103/PhysRevD.97.123014>.
- [75] Koustav Chandra, Juan Calderón Bustillo, Archana Pai, and I. W. Harry. First gravitational-wave search for intermediate-mass black hole mergers with higher-order harmonics. *Phys. Rev. D*, 106:123003, Dec 2022. DOI: 10.1103/PhysRevD.106.123003. URL <https://link.aps.org/doi/10.1103/PhysRevD.106.123003>.
- [76] Deep Chatterjee, Shaon Ghosh, and Shasvath J. Kapadia. p-astro. PyPI, 2020.
- [77] Deep Chatterjee et al. A Machine Learning-based Source Property Inference for Compact Binary Mergers. *ApJ*, 896(1):54, June 2020. DOI: 10.3847/1538-4357/ab8dbe.

- [78] Nelson Christensen and Renate Meyer. Using Markov chain Monte Carlo methods for estimating parameters with gravitational radiation data. *Phys. Rev. D*, 64:022001, 2001. DOI: 10.1103/PhysRevD.64.022001.
- [79] Q. Chu et al. Capturing the electromagnetic counterparts of binary neutron star mergers through low-latency gravitational wave triggers. *MNRAS*, 459(1):121–139, June 2016. DOI: 10.1093/mnras/stw576.
- [80] Qi Chu. *Low-latency detection and localization of gravitational waves from compact binary coalescences*. PhD thesis, The University of Western Australia, 2017.
- [81] Dan Coe. Fisher Matrices and Confidence Ellipses: A Quick-Start Guide and Software. *arXiv e-prints*, art. arXiv:0906.4123, June 2009.
- [82] Michael W Coughlin et al. Optimizing searches for electromagnetic counterparts of gravitational wave triggers. *Monthly Notices of the Royal Astronomical Society*, 478(1):692–702, 04 2018. ISSN 0035-8711. DOI: 10.1093/mnras/sty1066. URL <https://doi.org/10.1093/mnras/sty1066>.
- [83] P. S. Cowperthwaite, E. Berger, V. A. Villar, B. D. Metzger, M. Nicholl, R. Chornock, P. K. Blanchard, W. Fong, R. Margutti, M. Soares-Santos, K. D. Alexander, S. Allam, J. Annis, D. Brout, D. A. Brown, R. E. Butler, H. Y. Chen, H. T. Diehl, Z. Doctor, M. R. Drout, T. Eftekhari, B. Farr, D. A. Finley, R. J. Foley, J. A. Frieman, C. L. Fryer, J. García-Bellido, M. S. S. Gill, J. Guillochon, K. Herner, D. E. Holz, D. Kasen, R. Kessler, J. Marriner, T. Matheson, Jr. Neilsen, E. H., E. Quataert, A. Palmese, A. Rest, M. Sako, D. M. Scolnic, N. Smith, D. L. Tucker, P. K. G. Williams, E. Balbinot, J. L. Carlin, E. R. Cook, F. Durret, T. S. Li, P. A. A. Lopes, A. C. C. Lourenço, J. L. Marshall, G. E. Medina, J. Muir, R. R. Muñoz, M. Sauseda, D. J. Schlegel, L. F. Secco, A. K. Vivas, W. Wester, A. Zenteno, Y. Zhang, T. M. C. Abbott, M. Banerji, K. Bechtol, A. Benoit-Lévy, E. Bertin, E. Buckley-Geer, D. L. Burke, D. Capozzi, A. Carnero Rosell, M. Carrasco Kind, F. J. Castander, M. Crocce, C. E. Cunha, C. B. D’Andrea, L. N. da Costa, C. Davis, D. L. DePoy, S. Desai, J. P. Dietrich, A. Drlica-Wagner, T. F. Eifler, A. E. Evrard, E. Fernandez, B. Flaugher, P. Fosalba, E. Gaztanaga, D. W. Gerdes, T. Giannantonio, D. A. Goldstein, D. Gruen, R. A. Gruendl, G. Gutierrez, K. Honscheid, B. Jain, D. J. James, T. Jeltema, M. W. G. Johnson, M. D. Johnson, S. Kent, E. Krause, R. Kron, K. Kuehn, N. Nuropatkin, O. Lahav, M. Lima, H. Lin, M. A. G. Maia, M. March, P. Martini, R. G. McMahon, F. Menanteau, C. J. Miller, R. Miquel, J. J. Mohr, E. Neilsen, R. C. Nichol, R. L. C. Ogando, A. A. Plazas, N. Roe, A. K. Romer, A. Roodman, E. S. Rykoff, E. Sanchez, V. Scarpine, R. Schindler, M. Schubnell, I. Sevilla-Noarbe, M. Smith, R. C. Smith, F. Sobreira, E. Suchyta, M. E. C. Swanson, G. Tarle, D. Thomas, R. C. Thomas, M. A. Troxel, V. Vikram, A. R. Walker, R. H. Wechsler, J. Weller, B. Yanny, and J. Zuntz. The Electromagnetic Counterpart of the Binary Neutron Star Merger LIGO/Virgo GW170817. II. UV, Optical, and Near-infrared Light Curves and Comparison to Kilonova Models. *ApJ*, 848(2):L17, October 2017. DOI: 10.3847/2041-8213/aa8fc7.

- [84] Curt Cutler and Éanna E. Flanagan. Gravitational waves from merging compact binaries: How accurately can one extract the binary’s parameters from the inspiral waveform? *Phys. Rev. D*, 49:2658–2697, Mar 1994. DOI: 10.1103/PhysRevD.49.2658. URL <https://link.aps.org/doi/10.1103/PhysRevD.49.2658>.
- [85] Siddharth Dhanpal, Abhirup Ghosh, Ajit Kumar Mehta, Parameswaran Ajith, and B. S. Sathyaprakash. A no-hair test for binary black holes. *Phys. Rev. D*, 99:104056, May 2019. DOI: 10.1103/PhysRevD.99.104056. URL <https://link.aps.org/doi/10.1103/PhysRevD.99.104056>.
- [86] Divyajyoti, Preet Baxi, Chandra Kant Mishra, and K. G. Arun. Detectability of gravitational higher order modes in the third-generation era. *Phys. Rev. D*, 104:084080, Oct 2021. DOI: 10.1103/PhysRevD.104.084080. URL <https://link.aps.org/doi/10.1103/PhysRevD.104.084080>.
- [87] D. Dobie et al. An optimised gravitational wave follow-up strategy with the Australian Square Kilometre Array Pathfinder. *PASA*, 36:e019, May 2019. DOI: 10.1017/pasa.2019.9.
- [88] Cyrille Doux, Emmanuel Schaan, Eric Aubourg, Ken Ganga, Khee-Gan Lee, David N. Spergel, and Julien Tréguer. First detection of cosmic microwave background lensing and lyman- $\alpha$  forest bispectrum. *Phys. Rev. D*, 94:103506, Nov 2016. DOI: 10.1103/PhysRevD.94.103506. URL <https://link.aps.org/doi/10.1103/PhysRevD.94.103506>.
- [89] M. R. Drout, A. L. Piro, B. J. Shappee, C. D. Kilpatrick, J. D. Simon, C. Contreras, D. A. Coulter, R. J. Foley, M. R. Siebert, N. Morrell, K. Boutsia, F. Di Mille, T. W. S. Holoién, D. Kasen, J. A. Kollmeier, B. F. Madore, A. J. Monson, A. Murguía-Berthier, Y. C. Pan, J. X. Prochaska, E. Ramírez-Ruiz, A. Rest, C. Adams, K. Alatalo, E. Bañados, J. Baughman, T. C. Beers, R. A. Bernstein, T. Bitsakis, A. Campillay, T. T. Hansen, C. R. Higgs, A. P. Ji, G. Maravelias, J. L. Marshall, C. Moni Bidin, J. L. Prieto, K. C. Rasmussen, C. Rojas-Bravo, A. L. Strom, N. Ulloa, J. Vargas-González, Z. Wan, and D. D. Whitten. Light curves of the neutron star merger GW170817/SSS17a: Implications for r-process nucleosynthesis. *Science*, 358(6370):1570–1574, December 2017. DOI: 10.1126/science.aaq0049.
- [90] A. Einstein. Zur Elektrodynamik bewegter Körper. *Annalen der Physik*, 322(10):891–921, January 1905. DOI: 10.1002/andp.19053221004.
- [91] A. Einstein. Die Grundlage der allgemeinen Relativitätstheorie. *Annalen der Physik*, 354(7):769–822, January 1916. DOI: 10.1002/andp.19163540702.
- [92] Albert Einstein. Näherungsweise Integration der Feldgleichungen der Gravitation. *Sitzungsberichte der Königlich Preussischen Akademie der Wissenschaften*, pages 688–696, January 1916.
- [93] Albert Einstein. Über Gravitationswellen. *Sitzungsberichte der Königlich Preussischen Akademie der Wissenschaften*, pages 154–167, January 1918.

- [94] Reed Essick. Semianalytic sensitivity estimates for catalogs of gravitational-wave transients. *Phys. Rev. D*, 108:043011, Aug 2023. DOI: 10.1103/PhysRevD.108.043011. URL <https://link.aps.org/doi/10.1103/PhysRevD.108.043011>.
- [95] Reed Essick and Will Farr. Precision Requirements for Monte Carlo Sums within Hierarchical Bayesian Inference. *arXiv e-prints*, art. arXiv:2204.00461, April 2022. DOI: 10.48550/arXiv.2204.00461.
- [96] Stephen Fairhurst. Triangulation of gravitational wave sources with a network of detectors. *New Journal of Physics*, 11(12):123006, December 2009. DOI: 10.1088/1367-2630/11/12/123006.
- [97] Stephen Fairhurst. Source localization with an advanced gravitational wave detector network. *Classical and Quantum Gravity*, 28(10):105021, May 2011. DOI: 10.1088/0264-9381/28/10/105021.
- [98] Amanda Farah, Maya Fishbach, Reed Essick, Daniel E. Holz, and Shanika Galaudage. Bridging the gap: Categorizing gravitational-wave events at the transition between neutron stars and black holes. *The Astrophysical Journal*, 931(2):108, may 2022. DOI: 10.3847/1538-4357/ac5f03. URL <https://doi.org/10.3847/1538-4357/ac5f03>.
- [99] Will M. Farr. Accuracy Requirements for Empirically Measured Selection Functions. *Research Notes of the American Astronomical Society*, 3(5):66, May 2019. DOI: 10.3847/2515-5172/ab1d5f.
- [100] Maya Fishbach and Daniel E. Holz. Where Are LIGO's Big Black Holes? *ApJ*, 851(2):L25, December 2017. DOI: 10.3847/2041-8213/aa9bf6.
- [101] Maya Fishbach and Vicky Kalogera. Apples and Oranges: Comparing Black Holes in X-Ray Binaries and Gravitational-wave Sources. *ApJ*, 929(2):L26, April 2022. DOI: 10.3847/2041-8213/ac64a5.
- [102] Maya Fishbach, Daniel E. Holz, and Will M. Farr. Does the Black Hole Merger Rate Evolve with Redshift? *ApJ*, 863(2):L41, August 2018. DOI: 10.3847/2041-8213/aad800.
- [103] Daniel Foreman-Mackey. corner.py: Scatterplot matrices in python. *The Journal of Open Source Software*, 1(2):24, jun 2016. DOI: 10.21105/joss.00024. URL <https://doi.org/10.21105/joss.00024>.
- [104] Francois Foucart. Black-hole–neutron-star mergers: Disk mass predictions. *Phys. Rev. D*, 86:124007, Dec 2012. DOI: 10.1103/PhysRevD.86.124007. URL <https://link.aps.org/doi/10.1103/PhysRevD.86.124007>.
- [105] Francois Foucart, Tanja Hinderer, and Samaya Nissanke. Remnant baryon mass in neutron star-black hole mergers: Predictions for binary neutron star mimickers and rapidly spinning black holes. *Phys. Rev. D*, 98(8):081501, October 2018. DOI: 10.1103/PhysRevD.98.081501.
- [106] William A. Fowler and F. Hoyle. Neutrino Processes and Pair Formation in Massive Stars and Supernovae. *ApJS*, 9:201, December 1964. DOI: 10.1086/190103.

- [107] D. Ganapathy, W. Jia, M. Nakano, V. Xu, N. Aritomi, T. Cullen, N. Kijbunchoo, S. E. Dwyer, A. Mullavey, L. McCuller, R. Abbott, I. Abouelfettouh, R. X. Adhikari, A. Ananyeva, S. Appert, K. Arai, S. M. Aston, M. Ball, S. W. Ballmer, D. Barker, L. Barsotti, B. K. Berger, J. Betzwieser, D. Bhattacharjee, G. Billingsley, S. Biscans, N. Bode, E. Bonilla, V. Bossilkov, A. Branch, A. F. Brooks, D. D. Brown, J. Bryant, C. Cahillane, H. Cao, E. Capote, F. Clara, J. Collins, C. M. Compton, R. Cottingham, D. C. Coyne, R. Crouch, J. Csizmazia, L. P. Dartez, N. Demos, E. Dohmen, J. C. Driggers, A. Effler, A. Ejlli, T. Etzel, M. Evans, J. Feicht, R. Frey, W. Frischhertz, P. Fritschel, V. V. Frolov, P. Fulda, M. Fyffe, B. Gateley, J. A. Giaime, K. D. Giardina, J. Glanzer, E. Goetz, R. Goetz, A. W. Goodwin-Jones, S. Gras, C. Gray, D. Griffith, H. Grote, T. Guidry, E. D. Hall, J. Hanks, J. Hanson, M. C. Heintze, A. F. Helmling-Cornell, N. A. Holland, D. Hoyland, H. Y. Huang, Y. Inoue, A. L. James, A. Jennings, S. Karat, S. Karki, M. Kasprzack, K. Kawabe, P. J. King, J. S. Kissel, K. Komori, A. Kontos, R. Kumar, K. Kuns, M. Landry, B. Lantz, M. Laxen, K. Lee, M. Lesovsky, F. Llamas, M. Lormand, H. A. Loughlin, R. Macas, M. MacInnis, C. N. Makarem, B. Mannix, G. L. Mansell, R. M. Martin, K. Mason, F. Matichard, N. Mavalvala, N. Maxwell, G. McCarrol, R. McCarthy, D. E. McClelland, S. McCormick, T. McRae, F. Mera, E. L. Merilh, F. Meylahn, R. Mittleman, D. Moraru, G. Moreno, T. J. N. Nelson, A. Neunzert, J. Notte, J. Oberling, T. O'Hanlon, C. Osthelder, D. J. Ottaway, H. Overmier, W. Parker, A. Pele, H. Pham, M. Pirello, V. Quetschke, K. E. Ramirez, J. Reyes, J. W. Richardson, M. Robinson, J. G. Rollins, C. L. Romel, J. H. Romie, M. P. Ross, K. Ryan, T. Sadecki, A. Sanchez, E. J. Sanchez, L. E. Sanchez, R. L. Savage, D. Schaetzel, M. G. Schiworski, R. Schnabel, R. M. S. Schofield, E. Schwartz, D. Sellers, T. Shaffer, R. W. Short, D. Sigg, B. J. J. Slagmolen, C. Soike, S. Soni, V. Srivastava, L. Sun, D. B. Tanner, M. Thomas, P. Thomas, K. A. Thorne, C. I. Torrie, G. Traylor, A. S. Ubhi, G. Vajente, J. Vanosky, A. Vecchio, P. J. Veitch, A. M. Vibhute, E. R. G. von Reis, J. Warner, B. Weaver, R. Weiss, C. Whittle, B. Willke, C. C. Wipf, H. Yamamoto, L. Zhang, and M. E. Zucker. Broadband quantum enhancement of the ligo detectors with frequency-dependent squeezing. *Phys. Rev. X*, 13:041021, Oct 2023. DOI: 10.1103/PhysRevX.13.041021. URL <https://link.aps.org/doi/10.1103/PhysRevX.13.041021>.
- [108] N. Gehrels. The Swift Gamma-Ray Burst Mission. In E. Fenimore and M. Galassi, editors, *Gamma-Ray Bursts: 30 Years of Discovery*, volume 727 of *American Institute of Physics Conference Series*, pages 637–641, September 2004. DOI: 10.1063/1.1810924.
- [109] Neil Gehrels, John K. Cannizzo, Jonah Kanner, Mansi M. Kasliwal, Samaya Nissanke, and Leo P. Singer. Galaxy Strategy for LIGO-Virgo Gravitational Wave Counterpart Searches. *Astrophys. J.*, 820(2):136, 2016. DOI: 10.3847/0004-637X/820/2/136.
- [110] Yi Gong, Zhoujian Cao, Junjie Zhao, and Lijing Shao. Including higher harmonics in gravitational-wave parameter estimation and cosmological implications for LISA. *arXiv e-prints*, art. arXiv:2308.13690, August 2023. DOI: 10.48550/arXiv.2308.13690.
- [111] Philip B. Graff, Alessandra Buonanno, and B. S. Sathyaprakash. Missing link: Bayesian detection

- and measurement of intermediate-mass black-hole binaries. *Phys. Rev. D*, 92:022002, Jul 2015. DOI: 10.1103/PhysRevD.92.022002. URL <https://link.aps.org/doi/10.1103/PhysRevD.92.022002>.
- [112] Ish Gupta, Ssohrab Borhanian, Arnab Dhani, Debatri Chattopadhyay, Rahul Kashyap, V. Ashley Villar, and B. S. Sathyaprakash. Neutron star-black hole mergers in next generation gravitational-wave observatories. *Phys. Rev. D*, 107(12):124007, 2023. DOI: 10.1103/PhysRevD.107.124007.
- [113] Ian Harry, Juan Calderón Bustillo, and Alex Nitz. Searching for the full symphony of black hole binary mergers. *Phys. Rev. D*, 97:023004, Jan 2018. DOI: 10.1103/PhysRevD.97.023004. URL <https://link.aps.org/doi/10.1103/PhysRevD.97.023004>.
- [114] Edward Higson, Will Handley, Mike Hobson, and Anthony Lasenby. Dynamic nested sampling: an improved algorithm for parameter estimation and evidence calculation. *Statistics and Computing*, 29(5):891–913, September 2019. DOI: 10.1007/s11222-018-9844-0.
- [115] S Hild. Beyond the second generation of laser-interferometric gravitational wave observatories. *Classical and Quantum Gravity*, 29(12):124006, jun 2012. DOI: 10.1088/0264-9381/29/12/124006. URL <https://doi.org/10.1088/0264-9381/29/12/124006>.
- [116] Kenta Hotokezaka et al. Remnant massive neutron stars of binary neutron star mergers: Evolution process and gravitational waveform. *Phys. Rev. D*, 88(4):044026, August 2013. DOI: 10.1103/PhysRevD.88.044026.
- [117] Tousif Islam, Ajit Kumar Mehta, Abhirup Ghosh, Vijay Varma, Parameswaran Ajith, and B. S. Sathyaprakash. Testing the no-hair nature of binary black holes using the consistency of multipolar gravitational radiation. *Phys. Rev. D*, 101(2):024032, 2020. DOI: 10.1103/PhysRevD.101.024032.
- [118] Željko Ivezić et al. LSST: From Science Drivers to Reference Design and Anticipated Data Products. *ApJ*, 873(2):111, March 2019. DOI: 10.3847/1538-4357/ab042c.
- [119] Fredrik Johansson et al. *mpmath: a Python library for arbitrary-precision floating-point arithmetic (version 0.18)*, December 2013. <http://mpmath.org/>.
- [120] Collaboration KAGRA, LIGO Scientific Collaboration, and Virgo Collaboration. Advanced ligo, advanced virgo and kagra observing run plans, 2019. URL <https://dcc.ligo.org/public/0161/P1900218/002/SummaryForObservers.pdf>.
- [121] Collaboration KAGRA, LIGO Scientific Collaboration, and Virgo Collaboration. Public user guide, 2019. URL [https://emfollow.docs.ligo.org/userguide/early\\_warning.html](https://emfollow.docs.ligo.org/userguide/early_warning.html).
- [122] Shasvath J. Kapadia, Mukesh Kumar Singh, Md Arif Shaikh, Deep Chatterjee, and Parameswaran Ajith. Of Harbingers and Higher Modes: Improved Gravitational-wave Early Warning of Compact Binary Mergers. *ApJ*, 898(2):L39, August 2020. DOI: 10.3847/2041-8213/aba42d.



- [123] D. L. Kaplan, A. Rowlinson, K. W. Bannister, M. E. Bell, S. D. Croft, T. Murphy, S. J. Tingay, R. B. Wayth, and A. Williams. A Deep Search for Prompt Radio Emission from the Short GRB 150424A with the Murchison Widefield Array. *ApJ*, 814(2):L25, December 2015. DOI: 10.1088/2041-8205/814/2/L25.
- [124] Daniel Kasen et al. Origin of the heavy elements in binary neutron-star mergers from a gravitational-wave event. *Nature*, 551(7678):80–84, November 2017. DOI: 10.1038/nature24453.
- [125] Lawrence E. Kidder. Using full information when computing modes of post-Newtonian waveforms from inspiralling compact binaries in circular orbit. *Phys. Rev. D*, 77:044016, 2008. DOI: 10.1103/PhysRevD.77.044016.
- [126] Manoj Kovalam, Md Anwarul Kaium Patwary, Anala K. Sreekumar, Linqing Wen, Fiona H. Panther, and Qi Chu. Early warnings of binary neutron star coalescence using the SPIIR search. *The Astrophysical Journal Letters*, 927(1):L9, mar 2022. DOI: 10.3847/2041-8213/ac5687. URL <https://doi.org/10.3847/2041-8213/ac5687>.
- [127] Ely D. Kovetz, Ilias Cholis, Patrick C. Breysse, and Marc Kamionkowski. Black hole mass function from gravitational wave measurements. *Phys. Rev. D*, 95(10):103010, May 2017. DOI: 10.1103/PhysRevD.95.103010.
- [128] M. Lampton, B. Margon, and S. Bowyer. Parameter estimation in X-ray astronomy. *ApJ*, 208: 177–190, August 1976. DOI: 10.1086/154592.
- [129] Yufeng Li, Ik Siong Heng, Man Leong Chan, Chris Messenger, and Xilong Fan. Exploring the sky localization and early warning capabilities of third generation gravitational wave detectors in three-detector network configurations. *Phys. Rev. D*, 105:043010, Feb 2022. DOI: 10.1103/PhysRevD.105.043010. URL <https://link.aps.org/doi/10.1103/PhysRevD.105.043010>.
- [130] LIGO Scientific Collaboration. Instrument science white paper, 2015. URL <https://dcc.ligo.org/public/0120/T1500290/002/T1500290.pdf>.
- [131] LIGO Scientific Collaboration. Instrument science white paper 2018, 2018. URL <https://dcc.ligo.org/public/0151/T1800133/004/T1800133-instrument-science-white-v4.pdf>.
- [132] LIGO Scientific Collaboration. LIGO Algorithm Library - LALSuite. free software (GPL), 2020.
- [133] LIGO Scientific Collaboration, Virgo Collaboration, et al. Binary Black Hole Population Properties Inferred from the First and Second Observing Runs of Advanced LIGO and Advanced Virgo. *ApJ*, 882(2):L24, September 2019. DOI: 10.3847/2041-8213/ab3800.
- [134] Ligo Scientific Collaboration, VIRGO Collaboration, KAGRA Collaboration, et al. Observation of Gravitational Waves from Two Neutron Star-Black Hole Coalescences. *ApJ*, 915(1):L5, July 2021. DOI: 10.3847/2041-8213/ac082e.

- [135] Xiaoshu Liu et al. Measuring the speed of gravitational waves from the first and second observing run of Advanced LIGO and Advanced Virgo. *Phys. Rev. D*, 102(2):024028, July 2020. DOI: 10.1103/PhysRevD.102.024028.
- [136] Lionel London et al. First higher-multipole model of gravitational waves from spinning and coalescing black-hole binaries. *Phys. Rev. Lett.*, 120:161102, Apr 2018. DOI: 10.1103/PhysRevLett.120.161102. URL <https://link.aps.org/doi/10.1103/PhysRevLett.120.161102>.
- [137] Thomas J. Loredo. Accounting for Source Uncertainties in Analyses of Astronomical Survey Data. In Rainer Fischer, Roland Preuss, and Udo Von Toussaint, editors, *Bayesian Inference and Maximum Entropy Methods in Science and Engineering: 24th International Workshop on Bayesian Inference and Maximum Entropy Methods in Science and Engineering*, volume 735 of *American Institute of Physics Conference Series*, pages 195–206, November 2004. DOI: 10.1063/1.1835214.
- [138] Ryan Magee and Ssohrab Borhanian. Realistic observing scenarios for the next decade of early warning detection of binary neutron stars. *arXiv e-prints*, art. arXiv:2201.11841, January 2022.
- [139] Ryan Magee, Deep Chatterjee, Leo P. Singer, Surabhi Sachdev, Manoj Kovalam, Geoffrey Mo, Stuart Anderson, Patrick Brady, Patrick Brockill, Kipp Cannon, Tito Dal Canton, Qi Chu, Patrick Clearwater, Alex Codoreanu, Marco Drago, Patrick Godwin, Shaon Ghosh, Giuseppe Greco, Chad Hanna, Shasvath J. Kapadia, Erik Katsavounidis, Victor Oloworaran, Alexander E. Pace, Fiona Panther, Anwarul Patwary, Roberto De Pietri, Brandon Piotrkowski, Tanner Prestegard, Luca Rei, Anala K. Sreekumar, Marek J. Szczepańczyk, Vinaya Valsan, Aaron Viets, Madeline Wade, Linqing Wen, and John Zweizig. First Demonstration of Early Warning Gravitational-wave Alerts. *ApJ*, 910(2):L21, April 2021. DOI: 10.3847/2041-8213/abed54.
- [140] Michele Maggiore. *Gravitational Waves. Vol. 1: Theory and Experiments*. Oxford University Press, 2007. ISBN 978-0-19-171766-6, 978-0-19-852074-0. DOI: 10.1093/acprof:oso/9780198570745.001.0001.
- [141] K. G. Malmquist. On some relations in stellar statistics. *Meddelanden fran Lunds Astronomiska Observatorium Serie I*, 100:1–52, March 1922.
- [142] K. G. Malmquist. A contribution to the problem of determining the distribution in space of the stars. *Meddelanden fran Lunds Astronomiska Observatorium Serie I*, 106:1–12, February 1925.
- [143] Ilya Mandel, Will M. Farr, and Jonathan R. Gair. Extracting distribution parameters from multiple uncertain observations with selection biases. *MNRAS*, 486(1):1086–1093, June 2019. DOI: 10.1093/mnras/stz896.
- [144] Jeffrey E. McClintock, Ramesh Narayan, and James F. Steiner. Black Hole Spin via Continuum Fitting and the Role of Spin in Powering Transient Jets. *Space Sci. Rev.*, 183(1-4):295–322, September 2014. DOI: 10.1007/s11214-013-0003-9.

- [145] Ajit Kumar Mehta, Chandra Kant Mishra, Vijay Varma, and Parameswaran Ajith. Accurate inspiral-merger-ringdown gravitational waveforms for nonspinning black-hole binaries including the effect of subdominant modes. *Phys. Rev. D*, 96:124010, Dec 2017. DOI: 10.1103/PhysRevD.96.124010. URL <https://link.aps.org/doi/10.1103/PhysRevD.96.124010>.
- [146] Cody Messick et al. Analysis framework for the prompt discovery of compact binary mergers in gravitational-wave data. *Phys. Rev. D*, 95(4):042001, February 2017. DOI: 10.1103/PhysRevD.95.042001.
- [147] Brian Metzger et al. Kilonovae: nUV/Optical/IR Counterparts of Neutron Star Binary Mergers with TSO. *Astro2020: Decadal Survey on Astronomy and Astrophysics*, 2020:306, May 2019.
- [148] Brian D. Metzger. Kilonovae. *Living Reviews in Relativity*, 20(1):3, May 2017. DOI: 10.1007/s41114-017-0006-z.
- [149] Cameron Mills and Stephen Fairhurst. Measuring gravitational-wave higher-order multipoles. *Phys. Rev. D*, 103(2):024042, January 2021. DOI: 10.1103/PhysRevD.103.024042.
- [150] Ehud Nakar. Short-hard gamma-ray bursts. *Physrep*, 442(1-6):166–236, April 2007. DOI: 10.1016/j.physrep.2007.02.005.
- [151] E. T. Newman and R. Penrose. Note on the bondi-metzner-sachs group. *Journal of Mathematical Physics*, 7(5):863–870, 1966. DOI: 10.1063/1.1931221. URL <https://doi.org/10.1063/1.1931221>.
- [152] Isaac Newton. *Philosophiae Naturalis Principia Mathematica*. 1687. DOI: 10.3931/e-rara-440.
- [153] Alexander H. Nitz, Marlin Schäfer, and Tito Dal Canton. Gravitational-wave Merger Forecasting: Scenarios for the Early Detection and Localization of Compact-binary Mergers with Ground-based Observatories. *apjl*, 902(2):L29, October 2020. DOI: 10.3847/2041-8213/abbc10.
- [154] Feryal Özel, Dimitrios Psaltis, Ramesh Narayan, and Jeffrey E. McClintock. The Black Hole Mass Distribution in the Galaxy. *ApJ*, 725(2):1918–1927, December 2010. DOI: 10.1088/0004-637X/725/2/1918.
- [155] A. A. Penzias and R. W. Wilson. A measurement of excess antenna temperature at 4080 mc/s. *The Astrophysical Journal*, 142:419–421, 1965. DOI: 10.1086/148307.
- [156] M. H. Poincaré. Sur la dynamique de l'électron. *Rendiconti del Circolo Matematico di Palermo (1884-1940)*, 21(1):129–175, Dec 1906. ISSN 0009-725X. DOI: 10.1007/BF03013466.
- [157] Geraint Pratten, Cecilio García-Quirós, Marta Colleoni, Antoni Ramos-Buades, Héctor Estellés, Maite Mateu-Lucena, Rafel Jaume, Maria Haney, David Keitel, Jonathan E. Thompson, and Sascha Husa. Computationally efficient models for the dominant and subdominant harmonic modes of precessing binary black holes. *Phys. Rev. D*, 103(10):104056, May 2021. DOI: 10.1103/PhysRevD.103.104056.

- [158] Frans Pretorius. Evolution of binary black-hole spacetimes. *Phys. Rev. Lett.*, 95:121101, Sep 2005. DOI: 10.1103/PhysRevLett.95.121101. URL <https://link.aps.org/doi/10.1103/PhysRevLett.95.121101>.
- [159] M. Punturo et al. The einstein telescope: a third-generation gravitational wave observatory. *Classical and Quantum Gravity*, 27(19):194002, sep 2010. DOI: 10.1088/0264-9381/27/19/194002. URL <https://doi.org/10.1088/0264-9381/27/19/194002>.
- [160] G. Rakavy and G. Shaviv. Instabilities in Highly Evolved Stellar Models. *ApJ*, 148:803, June 1967. DOI: 10.1086/149204.
- [161] David Reitze et al. Cosmic Explorer: The U.S. Contribution to Gravitational-Wave Astronomy beyond LIGO. In *BAAS*, volume 51, page 35, September 2019.
- [162] Surabhi Sachdev et al. An Early-warning System for Electromagnetic Follow-up of Gravitational-wave Events. *Astrophys. J. Lett.*, 905(2):L25, 2020. DOI: 10.3847/2041-8213/abc753.
- [163] Edwin E. Salpeter. The Luminosity Function and Stellar Evolution. *ApJ*, 121:161, January 1955. DOI: 10.1086/145971.
- [164] B. S. Sathyaprakash and B. F. Schutz. Physics, Astrophysics and Cosmology with Gravitational Waves. *Living Rev. Rel.*, 12:2, 2009. DOI: 10.12942/lrr-2009-2.
- [165] B.S. Sathyaprakash. Filtering post-Newtonian gravitational waves from coalescing binaries. *Phys. Rev. D*, 50(12):7111–7115, 1994. DOI: 10.1103/PhysRevD.50.R7111.
- [166] B. F. Schutz. Determining the Hubble constant from gravitational wave observations. *Nature*, 323(6086):310–311, September 1986. DOI: 10.1038/323310a0.
- [167] M. Shibata and K. Uryū. Gravitational waves from the merger of binary neutron stars in a fully general relativistic simulation. *Progress of Theoretical Physics*, 107:265–303, 2002. DOI: 10.1143/PTP.107.265.
- [168] Leo P. Singer and Larry R. Price. Rapid Bayesian position reconstruction for gravitational-wave transients. *Phys. Rev. D*, 93(2):024013, 2016. DOI: 10.1103/PhysRevD.93.024013.
- [169] Kulinder Pal Singh et al. ASTROSAT mission. In *Space Telescopes and Instrumentation 2014: Ultraviolet to Gamma Ray*, volume 9144 of *Society of Photo-Optical Instrumentation Engineers (SPIE) Conference Series*, page 91441S, July 2014. DOI: 10.1117/12.2062667.
- [170] Mukesh Kumar Singh, Shasvath J. Kapadia, Md Arif Shaikh, Deep Chatterjee, and Parameswaran Ajith. Improved early warning of compact binary mergers using higher modes of gravitational radiation: a population study. *MNRAS*, 502(2):1612–1622, April 2021. DOI: 10.1093/mnras/stab125.
- [171] John Skilling. Nested sampling for general Bayesian computation. *Bayesian Analysis*, 1(4):833 – 859, 2006. DOI: 10.1214/06-BA127. URL <https://doi.org/10.1214/06-BA127>.

- [172] Joshua S. Speagle. DYNesty: a dynamic nested sampling package for estimating Bayesian posteriors and evidences. *MNRAS*, 493(3):3132–3158, April 2020. DOI: 10.1093/mnras/staa278.
- [173] Simon Stevenson and Teagan A. Clarke. Constraints on the contributions to the observed binary black hole population from individual evolutionary pathways in isolated binary evolution. *MNRAS*, 517(3):4034–4053, December 2022. DOI: 10.1093/mnras/stac2936.
- [174] Colm Talbot and Jacob Golomb. Growing Pains: Understanding the Impact of Likelihood Uncertainty on Hierarchical Bayesian Inference for Gravitational-Wave Astronomy. *MNRAS*, September 2023. DOI: 10.1093/mnras/stad2968.
- [175] Colm Talbot, Rory Smith, Eric Thrane, and Gregory B. Poole. Parallelized inference for gravitational-wave astronomy. *Phys. Rev. D*, 100(4):043030, August 2019. DOI: 10.1103/PhysRevD.100.043030.
- [176] The LIGO Scientific Collaboration, the Virgo Collaboration, and the KAGRA Collaboration. The population of merging compact binaries inferred using gravitational waves through GWTC-3. *arXiv e-prints*, art. arXiv:2111.03634, November 2021.
- [177] Eric Thrane and Colm Talbot. An introduction to Bayesian inference in gravitational-wave astronomy: Parameter estimation, model selection, and hierarchical models. *PASA*, 36:e010, March 2019. DOI: 10.1017/pasa.2019.2.
- [178] Vaibhav Tiwari. Estimation of the Sensitive Volume for Gravitational-wave Source Populations Using Weighted Monte Carlo Integration. *Class. Quant. Grav.*, 35(14):145009, 2018. DOI: 10.1088/1361-6382/aac89d.
- [179] David Tsang, Jocelyn S. Read, Tanja Hinderer, Anthony L. Piro, and Ruxandra Bondarescu. Resonant Shattering of Neutron Star Crusts. *Phys. Rev. Lett.*, 108(1):011102, January 2012. DOI: 10.1103/PhysRevLett.108.011102.
- [180] Takuya Tsutsui, Atsushi Nishizawa, and Soichiro Morisaki. Early warning of precessing compact binary merger with third-generation gravitational-wave detectors. *Phys. Rev. D*, 104:064013, Sep 2021. DOI: 10.1103/PhysRevD.104.064013. URL <https://link.aps.org/doi/10.1103/PhysRevD.104.064013>.
- [181] Takuya Tsutsui, Atsushi Nishizawa, and Soichiro Morisaki. Early warning of precessing neutron-star black-hole binary mergers with the near-future gravitational-wave detectors, 2021.
- [182] A. Tsvetkova, D. Frederiks, S. Golenetskii, A. Lysenko, P. Oleynik, V. Pal’shin, D. Svinkin, M. Ulanov, T. Cline, K. Hurley, and R. Aptekar. The Konus-Wind Catalog of Gamma-Ray Bursts with Known Redshifts. I. Bursts Detected in the Triggered Mode. *ApJ*, 850(2):161, December 2017. DOI: 10.3847/1538-4357/aa96af.
- [183] Samantha A. Usman et al. The PyCBC search for gravitational waves from compact binary coalescence. *Class. Quant. Grav.*, 33(21):215004, 2016. DOI: 10.1088/0264-9381/33/21/215004.

- [184] Michele Vallisneri. Use and abuse of the fisher information matrix in the assessment of gravitational-wave parameter-estimation prospects. *Phys. Rev. D*, 77:042001, Feb 2008. DOI: 10.1103/PhysRevD.77.042001. URL <https://link.aps.org/doi/10.1103/PhysRevD.77.042001>.
- [185] Chris Van Den Broeck and Anand S. Sengupta. Binary black hole spectroscopy. *Classical and Quantum Gravity*, 24(5):1089–1113, March 2007. DOI: 10.1088/0264-9381/24/5/005.
- [186] Vijay Varma and Parameswaran Ajith. Effects of nonquadrupole modes in the detection and parameter estimation of black hole binaries with nonprecessing spins. *Phys. Rev. D*, 96:124024, Dec 2017. DOI: 10.1103/PhysRevD.96.124024. URL <https://link.aps.org/doi/10.1103/PhysRevD.96.124024>.
- [187] Vijay Varma, Parameswaran Ajith, Sascha Husa, Juan Calderon Bustillo, Mark Hannam, and Michael Pürrer. Gravitational-wave observations of binary black holes: Effect of nonquadrupole modes. *Phys. Rev. D*, 90(12):124004, 2014. DOI: 10.1103/PhysRevD.90.124004.
- [188] C.V. Vishveshwara. Scattering of gravitational radiation by a schwarzschild black-hole. *Nature*, 227:936–938, 1970. DOI: 10.1038/227936a0.
- [189] Salvatore Vitale, Davide Gerosa, Will M. Farr, and Stephen R. Taylor. Inferring the Properties of a Population of Compact Binaries in Presence of Selection Effects. In *Handbook of Gravitational Wave Astronomy*, page 45. 2022. DOI: 10.1007/978-981-15-4702-7\_45-1.
- [190] Digvijay Wadekar, Tejaswi Venumadhav, Javier Roulet, Ajit Kumar Mehta, Barak Zackay, Jonathan Mushkin, and Matias Zaldarriaga. A new search pipeline for gravitational waves with higher-order modes using mode-by-mode filtering. 5 2024.
- [191] J. Weber. Observation of the thermal fluctuations of a gravitational-wave detector. *Phys. Rev. Lett.*, 17:1228–1230, Dec 1966. DOI: 10.1103/PhysRevLett.17.1228. URL <https://link.aps.org/doi/10.1103/PhysRevLett.17.1228>.
- [192] Wolfram Research. Mathematica, Version 13.0.0. 2021. URL <https://www.wolfram.com/mathematica>. Champaign, IL.
- [193] S. E. Woosley and T. A. Weaver. The Physics of Supernovae. In Dimitri Mihalas and Karl-Heinz A. Winkler, editors, *IAU Colloq. 89: Radiation Hydrodynamics in Stars and Compact Objects*, volume 255, page 91. 1986. DOI: 10.1007/3-540-16764-1\_7.
- [194] Michael Zevin, Chris Pankow, Carl L. Rodriguez, Laura Sampson, Eve Chase, Vassiliki Kalogera, and Frederic A. Rasio. Constraining Formation Models of Binary Black Holes with Gravitational-wave Observations. *ApJ*, 846(1):82, September 2017. DOI: 10.3847/1538-4357/aa8408.
- [195] Michael Zevin, Simone S. Bavera, Christopher P. L. Berry, Vicky Kalogera, Tassos Fragos, Pablo Marchant, Carl L. Rodriguez, Fabio Antonini, Daniel E. Holz, and Chris Pankow. One Channel

to Rule Them All? Constraining the Origins of Binary Black Holes Using Multiple Formation Pathways. *ApJ*, 910(2):152, April 2021. DOI: 10.3847/1538-4357/abe40e.